

PHOTOCATALYSIS ON TITANIUM DIOXIDE SURFACES

by

Tracy Lea Thompson

B.S. Chemistry & Exercise Physiology, Baldwin-Wallace College, 2000

Submitted to the Graduate Faculty of

Arts and Sciences in partial fulfillment

of the requirements for the degree of

Doctor of Philosophy

University of Pittsburgh

2006

UNIVERSITY OF PITTSBURGH
FACULTY OF ARTS AND SCIENCES

This dissertation was presented

by

Tracy Lea Thompson

It was defended on

January 27, 2006

and approved by

Dr. David Waldeck

Dr. Kenneth Jordan

Dr. Hrvoje Petek

Dr. John T. Yates, Jr.
Dissertation Director

Photocatalysis on Titanium Dioxide Surfaces

Tracy Lea Thompson, Ph. D.

University of Pittsburgh, 2006

The adsorption, photo- and thermal- chemistry of adsorbates, and the photoactivation of $\text{TiO}_2(110)$ single crystalline surfaces are the central topics investigated and presented in this thesis.

The hole-induced photodesorption of chemisorbed O_2 from a defective $\text{TiO}_2(110)$ surface was studied to monitor the kinetics of electron-hole pair formation, recombination and hole-trapping. Two distinct O_2 desorption processes are found which are characteristic of low and high photon fluxes. At a critical photon flux, the slow O_2 desorption process converts to a fast process as a result of the saturation of hole trapping sites in the TiO_2 crystal. Both the slow and fast O_2 desorption processes are governed by the flux of UV radiation, $F_{\text{hv}}^{1/2}$, indicating that the steady state concentration of photogenerated holes can be described by second-order electron-hole pair recombination kinetics. A hole scavenger is used to probe the role of added hole trap centers on the photodesorption rate.

The photodesorption for O_2 from $\text{TiO}_2(110)$ was found to exhibit fractal kinetic behavior where the photodesorption process is described by a rate coefficient that varies throughout the measurement. A model is proposed in which the electrons associated with O-vacancy defects on the surface percolate from vacancy site to vacancy site via the filled orbitals at these sites to neutralize photo-produced holes. This electron percolation, causing e-h recombination, reduces the efficiency of charge transfer between a photoproduct hole and an $\text{O}_2^-(\text{a})$ species localized at

a vacancy defect site, causing the rate of O₂ photodesorption to follow a fractal rate law. We postulate that the fractal electron conduction path across the surface is one-dimensional.

The adsorption and thermal desorption of CO₂ on TiO₂(110) was investigated as a probe of the concentration of oxygen vacancy defects. For the stoichiometric and fully oxidized surface, a single thermal desorption feature ($E_d = 48.5$ kJ/mol) is measured and is attributed to CO₂ bound to regular 5-fold coordinated Ti⁴⁺ atoms. For the partially reduced TiO₂(110) surface, CO₂ binds not only to regular sites, but also to oxygen vacancy sites ($E_d = 54.0$ kJ/mol), created by thermal annealing. The variation in the characteristic CO₂ desorption kinetics was measured as a function of the surface reduction temperature and the systematic production of increasing levels of surface defects is observed in the temperature range of 600K- 1100K.

The effect of impurity doping on the photoactivity of TiO₂ rutile single crystals was subjected to a combined surface science and bulk analysis study. Two approaches were taken: First, the incorporation of nitrogen ions, N⁻, into TiO₂ single crystals was achieved by sputtering with N₂⁺/Ar⁺ mixtures and subsequent annealing to 900 K under ultra high vacuum conditions; Secondly, a chemical doping method where TiO₂(110) single crystals were exposed to gaseous NH₃ at 870 K was used. The nitrogen implantation method employed in the first study resulted in an unexpected blueshift of the photoexcitation threshold energy for the doped material compared to undoped TiO₂. For crystals doped using the second chemical doping method, a decrease in the required photoactivation energy was observed when compared to undoped TiO₂ crystals.

Finally, the thermal- and photo- chemistry of the mustard gas simulant molecule, 2-chloroethyl ethyl sulfide (2-CEES), was investigated on both TiO₂(110) single crystals and TiO₂ powdered materials. 2-CEES decomposition occurs through the incorporation of lattice oxygen from the TiO₂ material into the oxidized products.

A review of aspects of photochemistry on TiO₂ surfaces forms the concluding chapter of the thesis.

TABLE OF CONTENTS

1. CHAPTER ONE: Introduction to Semiconductor Photocatalysis.....	1
1.1. TiO ₂	2
1.1.1. Lattice Structure of TiO ₂	2
1.1.2. Surface and Electronic Structure of TiO ₂ (110).....	3
1.2. Photoexcitation of Semiconductor Surfaces	6
1.3. Photoexcitation of TiO ₂	7
1.3.1. Charge Carrier Trapping and Recombination.....	8
1.3.2. Lowering the Energy Threshold for Photoexcitation.....	10
1.4. Photo-decomposition of Pollutant Materials	18
1.5. Summary	18
2. CHAPTER TWO: Experimental Apparatus, Methods and Sample Details.....	19
2.1. Ultra-high Vacuum Apparatus.....	19
2.2. Experimental Techniques.....	19
2.2.1. Differentially Pumped QMS.....	20
2.3. TiO ₂ (110) Single Crystal.....	21
2.3.1. TiO ₂ (110) Single Crystal Mounting.....	22
2.3.2. TiO ₂ (110) Single Crystal Sample Cleaning and Preparation.....	23
2.4. Gas Handling and Exposure.....	24
3. CHAPTER THREE: Monitoring Hole Trapping in Photoexcited TiO ₂ (110) using a Surface Photoreaction	25
3.1. Introduction.....	25
3.2. Experimental	27
3.3. Results.....	28
3.4. Discussion.....	38
3.4.1. Dependence of O ₂ Photodesorption Rate on F _{hv} ^{1/2}	38
3.4.2. Electron and Hole Traps in TiO ₂	38
3.4.3. Recombination of Electrons and Holes.....	39
3.4.4. Observation of the Saturation of Hole Traps at a Critical Photon Flux.....	40
3.4.5. Estimate of the Concentration of Hole Trap Sites	41
3.4.6. Role of Added Trap Adsorbates	42
3.4.7. Future Directions	43
3.5. Conclusions.....	43
CHAPTER FOUR: Control of Surface Photochemical Process by Fractal Electron Transport Across the Surface: O ₂ Photodesorption from TiO ₂ (110).....	45
4.1. Introduction.....	45
4.2. Experimental	48
4.3. Results.....	48
4.4. Discussion.....	53
4.4.1. Kinetic Fit to Fractal Kinetics.....	53
4.4.2. The Fractal Rate Controlling Step in O ₂ Photodesorption From Detect Sites on TiO ₂ (110).....	57
4.5. Conclusions.....	59

5. CHAPTER FIVE: CO ₂ as a Probe for Monitoring the Surface Defects on TiO ₂ (110) – Temperature-Programmed Desorption	60
5.1. Introduction.....	60
5.2. Experimental.....	62
5.3. Results.....	63
5.3.1. Thermal Desorption of CO ₂ from TiO ₂	63
5.3.2. CO ₂ Thermal Desorption Spectra from a Sputtered and Annealed Surface	69
5.4. Discussion: Thermal Desorption of CO ₂ from TiO ₂ (110).....	70
5.5. Conclusions.....	72
6. CHAPTER SIX: Molecular Oxygen-Mediated Vacancy Diffusion on TiO ₂ (110) – New Studies of the Proposed Mechanism.....	74
6.1. Introduction.....	74
6.2. Experimental.....	76
6.3. Results.....	77
6.4. Discussion and Conclusions	79
7. CHAPTER SEVEN: The Effect of Nitrogen Ion Implantation on the Photoactivity of TiO ₂ Rutile Single Crystals	80
7.1. Introduction.....	81
7.2. Experimental.....	82
7.3. Results.....	83
7.3.1. Implantation of Nitrogen and Determination of Nitrogen Concentration and Depth Distribution	83
7.3.2. Transmission Electron Microscopy Cross Sections.....	85
7.3.3. O ₂ Photodesorption and the Photoaction Curve.....	87
7.4. Discussion.....	93
7.5. Conclusions.....	97
8. CHAPTER EIGHT: The Photochemical Activity of Nitrogen-Doped TiO ₂ (110) in Visible Light.....	99
8.1. Introduction.....	99
8.2. Experimental.....	102
8.3. Results and Discussion	104
8.3.1. Photoabsorption Spectrum.....	104
8.3.2. Ag Deposition on the Surface of Doped and Undoped TiO ₂ Crystals.....	105
8.3.3. X-ray Photoelectron Spectroscopy	110
8.3.4. Comparison of N-doping Effects in TiO ₂ with those in ZnO	112
8.4. Conclusions.....	113
9. CHAPTER NINE: Adsorption and Thermal Decomposition of 2-Chloro Ethyl Ethyl Sulfide on TiO ₂ Surfaces.....	114
9.1. Introduction.....	115
9.2. Experimental.....	117
9.2.1. Ultrahigh Vacuum Studies on TiO ₂ (110)	117
9.2.2. Transmission IR Studies on TiO ₂ Powders:.....	117
9.2.2.1. IR cell and High Vacuum System.....	117
9.2.2.2. TiO ₂ Powder Materials	119
9.2.2.3. TiO ₂ Activation; 2-CEES Adsorption and Thermal Stability Experiments	120
9.3. Results.....	121

9.3.1.	TiO ₂ (110) Results	121
9.3.1.1.	Adsorption, Desorption and Thermal Decomposition of 2-CEES on Reduced TiO ₂ (110)	121
9.3.2.	Powdered TiO ₂ Results	126
9.3.2.1.	Adsorption of 2-CEES on Partially-Dehydroxylated TiO ₂ Powders - Anatase and Rutile	126
9.3.2.2.	Thermal Activation of 2-CEES on High Area TiO ₂ - Anatase and Rutile ..	130
9.4.	Discussion	136
9.4.1.	Molecular Desorption of 2-CEES	136
9.4.2.	Reaction of 2-CEES with TiO ₂	137
9.5.	Conclusions	140
10.	CHAPTER TEN: Photodecomposition of Adsorbed 2-Chloro Ethyl Ethyl Sulfide on TiO ₂ : Involvement of Lattice Oxygen	141
10.1.	Introduction	142
10.2.	Experimental	144
10.2.1.	Ultra High Vacuum Study of 2-CEES on TiO ₂ (110)	144
10.2.2.	Transmission IR Studies on TiO ₂ Powder	145
10.2.2.1.	TiO ₂ Powder Material	145
10.2.2.2.	High Vacuum System and UV Photoreactor for IR Studies	145
10.2.2.3.	TiO ₂ Activation; 2-CEES Adsorption and Photodecomposition Experiments	147
10.2.3.	GC-MS Studies on TiO ₂ Powder	148
10.3.	Results	149
10.3.1.	Single Crystalline TiO ₂	149
10.3.1.1.	Thermal Desorption of 2-CEES from TiO ₂ (110)	149
10.3.1.2.	Photodecomposition of 2-CEES on TiO ₂ (110) in Vacuum	149
10.3.2.	Powdered TiO ₂ Results-IR Spectroscopy	153
10.3.2.1.	Adsorption of 2-CEES on TiO ₂ Powder	153
10.3.2.2.	IR Measurements of 2-CEES Photodecomposition on TiO ₂ Powder	153
10.3.2.3.	Photodecomposition of 2-CEES on TiO ₂ Powder in Vacuum	156
10.3.2.4.	Formation of Oxidized Products During Photodecomposition of 2-CEES	156
10.3.2.5.	Selected Kinetics Results for 2-CEES Photodecomposition Using Infrared Absorbances	158
10.3.2.6.	Absence of Reactivity after Switching from UV Illumination to Dark Conditions	159
10.3.3.	Powdered TiO ₂ Results- GC-MS Studies	160
10.4.	Discussion	161
10.4.1.	Photodecomposition of 2-CEES on TiO ₂ (110)	161
10.4.2.	Reaction of Lattice O in TiO ₂	164
10.4.3.	Radical Production by Anaerobic Photodecomposition of 2-CEES on TiO ₂	166
10.4.4.	Connection to Photooxidation Chemistry on TiO ₂	167
10.5.	Conclusions	167
11.	CHAPTER ELEVEN: The Photoactivation of TiO ₂ : A Review	169
11.1.	Introduction	169
11.2.	Properties of TiO ₂ Materials	171
11.2.1.	Bulk Structure	171

11.2.2.	Surface Structure of TiO ₂ (110).....	172
11.2.2.1.	Measuring Defects: TiO ₂ (110) – (1 x 1).....	173
11.2.2.2.	Extensive Defect Formation: TiO ₂ (110) - (1 x 2).....	175
11.3.	Excitation of Charge Carriers	176
11.3.1.	Lowering the Threshold Energy for Excitation	177
11.3.1.1.	Nitrogen Doping	177
11.3.1.2.	Carbon Doping.....	184
11.3.1.3.	Transition metal dopants.....	186
11.3.2.	Monitoring Charge Carrier Excitation and Recombination.....	187
11.3.3.	IR Spectroscopy as a Tool for Monitoring CB Electrons.....	188
11.3.3.1.	EPR	191
11.4.	Recombination of Excited Electrons and Holes	193
11.4.1.	Shockley-Read-Hall Recombination At Trap Sites	193
11.4.2.	Kinetics of Recombination	194
11.4.3.	Evidence for Trap Filling – Photodesorption of O ₂	196
11.4.4.	Electron and Hole Scavengers on TiO ₂ Surfaces.....	198
11.5.	Charge Transfer to Adsorbed Species.....	198
11.5.1.	Oxygen Chemisorbed on TiO ₂ Surfaces.....	199
11.5.1.1.	Fractal Kinetics for Charge Transport to Chemisorbed Oxygen during Photodesorption	199
11.5.2.	The Role of Adsorbate Electrophilicity on Charge Transport.....	203
11.6.	UV-Induced Hydrophilicity of TiO ₂	205
11.6.1.	Introduction.....	205
11.6.2.	Contact Angle Measurements.....	207
11.6.3.	Proposed Models.....	209
11.6.3.1.	UV-Induced Defect Production	209
11.6.3.2.	UV-Induced Rupture of Ti-OH Bonding.....	210
11.6.3.3.	Photooxidation of Hydrophobic Contaminant Layers	212
11.7.	Summary and Outlook	217
11.8.	Acknowledgements.....	218
	APPENDIX.....	219
	APPENDIX A.....	220
	New Concepts about TiO ₂ -Based Photocatalysis: Surface Defects, Oxygen and Charge Transfer.....	220
A.	Introduction.....	220
B.	Results and Discussion	222
i.	Defect Creation and Detection on TiO ₂ (110)	222
ii.	Molecular Oxygen Adsorption on Defective TiO ₂	230
iii.	O ₂ -Mediated Vacancy Diffusion on TiO ₂ (110).....	239
iv.	Extension of the Photothreshold of TiO ₂ into the Visible: Doping of TiO ₂	240
v.	Spectroscopic Detection of Electrons, Holes and O ₂ ⁻ Superoxide Species on UV-Irradiated TiO ₂ : Observing Charge Transfer to Adsorbed Molecules.....	244
C.	Summary.....	249
	APPENDIX B.....	251
	UV Lamp Calibration and Photon Flux Calculation.....	251
	APPENDIX C	255

Calculation of the UV Penetration Depth in TiO ₂	255
APPENDIX D	257
Calibration of the Molecular Beam Doser for Accurate Gas Exposure.....	257
APPENDIX E	261
List of Publications (in Ascending Chronological Order)	261
BIBLIOGRAPHY	263

LIST OF TABLES

Table 1: Compliation of the Literature Findings that deal with the use of nitrogen as a dopant for TiO ₂ materials.....	17
Table 2: Energy Dependence of Silver Deposition on Undoped and Nitrogen-Doped Rutile TiO ₂ Single Crystals.....	108
Table 3: Evidence for thermal decomposition products of 2-CEES from TiO ₂ (110).....	126
Table 4: Vibration Frequencies (cm ⁻¹) of 2-CEES: Gas, Ice and Species Adsorbed on TiO ₂ Powders at 255K.....	129
Table 5: Relative Amounts of the Products of the Photoreaction of 2-CEES on TiO ₂ Detected in the Gas Phase.....	160
Table 6:Relative Amounts of the Products of the Photoreaction of 2-CEES on TiO ₂ Detected in Acetonitrile Extract.....	161

LIST OF FIGURES

Figure 1: Picture of photocatalytic self-cleaning ceramic building tiles that have been coated with titania films (white tiles). The dirty brown tiles are uncoated for comparison. Photograph is taken from Reference ²	1
Figure 2: Bulk structure of rutile and anatase titanium dioxide showing the bond lengths and angles between atoms. Figure is reproduced from Reference ³	3
Figure 3: Surface structure of the TiO ₂ (110) surface depicting the 2 types of surface oxygen atoms and 2 types of surface titanium atoms present.	4
Figure 4: STM image of the thermally reduced, oxygen-deficient TiO ₂ (110) - (1 x 1) surface. Image courtesy of Peter Maksymovych.....	5
Figure 5: Schematic diagram of the electronic band structure of an insulator, semiconductor and a metal.....	7
Figure 6: Solar spectrum at sea level on Earth for the sun at Zenith ²³	11
Figure 7: Top-down schematic diagram of the UHV apparatus and surface science tools employed for the work presented in this thesis.....	20
Figure 8: Diagram showing the TiO ₂ (110) crystal mounted to a Ta plate.....	23
Figure 9: Typical Auger spectrum for a clean TiO ₂ (110) surface.	24
Figure 10: Schematic diagram for the experimental apparatus used to measure the photodesorption of oxygen from TiO ₂ . The inset shows an example of the measured photodesorption signal for ¹⁸ O ₂ from TiO ₂ (110).	29
Figure 11: Plot showing the initial photodesorption yield of ¹⁸ O ₂ from TiO ₂ (110) as a function of the square root of the incident light flux, F _{hv} ^{1/2}	30
Figure 12: Schematic diagram of the localization of recombination centers in the near surface region of TiO ₂ (110). The diameter of the light circles schematically represents a mean range for e-h recombination at the recombination center, *. The distance, d _{hv} , corresponds schematically to the mean penetration depth for band gap UV irradiation.	31
Figure 13: Plot showing the decrease in the initial photodesorption yield of ¹⁸ O ₂ from TiO ₂ (110) when exposed to methanol at various coverage. The two straight lines show the predominating behavior as a result of two different bonding configurations for methanol on TiO ₂ (110). The inset shows the characteristic TPD spectra for CH ₃ OH from TiO ₂ (110). TPD spectrum (a) corresponds to 1ML CH ₃ OH coverage.	33
Figure 14: Plot of the initial photodesorption yield for ¹⁸ O ₂ from TiO ₂ (110) versus the square root of the photon flux at two different coverage of CH ₃ OH, compared to clean TiO ₂ (110).	34
Figure 15: Diagram showing possible scattering of O ₂ molecules by adsorbed CH ₃ OH, leading to the slope changes in shown in Figure 14.	36
Figure 16: Plot showing the lack of photooxidation chemistry that might occur when adsorbed ¹⁸ O ₂ and CH ₃ OH are exposed to UV light.	37
Figure 17: Example of the measured oxygen desorption pulse from TiO ₂ (110) after the defective surface was exposed to a saturation coverage of O ₂ . The data illustrate the measurable decrease in the oxygen partial pressure even after 250 seconds.	49

Figure 18: Measurement of the initial oxygen photodesorption rate versus the square root of the incident photon flux.	50
Figure 19: Plot showing the slope change related to the value of k_4 throughout the measurement time for the oxygen photodesorption experiment.	52
Figure 20: Plot showing the measured change in the value of $k_4(k_1/k_3)^{1/2}$ as the coverage of oxygen decreases during the photodesorption process.	53
Figure 21: Plot showing the measured fractal behavior of the oxygen photodesorption process. The data are fit to the scaling law, and shows one-dimensional fractal character. The slight downward curvature of this plot has been reproduced in experiments at lower values of F_{hv}	56
Figure 22: Schematic diagram showing the electron transport that is postulated to occur through the extended filled electronic states surrounding oxygen vacancy sites. As the coverage of adsorbed oxygen decreases, the surface density of the overlapping filled electronic states at vacancy sites increases thus decreasing the rate coefficient for O_2 photodesorption with time.	58
Figure 23: Coverage dependent thermal desorption spectra for $^{13}CO_2$ adsorbed on a fully oxidized $TiO_2(110)$ surface. CO_2 exposures are (a) $3.5 \times 10^{13} CO_2/cm^2$; (b) $5.0 \times 10^{13} CO_2/cm^2$; (c) $8.0 \times 10^{13} CO_2/cm^2$; (d) $9.6 \times 10^{13} CO_2/cm^2$; (e) $1.3 \times 10^{14} CO_2/cm^2$; (f) $1.6 \times 10^{14} CO_2/cm^2$; (g) $2.0 \times 10^{14} CO_2/cm^2$; (h) $2.5 \times 10^{14} CO_2/cm^2$; (i) $3.5 \times 10^{14} CO_2/cm^2$	63
Figure 24: Simulated data versus experimental data for CO_2 thermal desorption from a fully oxidized $TiO_2(110)$ surface for low coverage ranging from 1.5×10^{13} molecules cm^{-2} to 1.5×10^{14} molecules cm^{-2}	65
Figure 25: Normalized coverage dependent thermal desorption spectra for $^{13}CO_2$ adsorbed on $TiO_2(110)$ for surfaces preannealed to (a) 600K; (b) 700K; (c) 800K; (d) 900K; (e) 1000K; (f) 1100K. In these experiments, the $^{13}CO_2$ exposure ranged from 1.5×10^{13} molecules cm^{-2} to 3.5×10^{14} molecules cm^{-2}	67
Figure 26: Simulated data versus experimental data for CO_2 thermal desorption from a fully reduced (900 K) $TiO_2(110)$ surface for low coverage, ranging from 1.5×10^{13} molecules cm^{-2} to 1.5×10^{14} molecules cm^{-2}	68
Figure 27: Characteristic CO_2 thermal desorption spectra from a $TiO_2(110)$ crystal that has been sputtered then annealed prior to CO_2 adsorption according to procedure B. Spectra are shown for various preannealing temperatures, as noted. Each spectrum shown is for the same CO_2 exposure, $1.5 \times 10^{14} CO_2/cm^2$	70
Figure 28: Schematic of O_2 -mediated surface vacancy diffusion on $TiO_2(110)$ taken from ¹²³ . Step 1 involves O_2 dissociation causing defect removal, step 2 involves O atom transport, and step 3 involves lattice O extraction by the O atom, producing a new O vacancy defect plus adsorbed O_2 . Typical vacancy migration distances in this mechanism are $\sim 10\text{\AA}$. The observed vacancy migration direction is in the $\langle 1\bar{1}0 \rangle$ direction across O atom rows and is measured by STM above 180 K on a time scale of seconds ¹²³	75
Figure 29: Isotopomer O_2 photodesorption from $TiO_2(110)$ containing vacancy defect sites produced by annealing in ultrahigh vacuum at 900 K. The experiment at 180 K corresponds to surface conditions which are the same as in the STM experiments. O_2 exposure = $1 \times 10^{15} cm^{-2}$	77
Figure 30: Isotopomer O_2 thermal desorption from $TiO_2(110)$ containing vacancy defect sites produced by annealing in ultrahigh vacuum at 900 K. O_2 desorption occurs at temperatures below, within and above the range of surface temperatures which were studied in the STM	

experiments. The TPD measurements are made in 10 sequential experiments and are averaged together to give better signal-to-noise. Because of some variability in the individual TPD measurements (also observed by others⁸) one should not use the composite curves for kinetic modeling. 78

Figure 31: Nitrogen (1s) spectrum from a nitrogen-implanted TiO₂(110) crystal at two different Ar⁺ sputter depths. 84

Figure 32: SIMS profile of nitrogen-implanted TiO₂(110) crystal. 85

Figure 33: Low magnification TEM image of the cross section of a nitrogen-implanted single crystal. 86

Figure 34: Cross-sectional high-resolution TEM image of the nitrogen-implanted crystal. On top of the monocrystalline rutile lattice are recrystallized rutile grains. The blackened regions in the image indicate lattice strain. 87

Figure 35: Time-dependent ¹⁸O₂ desorption signal for (a) a nitrogen implanted and (b) undoped TiO₂(110) crystal. Total oxygen exposure was 1 x 10¹⁵ molecules cm⁻² causing saturation coverage. The photon flux at 3.96 eV was 1x10¹⁵ photons cm⁻²s⁻¹. The crosshatched areas show the integration range employed in measuring the photodesorption yield. 89

Figure 36: The photoaction curve for O₂ photodesorption from vacuum annealed TiO₂(110) surfaces. The integrated photodesorption magnitude at each energy has been divided by the photon flux at each respective energy to obtain Y_{hv}. Both action curves shown here were normalized to the photodesorption yield measured at 4.1eV. Open squares and triangles represent values that were measured independently on two different nitrogen-doped single crystals. 91

Figure 37: Plots of (O₂ photodesorption yield x hv)^{1/2} vs. photon energy (eV) for undoped and nitrogen-implanted TiO₂(110) crystals. 92

Figure 38: Schematic presentation of the effect of band filling on the photoexcitation threshold energy for a semiconductor with a band gap of E_g (adopted from ref. ¹⁴³). In this energy-momentum diagram for a degenerate n-type semiconductor, two-phonon assisted transitions (E_g ± E_p) are shown to illustrate the usual photon absorption mechanism. If the semiconductor is heavily doped, the Fermi level, E_f, is inside the conduction band in an n-type material by a quantity ξ_n. Since the states below ξ_n are already filled, electronic transitions to states below E_g+ ξ_n are forbidden; hence, the absorption edge should shift to higher energies by a value equal to ξ_n. 96

Figure 39: Absorption spectra of nitrogen-doped and undoped rutile TiO₂ single crystals measured at room temperature. The data have not been corrected for reflection loss. 105

Figure 40: Contact-mode AFM images of silver deposits on the surface of undoped (images ‘a’ and ‘c’) and NH₃-nitrogen doped (images ‘b’ and ‘d’) TiO₂ single crystals after photoreduction with hv = 2.47 eV. Black-to-white vertical contrast in images a and b is 5 nm, whereas in images c and d, vertical contrast scale is 20 nm. 106

Figure 41: Contact-mode AFM images of silver deposits on the surface of undoped (a and c) and NH₃-nitrogen-doped (b and d) TiO₂ single crystals after photoreduction with hv = 2.98 eV. Black-to-white vertical contrast in panels a and b (2D images) is 10 nm, whereas the 3D representation in panels c and d have a vertical scale of 50 nm. 107

Figure 42: Action curve showing the quantum yield versus excitation energy for the photoreduction of silver on the surface of undoped and NH₃-nitrogen-doped TiO₂ single crystals. Error bars in the quantum yield are based on the standard deviation from measurements on 8-18 images from different regions of the crystal (see Table 2). Error bars

in the photon energy correspond to the bandwidth of the interference filters used, where the location of the point is the band maximum of the respective filter transmission spectrum.108

Figure 43: Contact-mode AFM images of silver deposits on the surface of undoped (a and c) and NH₃-nitrogen-doped (b and d) TiO₂ single crystals after photoreduction with $h\nu = 3.16$ eV. Black-to-white vertical contrast in panels a and b (2D images) is 100 nm, whereas the 3D representations in panels c and d have a vertical scale of 200 nm. 109

Figure 44: Nitrogen (N 1s) spectrum from a doped TiO₂(110) crystal at two different Ar⁺ sputter depths: a) 5 Å and b) 60 Å. 111

Figure 45: Schematic of high vacuum apparatus used for infrared studies of TiO₂ powders. ... 118

Figure 46: Thermal desorption spectra for 2-CEES adsorbed on TiO₂(110) for exposures ranging from 0 to 1.5×10^{15} molecules cm⁻². The inset depicts the coverage versus exposure behavior for this system. 122

Figure 47: Simulated data versus experimental data for 2-CEES thermal desorption from TiO₂(110) for low coverage ranging from 5×10^{13} to 3.5×10^{14} molecules cm⁻². 123

Figure 48: Change in surface coverage of S, Cl and C as a function of annealing temperature. Points are normalized to the amount of each element measured by Auger spectroscopy for 1 ML of 2-CEES (shown at 100 K). Inset shows two representative spectra for 1 ML of 2-CEES and for the same exposure after annealing momentarily to 900 K. The enlarged spectra show the same for the Auger regions for S, Cl and C. 124

Figure 49: Representative thermal desorption spectra showing decomposition products from 2-CEES at masses 28 and 29, assigned to the thermal desorption of ethane and ethylene. Initial 2-CEES coverage = 1 ML. 125

Figure 50: Difference IR spectra of 2-CEES adsorbed on TiO₂ anatase and rutile powders at 255K. 127

Figure 51: Difference IR spectra for 2-CEES/TiO₂ (anatase) during heating from 255 to 732 K. 131

Figure 52: Difference IR spectra for 2-CEES/TiO₂ (rutile) during heating from 255 to 732 K. 134

Figure 53: Difference IR spectra for carbonyl, carboxylate, and carbonate species formed during heating of 2-CEES/TiO₂ anatase and rutile powders. 135

Figure 54: Schematic of the thermal processes observed and the formation of products upon heating of 2-CEES on TiO₂(110) and TiO₂ anatase and rutile powders in vacuum. 139

Figure 55: Measurement of the decrease in the TPD peak area of adsorbed 2-CEES with increasing photon fluence. Fitting of the experimental data shows two simultaneous processes which occur, each with a different cross section. 151

Figure 56:a) Measurement of the lack of observed photodesorption of the parent 2-CEES molecule. b) Simulated curve for the expected photodesorption of 2-CEES. The simulation intensity is for the desorption of 0.03 ML of 2-CEES, corresponding to a photodesorption cross section of 4.4×10^{-20} cm². 152

Figure 57: Change in the IR absorbance due to the loss of lattice oxygen as a function of UV exposure during 2-CEES decomposition. The depicted increase in the background IR absorbance signifies the presence of mobile electrons in the conduction band as a result of UV excitation. 155

Figure 58: Loss of alkyl absorbance with increasing UV exposure measured by IR spectroscopy during 2-CEES photodecomposition. 156

Figure 59: Formation of hydrogen-bonded and oxygen-containing products with increasing UV exposure during 2-CEES photodecomposition. 157

Figure 60: Measured kinetics for the formation of products as a result of UV radiation for both hydrogen bonded and other oxygenated products.	158
Figure 61: Absence of additional 2-CEES degradation in the dark.	160
Figure 62: UV absorbance spectra for 2-CEES diluted in n-hexane. The absorbance at wavelengths above 250 nm may be used to estimate the fraction of incident radiation absorbed by 2-CEES on the TiO ₂ (110) crystal.	164
Figure 63: Annual number of papers published where “TiO ₂ or titanium dioxide” and “photo-” are mentioned, beginning in 1992 through November of 2005. Literature search was done using ISI’s Web of Science (www.isiknowledge.com).	170
Figure 64: Bulk crystal structure of rutile (left) and anatase (right). Titanium atoms are grey and oxygen atoms are red.	171
Figure 65: Surface structure of the stoichiometric TiO ₂ (110)-(1x1) surface depicting the 2 different types of titanium and oxygen atoms present.	172
Figure 66: Comparison of the thermal desorption spectra for CO ₂ from an oxidized stoichiometric surface to the CO ₂ desorption from a reduced (900K, 1hr) surface. CO ₂ preferentially adsorbs at defect sites on the reduced surface. The inset to (a) shows the coverage (θ) versus exposure (ϵ) data for CO ₂ adsorbed on the oxidized surface: a mobile precursor mechanism describes the adsorption process. Reproduced with permission from Reference ¹⁵ . Copyright 2003 American Chemical Society.	174
Figure 67: STM images of the reduced TiO ₂ (110)-(1x1) surface (left) and the extensively reduced TiO ₂ (110)-(1x2) surface (right). The (1x2) surface reconstruction forms after extensive annealing at temperatures near 1100 K. The (1x2) surface exhibits both single link and cross-link features, shown schematically in the ball model on the right hand side of the figure. Reprinted with permission from Reference ²²⁶ . Copyright 2003 Elsevier B.V.	176
Figure 68: Comparison of the N (1s) XPS data presented (A) by Asahi et al. ³⁶ and (B) by Diwald et al. ³⁹ . Figure A: Reprinted with permission from Reference ³⁶ . Copyright 2001 AAAS. (www.sciencemag.org). Figure B: Reprinted with permission from Reference ³⁹ . Copyright 2004 American Chemical Society.	179
Figure 69: AFM images of Ag clusters deposited on (a) undoped and (b) NH ₃ -doped TiO ₂ rutile single crystals. Reprinted with permission from Reference ³⁹ . Copyright 2004 American Chemical Society.	180
Figure 70: Comparison of the photoactivation of undoped versus NH ₃ doped TiO ₂ (110) single crystals. The points shown here were measured using the photoreduction of Ag as measured by AFM and reported in Reference ³⁹ . Reprinted with permission from Reference ³⁹ . Copyright 2004 American Chemical Society.	181
Figure 71: Comparison of the calculated electronic structures for N-doped anatase and rutile TiO ₂ as described by Selloni et al. ⁴⁷ . Reprinted with permission from Reference ⁴⁷ . Copyright 2004 American Physical Society.	183
Figure 72: Characteristic EPR signature for photogenerated electrons and holes in fully oxidized anatase TiO ₂ . Right hand schematic shows the location of the conduction band electrons (detected by IR spectroscopy), electrons trapped at shallow trap sites (EPR detection) and charge carrier holes present in the valence band (EPR detection). Reprinted with permission from Reference ⁵⁹ . Copyright 2005 American Chemical Society.	188
Figure 73: Schematic diagram depicting the thermally-activated charge injection of electrons from shallow trap sites into a continuum of states in the conduction band of this wide-band gap semiconductor.	189

Figure 74: IR absorbance spectra for oxidized and reduced TiO ₂ . Trapped electrons are measured by the increase in the background absorbance measured at 2000 cm ⁻¹	190
Figure 75: Correlation between the concentration of trapped electrons and trapped holes as observed by EPR spectroscopy of photoexcited TiO ₂ . At high UV light intensity, trapped electrons are excited into the conduction band (EPR silent). As a result, the concentration of trapped electrons is not equal to the concentration of trapped holes and a break in the linear correlation occurs. Reprinted with permission from Reference ⁵⁹ . Copyright 2005 American Chemical Society.	192
Figure 76: Schematic diagram showing the 4 electronic transition processes that may occur for the charge carrier recombination as described by Reference ²⁵	194
Figure 77: Yield of photodesorbing oxygen for increasing photon flux. A linear correlation between the yield of photodesorbing oxygen and the square-root of the photon flux proves that the recombination process is second-order. Reprinted with permission from Reference ²⁶ . Copyright 2005 American Chemical Society.....	196
Figure 78: Schematic diagram showing the active range of sites for hole trapping. Reprinted with permission from Reference ²⁶ . Copyright 2005 American Chemical Society.	197
Figure 79: Oxygen photodesorption experiment for O ₂ on TiO ₂ (110). Significant desorption is still measured even after 200 seconds. Reprinted with permission from Reference ²⁵⁴ . Copyright 2006 American Chemical Society.	200
Figure 80: Plot of $k_4(k_1/k_3)^{1/2}$ for the photodesorption of oxygen from TiO ₂ as a function of the remaining O ₂ coverage. Reprinted with permission from Reference ²⁵⁴ . Copyright 2006 American Chemical Society.	201
Figure 81: Scaling plot which describes the fractal kinetic behavior for O ₂ desorption from TiO ₂ (110). The scaling factor, <i>h</i> , for this fit suggests that electron transport across the TiO ₂ (110) surface may be one-dimensional. Reprinted with permission from Reference ²⁵⁴ . Copyright 2006 American Chemical Society.	202
Figure 82: Diagram of the electronic charge clouds associated with oxygen vacancy sites on the reduced TiO ₂ (110) surface. Percolation through the charge clouds at unoccupied vacancies is postulated to be one-dimensional. Reprinted with permission from Reference ²⁵⁴ . Copyright 2006 American Chemical Society.	203
Figure 83: Preferential charge transfer from the conduction band of TiO ₂ to molecules adsorbed through an electrophilic moiety. Reproduced in part from Reference ¹⁸⁰ . Copyright 2003 Elsevier B.V.	205
Figure 84: Diagram of the vector forces present at the solid-liquid interface. The measured contact angle (θ) is shown.	208
Figure 85: STM images of the partially reduced TiO ₂ (110)-(1x1) surface before and after UV irradiation. No additional defect formation is observed as a result of UV irradiation, negating the proposed UV induced hydrophilicity model that suggests otherwise.	210
Figure 86: IR absorption spectra for -OH groups on TiO ₂ both before and after UV irradiation in O ₂ and in vacuum. No observed change in the spectrum due to OH groups is measured. Reprinted with permission from Reference ²⁵⁵ . Copyright 2005 American Chemical Society.	212
Figure 87: Diagram of the apparatus used for in situ measurements of the water contact angle on TiO ₂ (110). Reprinted with permission from Reference ²⁵⁵ . Copyright 2005 American Chemical Society.	214

Figure 88: a) Water droplet on unirradiated TiO ₂ in mixed O ₂ + hexane atmosphere. b) The same water droplet after 154 seconds of UV exposure. c) Sudden and complete wetting of the water droplet on the TiO ₂ surface after 155 seconds. Reprinted with permission from Reference ²⁵⁵ . Copyright 2005 American Chemical Society.	215
Figure 89: Measured contact angles for water droplets on the TiO ₂ surface exposed to varying levels of hexane. The induction period before complete wetting increases with increasing hexane partial pressure as shown in the right hand side. Reprinted with permission from Reference ²⁵⁵ . Copyright 2005 American Chemical Society.	216
Figure 90: Diagram showing the mechanism for the measured photoinduced hydrophilicity effect on TiO ₂ surfaces. Reprinted with permission from Reference ²⁵⁵ . Copyright 2005 American Chemical Society.	217
Figure 91: CO ₂ TPD from oxidized (left) and reduced (right) TiO ₂ (110) surfaces. Inset to Figure 91a shows a departure from Langmuirian kinetics, proving that CO ₂ adsorbs through a mobile precursor mechanism. Figure 91a and b are taken from Reference ¹⁵	224
Figure 92: (a) STM image showing the point defects (oxygen vacancies) on the TiO ₂ (110) surface. Image taken from Reference ²¹¹ . (b) Structural diagram of the TiO ₂ (110)-(1x1) surface. (c) Structural diagram of the TiO ₂ (110)-(1x2) surface presented by Pang et al. ¹²¹	226
Figure 93: Figure 93a shows the 2PPE spectra for TiO ₂ (110) with varying defect densities. Figure 93b is a representative band energy diagram depicting the 2PPE process. The figure has been slightly modified from reference ¹³	228
Figure 94: Band energy diagram depicting the Knotek-Feibelman mechanism for core hole Auger decay after electron bombardment ^{275,276} , leading to O ⁺ ejection (Electron Stimulated Desorption, ESD).	230
Figure 95: Schematic diagram showing the mechanism for O ₂ adsorption and photo-induced desorption from a defective TiO ₂ (110) surface.	232
Figure 96: Experimental data for O ₂ photodesorption yield versus photon energy (shown as ■) and the theoretical results for the same process ⁶²	234
Figure 97: Data for O ₂ photodesorption and the correlation to the CO ₂ yield from CO oxidation as a result of the presence of α-type O ₂ . Figure taken from reference ⁵⁵	236
Figure 98: Data for the thermal- and photo- desorption behavior for TiO ₂ (110) surfaces prepared either by annealing in vacuum, or by sputtering and annealing.	237
Figure 99: Schematic diagram presented by Besenbacher et al. for the mechanism for O ₂ mediated vacancy diffusion on TiO ₂ (110) ¹²³	239
Figure 100: Isotopic mixing experiment for the photo- and thermal-desorption of ¹⁸ O ₂ adsorbed on Ti ¹⁶ O ₂ (110). No isotopic mixing is observed ²⁷⁹	240
Figure 101: Change in the photothreshold energy TiO ₂ (110) doped by N ₂ ⁺ implantation or by high temperature NH ₃ treatment. XPS data for either doping situation is also presented ^{39,53}	243
Figure 102: EPR signatures for photogenerated Ti ³⁺ (electrons) and O ⁻ (holes). Image on the right side is a schematic diagram for the UV-induced generation of electron-hole pairs and the respective measurement method utilized for their detection ⁵⁹	244
Figure 103: Characteristic EPR signature for O ₂ adsorbed as O ₂ ⁻ on TiO ₂ ⁵⁹	246
Figure 104: (a) Diagram showing the photoexcitation of electrons into a continuum of states within the conduction band. (b) IR background absorbance change for (i) 0 seconds and (ii) 1200 seconds irradiation by UV light (3.0 eV ≤ hv ≤ 6.2 eV) ⁵⁹	247

Figure 105: Selective electron scavenging by more electronegative molecules. The figure represents the preferential charge transfer through the electronegative chlorine molecule and lack of charge transfer to the less electronegative molecule ¹⁸⁰	248
Figure 106: Irradiance profile for 500 W Hg Arc Lamp Model 6285 employed for photochemical experiments presented in this thesis.....	251
Figure 107: Geometrical position of the various components of the UV Lamp, Quartz Beam Splitter, Thermopile and Photodiode used for lamp calibration measurements.	252
Figure 108: Calibration data for the photodiode used in conjunction with the thermopile at varied photon energies.	253
Figure 109: UV transmittance data for a TiO ₂ (110) single crystal (1mm thickness) and TiO ₂ films of varying thickness.	255
Figure 110: Measured UV transmission through TiO ₂ films of varying thickness at 312 nm. ..	256
Figure 111: Schematic diagram of the design of the microcapillary array beam doser used for accurate gas exposures to a single crystal surface. Figure taken from Reference ⁵⁴	258
Figure 112: Calibration of the capillary array molecular beam doser for Ar(g).....	259
Figure 113: Percent of gas flux intercepted by a crystal for varying geometrical arrangements. Figure reproduced from Reference ¹²⁵	260

PREFACE

If one were to consider the significant milestones in their own lives, it would become necessary to also consider those who have made these milestones possible. Here, I will do my best to acknowledge the people who have made this thesis a reality.

I would like to begin by thanking my advisor and mentor, Dr. John T. Yates, Jr. for his persistence, guidance and advice. John offers to his students not only his scientific input and mentoring support, but provides an example of someone who has truly found their calling in life. John demonstrates this daily with a passion for his work that exceeds that which I have ever experienced in any of my colleagues or peers. I can only hope to find such fortune in my own career.

There are many individuals with whom I have directly worked in the Surface Science Center who deserve my sincere gratitude: To Dr. Tykhon Zubkov, thank you so very much for the time you spent introducing me to the intricacies of ultra-high vacuum technology. Throughout the time we shared in the SSC, you were an excellent source of information and provided patient, thorough answers to my often tedious questions. I would like to thank Dr. Oliver Diwald for his significant contributions to the experimental work presented in this document. Oliver is an incredible resource: his insight and creativity are especially appreciated. I also wish to acknowledge Dr. Olivier Guise, who has been a wonderful friend and confidant during my time here. I also thank Margie Augenstein for all of her invaluable assistance, including daily lunch conversations. Margie has been a wonderful source for honest, helpful advice. She has been, and will continue to be, a critical element in the success of the Surface Science Center. To my other

co-workers in the SSC who are too numerous to name here, I thank all of you for your help, time and input. I am lucky to have had the opportunity to meet all of you.

The staff in the Department of Chemistry at the University of Pittsburgh is an amazing group. Primarily, I wish to thank the individuals in the Machine, Electronics and Glass Shop who provide wonderful service. Their assistance has been invaluable in projects ranging from equipment repair to attempts made at the impossible. To the main office staff, I thank you for your professional assistance and personal encouragement.

My time in Pittsburgh has been blessed with many great friends, mainly centered around my involvement with Three Rivers Rowing Association. Rowing has provided me with a physical outlet, some amazing experiences and a superb group of friends that I will never forget.

I wish to thank my family and friends for their support and encouragement. To my parents, Stephanie and Douglas Thompson, I thank you for the values that you have instilled in me. From you, I have learned what it means to set goals and to work hard to achieve them. Thank you for your encouragement and confidence. To my brothers, Lucas and Garrett, I hope I have provided for you an example of persistence: You both are nothing short of the best brothers any girl could have. I also wish to acknowledge my grandparents, great-grandmother and other extended family for their prayers, love and support. My grandfather always wanted me to become a doctor, so I hope this is good enough.

I wish to thank my best friend and fiancé Joshua Albers, who has refused to allow me to become anything other than what I have set out to be. Thank you for your support throughout this long journey.

“Life is not easy for any of us. But what of that? We must have perseverance, and above all, confidence in ourselves. We must believe that we are gifted for something and that this thing must be attained.”

-Marie Curie

“It is not so very important for a person to learn facts. For that he does not really need a college. He can learn them from books. The value of an education... is not learning of many facts but the training of the mind to think something that cannot be learned from textbooks.”

-Albert Einstein

1. CHAPTER ONE: Introduction to Semiconductor Photocatalysis

The field of photocatalysis on titanium dioxide surfaces has grown exponentially with time since the initial discovery of photoinduced water splitting over titanium dioxide electrodes reported by Fujishima and Honda¹. This initial discovery has sparked unprecedented interest in basic fundamental research of the mechanism of the photoactivation of semiconductors, the subsequent photo-oxidation or photo-reduction of adsorbates, and the resulting product formation. Even without a complete understanding of these basic fundamentals, there exists a large number of consumer based products that utilize the self-cleaning technology caused by photocatalysis. These products range from photocatalytic TiO₂-coated self-cleaning building materials including ceramic tiles (see Figure 1), glass windows, textiles and aluminum siding, to novel items like self-cleaning window blinds, stain-proof plastic films and photocatalytic air cleaners².

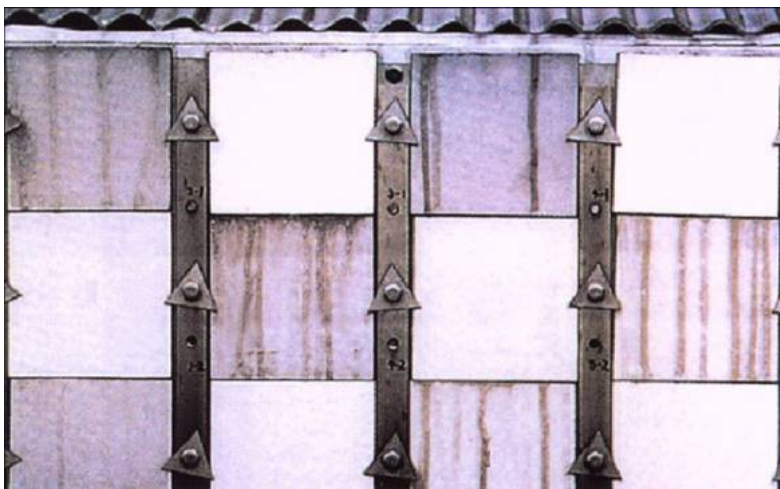


Figure 1: Picture of photocatalytic self-cleaning ceramic building tiles that have been coated with titania films (white tiles). The dirty brown tiles are uncoated for comparison. Photograph is taken from Reference ².

Because the applicability of titania-based photocatalytic technology has been clearly demonstrated, strong motivation exists to elucidate the mechanism of photocatalysis on TiO₂,

and of course, to improve upon the existing technology. The work presented in this thesis focuses on this goal.

1.1. TiO₂

1.1.1. Lattice Structure of TiO₂

The bulk structure of titanium dioxide materials can exist in one of three forms: rutile, anatase and brookite. Diebold³ has reviewed the basic structural characteristics of both anatase and rutile materials, as the brookite structure is not often used for experimental investigations. In addition, Henrich and Cox⁴ present a generalized discussion of the bulk structures of most metal oxide crystals. Both the rutile and anatase crystal structures are in the distorted octahedron class⁵. In rutile, the distortion is slightly orthorhombic where the unit cell is stretched beyond a cubic shape. In anatase, the distortion of the cubic lattice is more significant, and thus the resulting symmetry is less than orthorhombic. Figure 2 shows a structural diagram of the bulk rutile and anatase materials³. The bond lengths and angles between atoms are depicted, showing the stretched cubic shape.

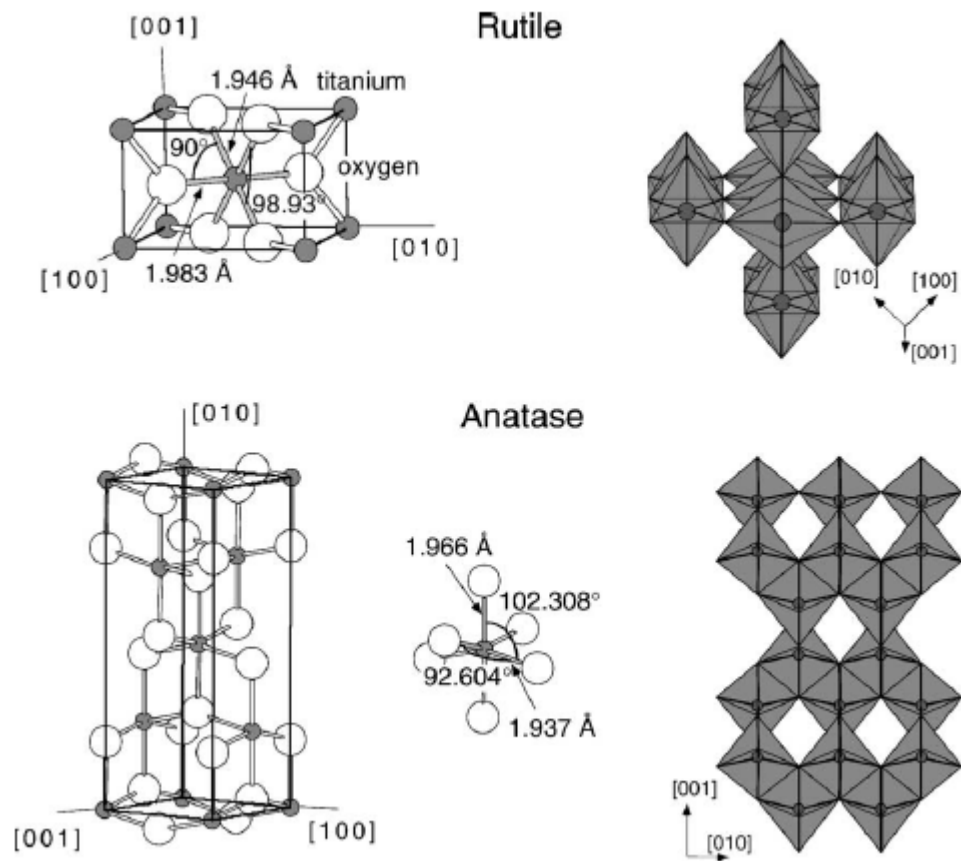


Figure 2: Bulk structure of rutile and anatase titanium dioxide showing the bond lengths and angles between atoms. Figure is reproduced from Reference ³.

1.1.2. Surface and Electronic Structure of TiO₂(110)

The surface structure of the rutile TiO₂(110) single crystal surface has been well characterized, as it is the most commonly investigated titania material. The surface consists of rows of bridging oxygen atoms that lie above the in plane surface. The rows of bridging oxygen atoms are located directly on top of 6-fold coordinated Ti rows. The 6-fold coordinated Ti rows exist in the same plane as 5-fold coordinated Ti atoms. The rows of 5- and 6- fold Ti atoms are separated by rows of in-plane oxygen. A model of the stoichiometric surface depicting all four types of surface atoms is shown in Figure 3.

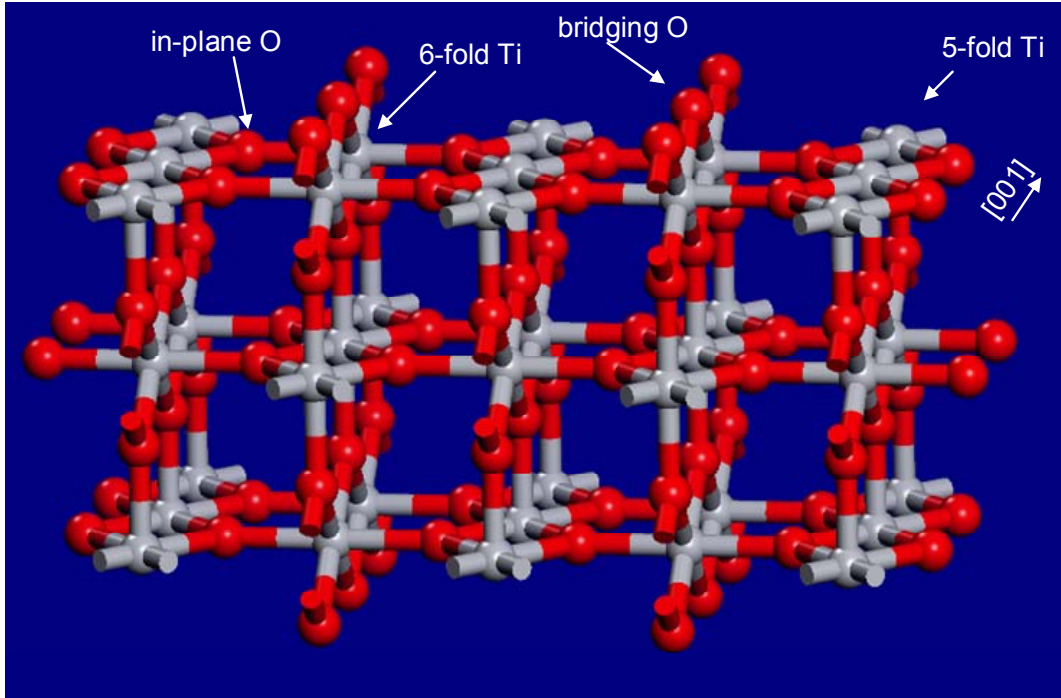


Figure 3: Surface structure of the TiO₂(110) surface depicting the 2 types of surface oxygen atoms and 2 types of surface titanium atoms present.

The photoactivity of the TiO₂(110) surface is critically dependent on the presence of defects in the surface region of the crystal substrate. These defects, known to be oxygen vacancies located in the bridging oxygen rows, can be created by thermal annealing^{3,6-8} or by ion sputtering^{9,10}, and have been previously quantified using He ion scattering¹¹, scanning tunneling microscopy^{3,12}, photoelectron spectroscopies^{13,14} or by adsorption/desorption methods¹⁵⁻¹⁹. The presence of these defects changes the electronic structure of the material through the introduction of an interband electronic donor state (Ti 3d character) 0.8 eV below the Fermi level²⁰. Thermal annealing to temperatures near 900K produces 8-10% of surface vacancy sites^{7,16}. This defect density is maintained even with additional annealing for longer times due to the diffusion of titanium interstitial atoms from the surface region to regions within the bulk of the crystal or by the diffusion of oxygen atoms from the bulk to the surface, thus maintaining this measured defect density⁹. The interband donor state disappears with molecular oxygen exposure at room

temperature and above as caused by the defect states becoming filled with oxygen atoms by the dissociative adsorption of molecular O_2 ^{7,8}. When reduced by thermal annealing, defective TiO_2 surfaces that have donor levels as discussed above are considered to be n-type semiconductors²¹.

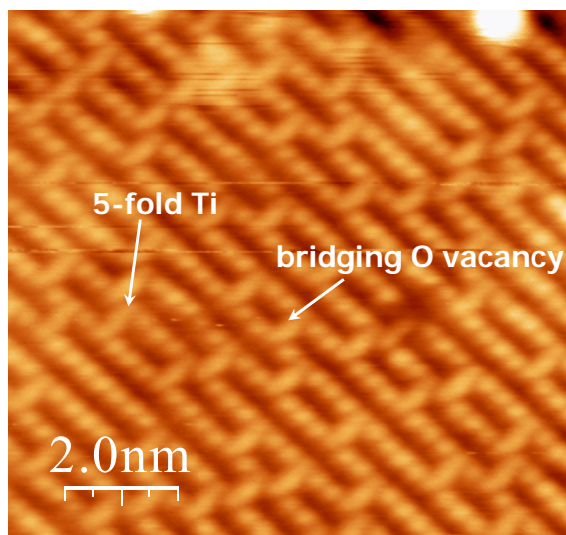


Figure 4: STM image of the thermally reduced, oxygen-deficient $TiO_2(110)$ - (1 x 1) surface. Image courtesy of Peter Maksymovych.

The quantity of defects that are created by thermal annealing can be analyzed through the adsorption and subsequent thermal desorption of CO_2 from the $TiO_2(110)$ surface¹⁵ (see Chapter 5). On the stoichiometric $TiO_2(110)$ surface, CO_2 adsorbs at regular Ti^{4+} sites on the surface of the crystal ($E_{des} = 48.5 \text{ kJ mol}^{-1}$). The coverage dependent thermal desorption spectra for CO_2 adsorbed at these sites consists of a single feature peak at near 160 K. Upon thermal annealing to temperatures near 600 K, defect formation on the $TiO_2(110)$ -(1 x 1) surface begins to occur. The presence of defects can be detected using CO_2 as a probe molecule: CO_2 preferentially adsorbs at defect sites at low coverages²². At higher coverage, when defects are present, CO_2 adsorbs to both defect sites ($E_{des} = 54.0 \text{ kJ mol}^{-1}$) and at regular sites. The thermal desorption profile for CO_2 from TiO_2 consists of a 2 peak pattern characteristic of the quantity of defects present as the

annealing temperature is increased. This method serves as a simple quantitative measure for the defect density in TiO₂(110) single crystalline substrates.

1.2. Photoexcitation of Semiconductor Surfaces

Semiconductor materials are characterized by their electronic structure, which can be described by the band theory of materials²¹. Band theory describes all materials as a function of the allowed electronic energy levels, defined as bands. Materials are classified by the energy gap that exists between these bands, also known as the band gap. Figure 2 schematically illustrates the differences in the electronic structure of an insulator (very large band gap), a semiconductor (some bandgap) and a metal (no band gap, but rather a continuum of electronic states throughout the material). According to band theory, the valence band exists as filled energy levels, while the conduction band consists of available electronic states that are vacant, until the material is thermally or electronically excited. For an intrinsic (pure) semiconductor, the Fermi level, E_f , depicted in Figure 5 as a dotted line, is defined as the energy level in the middle of the bandgap. The location of the Fermi level for an extrinsic or doped semiconductor varies based on the concentration and type of dopant. For an n-type semiconductor like TiO₂, the Fermi level is can be derived according to:

$$E_F = E_i + k_B T \ln \left(\frac{N_D}{n_i} \right) \quad (1.1)$$

where E_f is the Fermi energy, E_i is the initial energy (or the position of E_f for an intrinsic semiconductor), k_B is the Boltzmann constant, T is the temperature (K), N_D is the concentration of donors, and n_i is the intrinsic carrier density. As such, for n-type semiconductors, the Fermi level is slightly elevated towards the conduction band.

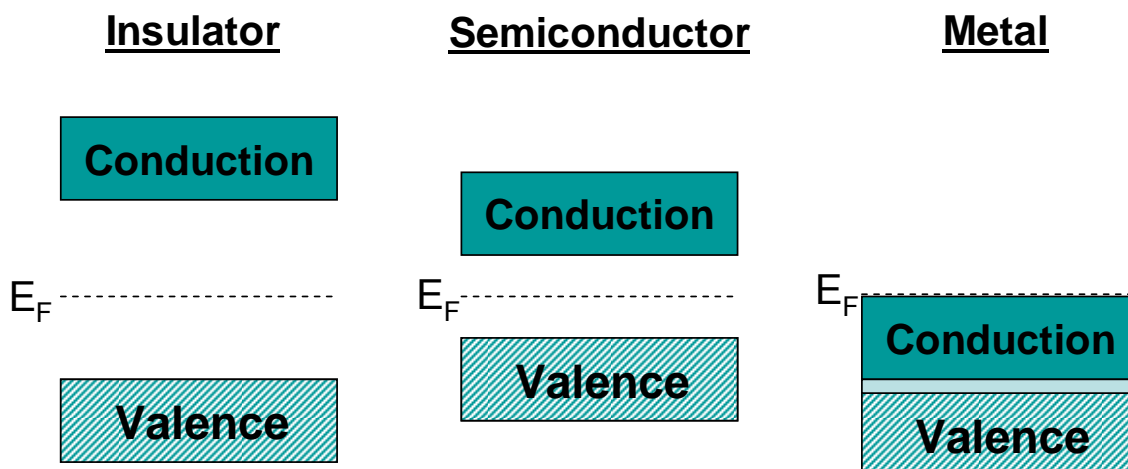


Figure 5: Schematic diagram of the electronic band structure of an insulator, semiconductor and a metal.

Excitation of any semiconductor occurs when the material is exposed to photons that have the same or greater energy than the inherent bandgap of the semiconductor material. When this occurs, electrons are promoted from the valence band, across the band gap, to the conduction band, leaving behind a hole. Both the electron and hole pair are then active to do chemistry at the surface of the semiconductor material. The electron acts as a reducing agent and the hole as an oxidizing agent.

1.3. Photoexcitation of TiO_2

Non-Defective TiO_2 Surfaces

Photoexcitation occurs when photon energy greater than the bandgap of the TiO_2 (3.05 eV for rutile, 3.2 eV for anatase) is absorbed, thus creating mobile electron-hole pairs in the near surface region of the substrate. The surface electronic structure for TiO_2 is very similar to the bulk structure, as the conduction band consists of mainly of Ti 3d character while the valence band has O 2p character²³.

Defective TiO₂

As mentioned above, surface oxygen vacancies create inter-band gap donor states below the conduction band of TiO₂. The loss of an oxygen atom from the surface of the TiO₂ results in the presence of 2 excess electrons in the conduction band. These extra electrons are available for charge transfer to adsorbate molecules: the accumulation of these extra electrons cause downward band bending of the conduction band³. The photon induced creation of electrons and holes occurs in the same manner as for the stoichiometric surface, and is affected by the incident light intensity (Chapter 3), charge trapping and recombination (Chapter 3) and the presence of electronic charge clouds on the surface (Chapter 4). Experimental work on the lowering of the threshold energy necessary for excitation is presented in Chapters 7 and 8. A brief overview of these topics is introduced here.

1.3.1. Charge Carrier Trapping and Recombination

The concentration of charge carriers produced upon UV excitation in any semiconductor is reduced by the inherent recombination process which may occur, leading to the destruction of active electron-hole pairs. For TiO₂, this action can be explained by the Shockley-Read-Hall model for nonradiative recombination which describes the capture of mobile electrons and/or holes at trap sites within the semiconductor^{24,25}. Once trapped, the electron (or hole) is then annihilated via recombination with holes from the valence band (or electrons from the conduction band). The active sites for electron or hole trapping may vary and are usually described as defect states within the crystal which may be due to interstitial atoms, defect states, grain boundaries and the like. In the Shockley-Read-Hall mechanism four transition processes may occur: 1) electron capture; 2) electron emission; 3) hole capture; 4) hole emission. This model assumes that the semiconductor is non-degenerate and that the density of trap states is

relatively small compared to the majority carrier density present in the material. A non-degenerate semiconductor is defined as a material where the Fermi level lies in the bandgap at an energy level at least $3k_B T$ above the valence band edge and at least $3k_B T$ below the conduction band edge. For a $\text{TiO}_2(110)$ single crystal the concentration of hole-trapping sites was estimated by Thompson et al.²⁶ (see Chapter 3) to be on the order of $2.5 \times 10^{18} \text{ cm}^{-3}$, which is equivalent to an atomic fraction of 3×10^{-5} of the bulk atomic sites in the crystal.

Very recently, the kinetic processes by which photochemistry on TiO_2 is governed was investigated using a simple surface photochemical reaction, namely the photon induced desorption of molecular oxygen from $\text{TiO}_2(110)$. In order to study the relative activity of photogenerated charge carriers, the effect of the incident light intensity on the rate of photodesorption of O_2 was investigated. This work builds on that of other authors who have reported a poorly-established correlation between reaction rate or photo-oxidation rate to the square root of the incident light intensity²⁷⁻³². Those experiments differ significantly from the work where experiments presented in Reference²⁶ (see Chapter 3) which involve carefully controlled studies of a simple photoprocess which occurs in ultrahigh vacuum on a planar single crystal of TiO_2 with known surface structure³, known surface defect density⁷, and in the absence of solvents and surface-bound chromophores. In addition, in our studies presented in Chapters 3 and 4, both the photon flux and photon energy are accurately measured. Thus, quantification of the rate of a well-defined photoprocess compared to the photon flux received by the planar single crystal surface can be accurately made in this model system involving a $\text{TiO}_2(110)$ single crystal.

The rate constant for oxygen photodesorption, which describes the interaction on the surface of a photogenerated hole with an adsorbed O_2 molecule, was found to vary with time throughout the oxygen photodesorption experiment (see Chapter 4). This finding is contrast to

earlier published reports that describe the oxygen photodesorption process by a multi-exponential function corresponding to a sequence of discrete cross sections for the photodesorption process. In Chapter 4, the experimental work presented suggests that the rate constant for photodesorption is more appropriately defined as a rate “coefficient”: the rate coefficient changes by a factor of more than 100 over the time of the photodesorption experiment (262 seconds). The behavior of this process and the variation in the rate coefficient with time can be described by a fractal kinetic rate law defined by Kopelman^{33,34} and described in Chapter 4. The fractal nature of the oxygen photodesorption experiment is directly related to the electronic state that is known to surround an oxygen vacancy site³⁵, and to the percolation network that forms on the TiO₂(110) surface when the electronic states interact with one another. During the oxygen photodesorption experiment, as the coverage of oxygen decreases, there is a subsequent increase in the electronic charge cloud overlap on the surface, thus providing continually improving percolation pathways for charge recombination, thus reducing the probability for photogenerated holes to transfer to adsorbed O₂ molecules.

1.3.2. Lowering the Energy Threshold for Photoexcitation

Due to the inherent relatively large bandgap characteristic of TiO₂ materials (3.05 for rutile, 3.2 eV for anatase)³, a great deal of research has focused on lowering the threshold energy for excitation in order to utilize a larger fraction of visible light for conversion to photochemical energy. Figure 6 depicts the solar spectrum measured at sea level for the sun at zenith. As shown here, only a small fraction of sunlight is currently useful for the activation of TiO₂. Recently, significant progress has been made in lowering the photothreshold energy for TiO₂ photoexcitation thru doping with impurity atoms including N, C, S or transition metals. Chapters

7 and 8 of this thesis present experimental work of 2 different attempts made at doping TiO₂(110) single crystalline substrates with nitrogen species.

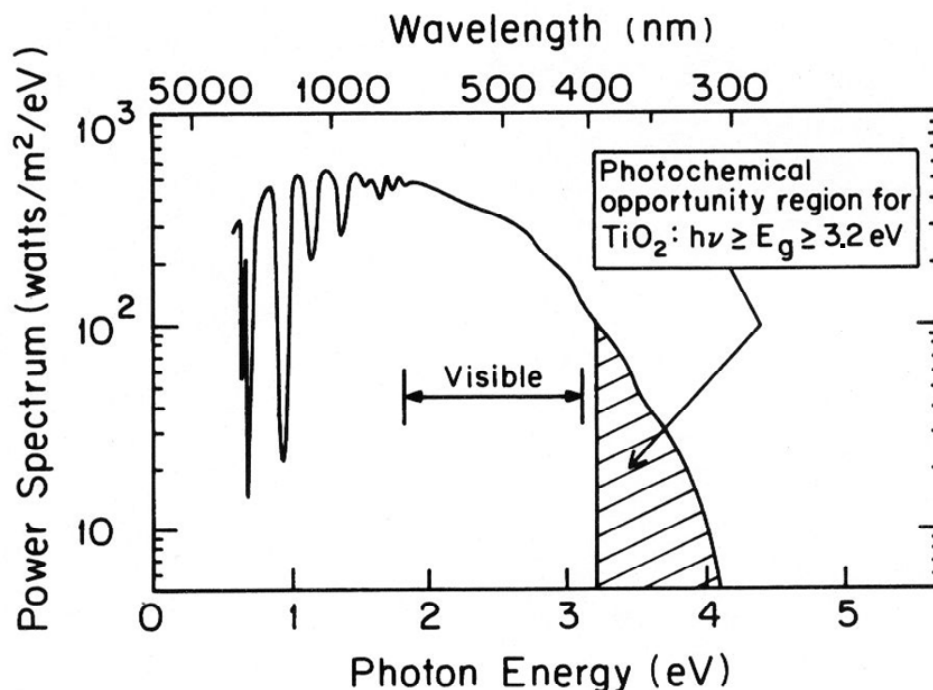


Figure 6: Solar spectrum at sea level on Earth for the sun at Zenith²³.

The idea of doping titanium dioxide materials with nitrogen and other anionic species was first presented by Asahi et al. in 2001³⁶. They report theoretical results where they have substituted C, N, F, P or S for oxygen atoms in the titania lattice. Results of density of states (DOS) calculations for anatase TiO₂ suggest that substitutional type doping (interstitial type doping, or a mixture of both substitutional and interstitial type were both found to be ineffective) using nitrogen is effective due to the mixing of nitrogen 2p states with oxygen 2p states, thus causing a significant decrease in the width of the overall bandgap. Similar calculated results were also measured for S-doping, however, S is not commonly employed due to its large ionic radius. Asahi et al. further investigated the use of nitrogen as a substitutional dopant experimentally through characterization of TiO_{2-x}N_x films. The doped material, made by sputtering TiO₂ films

with N₂/Ar mixtures³⁶, was found to consist of both anatase and rutile grain structure, and was shown to absorb light below 500nm. The photocatalytic activity of the films was analyzed by measuring the decomposition rates for the photooxidation of methylene blue as a function of photon energy in addition to the measurement of the photodecomposition of gaseous acetaldehyde³⁶. All of the films showed enhanced photocatalytic activity in the visible light region. The films exhibit N 1s XPS features at 396, 400 and 402 eV binding energy. The authors of this work claim that the nitrogen species responsible for the overall bandgap narrowing effect exhibits the 396 eV N1s binding energy. Similar doped powders which did not show the 396eV XPS feature also did not show enhanced photocatalytic activity³⁶.

A number of other groups have also extensively investigated the effect of nitrogen doping on titania materials including work done by Hoffmann³⁷. The work was focused on investigating the photooxidation products of HCOO- for N-doped materials prepared by the method earlier reported by Burda and Gole³⁸. These materials, while active in the visible range, fail to produce the final oxidation products for the reaction mentioned above, and thus the authors suggest that molecules like methylene blue, commonly employed to monitor photo-oxidative processes, may be uninformative as to the actual activity of the TiO₂. It is likely that photo-oxidation of methylene blue and other dyes may be directly activated by UV or VIS illumination, thus they are oxidized with or without the presence of TiO₂³⁷, and will give false results when used to investigate photooxidation chemistry on TiO₂.

Chapter 8 of this thesis presents the experimental results of the doping of TiO₂(110) with NH₃-derived impurities. In Chapter 8³⁹, doping of the TiO₂(110) crystal was done in a high temperature flow reactor where the crystal could be simultaneously heated and exposed to NH₃ gas at high temperature. After treatment, the crystal was subjected to XPS analysis where a pair

of N(1s) features were revealed, one at 396.5 eV (seen previously and assigned to substitutionally bound N⁻) and one at 399.6 eV, which has been attributed to an N[·]H complex interstitially bound in the TiO₂ lattice³⁹. The 2 feature XPS spectrum observed for the NH₃ treated samples is comparable to that presented by Asahi et al.³⁶. However in that work, the authors claim that the N(1s) XPS feature at 396.5eV (attributed to be substitutionally bound N⁻) is related to the photo threshold energy decrease observed, whereas the work in reference³⁹ finds that the 399.6 eV N 1s state due to N[·]H species is the active dopant.

A novel test, developed by Fleischauer et al.⁴⁰⁻⁴², was employed by Diwald et al.³⁹ to determine the photoactivity of the N[·]H doped crystal as a function of photon energy, and the results yielded a significant decrease of 0.6 eV in the photothreshold energy needed for substrate excitation. This test involved the photoreduction of Ag⁺(aq) ions to form Ag⁰ deposits on the TiO₂ crystal surface. The surface, once exposed to UV, was then imaged using atomic force microscopy (AFM), which was used to evaluate the density and size of the Ag⁰ clusters produced photolytically. It should be noted that this effect of N[·]H doping has been studied for a photoreduction reaction, not for a photooxidation reaction.

Prior to the work done where NH₃ was used as a dopant³⁹, doping of TiO₂(110) was also attempted and is presented in Chapter 7 of this thesis⁴³ using a high energy ion gun (in UHV) in order to implant the TiO₂(110) using a N₂/Ar⁺ mixture⁴³. After 3.0 keV N₂⁺ implantation, the crystal was annealed extensively, allowing diffusion of implanted N atoms further into the bulk of the crystal. The crystal photoactivity was then tested using the photodesorption of adsorbed O₂ at varying photon energies. XPS, TEM and SIMS were also used to examine the nature and depth of the implanted nitrogen species. Results of this work showed an *increase* in the photothreshold energy, opposite to that observed by others. The XPS data for the ion implanted

surface show a single 396.5 eV N(1s) feature attributed to substitutional nitrogen, assigned as N⁻, therefore suggesting that substitutionally bound N⁻ alone is not responsible for the decrease in the photothreshold of TiO₂(110) as suggested by Asahi et al.³⁶. Work done by Burda et al.⁴⁴ on nitrogen-doped TiO₂ nanoparticles reports substitutionally bound nitrogen as the active dopant species, in agreement with Asahi³⁶. This work however, differs from that of Asahi in that the measured N 1s XPS feature exhibits a binding energy near 400 eV, and no peak is measured at or near 396 eV as found by Asahi³⁶. Other authors also report N 1s XPS features for nitrogen doped titania at 400 eV⁴⁵, yet assignment of this species remains an issue. Burda et al. reports that the substitutional type nitrogen species responsible for the observed increase in the measured photocatalytic activity in the visible region is due to N-O type bonding as reported in Reference⁴⁶. Thus while the work presented in Chapter 7³⁹ and Burda et al.⁴⁴ agree that a nitrogen species with an N 1s binding energy near 400 eV is an active dopant, the assignment of its chemical nature differs.

Recent calculations have addressed the variances in the photoactivity measurements⁴⁷ using density functional theory to consider both anatase and rutile-type samples which have been substitutionally doped with nitrogen. The conclusions of the theoretical work are profound: for anatase samples, substitutional N-doping results in a decrease in the photon energy necessary to excite the material; for rutile TiO₂ materials, the opposite effect is observed, and is attributed to the contraction of the valence band and the stabilization of the N 2p state thus causing an overall increase in the effective bandgap in agreement with the work presented in Chapter 7⁴³. For anatase TiO₂, substitutionally bound nitrogen atoms create localized occupied electronic states (N 2p in character) above the top of the O 2p valence band. The creation of this occupied electronic state has also been shown experimentally^{48,49}. As a result, the mechanism for

photoexcitation of N-doped anatase is most probably direct excitation of electrons from the N 2p state located within the bandgap of the TiO₂, into the conduction band. The measured inter-band gap density of states have been postulated to reduce the rate of electron-hole pair generation which may readily occur without the presence of these states⁴⁸. Similar calculations recently presented by other authors⁵⁰ agree with the work presented by Selloni et al⁴⁷.

The difference in the dopant states for substitutional- versus interstitial- type impurities in anatase TiO₂ was investigated both experimentally using electron paramagnetic resonance spectroscopy (EPR) and XPS, and theoretically using DFT calculations⁵¹. This recent work reveals a distinct N 1s XPS feature at 400eV, but the authors note that preparation methods and differing experimental conditions can drastically affect the nature of the measured XPS signals. In addition, the authors also point out that the observed XPS feature ascribed to N 1s transitions may originate from the presence of any number of differing nitrogen species. Although the EPR characterization of the nitrogen species in the anatase material considered in this work is inconclusive, the theoretical findings indicate very distinct differences in the calculated electronic structure for substitutional versus interstitial type nitrogen. Both types of impurities are found to add localized states within the bandgap. For substitutional type nitrogen, these states are located 0.14 eV above the valence band, and for interstitial type nitrogen species (referred to as N-O) the localized states are calculated to lie 0.73 eV above the valence band. In addition, these calculations have also found that there is a large decrease in the formation energy for oxygen vacancies as a result of additional nitrogen atoms in the lattice. Therefore, oxygen vacancies are most probably induced by N-doping of TiO₂. This work, while quite useful in realizing the actual electronic nature of doped titania materials, fails to address the actual observed change in the photocatalytic activity as a result of impurity addition.

Table 1 presents a synopsis of the literature results dealing with the doping of TiO₂ materials with nitrogen species that are discussed in this thesis.

Table 1: Compilation of the Literature Findings that deal with the use of nitrogen as a dopant for TiO₂ materials.

Author (Ref)	Method - Substrate	Dopant Type	Result
Asahi et al. ³⁶	<ul style="list-style-type: none"> •Theoretical: Density of States Calculations •Experimental: Sputtering of rutile/anatase TiO₂ films with N₂/Ar 	Substitutional; Mixed (Substitutional and Interstitial); Interstitial	Substitutional-type dopant causes increase in photocatalytic activity. Authors correlate finding to N1s binding energy at 396 eV. Interstitial or mixed dopant states are found to be ineffective.
Hoffmann et al. ³⁷	Experimental: NH ₃ -doped anatase TiO ₂	Not characterized.	Doped TiO ₂ material absorbs light up to 520 nm, but fails to completely photooxidize HCOO ⁻ .
Burda et al. ^{38,44,46,52}	Experimental: Chemical doping method for TiO ₂ nanoparticles ⁵²	Substitutional	Substitutional type dopant measured at 400 eV N 1s binding energy due to N-O type bonds in the lattice.
Diwald et al. ^{39,53}	Experimental: 1)High Temperature gaseous doping with NH ₃ (also TiO ₂ (110)) 2)Sputtering of Rutile TiO ₂ (110)	1)Interstitial (high T treatment) 2)Substitutional (sputtering treatment)	Interstitial dopant (400 eV N 1s binding energy) is active dopant, suppressing photothreshold. Substitutional dopant (396 eV N 1s binding energy) increases photothreshold energy.
Di Valentin et al. ⁴⁷	Theoretical: Anatase and Rutile TiO ₂	Substitutional	Substitutional dopant causes decrease in photothreshold energy for anatase samples only. For rutile, an increase in the photothreshold energy is observed.
Di Valentin ⁵¹	Theoretical and Experimental : Anatase	Substitutional and Interstitial	Both dopant types create a discrete energy level within the bandgap, suggesting that either dopant may cause a decrease in the photothreshold energy for TiO ₂ activation.

In summary, there is a great deal of literature available on the topic of nitrogen doping of TiO₂ materials, most of which agree that the addition of nitrogen to the lattice of TiO₂ results in increased photocatalytic activity at lower photon energies. Theoretical results have also clearly illustrated that the addition of either substitutionally or interstitially bound nitrogen species result in localized N 2p states that are discrete levels above the valence band, in contrast to past reports which suggested valence band broadening.

1.4. Photo-decomposition of Pollutant Materials

Chapters 9 and 10 of this thesis present experimental work on the investigation of 2-chloroethyl ethyl sulfide (2-CEES) adsorption, thermal decomposition and photochemical decomposition on TiO₂(110) and TiO₂ powders. 2-CEES is the simulant molecule for bis (2-chloroethyl) sulfide, more commonly known as sulfur mustard. In Chapter 9, experimental work dealing with the adsorption and thermal decomposition of 2-CEES on TiO₂(110) and TiO₂ powders is presented. The 2-CEES molecule is found to thermally oxidize on both single crystalline and powdered TiO₂ samples and results suggest the involvement of lattice oxygen atoms in the oxidation mechanism. Chapter 10 of this thesis deals with the UV-induced photodecomposition of 2-CEES where the photooxidation of adsorbed 2-CEES is measured in the absence of adsorbed O₂. A mechanism involving the oxidative participation of lattice oxygen is proposed and confirmed using 3 different analytical methods. Additional reactions are also observed and can be explained by a free radical mechanism as described in Chapter 10.

1.5. Summary

Two separate and complete literature reviews were written and are presented in Chapter 11 (Chemical Reviews) and Appendix A (Topics in Catalysis) of this thesis.

2. CHAPTER TWO: Experimental Apparatus, Methods and Sample Details

2.1. Ultra-high Vacuum Apparatus

The ultra-high vacuum (UHV) apparatus used for all photochemical and photophysical measurements presented in this thesis were conducted in a stainless steel UHV apparatus manufactured by Leybold-Heraeus Vacuum Products. This chamber operates at a base pressure of $< 1 \times 10^{-10}$ mbar and is pumped by a 270 L/s triode ion pump (Leybold-Heraeus), a 360 L/s turbomolecular pump (Leybold-Heraeus) and a 1200 L/s titanium sublimation pump. The base pressure of the UHV system described is measured with an ionization gauge located in the lower portion of the chamber.

2.2. Experimental Techniques

The UHV system described above is equipped with the following surface analysis tools: 1) a Perkin-Elmer single pass cylindrical mirror analyzer (CMA) for Auger electron spectroscopy (AES); 2) a differentially pumped and shielded and apertured UTI 100C quadrupole mass spectrometer for thermal- and photo- desorption measurements (see Section 2.2.1); 3) a collimated and calibrated micro-capillary array doser for accurate gas exposure to the crystal surface⁵⁴; 4) an ion gun and leak valve for Ar⁺ sputter cleaning and ion implantation experiments (see Section 2.3.2); and 5) an external high pressure 500 W mercury arc lamp for accurate UV exposures to the crystal surface (see Appendix B). Figure 7 shows a schematic diagram of the placement of each instrument on the UHV apparatus.

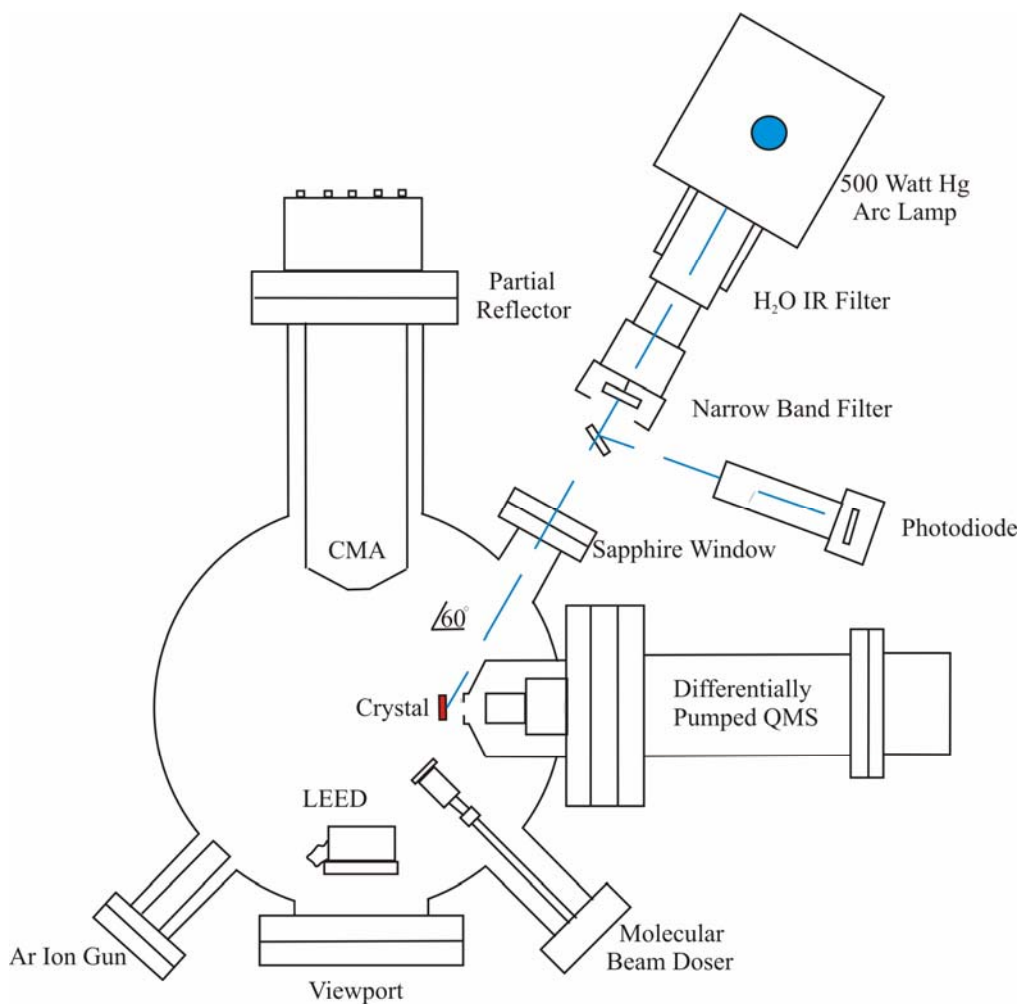


Figure 7: Top-down schematic diagram of the UHV apparatus and surface science tools employed for the work presented in this thesis.

2.2.1. Differentially Pumped QMS

The apertured and differentially-pumped quadrupole mass spectrometer (QMS) is specially designed to perform photo- and thermal- desorption experiments from a single crystal substrate. The QMS is differentially pumped with a 60 L/s ion pump (Leybold-Heraeus) and a 1200 L/s titanium sublimation pump that can be ℓ -N₂ cooled to improve pumping speed. The crystal surface studied is positioned approximately 4 mm from the 1.6 mm diameter QMS aperture (See Crystal Mounting procedure in Section 2.3.1). In this configuration, the apertured

QMS preferentially samples molecules desorbing from the center of the crystal, excluding sampling of possible spurious desorption from the crystal supports and the chamber walls. Gas molecules desorbed from the crystal make (on average) multiple passes through the QMS ionization source causing the effective sensitivity to be considerably enhanced when compared to a single pass characteristic of an unshielded mass spectrometer. The aperture is electrically isolated from the shield so that it may be electrically biased negatively to a potential greater than the electron energy of the mass spectrometer thermionic emitter (70 eV). This procedure retards electrons emitted from the mass spectrometer that may otherwise produce spurious electron stimulated desorption and reaction processes on the crystal containing adsorbed molecules. Measurements of the pumping speed of the mass spectrometer located inside the shield yields a pumping time constant of ~ 0.19 s

2.3. TiO₂ (110) Single Crystal

The work presented in this thesis involves direct sampling of desorption processes from single crystalline rutile TiO₂(110) as described above. The use of single crystalline substrates is advantageous over the use of polycrystalline and/or amorphous samples commonly employed for photochemical measurements reported in the literature. Primarily, the single crystal substrate affords knowledge of the precise atomic structure, quantitative methodologies for surface defect characterization and analysis, as well as the ability to quantify the photochemical efficiency of processes experimentally measured due to the simple geometry of the adsorbing surface of the crystal. As a result, the use of ultra-high vacuum techniques in combination with single crystalline substrates allow for absolute control of the experimental conditions involved in each measurement.

2.3.1. $\text{TiO}_2(110)$ Single Crystal Mounting

Two titanium dioxide single crystals used for experiments are mounted 180 degrees apart from one another on a home built crystal mount constructed from oxygen-free high conductivity (OFHC) copper. OFHC materials are commonly used for ultra-high vacuum applications due to the characteristic high thermal and electrical conductivity of the material. In addition, the oxygen-free property of OFHC limits potential outgassing that may increase the background pressure in the UHV system. The OFHC crystal mount is directly attached to a $\ell\text{-N}_2$ cold finger, but electrically isolated with thermally conductive sapphire plates. Cooling in this manner allows crystal temperatures as low as 105 K to be achieved. The cold finger is mounted on a Varian precision manipulator which provides rotary motion as well as motion in the x, y and z directions. The cold finger shaft is sealed by two viton rubber seals, and the space between the seals is differentially pumped by an oil diffusion pump and rotary vane pump⁵⁴. The use of differential pumping for the manipulator rotary seal limits pressure bursts in the main chamber when the manipulator is rotated. In addition, differential pumping eliminates any possible small leaks from atmosphere when the manipulator is stationary.

Single crystal substrates of rutile $\text{TiO}_2(110)$ (1 cm x 1 cm x 0.1 cm; Princeton Scientific) were mounted on either side of the manipulator described above for electrical heating following a design developed in this laboratory^{54,55}. Briefly, the $\text{TiO}_2(110)$ crystal is mounted with direct contact to a polished Ta wafer by Ta clips. The clips are inserted into slots cut in the edges of the crystal. Mounting in this manner allows for high thermal conductivity between the $\text{TiO}_2(110)$ crystal and the Ta plate. Heating of the sample is done by passing current through two tungsten wires (0.38 mm) that are spot welded to the back of the Ta plate. The sample temperature is measured using a type K thermocouple that is inserted and fixed into the pre-cut slots around the

sides of the crystal. The ceramic adhesive used for this procedure is provided by Aremco Corporation (Ceramic Adhesive No. 516) and is known to have the same thermal expansion properties of the $\text{TiO}_2(110)$ crystal, preventing contact breakage during crystal heating. Temperature ramping is achieved using a home built power supply in conjunction with a LabView program which functions as the temperature control using feedback from the embedded thermocouple. A general diagram showing the mounted crystal is depicted in Figure 8.

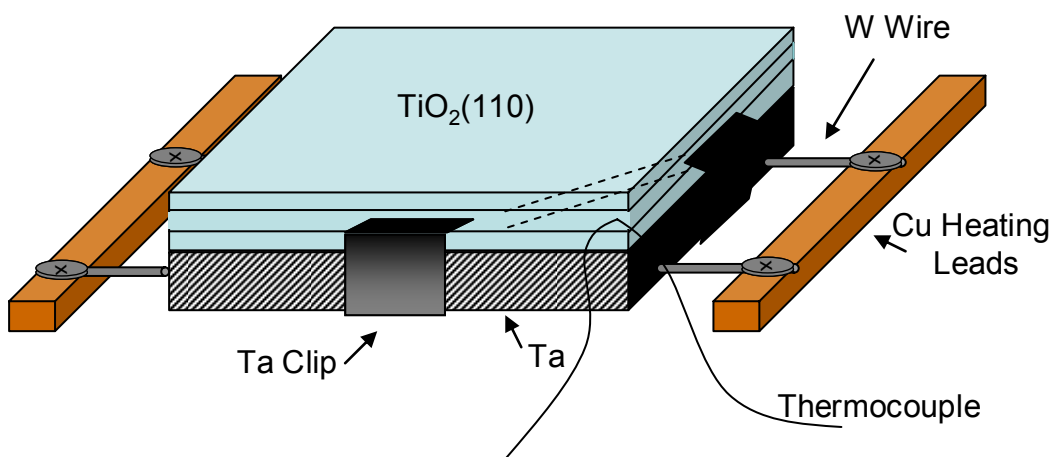


Figure 8: Diagram showing the $\text{TiO}_2(110)$ crystal mounted to a Ta plate.

2.3.2. $\text{TiO}_2(110)$ Single Crystal Sample Cleaning and Preparation

The $\text{TiO}_2(110)$ -(1x1) crystal surface was cleaned via several cycles of Ar^+ sputtering (1500 eV, 45 min.) and annealing (900 K, 1 hour), followed by an oxidation step that involves annealing the sample in flowing $\text{O}_2(\text{g})$ (5×10^{14} molecules $\cdot \text{cm}^{-2} \cdot \text{s}^{-1}$, 1 hour). The crystal is also cooled in the same flux of $\text{O}_2(\text{g})$. Auger spectroscopy measurements done following the oxidation procedure indicate that the surface is free of contaminants within the depth of Auger sampling. A typical Auger spectrum is shown in Figure 9. Once oxidized, a stoichiometric TiO_2 surface is achieved. Following oxidation, the crystal was reduced again by annealing in vacuum to 900K for 30 minutes producing surface O-vacancy defects located in the bridging oxygen

rows. The reduced state of the surface was then tested for surface defect reproducibility in most experiments using a method developed in this laboratory¹⁵.

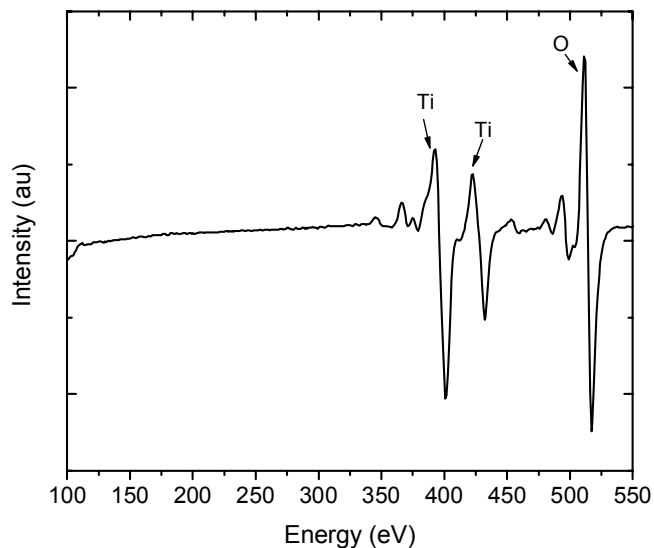


Figure 9: Typical Auger spectrum for a clean TiO₂(110) surface.

2.4. Gas Handling and Exposure

Gas exposures to the TiO₂(110) crystal surface is done using a calibrated microcapillary array molecular beam doser. The calibration of the conductance of the doser is addressed in Appendix D. The intercepted flux from the beam doser by the crystal surface (for Ar(g)) is 8.0×10^{13} molecules torr⁻¹ sec⁻¹. Each experimental chapter presented hereafter describes the quantities and procedures for gas purification and exposure.

3. CHAPTER THREE: Monitoring Hole Trapping in Photoexcited TiO₂ (110) using a Surface Photoreaction*

Abstract

The hole-induced photodesorption of chemisorbed O₂ from a TiO₂ (110) single crystal has been employed to monitor the kinetics of electron-hole pair (e-h) formation and hole trapping. Excitation is produced by 3.4 ± 0.05 eV photons at 110 K. Two separate O₂ desorption processes have been found which are characteristic of low photon fluxes and high photon fluxes. At a critical photon flux, $F_{\text{hv}}(\text{crit.})$, the slow O₂ photodesorption process suddenly converts to a fast process, signaling the saturation of hole traps in the TiO₂ crystal. Consequently, this allows photogenerated holes to more efficiently reach the surface, causing more rapid O₂ photodesorption. The estimated bulk concentration of hole-traps is $\sim 2.5 \times 10^{18} \text{ cm}^{-3}$, involving a fraction of about $\sim 3 \times 10^{-5}$ of the atomic sites in the bulk. Both the slow and fast O₂ photodesorption processes are described by a rate law which is proportional to $F_{\text{hv}}^{1/2}$, indicating that the steady-state concentration of holes, [h], is governed by second-order e-h pair recombination kinetics. Effective use is made of a hole scavenger molecule, adsorbed CH₃OH, to probe the role of added hole traps on the rate of the photodesorption of adsorbed O₂ molecules and on the magnitude of $F_{\text{hv}}(\text{crit.})$.

3.1. Introduction

The excitation of TiO₂ by photons with energy above the bandgap (3.05 eV) is the primary process underlying the vast area of photochemistry on TiO₂^{23,56}. Electrons and holes are generated and a fraction of these charge carriers arrive at the TiO₂ surface, where charge

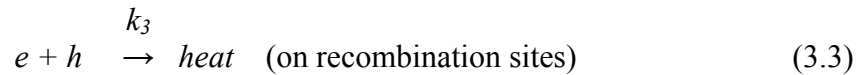
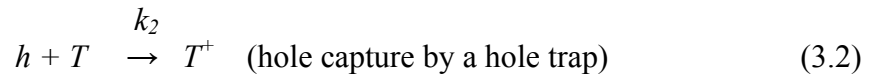
* Reproduced in part with permission from Tracy L. Thompson and John T. Yates, Jr. "Monitoring Hole Trapping in Photoexcited TiO₂(110) Using a Surface Photoreaction", *Journal of Physical Chemistry B*, **109** (2005) 18230-18236. Copyright 2005 American Chemical Society.

exchange with adsorbed molecules leads to the desirable surface photochemistry. Recombination of electrons and holes reduces the efficiency of the surface photochemistry^{57,58}.

In addition, the trapping of charge carriers by trap sites in bulk TiO₂ and on the surface of TiO₂ can reduce the efficiency of a hole-induced surface photochemical process. When these hole traps become filled by photoexcitation, a sudden increase in the rate of a hole-induced photochemical process should be observed. By working at cryogenic temperatures the thermally activated recombination of electrons with trapped holes is suppressed⁵⁹.

In this work we have investigated the details of the e-h pair formation and trapping/recombination processes in TiO₂(110) by using the rate of hole-induced O₂ photodesorption to monitor the arrival of photogenerated holes at the surface where they interact with adsorbed O₂ molecules. The mechanism for the photoinduced desorption of molecular oxygen from TiO₂(110) has been studied extensively in the past both experimentally^{16,55,60,61} and theoretically⁶²⁻⁶⁴. It is known that O₂ molecules adsorb on oxygen-vacancy sites on TiO₂(110)^{8,16,55}.

A kinetic scheme describing the elementary steps of e-h pair excitation, e-h pair trapping at a trap site, T, to produce T⁺, e-h recombination, and O₂ photodesorption is shown below:



After hole trap filling by reaction (3.2) and assuming a fast equilibrium is established between the e-h pair formation (step 3.1) and recombination (step 3.3), the rate of $O_2^-(a)$ photodesorption will be according to the steady state approximation:

$$-d[O_2^-(a)]/dt = k_4[O_2^-(a)] \left[\frac{k_1}{k_3} \right]^{1/2} F_{hv}^{1/2} \quad (3.5)$$

where the recombination process (step 3.3) is second-order in the hole concentration, $[h]$, leading to a desorption rate containing the factor $F_{hv}^{1/2}$. This assumes that at steady state conditions, $[e] \approx [h] = \text{constant}$.

Photochemical investigations of TiO_2 colloids or powdered surfaces presented in the literature also report similar findings, where correlations of the reaction rate or photo-oxidation rate to the square root of the incident light intensity are made²⁷⁻³². These experiments differ significantly from those to be presented here in that the experiments to be described involve carefully controlled studies of a simple photoprocess which occurs in ultrahigh vacuum on a planar single crystal of TiO_2 with known surface structure³, known surface defect density⁷, and in the absence of solvents and surface-bound chromophores. In addition the photon flux and photon energy are well known. Thus, quantification of the rate of a well-defined photoprocess compared to the photon flux received by the planar single crystal surface can be accurately made in this model system involving a $TiO_2(110)$ single crystal. The kinetic interpretation is supported by experiments involving the addition of controlled coverage of a hole-scavenger molecule to the $TiO_2(110)$ surface.

3.2. Experimental

We have experimentally measured the rate of $^{18}O_2$ photodesorption using line-of-sight mass spectrometry. $^{18}O_2(g)$ (99 % isotopic purity) is adsorbed at 110 K to full coverage on the

slightly defective surface, and then exposed to UV irradiation (3.4 ± 0.05 eV). The 36 amu signal originating from $^{18}\text{O}_2$ photodesorption from the crystal is sampled at 0.083 s intervals. Oxygen exposures were carried out using a calibrated molecular beam doser in order to obtain the saturation coverage of $^{18}\text{O}_2$ for each successive experiment. Varied photon fluxes in the range of $F_{\text{hv}} = 1.4 \times 10^{12} - 4.0 \times 10^{14}$ photons $\text{cm}^{-2} \text{s}^{-1}$ were directed to the $\text{TiO}_2(110)$ single crystal by using an interference filter in conjunction with screen-wire neutral density filters. During each experiment, the photon flux was measured by using a partial beam reflector and a bolometer-calibrated photodiode detector. This combination allows for accurate measurement of the received photon flux during each consecutive experiment. After each consecutive experiment, the crystal was flashed to 900K to remove all remaining chemisorbed molecular oxygen. Once cooled, the photodesorption experiment could be repeated on the $\text{TiO}_2(110)$ surface with reproducible properties.

For experiments where an added hole scavenger molecule, methanol, was used, the methanol vapor was directed to the crystal in a similar manner to that used for oxygen exposures using a calibrated molecular beam doser. Methanol (Aldrich, 99.9% pure) was further purified by several freeze-pump-thaw cycles. Thermal desorption measurements of methanol from $\text{TiO}_2(110)$ were carried out after methanol adsorption at 110K. A linear heating rate of 1 K s^{-1} was used throughout.

3.3. Results

An example of the measured $^{18}\text{O}_2$ photodesorption signal is shown in the right hand portion of Figure 10. To avoid uncertainties in kinetically fitting the $^{18}\text{O}_2$ photodesorption curves, the measurements reported here are concerned only with the initial yield of $^{18}\text{O}_2$, designated $Y^{\text{O}}_{\text{O}_2}$. Since the initial yield is measured in multiple experiments at different F_{hv} and at

a constant $^{18}\text{O}_2(\text{a})$ coverage $[^{18}\text{O}_2^-(\text{a})]$, measurements of $Y^{\text{o}}_{\text{O}_2}$, may be used to confirm the $F_{\text{hv}}^{1/2}$ dependence of the kinetic rate law for O_2 photodesorption as shown in Equation 5. Thus for the initial point in each photodesorption experiment, different levels of hole-trap filling will have occurred at different values of F_{hv} . Thus, it is expected that as F_{hv} increases the trap sites will become saturated at the photon exposure achieved during the time interval needed for the measurement of the first point in the photodesorption experiment. At this photon flux, $F_{\text{hv}}(\text{crit.})$, transfer of the photodesorption kinetics to a new curve will occur, as a faster rate of hole delivery to the surface is achieved due to cessation of hole trapping.

$^{18}\text{O}_2$ Photodesorption from $\text{TiO}_2(110)$

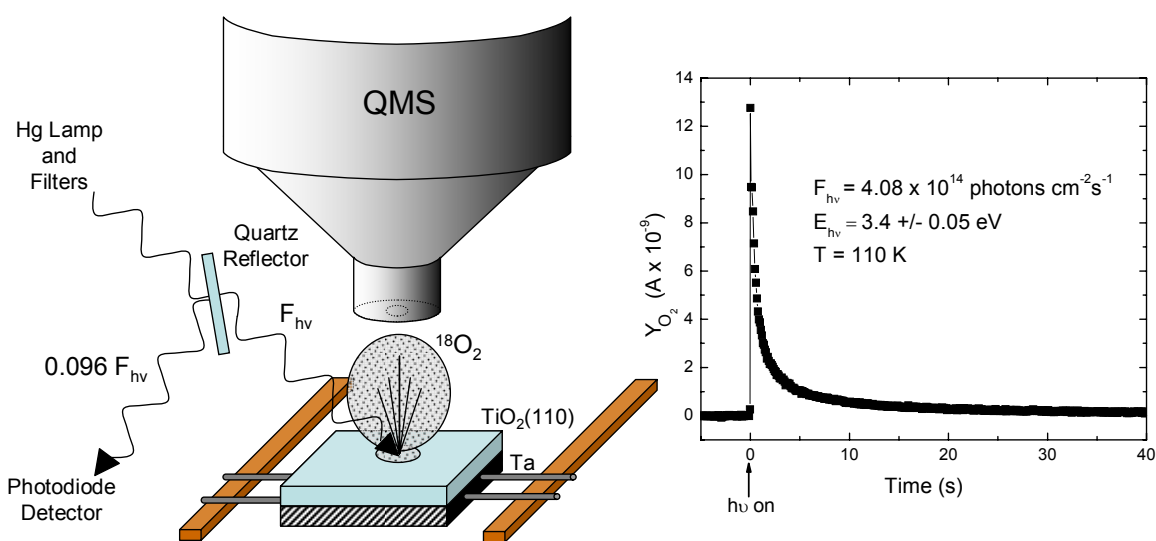


Figure 10: Schematic diagram for the experimental apparatus used to measure the photodesorption of oxygen from TiO_2 . The inset shows an example of the measured photodesorption signal for $^{18}\text{O}_2$ from $\text{TiO}_2(110)$.

Figure 11 shows the dependence of $Y^{\text{o}}_{\text{O}_2}$ on the magnitude of $F_{\text{hv}}^{1/2}$. Two linear branches, A and B, are observed with a branch point which occurs at a critical photon flux, $F_{\text{hv}}^{1/2}(\text{crit.})$. Branch A corresponds to a photodesorption process of low efficiency, compared to branch B.

$^{18}\text{O}_2$ Initial Photodesorption Yield – $\text{TiO}_2(110)$

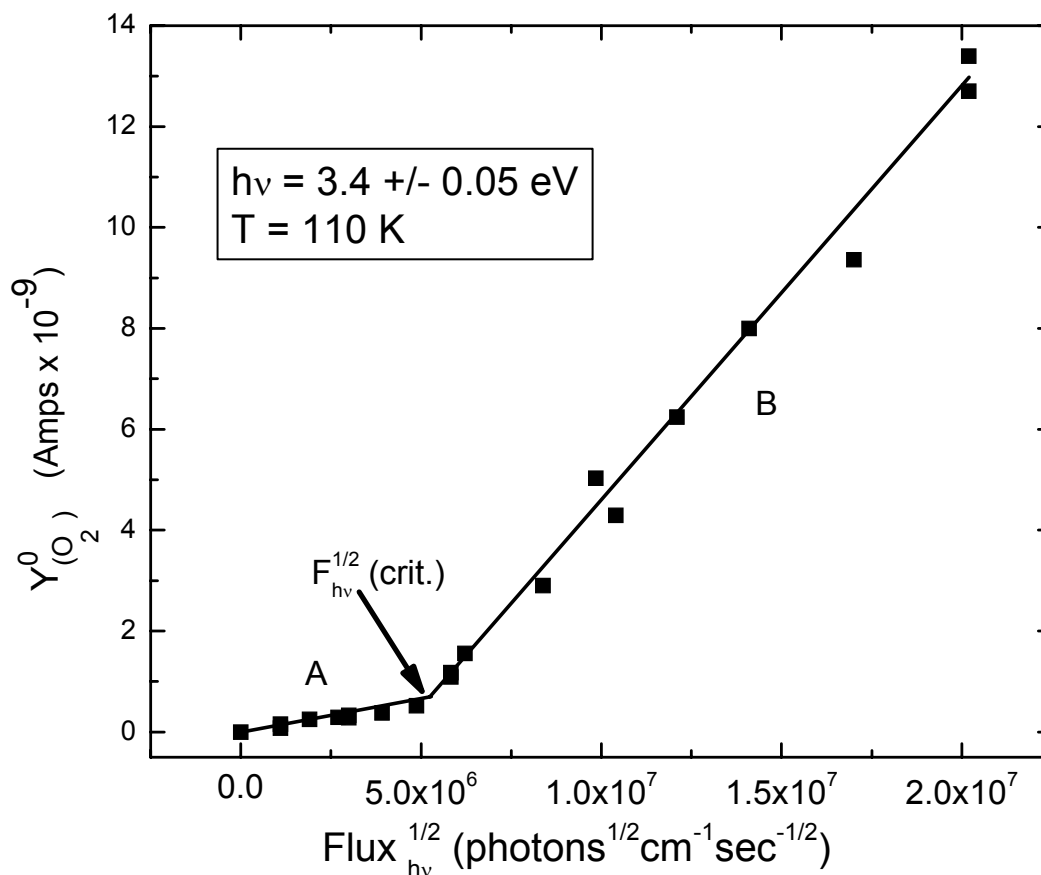


Figure 11: Plot showing the initial photodesorption yield of $^{18}\text{O}_2$ from $\text{TiO}_2(110)$ as a function of the square root of the incident light flux, $F_{h\nu}^{1/2}$.

We believe that branch A is accompanied by rapid hole trapping on T-site centers within the crystal. At $F_{h\nu}(\text{crit.})$, the T-site hole capture process culminates on the time scale of data acquisition for the first experimental point, allowing the flow of photogenerated holes to the surface to be enhanced at $F_{h\nu} > F_{h\nu}(\text{crit.})$, and the more efficient branch B photodesorption process is then observed. Figure 12 schematically illustrates this effect.

Bulk Hole Trap Sites within TiO₂

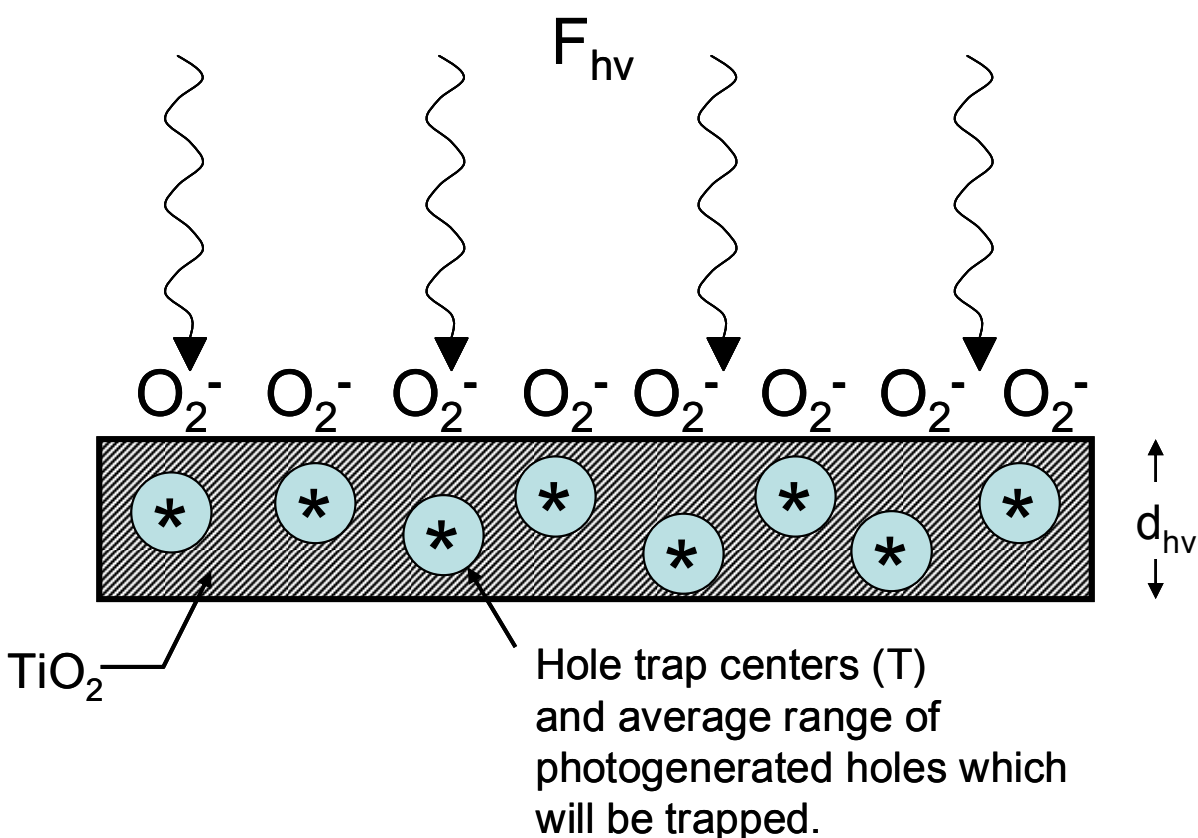


Figure 12: Schematic diagram of the localization of recombination centers in the near surface region of TiO₂(110). The diameter of the light circles schematically represents a mean range for e-h recombination at the recombination center, *. The distance, d_{hv} , corresponds schematically to the mean penetration depth for band gap UV irradiation.

UV photons penetrate only a distance $d_{hv} \sim 100 \text{ \AA}$ into the crystal based on the measured UV absorbance of thin films of TiO₂ at 3.4 eV⁶⁵. Electron-hole pairs are generated and diffuse throughout the excitation region near the crystal surface. They may undergo a recombination process within the crystal with rate constant, k_3 . As shown in Figure 12, about each T-site there is a spatial range in which photogenerated holes produced in this region will on average reach the T-site and become trapped. A fraction of the photogenerated holes produced outside the range of T-sites will reach the surface, where the holes can produce O₂ photodesorption with a probability governed by the factors $F_{hv}^{1/2}$ and $[k_1/k_3]^{1/2}$ in our series of experiments at constant $[O_2^-(a)]$. A

linear dependence of branch B on $F_{\text{hv}}^{1/2}$ is seen in Figure 11 in accordance with equation 3.5. Below $F_{\text{hv}}(\text{crit.})$ (branch A) it appears that a linear dependence on $F_{\text{hv}}^{1/2}$ also exists.

In an attempt to test the role of the trapping of photogenerated holes, a known hole scavenger, methanol⁶⁶⁻⁶⁹, was quantitatively added to the $\text{O}_2^-(\text{a})$ -covered TiO_2 surface. The initial yield of photodesorbing $^{18}\text{O}_2$, $Y_{\text{O}_2}^{\text{o}}$, decreases monotonically as the CH_3OH coverage is increased, as shown in Figure 4. The decrease of the $^{18}\text{O}_2$ photoyield may be resolved into two methanol coverage regions, deconvolved in Figure 13 as two straight lines which intersect at a methanol coverage near 1ML. These two regions may be due to a more efficient hole scavenging process caused by molecularly adsorbed CH_3OH bonded to non-vacancy sites at lower coverage (thus causing the decreased yield of O_2 photodesorption), followed by less efficient hole scavenging for CH_3OH which is H-bonded to the $\text{TiO}_2(110)$ surface at bridging oxygen sites.

Role of CH₃OH Surface Hole Traps on ¹⁸O₂ Photodesorption Yield

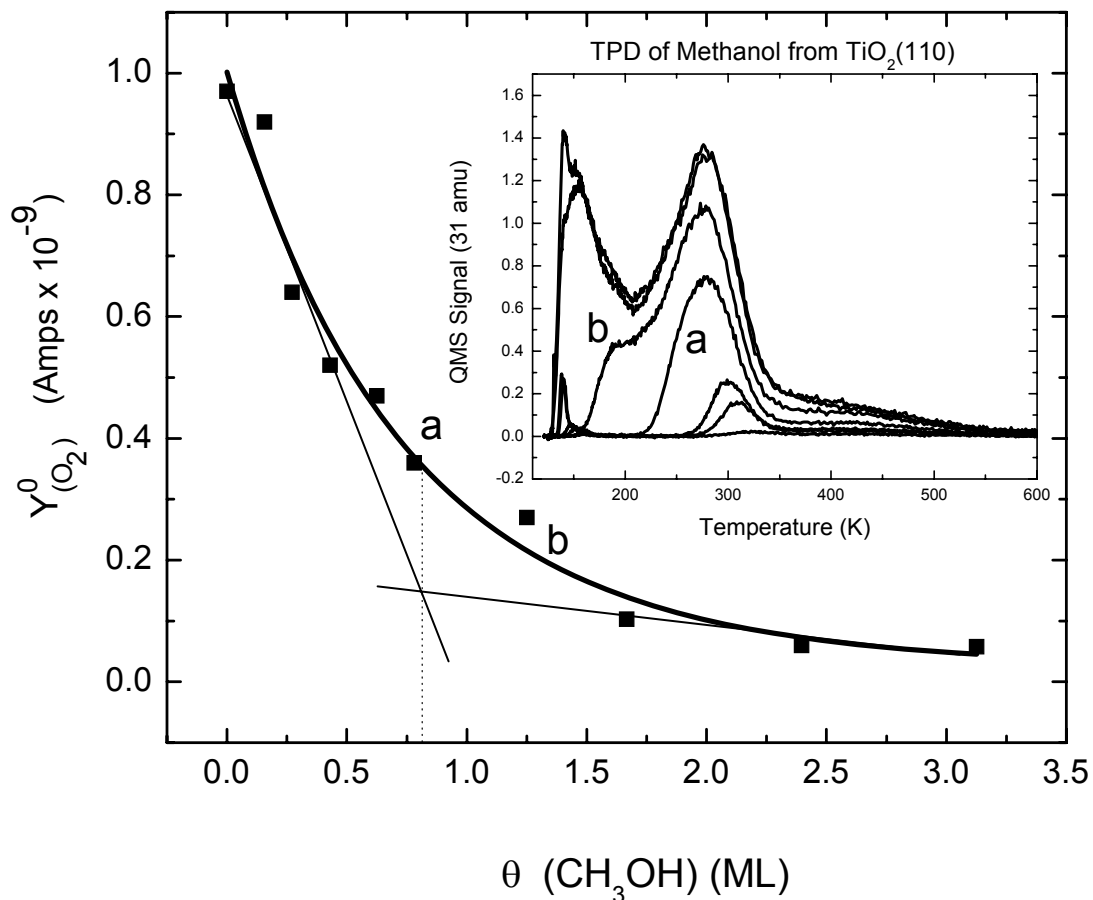


Figure 13: Plot showing the decrease in the initial photodesorption yield of ¹⁸O₂ from TiO₂(110) when exposed to methanol at various coverage. The two straight lines show the predominating behavior as a result of two different bonding configurations for methanol on TiO₂(110). The inset shows the characteristic TPD spectra for CH₃OH from TiO₂(110). TPD spectrum (a) corresponds to 1ML CH₃OH coverage.

The multiple adsorption modes and interactions of methanol with the TiO₂(110) surface has been previously reported by Henderson¹⁸. The inset to Figure 13 shows the temperature programmed desorption (TPD) behavior for CH₃OH. Desorption from both multilayer and monolayer CH₃OH is observed at higher coverage, in agreement with the measurements by Henderson¹⁸.

Effect of CH₃OH Hole Traps on Initial ¹⁸O₂ Photodesorption Yield

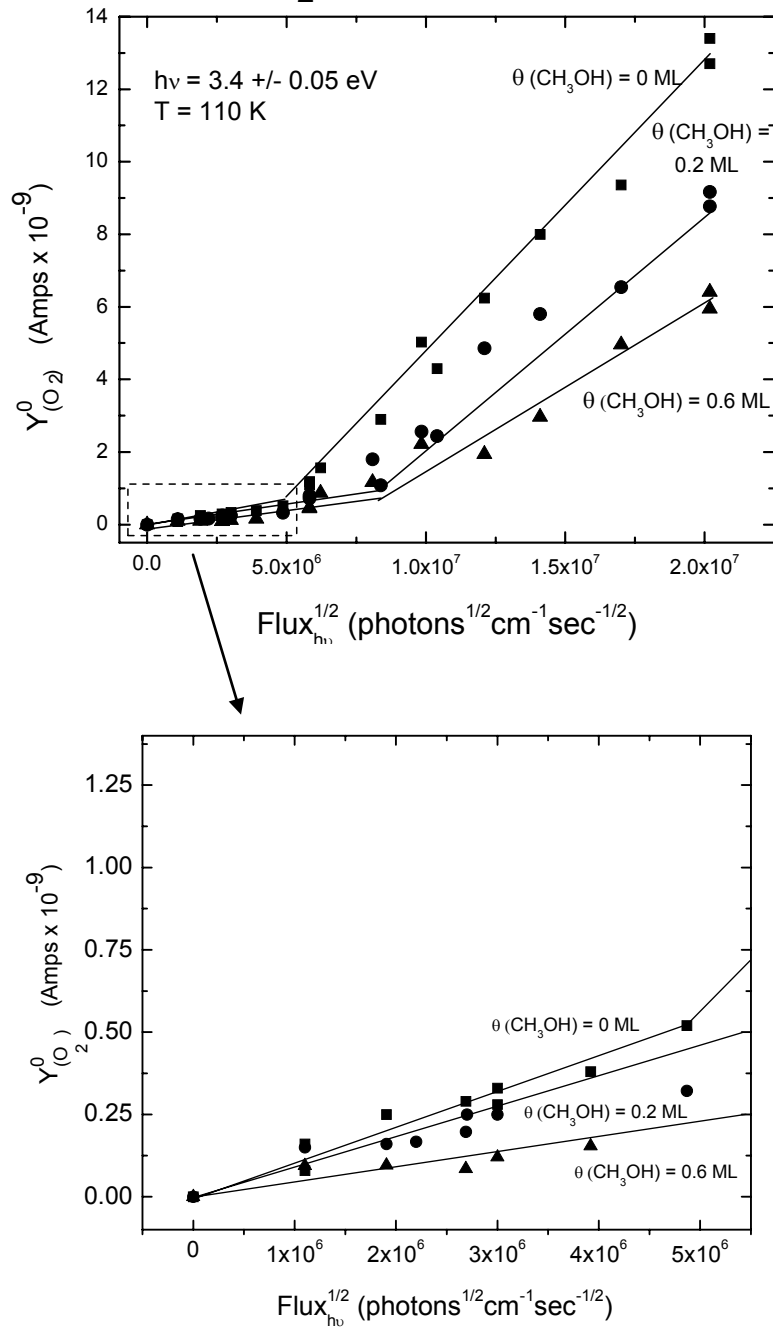


Figure 14: Plot of the initial photodesorption yield for ¹⁸O₂ from TiO₂(110) versus the square root of the photon flux at two different coverage of CH₃OH, compared to clean TiO₂(110).

Figure 14 shows the dependence of $Y_{O_2}^0$ on $F_{hv}^{1/2}$ for two submonolayer coverages of CH_3OH compared with the result found without added hole-scavenger molecules. Several effects are observed:

1. The initial $^{18}O_2$ photoyield, $Y_{O_2}^0$, is diminished by added CH_3OH in both branches, A and B.
2. The value of $F_{hv}(\text{crit.})$ moves higher when coverage of CH_3OH is present.
3. The dependence of $Y_{O_2}^0$ remains linear with $F_{hv}^{1/2}$ in both the A and B branches at the two CH_3OH coverages.

These three phenomena may be easily explained. As hole scavenger molecules are added to the surface, the value of $F_{hv}(\text{crit.})$ is expected to shift to higher values as the number of sites capable of scavenging a hole is increased. Adsorbed CH_3OH molecules complement the T-sites as hole scavengers. When the hole removal rate culminates for the T-sites combined with added adsorbed hole-scavenger molecules, branch A ceases to describe the O_2 photodesorption, and branch B, exhibiting a higher slope than branch A, appears. The higher slope of branch B is due to the saturation of available T-site hole scavenging centers combined with hole-trap sites provided by adsorbed CH_3OH . Once saturation of these hole-trap sites has occurred, photogenerated holes travel more efficiently to the surface where they cause O_2 photodesorption.

The linear dependence of branch A and branch B on $F_{hv}^{1/2}$ for all conditions in this experiment indicates that the maintenance of second-order e-h pair recombination kinetics is not influenced by added hole scavenger molecules.

In addition to the three observations above, it is also seen in Figure 14 that the slopes of both the branch A and branch B curves monotonically decrease as CH_3OH molecules are added to the surface. This phenomenon may result from O_2 scattering from adsorbed CH_3OH molecules

during photodesorption, reducing the efficiency of collection by the apertured QMS shown in Figure 15. A broadening of the angular distribution of photodesorbing O_2 molecules by scattering from adsorbed CH_3OH molecules is schematically illustrated in Figure 15. Surface scattering should increase with increased CH_3OH coverage, and this is observed by decreasing slopes for both branch A and branch B processes as CH_3OH is added to the surface.

Photodesorbing O_2 Scattering by CH_3OH Adsorbates

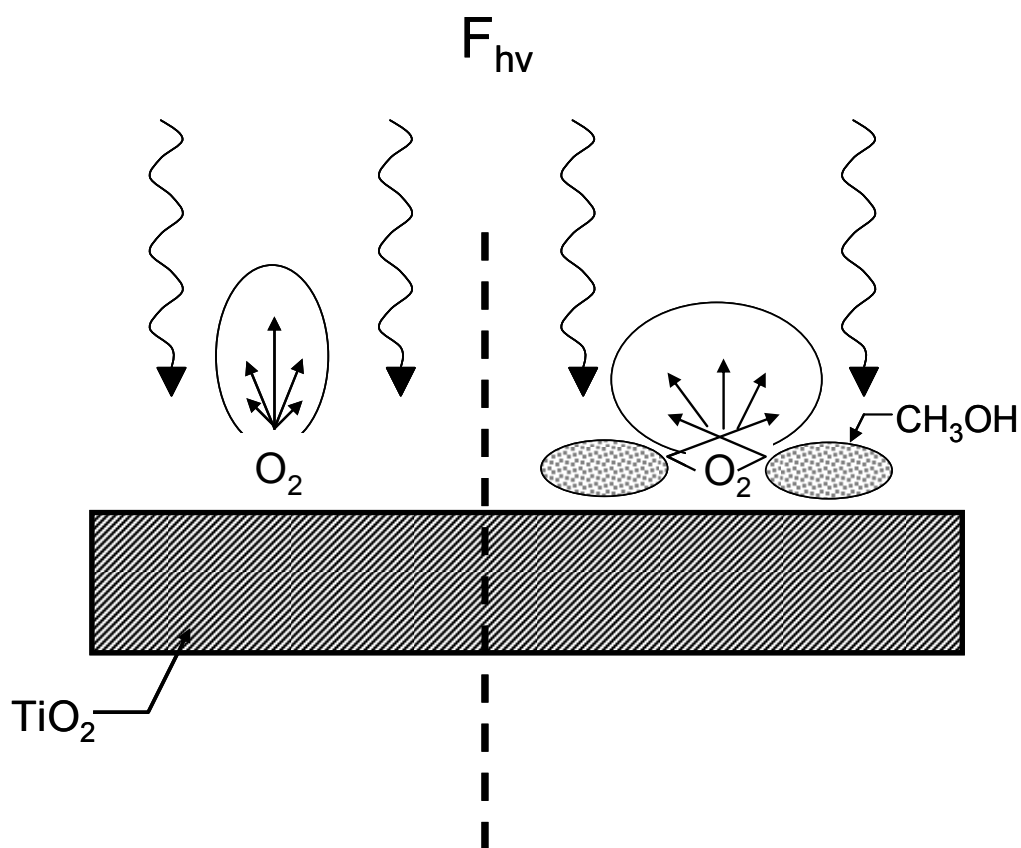


Figure 15: Diagram showing possible scattering of O_2 molecules by adsorbed CH_3OH , leading to the slope changes in shown in Figure 14.

To check that chemical reactions between photodesorbing $^{18}O_2$ and added CH_3OH molecules are not influencing these results, a careful study involving the monitoring of various possible oxidation products was carried out after co-adsorption of $^{18}O_2$ and CH_3OH on the

vacuum-annealed TiO₂(110) surface. Results from this measurement are presented in Figure 16 where no photodesorption of potential photooxidation products such as C¹⁸O, C¹⁸O₂ or H₂¹⁸O is measured. In this case, as in the case for the results shown in Figure 13 and Figure 14, only the photodesorption of ¹⁸O₂ was observed. Previous measurements studying adsorbed CO photooxidation during irradiation of mixed CO(a) and ¹⁸O₂(a) layers revealed that the photooxidation product, CO₂, was evolved at 100K together with photodesorbing ¹⁸O₂¹⁷.

Lack of Photooxidation Chemistry for CH₃OH/TiO₂(110)

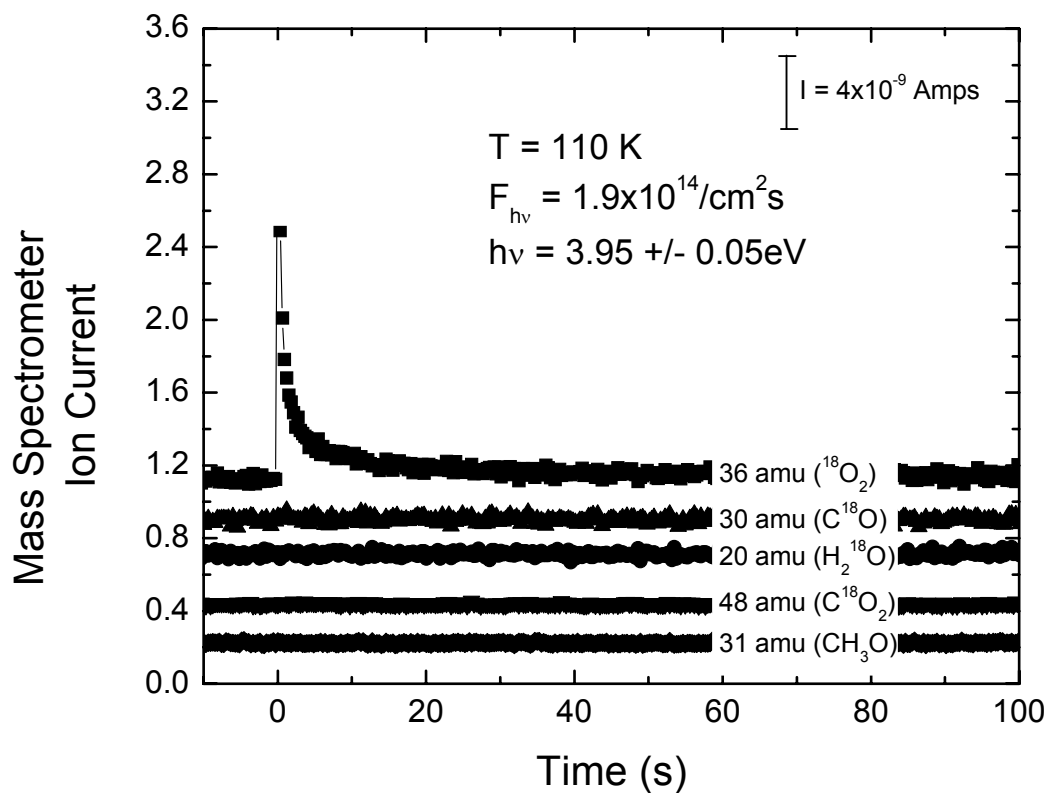


Figure 16: Plot showing the lack of photooxidation chemistry that might occur when adsorbed ¹⁸O₂ and CH₃OH are exposed to UV light.

3.4. Discussion

3.4.1. Dependence of O₂ Photodesorption Rate on $F_{\text{hv}}^{1/2}$

The dependence of the rate of O₂ photodesorption on $F_{\text{hv}}^{1/2}$ has been demonstrated in Figure 11 over the full range of monoenergetic photon fluxes employed in this work. This is in agreement with other experiments on TiO₂ powders and colloidal suspensions as first reported by Egerton and King²⁷, and then by others²⁸⁻³². The $F_{\text{hv}}^{1/2}$ dependence of the rate of TiO₂-mediated photochemistry (O₂ desorption) is explained by the second-order kinetics for e-h pair recombination in the TiO₂ crystal which would result from the interaction of mobile charge carriers. This work is the first to measure the $F_{\text{hv}}^{1/2}$ dependence for a photochemical process on single crystalline TiO₂, avoiding additional effects present in powdered TiO₂ due to grain boundaries, polycrystallinity, and the role of solvents on the process.

3.4.2. Electron and Hole Traps in TiO₂

Only a few papers have been concerned with electronic defect states in macroscopic single crystals of TiO₂^{70,71}. Fully oxidized TiO₂ is an insulator, while reduced TiO_{2-x} is an n-type semiconductor. Reduction (usually by thermal annealing) results in the production of a large number of different defect energy levels⁷⁰. Levels having thermal ionization energies < 1eV are termed shallow electron-trap levels; levels having optical ionization energies > 1.5eV are termed deep electron-trap levels. On the basis of optical and electron paramagnetic resonance spectroscopy (EPR) experiments, Ti³⁺ levels resulting from Ti³⁺ at interstitial sites have been reported in single crystalline rutile⁷²⁻⁷⁵ and the concentration of the Ti³⁺ increases with increasing reduction. Yagi et al.⁷¹ have measured O vacancy defect concentrations in the range from 3.7 x 10¹⁸ cm⁻³ to 1.3 x 10¹⁹ cm⁻³ and have correlated these vacancies with Ti³⁺ interstitial species. A Ti³⁺ species may be considered as a trapped electron in the bandgap region.

A number of surface science studies on rutile single crystals of TiO_2 have been carried out. It is known that the reduction of the $\text{TiO}_2(110)$ surface leads to oxygen vacancy formation at the surface and ion scattering spectroscopy studies⁷ indicate that about 8-10% of the TiO_2 surface becomes defective following reduction in vacuum at 900K. STM investigations of surface defect formation indicate similar findings, where point defects are clearly seen, and assigned as oxygen vacancy sites³. Such vacancies exhibit characteristic surface chemistries¹⁶ and are revealed by the formation of a characteristic CO_2 adsorption state, more strongly bound than adsorbed CO_2 on non-defective regions on $\text{TiO}_2(110)$ ¹⁵.

Several EPR studies of photochemically produced trapped hole states have been carried out on TiO_2 colloids^{66,76} and on powders⁵⁹. These studies indicate that the trapped hole is produced on the TiO_2 lattice as an O^- species covalently bound to Ti atoms. The holes are present in both the subsurface and the surface region of the TiO_2 ⁷⁷ and are considered to be deep trap states. Since the O^- EPR signal disappears upon the adsorption of hole-trap molecules, the hole is considered to be a mobile species in the TiO_2 lattice. The O^- species has been observed by EPR in a number of metal oxides including MgO , ZnO and BeO ⁷⁶.

3.4.3. Recombination of Electrons and Holes

Recombination of electrons and holes in semiconductors has been actively investigated in the literature^{25,69,70,78-90}. On direct bandgap semiconductors, such as TiO_2 , with impurity states present (defect sites), electron-hole pair recombination is described by the Shockley-Read-Hall mechanism where electron or hole traps are the predominant sites for recombination^{25,91}. In the near-surface region of the crystal there are not only oxygen vacancies³ but also Ti^{3+} sites⁷¹, Ti^{4+} interstitials⁷¹, Ti interstitial pairs (defined as W-sites in EPR spectroscopy)⁷⁵, and other planar defects related to crystallographic shear planes (CSP)⁹². Work done by de Jongh et al.⁷⁸ and

others^{70,84}, clearly suggest that electron trapping in TiO₂ lattices occur at these defect sites, which are distributed in energy within the forbidden band. As a result, the localized residence time for an electron or hole varies over a wide range of lifetimes^{84,93}. Photocurrent and transient measurement methods at 300 K suggest the time frame for detrapping could be as slow as ms or s, dependent on temperature as thermally-activated recombination or detrapping occurs⁹⁴. Work done at 300 K on dye-sensitized TiO₂ films suggest that the rate of recombination is directly related to the mobility of charge carriers, governed in part by the kinetics of recombination at trap sites, where a typical time for recombination is estimated to be about 1 ms⁹⁵. It has been shown by intensity modulated photocurrent spectroscopy of polycrystalline TiO₂ electrodes that the transport of charge carriers to the electrode surface is limited by the localization time at trap sites, which is dependent on the incident light intensity⁷⁸.

3.4.4. Observation of the Saturation of Hole Traps at a Critical Photon Flux

Most studies of the photochemical filling of trap states have concerned electron trapping. When an electron trap becomes filled the quasi Fermi level crosses the energy level of the trap and the trap becomes inactivated for further electron capture. This trap saturation effect can enhance the lifetime of photogenerated charge carriers and can improve the quantum yield of carriers at higher light intensities⁸⁰. We believe these ideas also apply to hole trapping in TiO₂.

The photon-induced filling of deep trap recombination centers is known to occur for semiconducting silicon substrates^{79,96} and has been suggested for rutile single crystals⁷⁰. More recently, similar effects have been noted for polycrystalline TiO₂ electrodes⁸⁰ and ZnO nanoparticles⁹⁴. The result of the saturation of deep trap levels is enhanced carrier mobility and carrier lifetime. In the work presented here, the filling of deep hole traps at $F_{h\nu}(\text{crit.})$ causes a

sharp increase in the rate for O₂ photodesorption, caused by an increase in the flux of holes to adsorbed O₂⁻.

In the presence of unfilled deep hole traps, equation 5 no longer applies for the rate of photodesorption of O₂(g). It is replaced by:

$$-\frac{d[O_2^-(a)]}{dt} = k_4 [O_2^-(a)] \left[\frac{k_1}{k_2[T - T^+] + k_3} \right]^{1/2} F_{hv}^{1/2} \quad (3.6)$$

where $[T - T^+]$ = concentration of unfilled hole trap states. Equation 3.6 becomes equation 3.5 when all hole trap states are filled and $[T - T^+] = 0$.

Equation 3.6 indicates that the rate of O₂ photodesorption will be smaller when $k_2[T - T^+]$ is non-zero (branch A). At the critical UV flux, $F_{hv}(\text{crit.})$, and above, hole trap sites have become filled and more rapid O₂ photodesorption kinetics are observed in branch B. Since $[T - T^+]$ is dependent on F_{hv} , the kinetic dependence of branch A on $F_{hv}^{1/2}$ will not be exactly followed, but our experiments do not detect a departure from $F_{hv}^{1/2}$ -governed desorption kinetics in branch A.

3.4.5. Estimate of the Concentration of Hole Trap Sites

If we assume that during one mass spectrometer sampling period (0.10 s) the fluence of photons at $F_{hv}(\text{crit.})$ is entirely consumed by trap-filling by holes, it is possible to estimate an upper limit for the hole-trap site concentration in this sample of TiO₂(110). From Figure 2, we observe that $F_{hv}(\text{crit.}) = 2.5 \times 10^{13}$ photons cm⁻²s⁻¹. Therefore in a sampling time of 0.10 s, 2.5×10^{12} photons contribute to hole-trap filling, causing trap saturation. Since the photon absorption depth is $\sim 10^{-6}$ cm (See Appendix C) we estimate that approximately 2.5×10^{18} hole traps cm⁻³ are filled at $F_{hv}(\text{crit.})$. Our model considers that the majority of the hole traps exist in the bulk of the crystal. Since there is 9.6×10^{22} atoms cm⁻³ in rutile TiO₂, the fraction of bulk atoms hosting a hole-trap site is $\sim 3 \times 10^{-5}$.

3.4.6. Role of Added Trap Adsorbates

The addition of methanol to the surface of the TiO₂(110) crystal provides additional hole trapping capacity and causes the branch point between the slow (branch A) and the fast (branch B) O₂ photodesorption processes to move to higher photon flux, as would be expected. Methanol is a known hole trap molecule⁶⁶⁻⁶⁸. The mode of operation of the methanol molecule as a hole trap has been described by a number of authors noted here, but never directly investigated spectroscopically. Proposed mechanisms include: the donation of an electron by adsorbed methoxy or by the adsorbed radical oxidation product ·CH₂OH. The electron donating character of the adsorbed species serves to make it a hole scavenger. More work should be done in order to completely understand these proposed mechanisms.

The efficiency of hole trapping by methanol in this work is found to be highest for the first monolayer of chemisorbed methanol (Figure 13), indicating that chemical coupling of the adsorbate hole-trap molecule to the TiO₂ surface is important for efficient charge transfer. Such effects have been found for other organic molecules undergoing charge transfer with trapped conduction band electrons in TiO₂⁹⁷. The observation of the effect of an added hole-trap molecule on the O₂ photodesorption kinetics lends support to the kinetic model of equations (3.1)-(3.6).

An estimate of the efficiency of adsorbed methanol molecules for trapping photogenerated holes originating from the TiO₂ may be made from the observed change in F_{hv}(crit.) upon adsorption of ~1ML of CH₃OH (Figure 14). This coverage of CH₃OH results in a shift of F_{hv}(crit.) from 2.5 x 10¹³ photons cm⁻²s⁻¹ to ~ 6.4 x 10¹³ photons cm⁻² s⁻¹. The difference (~ 4 x 10¹³ photons cm⁻²s⁻¹) is caused by the addition of ~ 2 x 10¹⁴ (0.6 ML) CH₃OH cm⁻². Assuming the difference in F_{hv}(crit.) for the CH₃OH-covered surface and the clean surface is due

to hole trapping by added CH₃OH and that each photon absorbed results in one hole which reaches the surface, the efficiency of hole trapping by a CH₃OH molecule is ~ 0.2 . Recombination of holes and electrons in the bulk would reduce the calculated CH₃OH hole trapping efficiency to values < 0.2 .

3.4.7. Future Directions

Studies of the surface photochemistry of model systems involving relatively simple model reactions (like O₂ photodesorption) on single crystal substrates (like TiO₂(110)) can supply simplifications which allow underlying physical issues to become visible. Similar studies, involving complicated molecules and multi-step photoprocesses, when carried out on heterogeneous photoactive surface such as powders or colloids, can introduce complexities which can mask the key physical processes at work. Just as the field of thermally-activated heterogeneous catalysis has benefited from the use of highly controlled experiments on single crystal model catalysts, so it is likely that advances may occur in surface photochemistry when model systems are studied under highly controlled experimental conditions. The kinetic detection of hole-traps, the quantitative use of hole-scavenger molecules, and the demonstration of the rapid achievement of a steady state condition for the electron-hole recombination process (rate dependence on $F_{\text{hv}}^{1/2}$) represent examples of the advances which may be expected in research of this type on model systems. Such understanding can benefit key technologies useful for the field of photochemical environmental remediation, for example.

3.5. Conclusions

The role of the saturation of the hole traps in TiO₂ has been investigated using a simple photochemical surface reaction which detects the transport of holes to the surface of a TiO₂(110) single crystalline substrate. The rate of O₂ photodesorption is used as a measure of the

availability of photochemically generated holes arriving at the TiO₂ surface. It has been shown that under conditions where hole traps are saturated, the rate for O₂ photodesorption is directly proportional to the square root of the incident light intensity ($F_{\text{hv}}^{1/2}$), indicating that the second-order recombination of electrons and holes is a limiting factor in determining the rate of photooxidation processes which occur on TiO₂. At a critical photon flux, $F_{\text{hv}}(\text{crit.})$, the rate for O₂ photodesorption per photon suddenly increases due to the saturation of deep hole-trap levels, causing a significant increase in the availability of charge carriers at the surface. We estimate that a hole-trap concentration of $\sim 2 \times 10^{18} \text{ cm}^{-3}$ is involved, and that the majority of these hole-trap sites are in the bulk of the TiO₂ single crystal, constituting about 2×10^{-5} of the atomic sites in the bulk lattice. The addition of an adsorbed hole-scavenging molecule, CH₃OH, which acts as an additional site for hole trapping, causes the value of $F_{\text{hv}}(\text{crit.})$ to shift toward higher light fluxes, while reducing the photoyield of O₂. This is the first research to quantitatively measure hole trapping effects for photochemistry on a TiO₂ single crystal which is uninfluenced by adsorbates, solvents and polycrystallinity.

4. CHAPTER FOUR: Control of Surface Photochemical Process by Fractal Electron Transport Across the Surface: O₂ Photodesorption from TiO₂(110)[♦]

Abstract

The photodesorption of O₂ from TiO₂(110) has been found to exhibit fractal kinetic behavior. The rate coefficient for photodesorption is measured throughout the entire experiment, and is shown to decrease by a factor of ~100 over a time period of ~250 s. A model is proposed in which the electrons associated with O-vacancy defects on the surface percolate from vacancy site to vacancy site via the filled orbitals at these sites to neutralize photo-produced holes. This electron percolation, causing e-h recombination, reduces the efficiency of charge transfer between a photoproduct hole and an O₂⁻(a) species localized at a vacancy defect site, causing the rate of O₂ photodesorption to follow a fractal rate law. We postulate that the fractal electron conduction path across the surface is one-dimensional.

4.1. Introduction

Understanding the kinetics of photochemical reactions of adsorbed species on semiconductor surfaces provides insights into the mechanism of the electronic excitation of a semiconductor as well as the mechanism of charge transfer at the surface⁹⁸. In the case of TiO₂ surfaces, the vast majority of the published photokinetic studies involve powdered or thin film TiO₂ material which contain mixed crystal structures and a variety of exposed crystal faces, unknown levels of surface and bulk defects, grain boundaries and dislocations, as well as electrical contact points between TiO₂ particles⁹⁹⁻¹⁰². In addition, surface impurities and solvent

[♦] Reproduced in part with permission from Tracy L. Thompson and John T. Yates, Jr. "Control of Surface Photochemical Process by Fractal Electron Transport Across the Surface: O₂ Photodesorption from TiO₂(110)", *Journal of Physical Chemistry B*, **Accepted for Publication**. Copyright 2006 American Chemical Society.

molecules are often present in the surface region, causing added complexity⁵⁸. The investigation of elementary photochemical processes on single crystalline substrates eliminates many of these complicating factors.

Many surface photochemical processes involving complex molecules consist of multiple elementary steps which include a series of charge exchange processes feeding into a series of chemical intermediate species which are involved in the overall photochemical reaction. Complex photochemical reactions of this sort are not easily amenable to detailed physical interpretation. In order to better understand the fundamental issues controlling surface photochemistry, it is appropriate to study simple model one-step photochemical reactions, induced by monochromatic UV irradiation. In addition, by using a single crystalline semiconductor substrate, containing known types of surface defects at known densities, one can control surface inhomogeneity effects. Finally ultrahigh vacuum studies on single crystalline surfaces known to be atomically clean and containing known surface coverage of the target molecule can provide an additional simplicity needed to perceive kinetic features which could be masked on inhomogeneous surfaces. This experimental report involves a high degree of control of the above-mentioned factors.

The photodesorption of chemisorbed molecular oxygen from TiO₂(110) is the model surface reaction investigated here. Molecular O₂ is known to adsorb on oxygen anion vacancy defects on TiO₂(110) at cryogenic temperatures^{8,16,55,103}. The density of these defect sites is about 8-10 %, based on studies made on TiO₂(110) crystals prepared in a similar manner to the crystal studied here^{3,7,16}. The O₂ molecule acquires a negative charge when adsorbed on these sites^{62-64,103,104}. The production of electron-hole pairs in TiO₂ by UV irradiation²³ with photon energies above the 3.05 eV bandgap energy produces holes which migrate through the near surface bulk

region to the adsorbed O_2^- species, causing charge exchange and photodesorption of O_2 ^{55,62,105}, as shown in the sequence of elementary steps described in Chapter Three equations 3.1 - 3.4. There, F_{hv} is equal to the incident UV photon flux, k_2 is the rate constant for capture of holes by hole-traps, T, in the TiO_2 , k_3 is the rate constant for electron-hole pair recombination, and k_4 is the rate constant for hole-induced desorption of $O_2(g)$. At UV light fluxes above a critical value, F_{hv} (crit.), where the hole-trap states have become saturated with holes, process (2) stops contributing to the kinetics²⁶. In this case, the rate of change of the relative O_2 coverage, $d[\theta_{O_2}]/dt$, may be written:

$$\frac{d[\theta_{O_2}]}{dt} = -k_4 \left(\frac{k_1}{k_3} \right)^{1/2} F_{hv}^{1/2} [\theta_{O_2}] \quad (4.1)$$

where the factor $F_{hv}^{1/2}$ originates from the establishment of a rapid equilibrium between electrons and holes, governed by k_1 and k_3 respectively. Since k_1 and k_3 are likely to be governed only by the properties of the bulk TiO_2 single crystal, they may be considered to be constant in our O_2 photodesorption experiments. Thus measurements of the rate of O_2 photodesorption as a function of O_2 coverage at known values of F_{hv} may be used to infer the functional character of the rate constant, k_4 , for the primary charge exchange process between a photoproduced hole and an adsorbed O_2 molecule.

We describe our measurements of the variation of k_4 as O_2 photodesorption proceeds. The measurements show that k_4 decreases by a factor of ~ 100 or more as the chemisorbed O_2 is photodesorbed, indicating that a fractal kinetic process is involved and the functional dependence of the value of k_4 on time during photodesorption supports this model. A possible mechanism involving hole neutralization by percolating electrons present at O-vacancy defects (which do not contain $O_2^-(a)$ species) is presented in Section 4.4 .

4.2. Experimental

The details of the experimental apparatus used for this work are presented in Chapter Two of this thesis. The adsorption and photodesorption procedures for molecular oxygen on TiO₂(110) are described in Chapter Three. Lamp calibration information can be found in Appendix B.

4.3. Results

Figure 17 shows a typical photodesorption measurement from a saturated coverage of ¹⁸O₂ on the slightly defective TiO₂(110) surface. Upon retracting the shutter on the filtered UV light source, the O₂ signal measured by the shielded and differentially pumped mass spectrometer reaches a maximum within the mass spectrometer sampling time (0.10 s), and then monotonically decreases over time as chemisorbed O₂ depletion occurs by photodesorption. In the rapidly-pumped vacuum system, the magnitude of ΔI_{O_2} is directly proportional to $-d[\theta_{O_2}]/dt$, the rate of O₂ photodesorption, because the kinetics for O₂(a) depletion from the surface are slow compared to the mass spectrometer pumping speed¹⁰⁶.

Typical O₂ Photodesorption Experiment

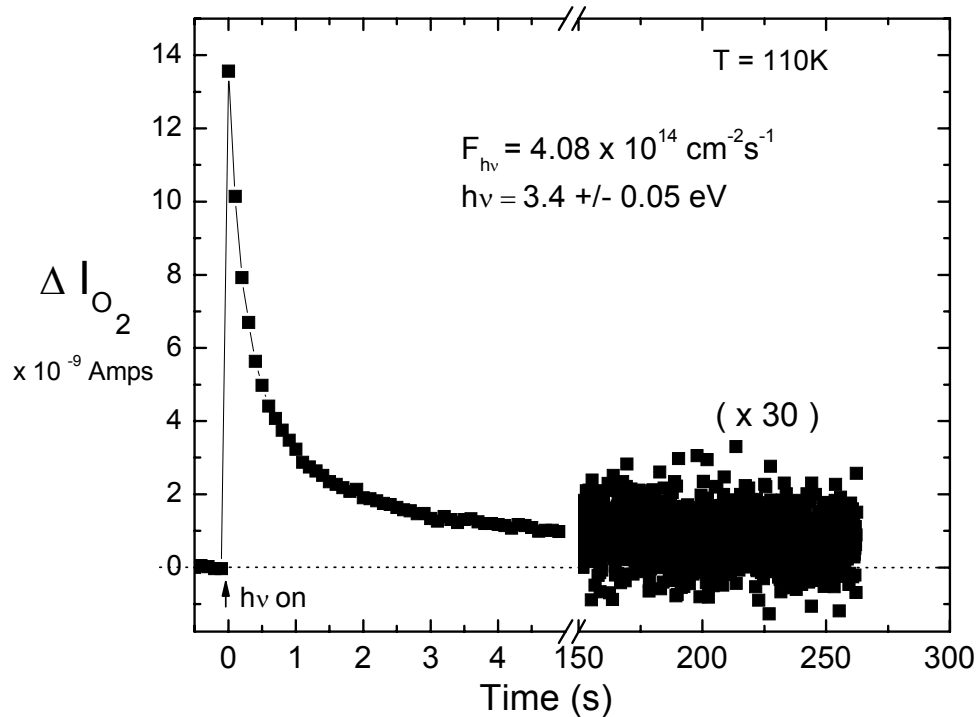


Figure 17: Example of the measured oxygen desorption pulse from TiO₂(110) after the defective surface was exposed to a saturation coverage of O₂. The data illustrate the measurable decrease in the oxygen partial pressure even after 250 seconds.

The photodesorption experiment is carried out to 262 s, when it is discontinued. It may be noted in Figure 17 that photodesorption continues to occur at a very slow rate even at the end of the experiment. Control experiments, with the crystal rotated out of the light beam and where the oxygen-exposed vacuum system is exposed to UV irradiation at fluxes and photon energies similar to those employed here, were negative; no photodesorption from the interior surfaces in the vacuum chamber was detected at the noise level. We estimate that we can measure the rate of O₂ desorption from the TiO₂(110) near the end of the experiment to within an accuracy of ± 20 % given the noise level and the negative results from background measurements of

photodesorption from the chamber walls. The accuracy is much higher over the majority of the experiment.

Figure 18 shows measurements of the *initial* rate of O₂ photodesorption achieved within ~0.1 s after first exposure to UV light for the O₂-saturated surface. This is designated $d[\theta^0_{O_2}]/dt$ and is plotted versus $F_{hv}^{1/2}$. Various values of F_{hv} were achieved using neutral density filters. The linearity of the curve indicates that the functional form of equation (4.1) is in accordance with the $F_{hv}^{1/2}$ dependence of the initial rate of O₂ photodesorption, as measured at the beginning of experiments such as that shown in Figure 17. The data in

Figure 18 are shown only for the range of photon fluxes above the critical flux, $F_{hv}^{1/2}(\text{crit.}) = 5 \times 10^6 \text{ cm}^{-1} \text{ s}^{-1/2}$, needed to saturate the hole traps in the TiO₂ crystal, and this is fully discussed in Reference ²⁶.

Initial Rate of O₂ Photodesorption from TiO₂(110)

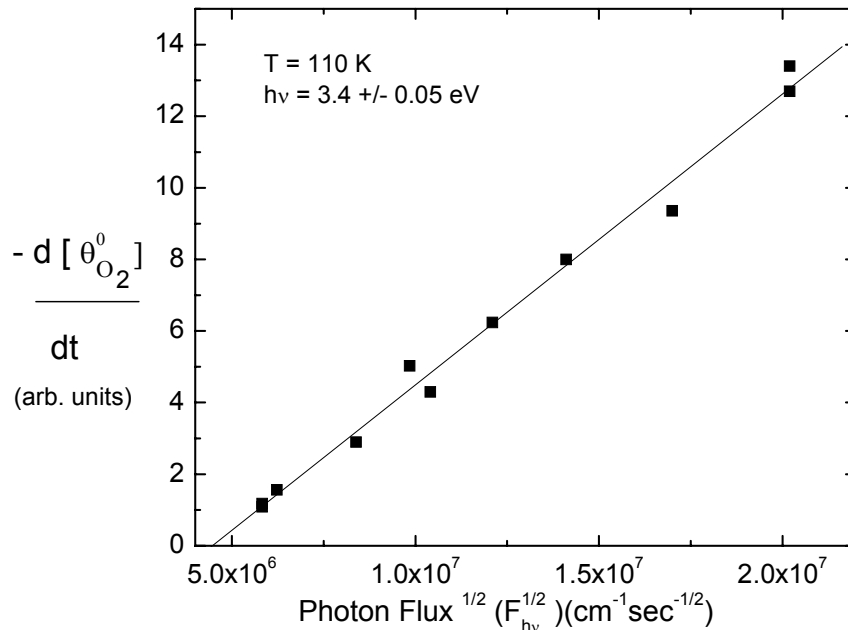


Figure 18: Measurement of the initial oxygen photodesorption rate versus the square root of the incident photon flux.

In order to evaluate the dependence of the rate of O₂ photodesorption on the relative coverage of O₂, θ_{O_2} , it is necessary to estimate the full coverage of O₂. This could be done by plotting the yield of evolved O₂ versus the time of irradiation, but we believe that even in the experiments at the largest value of F_{hv} , complete O₂ evolution does not occur in the experimental region where rates can be measured above the noise at long irradiation times (see Figure 17, where slow photodesorption of O₂ is still occurring at 262s). We have therefore selected an arbitrary value of the full O₂ coverage 30 % above the maximum measured value, and have examined how a reasonable range of assumed saturation O₂ coverage around the selected maximum coverage will affect the kinetic analysis. We find that a ± 20 % range in the assumed saturation value for the O₂ coverage does not influence the general conclusions about the wide range of the factor k_4 which may be extracted from the analysis. Highly fractal behavior exists and the fractal order remains constant independent of the saturation coverage assumed.

O₂ Photodesorption Kinetics – TiO₂(110)

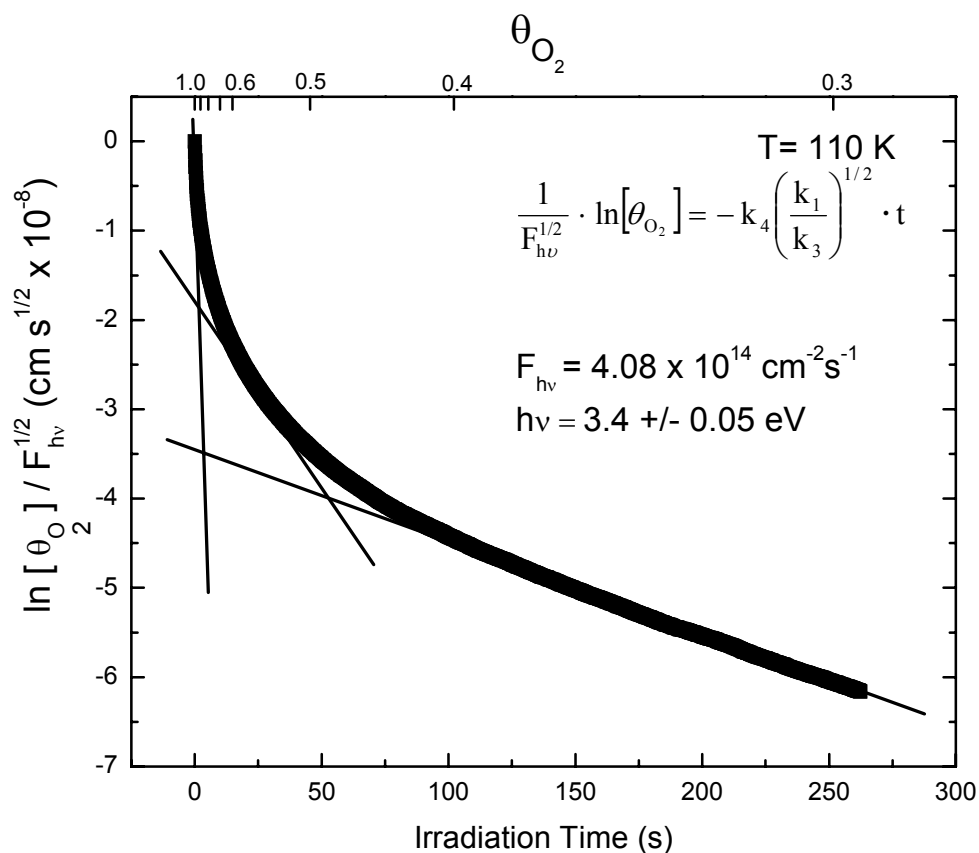


Figure 19: Plot showing the slope change related to the value of k_4 throughout the measurement time for the oxygen photodesorption experiment.

Figure 19 shows a plot of the integrated equation 4.1, using our estimate of the saturation value of the O₂ coverage. For a single value of the combination of rate constants, $k_4(k_1/k_3)^{1/2}$, Figure 19 should yield a single straight line of negative slope. Examination of the experimental curve indicates that a wide range of slopes are present, suggesting that fractal photodesorption kinetics are being observed. Figure 20 shows the range of slopes analytically determined from Figure 19. The factor $k_4(k_1/k_3)^{1/2}$ varies by about a factor of 100 over the experimentally measured range.

Range of Photodesorption Rate Coefficients
Experimentally Measured – O₂/TiO₂(110)

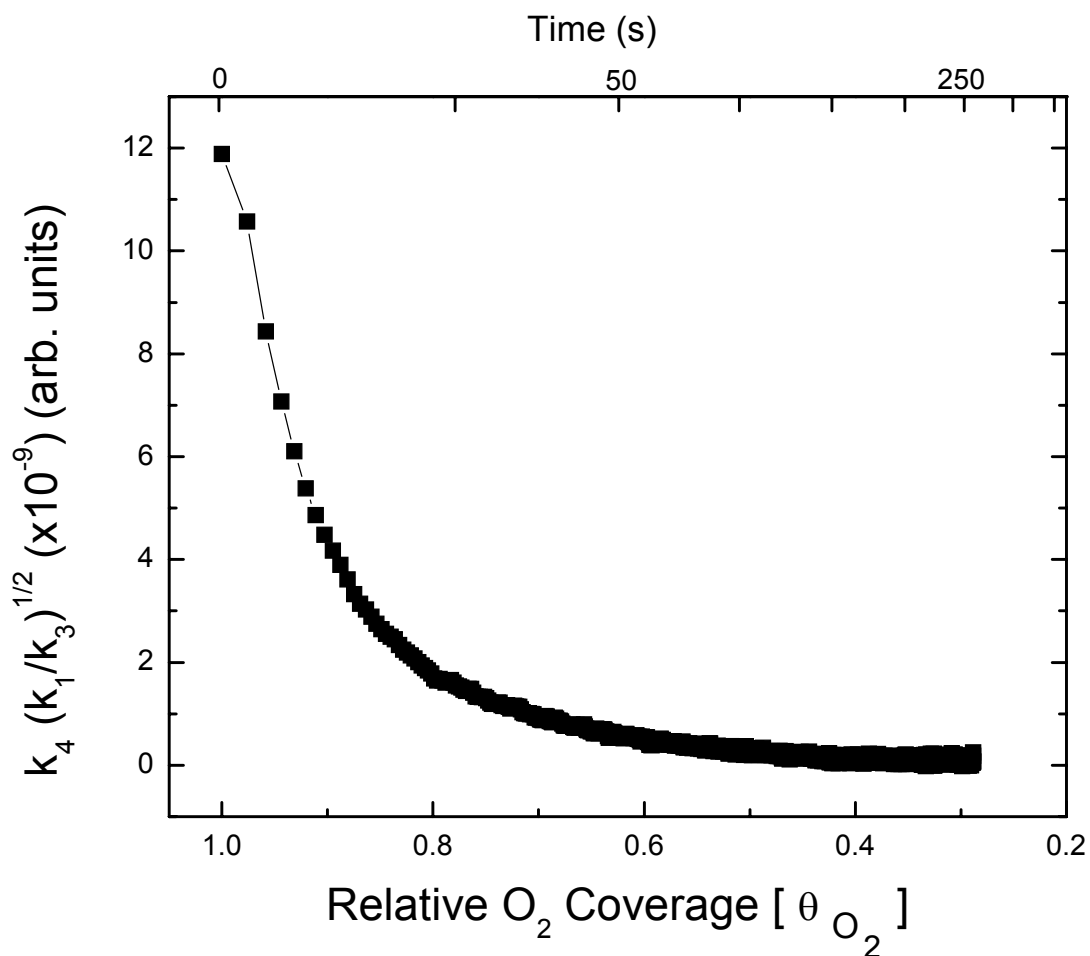


Figure 20: Plot showing the measured change in the value of $k_4(k_1/k_3)^{1/2}$ as the coverage of oxygen decreases during the photodesorption process.

4.4. Discussion

4.4.1. Kinetic Fit to Fractal Kinetics

Early experimental work investigating the nature of O₂ photodesorption from TiO₂(110) discovered the existence of at least 3 differing rates for the photodesorption process. The initial discovery of the so-called α and β channels showed that the α and β forms of adsorbed O₂

possessed distinctly different chemical characteristics^{55,60}. The β -O₂ species were found to exclusively photodesorb; the α -O₂ species were found also to be active in the photo-oxidation of CO to CO₂. It was found that α -O₂ converted to β -O₂ upon heating to near 200 K⁶⁰. The differing chemical activities of the adsorbed α - and β - O₂ species were postulated to be due to the presence of both peroxo- type and superoxo- type molecular O₂. Later work done by Rusu et al.¹⁰⁷ more thoroughly investigated the nature of the α -O₂ species initially reported by Lu^{55,60}. It was found that based on the pre-annealing temperature of the TiO₂(110) surface, at least 2 different states of the α -O₂ species could be observed. In that work¹⁰⁷, the possible variable nature of the thermally-produced defect sites were suggested to be responsible for differing adsorption states of the α -O₂ species. In Reference¹⁰⁷, the mechanism for O₂ photodesorption had not yet been theoretically investigated, nor had the experimental dependence of the rate of O₂ photodesorption on $F_{\text{hv}}^{1/2}$ been recognized. In the work reported here, the α -O₂ species has been prepared by adsorption at 110K.

In the results presented here, we have measured the kinetics of the O₂ photodesorption from a reduced TiO₂(110) surface in accordance with the kinetic scheme shown in equations (3.1) to (3.5). In equation (3.1) the rate constant k_1 represents the efficiency of the conversion of a photon into an electron-hole pair in the light absorption region of the TiO₂(110) crystal. Separate measurements have shown that the mean absorption distance for a photon is ~ 103 Å (See Appendix C). The value of k_1 , in this absorption depth, is of order unity since all photons are absorbed as long as the UV energy exceeds the bandgap (3.05 eV). In equation (3.2), the rate of hole trapping is described kinetically. Since this kinetic study was made under conditions where all hole traps are saturated, above $F_{\text{hv}}(\text{crit.})$, the elementary process in equation (3.2) does not contribute to the observed kinetics²⁶. In equation (3.3), the role of electron + hole

recombination is written. Since the concentration $[h^+] \approx [e^-]$, process (3.3) will exhibit a second-order dependence on $[h^+]$ leading to the proportional dependence of $[h^+]$ on $F_{hv}^{1/2}$; electrons and holes form and recombine at a rate which is rapid compared to hole consumption by process (3.4). Using the steady state approximation for describing the hole concentration, $[h^+]$, the kinetic rate of O_2 photodesorption above $F_{hv}(\text{crit.})$ is described by equation (4.1). Since we assume that k_1 and k_3 should depend only on the inherent properties of the TiO_2 crystal, which does not change during O_2 photodesorption, the measurement of the dependence of the rate of O_2 photodesorption on $[\theta_{O_2}]$ should provide the functional dependence of k_4 on $[\theta_{O_2}]$, or on the time during the photodesorption experiment.

Kopelman³³ has described the nature of the kinetic rate “constants” for processes which may be considered to be fractal in nature. For a large number of chemical or physical systems, the so-called rate “constant” is not a constant, but rather varies as a function of time during the kinetic process and in this case should be termed a rate coefficient which varies with time.

Fractal Kinetic Behavior of the Photodesorption of O₂ from TiO₂(110)

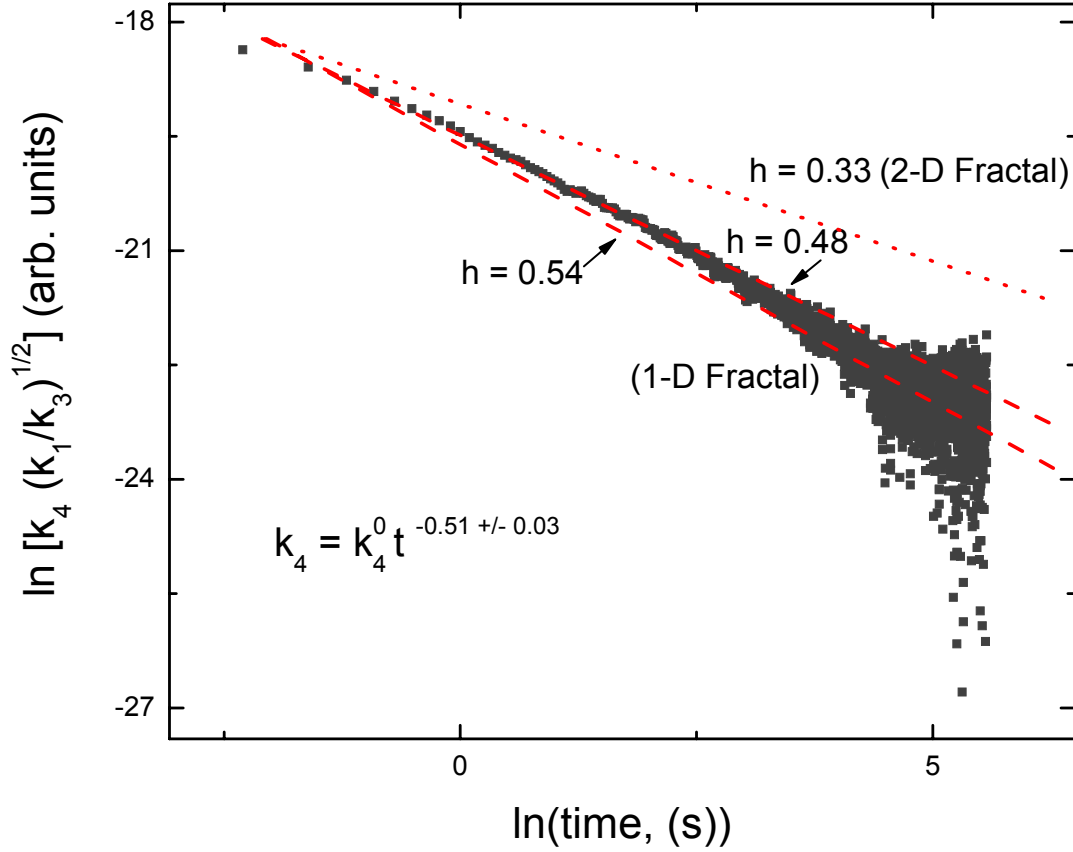


Figure 21: Plot showing the measured fractal behavior of the oxygen photodesorption process. The data are fit to the scaling law, and shows one-dimensional fractal character. The slight downward curvature of this plot has been reproduced in experiments at lower values of F_{hv} .

In Figure 21, we show that O₂ photodesorption from TiO₂ proceeds by fractal kinetics, where the time dependence of k_4 can be evaluated in the form as presented in reference³³ as:

$$k_4 = k_4^0 t^{-h} \quad (4.2)$$

or

$$\ln k_4 = -h \ln t + const. \quad (4.3)$$

This analysis yields a linear curve that has a value for $h = 0.51 \pm 0.03$, which is in accordance with the definition of a fractal kinetic system where $0 > h > 1$. The O_2 photodesorption reaction can therefore be classified as one which is controlled by a percolation process through a fractal network, as discussed below.

4.4.2. The Fractal Rate Controlling Step in O_2 Photodesorption From Defect Sites on $TiO_2(110)$

In the case of the O_2 photodesorption process, a photogenerated hole arriving at a surface O-vacancy defect site (occupied by $O_2^-(a)$) initiates the O_2 photodesorption event as a result of charge transfer between $O_2^-(a)$ and the hole. Fractal kinetics are expected for surface processes in which interconnected (interacting) surface sites are involved in the transport of energy, charge, or chemical species across the surface in the rate-determining kinetic step.

The charge cloud associated with an O-vacancy defect site has been shown to extend over the surface greatly beyond the point defect location³⁵. We propose that pathways exist for electron transport across the surface from one unoccupied defect site to another. Electron transport may occur via these extended charge clouds eventually causing the neutralization of a photoproduct hole, decreasing k_4 . Vijay et al. have postulated a similar electron transport process on $TiO_2(110)$ from a defect site to produce a negatively charged surface Au atom³⁵.

In this model, the fractal kinetics observed for O_2 photodesorption for the O-vacancy defect sites on $TiO_2(110)$ result from electron hopping from one unfilled defect site to a neighbor unfilled defect site through pathways involving the filled electronic state at each defect site. At high $O_2^-(a)$ coverage the interconnections between unfilled defect sites are sparse leading to efficient $O_2^-(a)$ -to-hole charge transfer as a result of a lower hole neutralization probability by electrons transported over the surface. This results in a high rate coefficient, k_4 , for O_2

photodesorption. As the $O_2^-(a)$ coverage decreases during the O_2 photodesorption, the fraction of interconnected filled electronic states at vacancy sites increases. Hole neutralization by electron transport through the interconnected vacancy site orbital therefore becomes more probable, thus reducing the effectiveness of the photoproducted holes to locally induce charge transfer from $O_2^-(a)$ species. This causes the O_2 desorption rate coefficient to decrease during O_2 photodesorption, leading to the observed fractal kinetics for k_4 . This process is schematically shown in Figure 22.

Schematic of Electron Transport via O-Vacancy Defect Sites, Leading to a Decreasing O_2 Photodesorption Rate Constant as Coverage Decreases

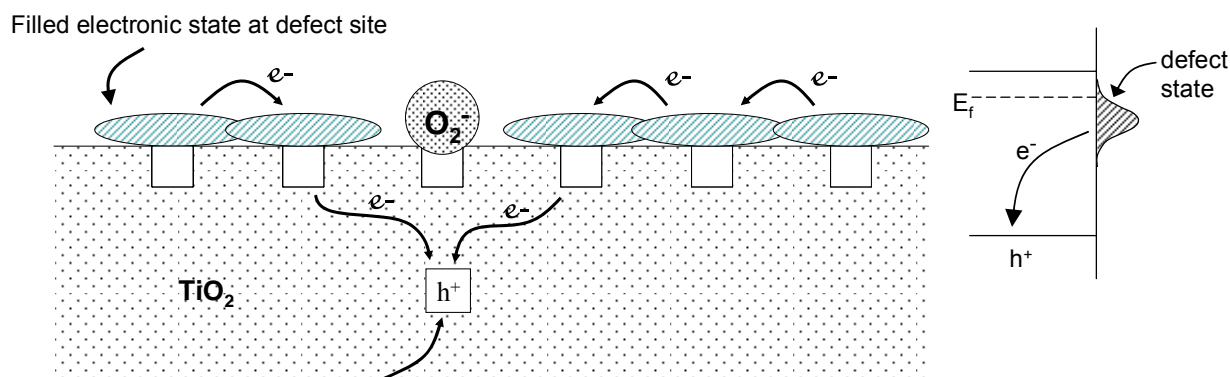


Figure 22: Schematic diagram showing the electron transport that is postulated to occur through the extended filled electronic states surrounding oxygen vacancy sites. As the coverage of adsorbed oxygen decreases, the surface density of the overlapping filled electronic states at vacancy sites increases thus decreasing the rate coefficient for O_2 photodesorption with time.

The log-log plot in Figure 21 is indicative of a one-dimensional fractal process, with a value of h near 0.5. A two-dimensional fractal network will yield a value of h near $0.33^{33,34,108}$ which is clearly not supported by our data as shown in Figure 21. While the scaling law in Figure 21 is consistent with one-dimensional fractal behavior and the kinetic data cover a range of more than two decades, one should be cautious in interpretation of such a scaling law.

We therefore postulate that one-dimensional fractal electrical conductivity across the TiO_2 surface controls the rate of O_2 photodesorption from the point defect sites randomly

arranged on $\text{TiO}_2(110)$. This takes place through favorable overlap of the interconnected filled orbitals along one of the orthogonal crystallographic axes on the surface. Confirmation of this observation awaits more detailed studies of the anisotropic effects in the surface conductivity of the defective $\text{TiO}_2(110)$ surface.

4.5. Conclusions

The photon induced desorption of molecular O_2 from defective $\text{TiO}_2(110)$ exhibits fractal reaction kinetics where the rate constant for desorption is observed to decrease in a time dependent manner by a factor of ~ 100 as O_2 photodesorption occurs. We hypothesize that the decrease in the rate coefficient is caused by hole neutralization effects from electrons localized on oxygen-vacancy defect sites in the TiO_2 surface. As the coverage of $\text{O}_2^-(a)$ decreases over time in the photodesorption process, the unfilled O-vacancy sites are generated and supply increasingly efficient percolating pathways of neutralizing electrons for photogenerated holes. The neutralizing electrons are transported over a fractal network in percolating electron pathways to the holes. During O_2 photodesorption as time evolves and the O_2^- occupied site density decreases, the efficiency of the photodesorption decreases enormously yielding fractal kinetics. We speculate that the fractal kinetics observed are consistent with one-dimensional electron percolation across the $\text{TiO}_2(110)$ surface.

5. CHAPTER FIVE: CO₂ as a Probe for Monitoring the Surface Defects on TiO₂(110) – Temperature-Programmed Desorption[♥]

Abstract

The adsorption and thermal desorption of CO₂ bound to both oxidized and reduced TiO₂(110) surfaces has been studied using temperature programmed desorption. For the stoichiometric and fully oxidized surface, a single thermal desorption feature ($E_d = 48.5$ kJ/mol) is measured and is attributed to CO₂ bound to regular 5-fold coordinated Ti⁴⁺ atoms. For the fully reduced TiO₂(110) surface, CO₂ binds not only to regular sites, but also to oxygen vacancy sites ($E_d = 54.0$ kJ/mol), created by thermal annealing. The variation in the characteristic CO₂ desorption kinetics was measured as a function of the surface reduction temperature and the systematic production of increasing levels of surface defects is observed in the temperature range of 600K- 1100K. This investigation was complimented by a comparison of the characteristic CO₂ desorption feature(s) from a TiO₂(110) surface which was prepared by sputtering and direct annealing, without annealing in O₂ flux. It was found that after annealing to temperatures above 900K that the CO₂ thermal desorption is very similar for surfaces prepared by the two methods, regardless of surface preparation.

5.1. Introduction

The interaction of carbon dioxide and the TiO₂(110) surface was studied as a method for the characterization of the degree of surface reduction by annealing in vacuum. It has been well documented that oxygen vacancy sites, created by thermal annealing in vacuum, are the active

[♥] Reproduced in part with permission from Tracy L. Thompson, Oliver Diwald and John T. Yates, Jr. "CO₂ as a Probe for Monitoring the Surface Defects on TiO₂(110) Temperature-Programmed Desorption" *Journal of Physical Chemistry B*, **107** (2003) 11700-11704. Copyright 2003 American Chemical Society.

sites for oxygen adsorption ⁸. The use of a variety of techniques including ion scattering spectroscopy ⁷, O₂ photodesorption ^{55,107}, and STM ¹² have confirmed the presence of O vacancy sites after thermal annealing. The density of these vacancy sites can reach 8-10% of a single monolayer ^{7,12,55,107}. The nature of defects on TiO₂ is well explained in a recent review by Diebold ³. Because the presence of these defect sites on TiO₂ is critical to its activity as a photo-oxidation catalyst, experimental methods that can be used to quantify the defect sites give insight into the overall activity of the single crystal TiO₂ substrate. Previous work of this nature involves the interaction of various adsorbed species with both 5-fold coordinated Ti⁴⁺ and oxygen vacancy sites (Ti³⁺) as reported by Lu et al. ¹⁶. In that work, the adsorption of D₂O, ¹³CH₂O and ¹⁵NO and the subsequent thermal desorption of reduced products was studied as a function of the crystal annealing temperature. Results show a direct correlation between the surface annealing temperature and the yield of the reduced products. The onset temperature for O-vacancy defect formation, as measured in this manner, was 500K.

Specific results relating to the nature of CO₂ chemisorption on TiO₂ have been obtained using both theoretical calculations for single crystals ¹⁰⁹ and experimental measurements for both powdered ¹¹⁰⁻¹¹⁴ and single crystal substrates ^{22,115}. For TiO₂(110), interactions of water and carbon dioxide were reported by Henderson ²². In that work, it was shown that CO₂ binds to both regular Ti⁴⁺ sites, as well as to oxygen vacancy sites, producing two features in the CO₂ thermal desorption spectra. The work to be presented here deals with the thermal desorption of CO₂ from TiO₂(110) where varying degrees of surface reduction affect the CO₂ thermal desorption behavior. Preparation procedure A involves heating the sputter-cleaned crystal to 900K for 60 minutes and then cooling in O₂ flux (5×10^{14} molecules cm⁻² s⁻¹). This crystal was then heated prior to each thermal desorption experiment to various temperatures ranging from 600K to

1100K in vacuum to produce different surface and bulk defect levels. Procedure A has been shown to oxidize Ti^{+3} interstitial species, creating re-grown surface islands of fully oxidized Ti^{+4}O_2 in a (1 x 1) structure^{3,116,117}. The area of the re-grown islands increases with increasing annealing temperature in O_2 , as shown in Stone et al.¹¹⁶. In our procedure A, we believe the surface to consist of regular (1 x 1) islands where the irregularities created by sputtering are significantly smoothed¹¹⁷.

Also, comparative studies were done by using CO_2 as a probe for the defect density on a $\text{TiO}_2(110)$ crystal which has been prepared via preparation procedure B, the so called “bulk oxidation” technique¹¹⁸, which does not involve a full oxidation procedure in a controlled O_2 flux. In procedure B, the sputter-cleaned crystal was annealed in vacuum to various temperatures ranging from 750K to 1100K. No oxidation in O_2 flux was performed.

5.2. Experimental

The experimental details regarding the ultra-high vacuum apparatus and crystal preparation procedures presented in this chapter are summarized in Chapter Two of this thesis.

For preparation procedure A, the fully oxidized surface is obtained by annealing the clean crystal to temperatures of 900K in O_2 flux of 5×10^{14} molecules cm^{-2} s for 1 hour. The crystal is also cooled in the same flux of $\text{O}_2(\text{g})$. Reduction of the crystal was done by annealing in vacuum to various temperatures each for 1 hour, starting at 600K. In preparation procedure B, the clean crystal surface was sputtered (500eV, 15 min.) and then annealed in vacuum to temperatures in the range of 750 to 1100K.

$^{13}\text{CO}_2$ (Cambridge Isotope Laboratories, 99%) was used in the experiments described in this Chapter. All gas exposures were carried out using a calibrated microcapillary array beam doser (7.3×10^{13} CO_2 molecules torr^{-1} cm^{-2} s^{-1}) at a crystal temperature of 110K⁵⁴. After gas

exposure, the sample was then rotated into position directly in front of the QMS aperture. For CO_2 thermal desorption measurements, a heating rate of 2K sec^{-1} was used.

5.3. Results

5.3.1. Thermal Desorption of CO_2 from TiO_2

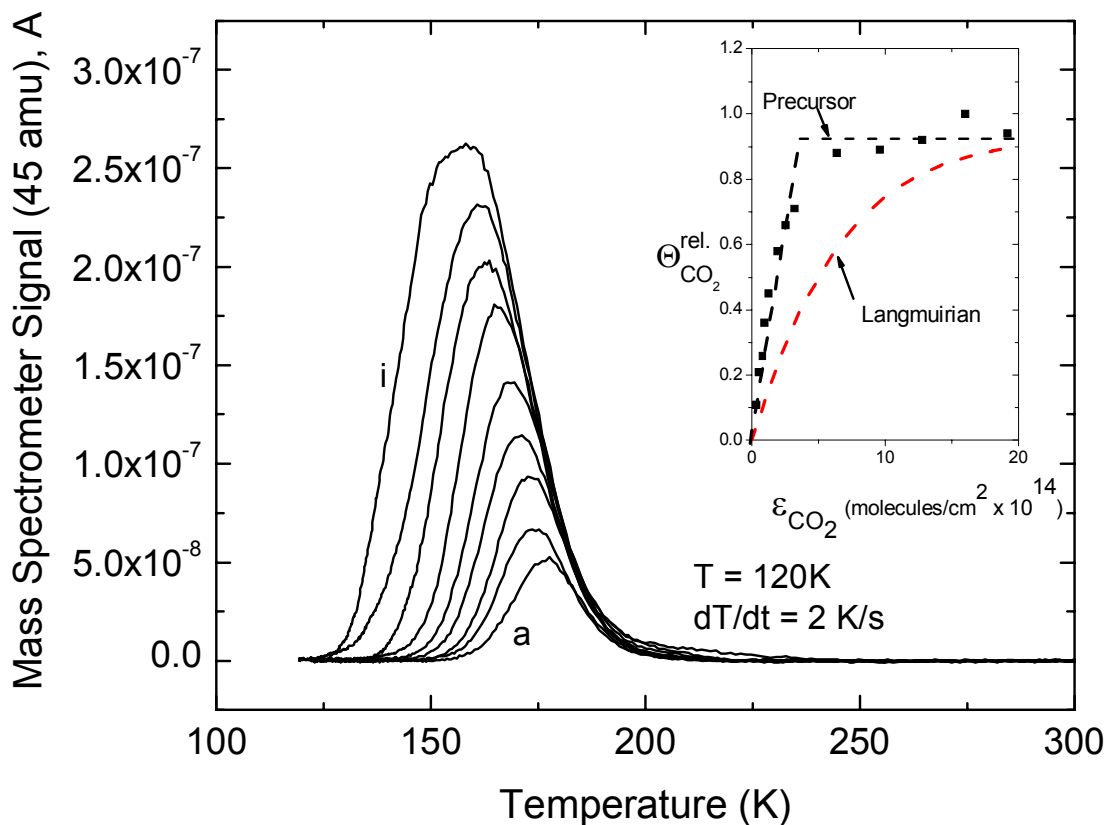


Figure 23: Coverage dependent thermal desorption spectra for $^{13}\text{CO}_2$ adsorbed on a fully oxidized $\text{TiO}_2(110)$ surface. CO_2 exposures are (a) $3.5 \times 10^{13} \text{ CO}_2/\text{cm}^2$; (b) $5.0 \times 10^{13} \text{ CO}_2/\text{cm}^2$; (c) $8.0 \times 10^{13} \text{ CO}_2/\text{cm}^2$; (d) $9.6 \times 10^{13} \text{ CO}_2/\text{cm}^2$; (e) $1.3 \times 10^{14} \text{ CO}_2/\text{cm}^2$; (f) $1.6 \times 10^{14} \text{ CO}_2/\text{cm}^2$; (g) $2.0 \times 10^{14} \text{ CO}_2/\text{cm}^2$; (h) $2.5 \times 10^{14} \text{ CO}_2/\text{cm}^2$; (i) $3.5 \times 10^{14} \text{ CO}_2/\text{cm}^2$.

Figure 23 shows thermal desorption spectra of varying $^{13}\text{CO}_2$ exposures for a fully-oxidized $\text{TiO}_2(110)$ surface. For this surface, low exposures of CO_2 reveal a single desorption peak at approximately 170 K, which grows to saturation after exposure to approximately 3×10^{14}

molecules cm^{-2} . The inset of Figure 23 shows the asymptotic rise of the $^{13}\text{CO}_2$ coverage to near saturation as the exposure is increased. The CO_2 feature seen at low coverage at 170K is attributed to CO_2 molecules that are bound to regular 5-coordinate Ti^{4+} sites. The first order thermal desorption spectra for the oxidized surface was simulated for CO_2 coverage between 1.5×10^{13} molecules cm^{-2} and 1.5×10^{14} molecules cm^{-2} according to the Polanyi-Wigner equation:

$$-\frac{dN}{dT} = R_{des} = \nu^0 \cdot \frac{1}{\beta} N \exp\left[-\frac{(E_{des}^{\circ} + E_{int}N)}{kT}\right] \quad (5.1)$$

where R_{eds} is the rate of desorption, dN/dt , N is the coverage, ν^0 is the pre-exponential factor, $\beta = dT/dt$, E_{des}° is the zero-coverage desorption activation energy, and E_{int} is the energy of the lateral interactions between adsorbed CO_2 molecules.

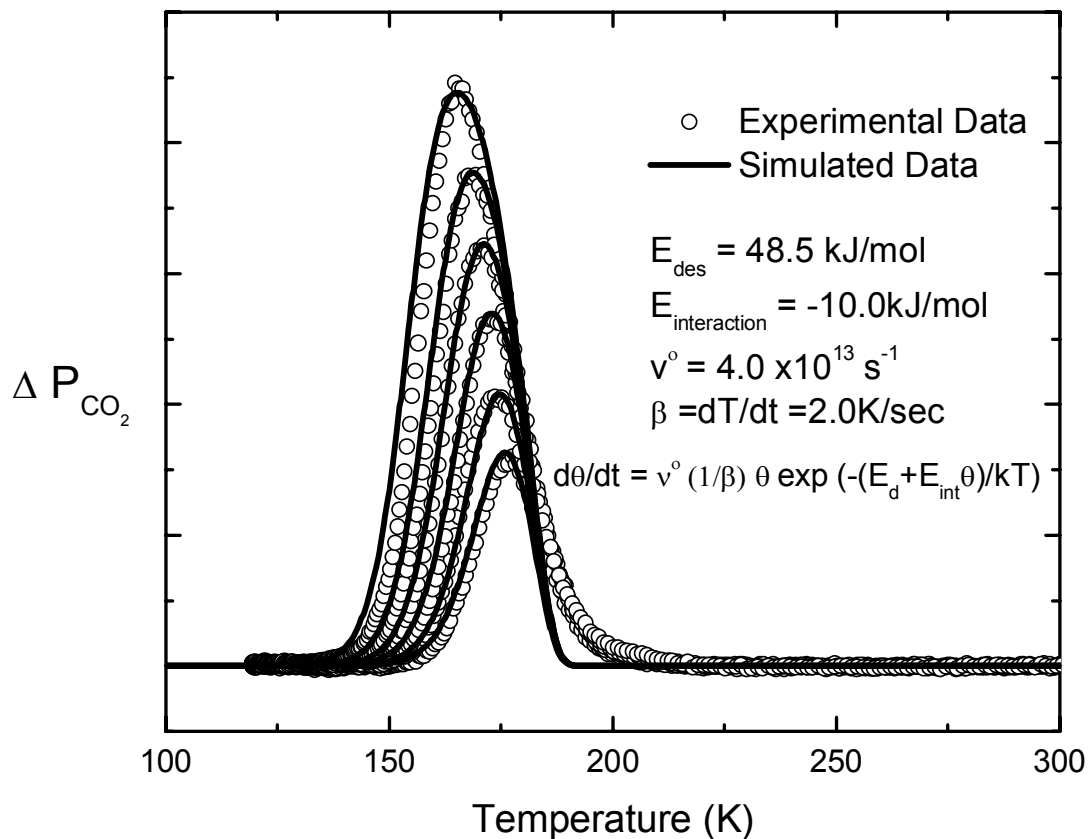


Figure 24: Simulated data versus experimental data for CO₂ thermal desorption from a fully oxidized TiO₂(110) surface for low coverage ranging from 1.5×10^{13} molecules cm⁻² to 1.5×10^{14} molecules cm⁻².

Figure 24 shows both the simulated data as well as the experimental results. It was found that CO₂, bound to regular 5-fold coordinated Ti⁴⁺ sites, exhibits a desorption activation energy of $E_{\text{des}}^{\circ} = 48.5 \text{ kJ mol}^{-1}$, with a pre-exponential term of $4 \times 10^{13} \text{ s}^{-1}$ and an interaction energy of -10 kJ mol^{-1} , signifying repulsive interactions between adsorbates. The linear increase in ¹³CO₂ coverage during the majority of the adsorption process indicates that adsorption occurs via a mobile precursor mechanism¹¹⁹. The fitting procedure has favored the leading edge of the desorption pulse since errors due to defect sites can easily influence the trailing edge.

Upon annealing the crystal in vacuum to higher temperatures, the appearance of an additional $^{13}\text{CO}_2$ peak desorbing at higher temperatures in the TPD spectra is evident, as shown in Figure 25 where a full set of coverage dependent TPD spectra is shown for each reduction temperature in the range of 600-1100K. Because of small experimental variations from day to day for the different adsorption measurements, a through f, we have chosen to normalize all of the $^{13}\text{CO}_2$ desorption spectra to the maximum coverage in each presentation. The appearance of the high temperature TPD feature (at about 200K) as a shoulder to the peak attributed to CO_2 bound to regular sites is first seen clearly on the surface that has been prepared by annealing at 700K for 1 hour. Because this peak grows after annealing to higher temperatures, it is attributed to CO_2 bound to the defective TiO_2 surface, specifically to oxygen vacancy sites. The development of the spectra for various annealing temperatures indicates that a maximum number of defects are achieved after annealing in vacuum to temperatures of $\sim 900\text{K}$.

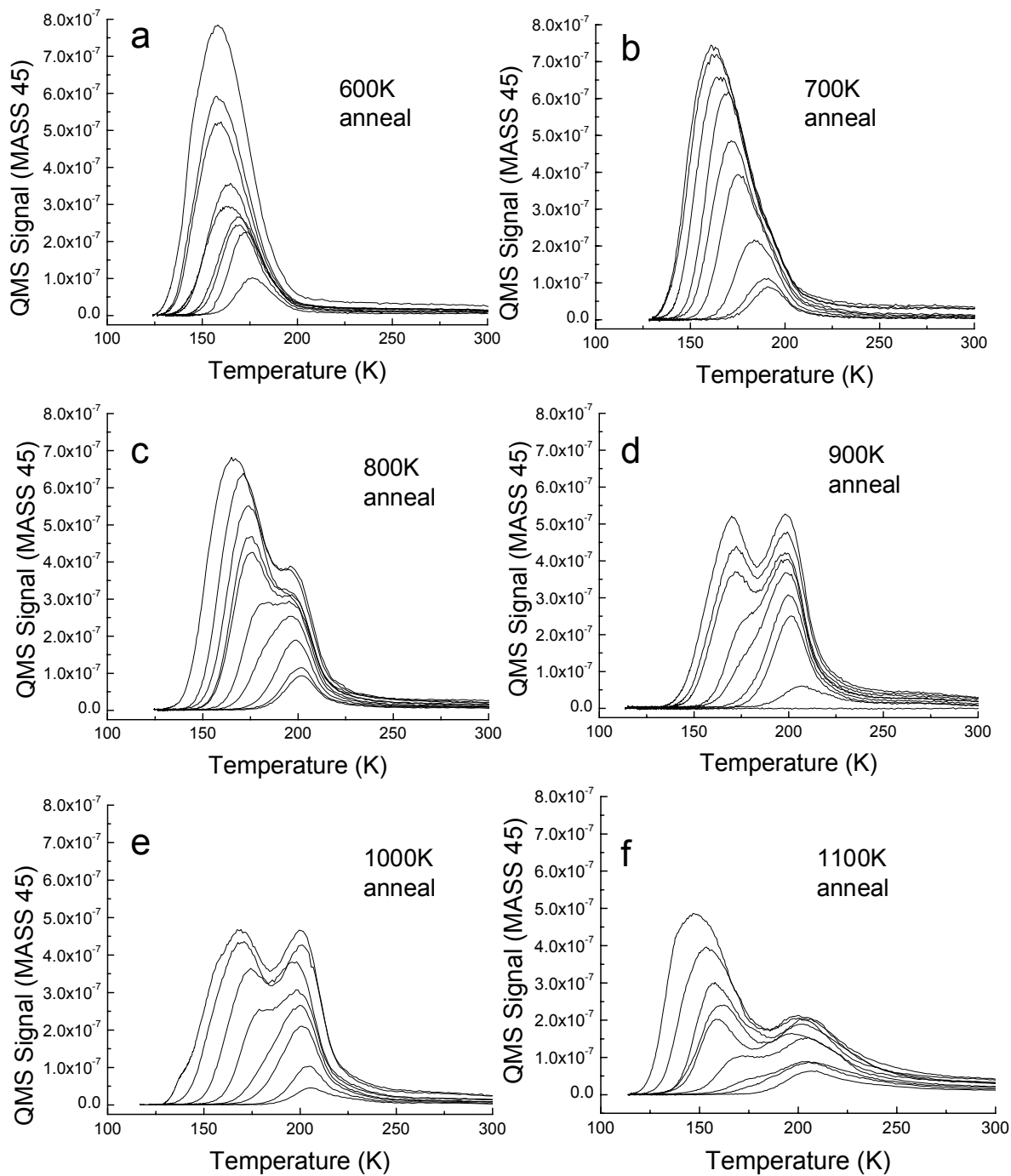


Figure 25: Normalized coverage dependent thermal desorption spectra for $^{13}\text{CO}_2$ adsorbed on $\text{TiO}_2(110)$ for surfaces preannealed to (a) 600K; (b) 700K; (c) 800K; (d) 900K; (e) 1000K; (f) 1100K. In these experiments, the $^{13}\text{CO}_2$ exposure ranged from 1.5×10^{13} molecules cm^{-2} to 3.5×10^{14} molecules cm^{-2} .

A simulation using the same method as for the data shown in Figure 24 was done for the high temperature CO₂ desorption feature, also for low coverage of CO₂ (1.5×10^{13} CO₂ cm⁻² to 1.5×10^{14} CO₂ cm⁻²) as shown in Figure 26. Isolation of the high temperature feature was achieved by subtraction of the low temperature CO₂ desorption feature from a fully oxidized surface from the data presented in Figure 25 d. The pre-exponential term was set to be 4×10^{13} s⁻¹ and the resulting desorption activation energy was $E_{\text{d}}^{\circ} = 54.0$ kJ mol⁻¹. Again, kinetic fits to the leading edge were favored in the analysis. The calculated value for the repulsive interaction energy between adsorbed CO₂ molecules at Ti³⁺ sites was estimated as -7 kJ mol⁻¹.

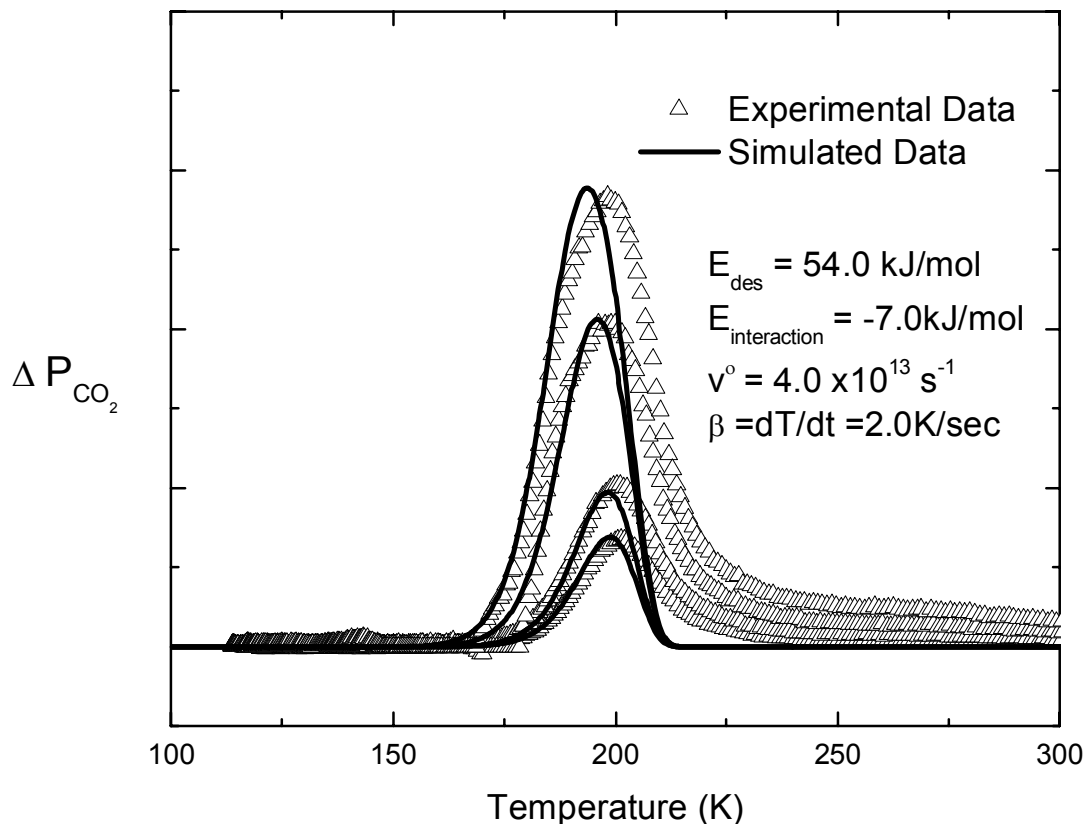


Figure 26: Simulated data versus experimental data for CO₂ thermal desorption from a fully reduced (900 K) TiO₂(110) surface for low coverage, ranging from 1.5×10^{13} molecules cm⁻² to 1.5×10^{14} molecules cm⁻².

5.3.2. CO₂ Thermal Desorption Spectra from a Sputtered and Annealed Surface

For the crystal surface which has been prepared via the “bulk assisted” oxidation technique¹¹⁸, procedure B, CO₂ thermal desorption spectra are shown as a function of the annealing temperature in Figure 27. The CO₂(g) exposure is the same for each experiment in this case. For lower annealing temperatures (750 K) a very broad single desorption feature is measured spanning a temperature range from ~140 K to 220 K. With increasing annealing temperature, this broad feature becomes sharper, and after annealing to temperatures above 900 K, a two peak thermal desorption is observed, qualitatively similar to that seen in Figure 25 c, d, e and f.

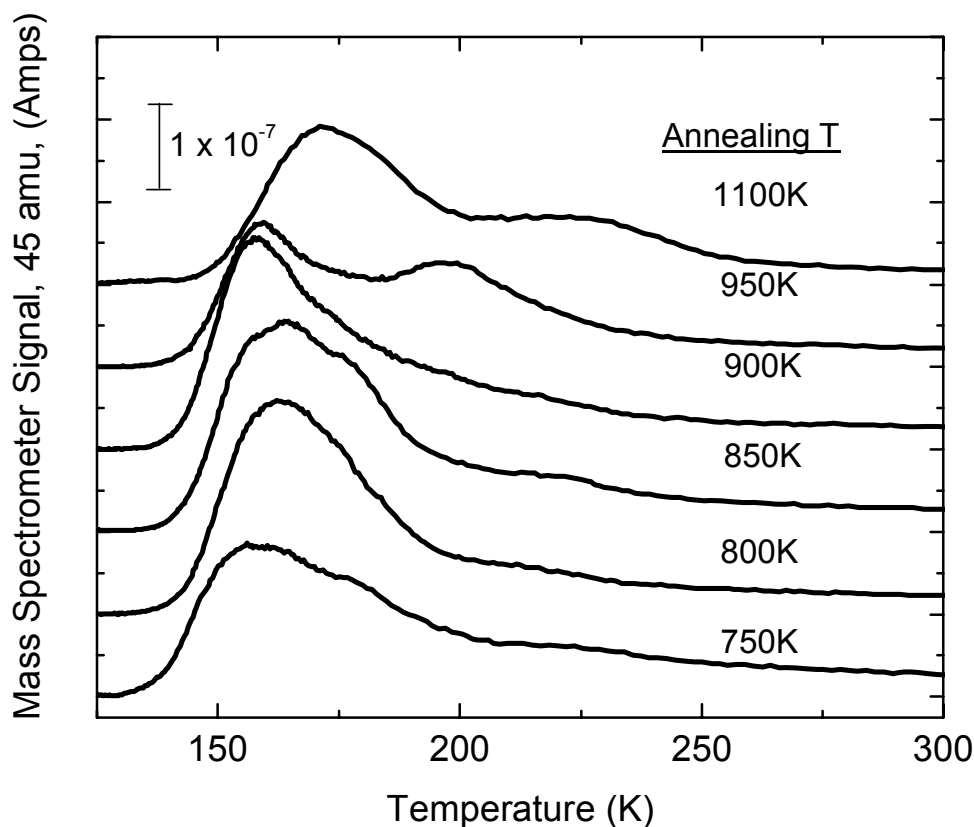


Figure 27: Characteristic CO₂ thermal desorption spectra from a TiO₂(110) crystal that has been sputtered then annealed prior to CO₂ adsorption according to procedure B. Spectra are shown for various preannealing temperatures, as noted. Each spectrum shown is for the same CO₂ exposure, 1.5×10^{14} CO₂/cm².

5.4. Discussion: Thermal Desorption of CO₂ from TiO₂(110)

Anion vacancy defect sites are of importance in the application of TiO₂ to photooxidation chemistry, since O₂ reactant is preferentially adsorbed on these sites⁸. Previous studies have measured the presence of these sites using chemical reduction reactions which are specific for these sites⁵⁵. However, a more simple method which is sensitive to the defect sites would be useful, and the specific high binding energy adsorption behavior of CO₂ on defect sites serves this purpose. Henderson has observed the characteristic two-step desorption process which is indicative of the presence of both vacancy defect and non-defective TiO₂ sites²². Our

experiments agree qualitatively with this work, and we have measured the activation energy for desorption of the two types of CO₂. We find that under the adsorption temperature conditions of our experiment it is difficult to completely saturate the CO₂ species which forms on the non-defective surface sites, so the ratio of the population of the two desorption states cannot be used to determine the ratio of the sites.

For CO₂ on TiO₂(110) and on partially reduced TiO₂(110) (adsorption kinetic experiments not shown on the latter surface), adsorption occurs via a mobile precursor mechanism causing a linear uptake curve to be observed as shown for example in the inset to Figure 23. This observation implies that delivery of the adsorbate to the higher binding energy defect sites occurs by means of a weakly-held species which can sample multiple sites before adsorption¹¹⁹. CO₂ adsorption via a Langmuirian kinetic model is not appropriate as seen in the inset to Figure 23.

For CO₂ adsorption on the fully-oxidized surface, where the CO₂ is bound to Ti⁴⁺ sites, we measure a zero-coverage activation energy for CO₂ desorption of 48.5 kJ mol⁻¹. Repulsive lateral interactions (~10 kJ mol⁻¹) occur between these species. Theoretical calculations report that the binding energy of CO₂ to TiO₂(110) occurs with an energy of 65 kJ mol⁻¹, in approximate agreement with our measurement of 48.5 kJ mol⁻¹¹⁰⁹. Calculations indicate that repulsive energies of ~ -15 kJ mol⁻¹ would be expected for CO₂ on TiO₂(110)¹⁰⁹ in satisfactory agreement with our measurements.

From the comparison of the experiment and the simulations of the kinetic behavior for CO₂ desorption from the defect sites produced by annealing TiO₂(110) in vacuum above about 700K, we measure a zero coverage activation energy of ~54 kJ mol⁻¹. It is surprising that this energy is only about 6 kJ mol⁻¹ above the activation energy for desorption from the fully

oxidized surface, since the electronic character of the defect site (Ti^{3+}) is very different from the Ti^{4+} site on the oxidized surface. The repulsive $\text{CO}_2\cdots\text{CO}_2$ interaction energy for CO_2 on the defect sites is somewhat less than for CO_2 on the oxidized surface, possibly because of the greater spatial separation of defect sites.

The sequence of CO_2 thermal desorption spectra seen in Figure 25 fit together into a logical sequence up to an annealing temperature of 1000 K. The high temperature desorption process becomes systematically more prominent for increasing annealing temperatures. However, annealing at 1100 K leads to a change in the nature of the sequence, with the development of a more prominent lower temperature CO_2 desorption state. The 1100 K temperature is the onset temperature for a massive reconstruction of $\text{TiO}_2(110)-(1 \times 1)$ to produce the (2×1) surface phase for which STM structural studies, and models for this structure have been presented^{116,120-122}.

It appears that the thermal treatment of $\text{TiO}_2(110)$ surfaces made by preparation method A and method B yield similar CO_2 desorption behavior when high temperature annealing occurs into the temperature range where the (1×1) to (2×1) reconstruction occurs, as seen from comparison of Figure 25 (f) and the upper CO_2 desorption spectrum in Figure 27.

5.5. Conclusions

The thermal desorption characteristics for CO_2 from $\text{TiO}_2(110)$ have been studied. The effect of surface preparation on these experiments has also been investigated. The following conclusions can be drawn:

- 1) Two types of adsorption sites, assigned as non-defective and defective, are available for the adsorption of CO_2 on a $\text{TiO}_2(110)$ vacuum annealed surface. The thermal desorption of

CO₂ from TiO₂(110) can therefore be used as a tool to investigate defect production on TiO₂(110) surfaces.

2) For a TiO₂(110) surface which has been prepared by Ar⁺ sputtering and subsequent annealing, the characteristic CO₂ thermal desorption becomes more like that of a fully oxidized (and then reduced crystal) with increasing annealing temperature.

6. CHAPTER SIX: Molecular Oxygen-Mediated Vacancy Diffusion on TiO₂(110) – New Studies of the Proposed Mechanism[Ⓢ]

Abstract

The recent report¹²³ in which the scanning tunneling microscope (STM) shows that adsorbed molecular oxygen locally induces anisotropic surface vacancy diffusion by dissociation near the vacancy, is inconsistent with negative observations of isotopic mixing between adsorbed ¹⁸O₂ and the ¹⁶O atoms in the TiO₂ lattice. Using adsorbed ¹⁸O₂ on TiO₂(110), prepared identically to the surface studied by STM, both the photodesorption and thermal desorption of adsorbed O₂ fail to detect any isotopic exchange with lattice O. These results suggest that the mechanism proposed for the O₂-mediated vacancy diffusion must be modified.

6.1. Introduction

The behavior of oxygen anion vacancy defect sites on TiO₂ is of great interest since these sites are involved intimately in the surface chemistry and surface photochemistry of TiO₂^{3,23}. The rutile TiO₂(110) surface has been widely studied and serves as a prototype for metal oxide surface behavior. Recently it was reported that after oxygen-vacancy defect site production by annealing TiO₂(110) in ultra high vacuum the adsorption of O₂ molecules occurs preferentially near the defect sites produced by annealing. The presence of adsorbed O₂, as detected by the STM, was reported to locally induce low temperature (180 K - 250 K) defect migration, preferentially in the $\langle 1\bar{1}0 \rangle$ direction¹²³. Above 250 K, the O₂ mediated defect migration occurred too rapidly to be followed by STM. The mechanism to explain this observation

[Ⓢ] Reproduced in part with permission from Tracy L. Thompson, Oliver Diwald and John T. Yates, Jr. "Molecular-oxygen mediated vacancy diffusion on TiO₂(110)-new studies of the proposed mechanism" *Chemical Physics Letters*, **393** (2004) 28-30. Copyright 2004 Elsevier B.V.

postulated the dissociation of the O_2 molecule near the defect site, causing defect site annihilation by O atom addition. In this mechanism, defect annihilation is accompanied by the concomitant transport of the remaining O atom from the adsorbed O_2 molecule to extract a nearby lattice O atom, regenerating adsorbed O_2 and a new vacancy at a neighboring site. This process results in lateral migration of the vacancy¹²³. The proposed mechanism is schematically illustrated in Figure 28.

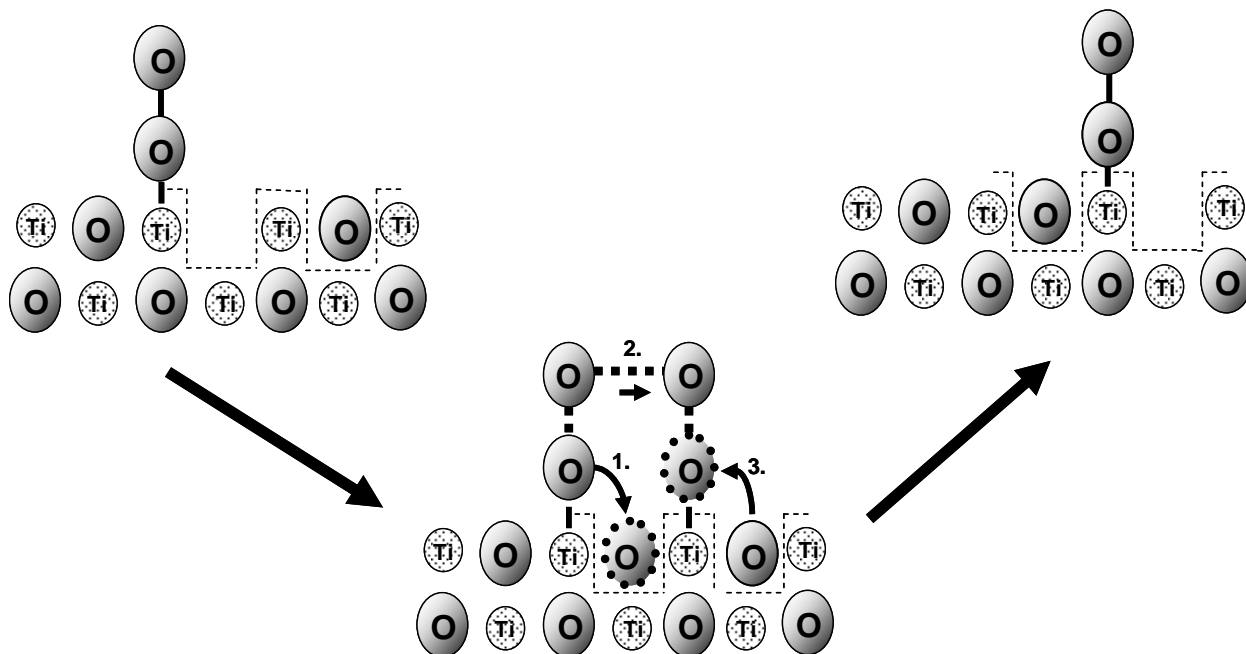


Figure 28: Schematic of O_2 -mediated surface vacancy diffusion on $TiO_2(110)$ taken from¹²³. Step 1 involves O_2 dissociation causing defect removal, step 2 involves O atom transport, and step 3 involves lattice O extraction by the O atom, producing a new O vacancy defect plus adsorbed O_2 . Typical vacancy migration distances in this mechanism are $\sim 10\text{\AA}$. The observed vacancy migration direction is in the $\langle 1\bar{1}0 \rangle$ direction across O atom rows and is measured by STM above 180 K on a time scale of seconds¹²³.

We have employed $^{18}O_2$ to investigate the validity of the mechanism of Figure 28, which would be expected to result in the production of an adsorbed $^{18}O^{16}O$ molecule for each vacancy migration event occurring on $Ti^{18}O_2(110)$. To do this, two independent methods for desorbing molecular O_2 from the surface have been used to sample the isotopic composition of the desorbing O_2 molecules in the temperature range where the STM experiments have been performed.

6.2. Experimental

The details of the UHV apparatus utilized for the experiments presented in this chapter are described in Chapter Two. For the experiments presented here, the mass spectrometer is operated in the multiplex mode sampling mass 36 and mass 34. Filtered ultraviolet light ($\lambda = 365 \pm 5$ nm; $h\nu = 3.4$ eV; flux = 2.43×10^{15} photons $\text{cm}^{-2} \text{s}^{-1}$) from a high pressure Hg arc is incident at 60° on the crystal, and causes O_2 isotopomer photodesorption directly into the mass spectrometer. In addition to sampling *photodesorbed* O_2 , the same geometry is employed in separate experiments for sampling O_2 isotopomers which are *thermally* desorbed from the surface. Here, the TiO_2 crystal is uniformly heated from 100 K by indirect ohmic heating from a Ta support plate behind the crystal, at a rate of 4 K s^{-1} .

The $\text{TiO}_2(110)$ crystal, mounted as described in Chapter Two, has been prepared in exactly the same manner as in the STM experiments ^{123,124}. The crystal was cleaned via successive cycles of Ar^+ sputtering (600 V, 20 min.) and annealing (in separate experiments annealing at either 900 K or 1050 K, 40 min. ¹²³). Auger spectroscopy indicates that the crystal is atomically clean. Highly pure $^{18}\text{O}_2$ (Isotec, 99 at %) was admitted to the crystal, using a collimated molecular beam doser which is accurately calibrated ¹²⁵. For the O_2 photodesorption measurements, O_2 exposures of 1×10^{15} molecules cm^{-2} were employed at 100 K, corresponding to the exposure used in the STM experiments ¹²³. In the second O_2 photodesorption experiment, the sample was warmed to 180 K after O_2 adsorption to correspond to the STM experiments ¹²³. Consequently, at 100 K the achieved coverage of $^{18}\text{O}_2$ was higher than at 180 K. For the separate temperature programmed desorption (TPD) studies of the isotopic composition of desorbing O_2 , $^{18}\text{O}_2$ adsorption was carried out at 100 K, and an exposure of 1×10^{17} $^{18}\text{O}_2 \text{ cm}^{-2}$ was employed to increase the coverage of the $^{18}\text{O}_2$ to bring it into a range for optimal detection by the mass spectrometer. In order to enhance the signal-to-noise ratio, 10 TPD measurements were averaged

together. The storage time in both photodesorption experiments for adsorbed O_2 at $T \leq 180$ K was 1-10 minutes to allow for significant defect migration to occur. (The vacancy migration events observed by STM occurred on a time scale of seconds¹²³).

6.3. Results

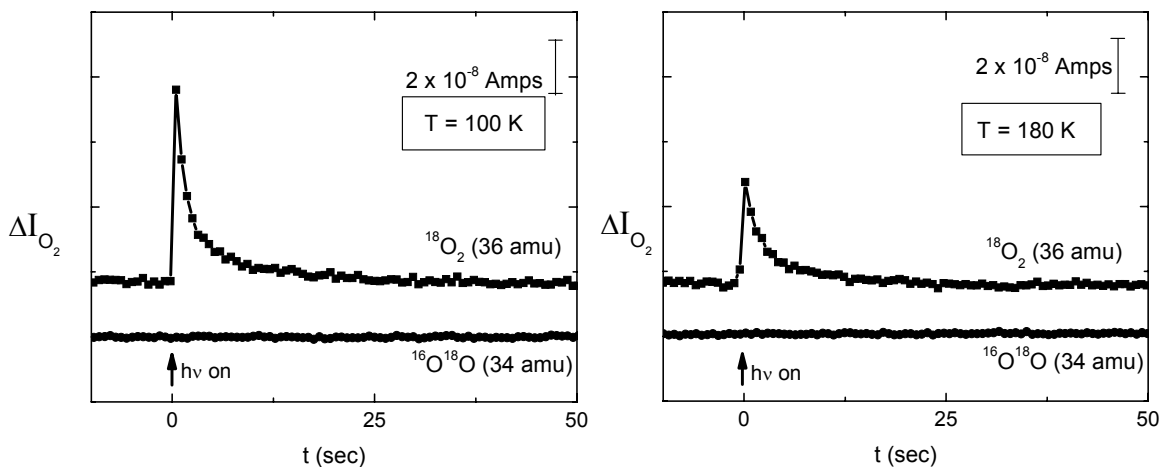


Figure 29: Isotopomer O_2 photodesorption from $TiO_2(110)$ containing vacancy defect sites produced by annealing in ultrahigh vacuum at 900 K. The experiment at 180 K corresponds to surface conditions which are the same as in the STM experiments. O_2 exposure = $1 \times 10^{15} \text{ cm}^{-2}$.

Figure 29 shows the results for O_2 isotopomers' photodesorption from the $TiO_2(110)$ crystal, where mass 36- and mass 34- O_2 were monitored. Results presented in Figure 29 are for the surface which has been sputtered and annealed to 900 K. Annealing to 1050 K induces the formation of the (1×2) reconstructed phase. We have performed the same photo- and thermal-desorption measurements for both surface preparations (900 K and 1050 K annealing) and find no isotopic mixing on either surface. In addition, at both adsorption temperatures, it is evident that no isotopic mixing of $^{18}O_2$ and ^{16}O from the TiO_2 lattice is observed when O_2 photodesorption is monitored. We estimate from the noise levels that at least 1 % isotopic mixing

would have been observed in the photodesorbed O_2 . The cross section for O_2 photodesorption in these experiments is approximately 10^{-16} cm^2 , in accordance with previous measurements⁵⁵.

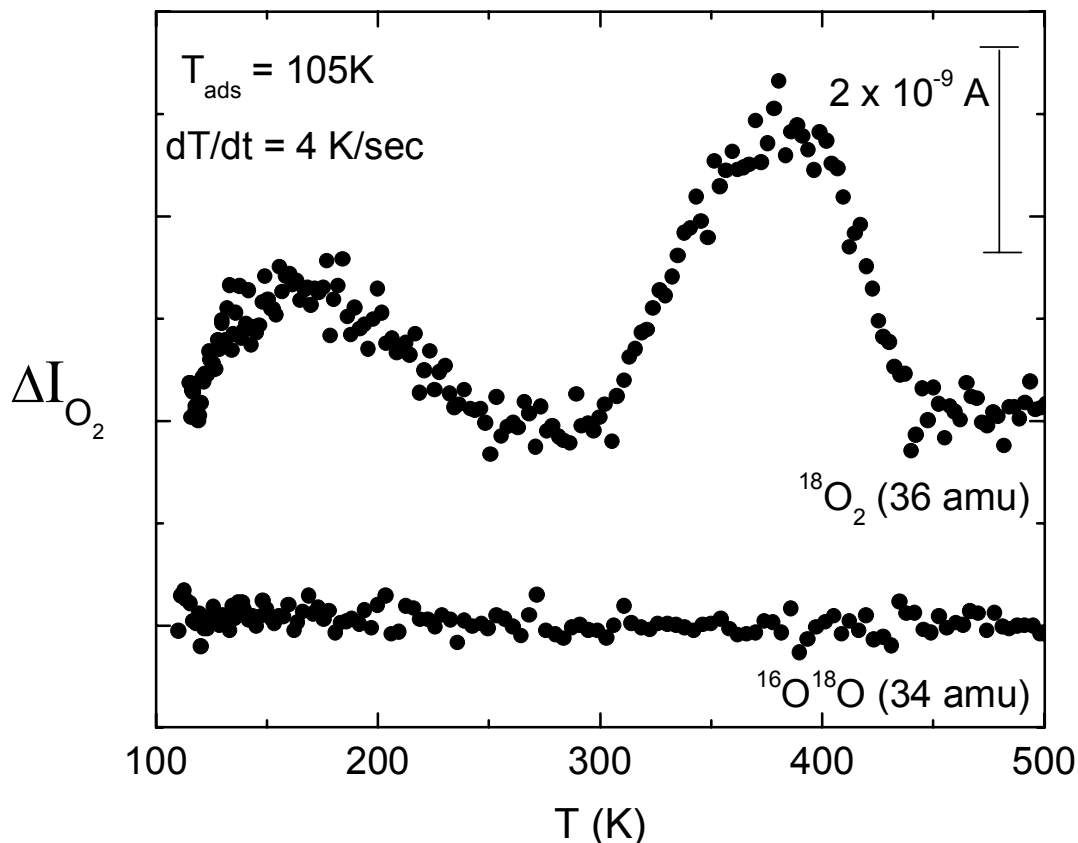


Figure 30: Isotopomer O_2 thermal desorption from $TiO_2(110)$ containing vacancy defect sites produced by annealing in ultrahigh vacuum at 900 K. O_2 desorption occurs at temperatures below, within and above the range of surface temperatures which were studied in the STM experiments. The TPD measurements are made in 10 sequential experiments and are averaged together to give better signal-to-noise. Because of some variability in the individual TPD measurements (also observed by others⁸) one should not use the composite curves for kinetic modeling.

Figure 30 shows the results for O_2 thermal desorption. Two regions of thermal desorption are observed with maximum rates at $\sim 170 \text{ K}$ and $\sim 380 \text{ K}$, in agreement with similar measurements reported by others on a $TiO_2(110)$ crystal prepared in a slightly different manner and yielding more intense O_2 thermal desorption features⁸. Once again, no isotopic mixing of

the adsorbed O₂ and the lattice O is observed. We estimate that 5 % isotopic mixing would have been detected in the TPD measurements.

6.4. Discussion and Conclusions

Photodesorption and thermal desorption are the only two methods known for the production of desorbing molecular O₂ from oxygen-covered TiO₂ and for its direct detection. Both of these O₂ desorption methods were used separately in these experiments designed specifically to investigate the mechanism of O₂ - mediated vacancy migration. In both cases, no isotopic exchange with lattice oxygen has been observed. Earlier experiments, not specifically designed to check the O₂ -mediated vacancy diffusion model, agree with the conclusions reported here^{8,55}.

It is possible that neither O₂-photodesorption nor O₂-thermal desorption will sample the particular adsorbed O₂ species observed by STM. However, the postulate of the STM observation of a particular O₂ species, which is shown to be preserved on a nearby site after vacancy migration has occurred, and which is invisible to two different experimental processes which induce O₂ desorption, stretches credibility, especially since the two desorption measurements and the STM experiments were carried out on identically-prepared TiO₂(110) surfaces as well as at the same temperature where vacancy migration is observed by STM. These measurements suggest that the mechanism of oxygen-mediated vacancy migration proposed¹²³ must be modified to explain the experimental STM measurements.

7. **CHAPTER SEVEN: The Effect of Nitrogen Ion Implantation on the Photoactivity of TiO₂ Rutile Single Crystals[^]**

Abstract

The effect of impurity doping on the photoactivity of TiO₂ rutile single crystals was subjected to a combined surface science and bulk analysis study. The incorporation of nitrogen ions, N⁻, into TiO₂ single crystals was achieved by sputtering with N₂⁺/Ar⁺ mixtures and subsequent annealing to 900 K under ultra high vacuum conditions. This procedure leads to a 90 Å thick structurally modified near surface region, which, by the use of cross sectional transmission electron microscopy (XTEM), can be described as rutile grains imbedded within a monocrystalline strained rutile matrix. The presence of N⁻ ions distributed in the first 200 Å below the surface was revealed by X-ray photoelectron spectroscopy (XPS), in agreement with sputter depth profiles obtained by secondary ion mass spectroscopy (SIMS). The concentration of N⁻ doping is about 10²⁰ cm⁻³ in the first 200 Å of the near surface region.

The photodesorption of O₂ was employed to study the changes in the photochemical properties of nitrogen-implanted crystals. The action curves for O₂ photodesorption exhibit an unexpected blueshift compared to undoped crystals. The effect is attributed to the deposition of electronic charge in the lower levels of the conduction band (band-filling mechanism), causing allowed indirect photoexcitation processes to shift to energies higher than the bandgap.

[^] Reproduced in part with permission from Oliver Diwald, Tracy L. Thompson, Ed. G. Goralski, Scott D. Walck and John T. Yates, Jr. "The Effect of Nitrogen Ion Implantation on the Photoactivity of TiO₂ Rutile Single Crystals" *Journal of Physical Chemistry B*, **108** (2004) 52-57. Copyright 2004 American Chemical Society.

7.1. Introduction

Titanium dioxide (TiO_2) is a promising material for many photochemical applications spanning the range from photoelectrochemical splitting of water into hydrogen and oxygen^{1,126} and wet solar cells¹²⁷ to photocatalysis^{5,23,56}. TiO_2 has long-term stability, is a nontoxic material and is relatively inexpensive. A major goal in the development of TiO_2 -based materials is to extend the photoactivity from 3.0 eV into the range of visible light in order to utilize solar light more efficiently. It is widely recognized that the electrical and photophysical properties of oxide materials are strongly influenced by electronic states associated with defects and dopants. Model studies of single crystal oxides have yielded a rich body of information about electronic states associated with oxygen anion vacancies. This is especially true for TiO_2 rutile (110) which serves as a prototype of a single crystal transition metal oxide surface³.

Most work on the electronic defects associated with impurity dopants has been restricted to polycrystalline materials. Recently, different groups have reported that substitutional doping with nonmetal atoms such as carbon¹²⁸, sulfur¹²⁹ and nitrogen^{36,130,131} in the TiO_2 lattice shifts the absorption edge to lower energies. For example, Asahi et al. reported that films and powders of $\text{TiO}_{2-x}\text{N}_x$ reveal a dramatic improvement over pure titanium oxide under visible light in their optical absorption and the level of photocatalytic activity^{36,131}. The authors claim that nitrogen doped into substitutional sites of TiO_2 has proven to be indispensable for “band gap narrowing”.

The aim of this study was to investigate the influence of substitutional nitrogen doping on the photoactivity of the TiO_2 rutile (110) single crystal surface. The structure and chemical composition of the nitrogen-doped near surface region were investigated with cross sectional Transmission electron microscopy (XTEM), Secondary ion mass spectrometry (SIMS) and X-ray photoelectron spectroscopy in conjunction with sputter depth profiling. The doping effect on the photoactivity was measured by the photodesorption of oxygen performed under controlled

ultrahigh vacuum conditions. It will be shown that incorporation of N⁻ ions with a concentration of about 1 atomic percent into the rutile lattice can be achieved by sputtering with a mixture of N₂⁺ and Ar⁺ ions. After subsequent annealing to 900 K the TiO₂ becomes electronically reduced and adsorbs oxygen on its surface. The photodesorption of oxygen, measured as a function of UV excitation energy, revealed an unexpected blue-shift effect compared to undoped rutile single crystals.

7.2. Experimental

Details of the experimental apparatus used here are described in Chapter Two and the method for performing the O₂ photodesorption experiments is described in Chapter Three.

Prior to sputter treatment with 3 keV ions (Ar⁺ ions or mixtures of Ar⁺ and N₂⁺ ions), the crystals are cleaned by successive intervals of Ar⁺ sputtering (1.5 kV), followed by full oxidation in O₂ at 900 K followed by cooling in O₂. This has been done until no traces of impurities were measured using AES.

X-ray photoelectron spectroscopy (XPS) and secondary ion mass spectroscopy (SIMS) measurements were carried out at the PPG Glass Technology Center. XPS spectra were acquired with an ESCALAB Mk II (Vacuum Generators) spectrometer using unmonochromatized Mg K-alpha X-rays (240 W). Cycles of XPS measurements and subsequent Ar⁺ sputtering steps (4 keV, I = 4 μA cm⁻²) were done in a high vacuum chamber with a base pressure of 10⁻⁸ Torr until a profile for nitrogen content versus sputter time was obtained. The binding energy of the N(1s) peaks was calibrated with respect to the O(1s) peak at 530.2 eV. The nitrogen concentration was estimated from the relative area intensities of the N(1s), Ti(2p) and O(1s) peaks. They were normalized with respective relative sensitivity factors in the Vacuum Generators software

package. Dynamic SIMS experiments were performed in positive mode with 5 keV Ar⁺ ions and a measured ion current density of $I = 1.25 \mu\text{A cm}^{-2}$.

XTEM samples were prepared using the small angle cleavage technique (SACT)¹³². All samples were cleaned in radio frequency coupled Ar/O₂ plasma. The transmission electron microscope was a 200 kV field emission gun instrument (Philipps Tecnai F20) located at the Material Research Center (MRCSC) at Carnegie Mellon University.

7.3. Results

7.3.1. Implantation of Nitrogen and Determination of Nitrogen Concentration and Depth Distribution

Implantation of nitrogen into the lattice of TiO₂ crystals was done by sputtering with a gas mixture of 80% nitrogen and 20 % Ar at room temperature and an acceleration voltage of 3 kV¹³³. The total fluence of ions incident to the crystals during the sputtering process was 10^{17} ions/ cm². For comparison a reference crystal was treated in the same way with Ar⁺ ions alone and subsequently subjected to the same treatment and experiments as the N⁻ implanted sample. All crystals have been annealed at 900 K for 3-5 hours in UHV after sputtering. For the nitrogen-implanted sample, Auger electron spectroscopy was used to provide evidence for incorporated nitrogen. Since only the nitrogen KLL transition is seen and its energy overlaps the titanium LMM transition located at 380 eV, the relative ratio for the Ti LMV (420 eV)/ Ti LMM transitions was used as an estimate of N concentration. A broad optical absorption from 1500 nm to almost 400 nm associated with electronically reduced defects in the bulk (e.g. color centers) was measured on the N-implanted sample and is similar to that observed for undoped crystals. These are typical effects for TiO₂ single crystals and originate from extensive annealing under

UHV conditions³. Additional sharper absorption bands, that may originate from beneficial nitrogen doping were not observed above $\lambda = 400$ nm ($h\nu < 3$ eV).

For the quantification of the implanted nitrogen and the determination of its chemical nature, X-ray photoelectron spectroscopy (XPS) was employed. No evidence of nitrogen was observed at the surface. However, using sputter depth profiling, an XPS feature centered at 396.5 eV can be observed after removal of the first 30 Å from the surface (Figure 31). This feature is assigned to the N(1s) transition of chemically bound N⁻ species within the crystalline TiO₂ lattice

36,131,134

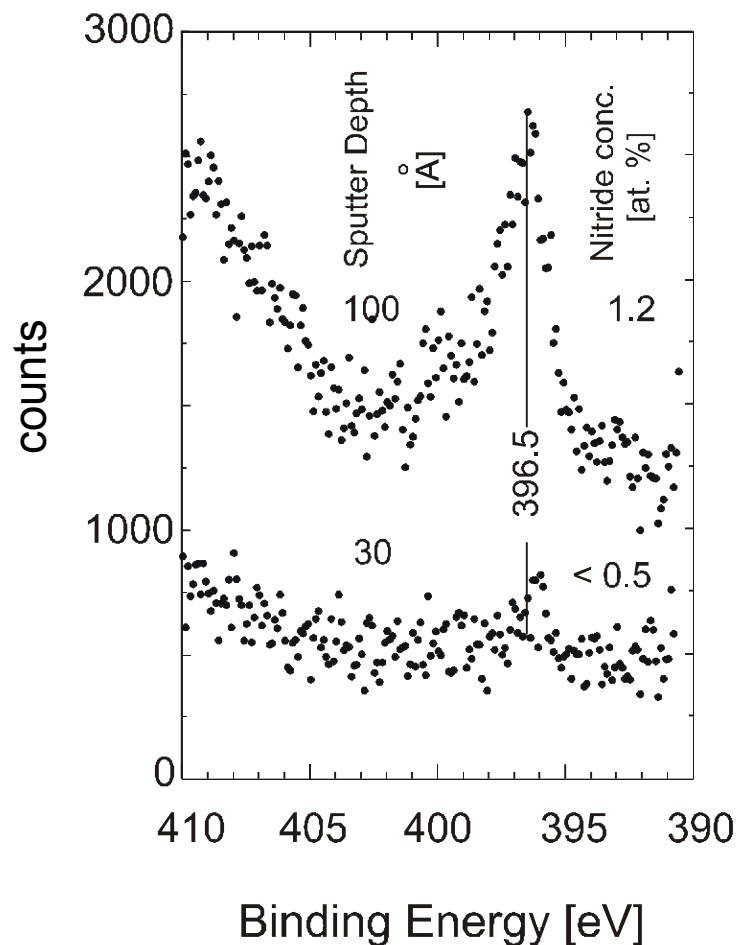


Figure 31: Nitrogen (1s) spectrum from a nitrogen-implanted TiO₂(110) crystal at two different Ar⁺ sputter depths.

The depth distribution of nitrogen species was determined by XPS using Ar^+ sputter depth profiling. The resulting profile (not shown) was in good agreement with the nitrogen profile obtained by secondary ion mass spectroscopy (SIMS, Figure 32). For comparison, the masses 80 (TiO_2^+), 14 (N^+) and 60 (TiN^+) were recorded¹³⁵. The nitrogen signal (14 amu) and the titanium nitride signal (60 amu) exhibit a maximum at approximately 90 Å beneath the surface. At this depth, the nitrogen concentration was 1.2 ± 0.5 atom % as determined by X-ray photoelectron spectroscopy. The two surface analysis methods agree with the implanted N^- species being present with a maximum concentration at a depth of about 90 Å.

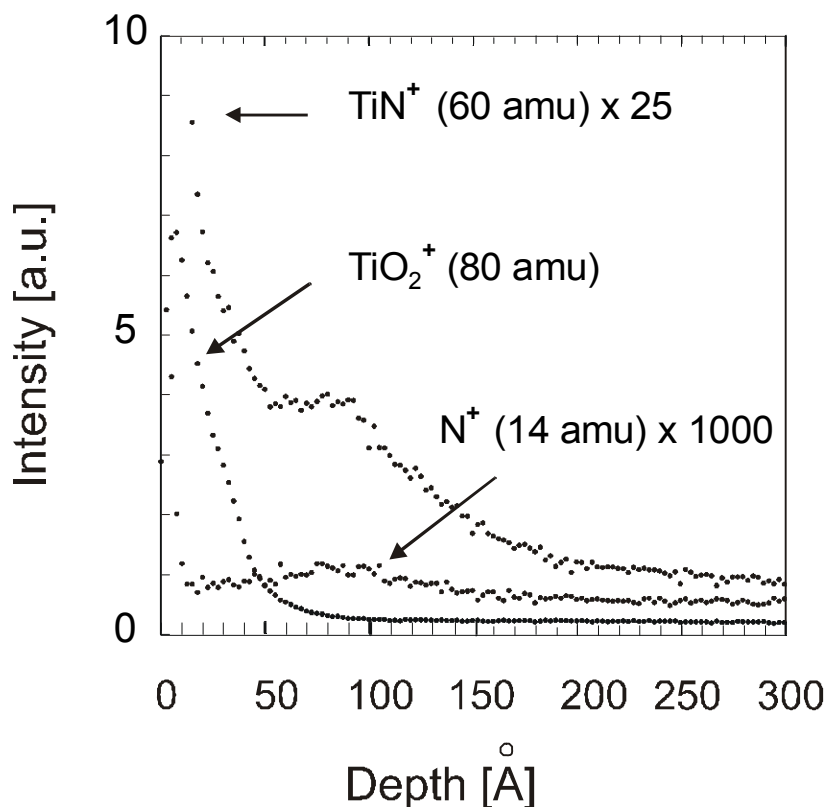


Figure 32: SIMS profile of nitrogen-implanted $\text{TiO}_2(110)$ crystal.

7.3.2. Transmission Electron Microscopy Cross Sections

The structure of the near-surface region of ion-sputtered and post-annealed (at 900K) TiO_2 crystals was investigated by XTEM. A low magnification image of the N-implanted sample

is shown in Figure 33. In contrast to similar images obtained from the undoped crystal (not shown), an outer layer with varied contrast compared to the bulk underneath is clearly observable. Its thickness was uniform and about 90 Å in size. (X-ray reflectivity measurements, performed on the same sample, indicated the presence of a 88 ± 4 Å thick upper layer of elastically strained rutile¹³⁶). A high-resolution TEM image in Figure 34 provides an example of the structural changes of this outer layer. The image reveals the transition from the monocrystalline bulk crystal structure through an area of strain (darker average contrast) to a polycrystalline grain structure in the near surface region.

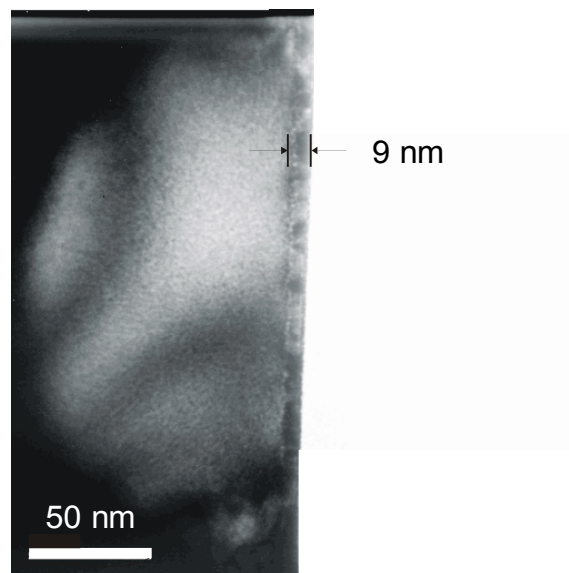


Figure 33: Low magnification TEM image of the cross section of a nitrogen-implanted single crystal.

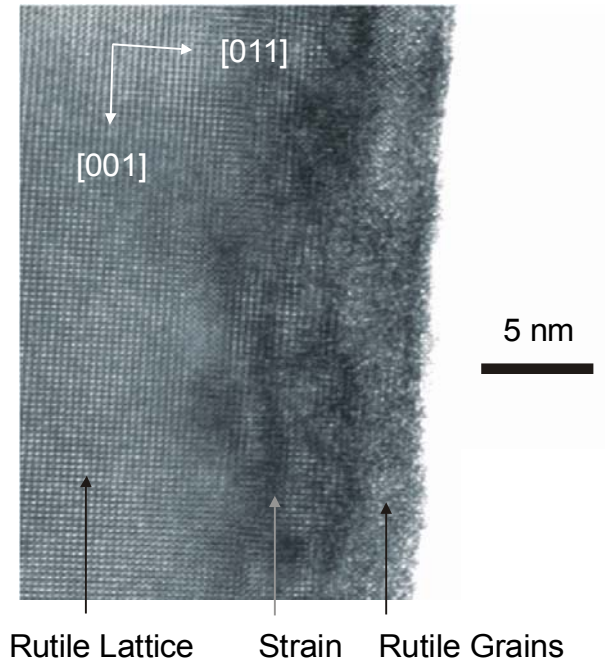


Figure 34: Cross-sectional high-resolution TEM image of the nitrogen-implanted crystal. On top of the monocrystalline rutile lattice are recrystallized rutile grains. The blackened regions in the image indicate lattice strain.

The presence of many structural defects prevented imaging of the atomic structure of the grains in detail in the near surface region. However, the contrast differed substantially from that expected for an amorphous region and local fringes from atomic columns were visible. Fourier transforms were used to determine d spacing and orientations in the polycrystalline surface region and were calibrated relative to the bulk rutile regions. Only patterns that were consistent with rutile were seen. The rutile grains that were analyzed in the near surface region were 20 - 70 Å in size.

7.3.3. O₂ Photodesorption and the Photoaction Curve

The TiO₂ crystals were heated to 900 K to generate reproducibly a surface oxygen anion vacancy concentration between 5 - 10% of a monolayer^{3,7,12}. Under UHV conditions, the chemisorption of oxygen can only occur on TiO₂ surfaces with anion vacancies (accompanied by electronically reduced cationic sites)^{12,17}. O₂ adsorption at 120 K leads to the formation of chemisorbed oxygen which, on the basis of high resolution electron energy loss

spectroscopy, was assigned to O_2^- species⁸. When these samples are exposed to UV, O_2 photodesorption takes place. This process is explained by the photogeneration of holes and concomitant electronic neutralization of the O_2^- species causing O_2 desorption. Molecular oxygen, released from the surface, is then detectable by the line-of-sight QMS.

Figure 35 contains typical O_2 photodesorption signals measured on vacuum annealed samples, which were previously sputtered with a mixture of N_2^+ and Ar^+ ions (N-implanted, Figure 35a) and samples sputtered only with Ar^+ ions (undoped, Figure 35b). For the N-implanted material a much longer decay time was observed. (The signal in Figure 35a was multiplied by a factor of five.) The time constants for both curves were obtained by curve fitting to equation 7.1:

$$N_{O_2} = N_{O_2}^0 \exp(-F_{hv}Qt) \quad (7.1)$$

where N_{O_2} is the O_2 coverage during photodesorption, $N_{O_2}^0$ is the initial coverage of O_2 , F_{hv} is the photon flux at 3.96 eV, t is the UV irradiation time and Q is the cross section for photodesorption of O_2 . The photodesorption signal, measured on the N-implanted sample (Figure 5a), occurs with a cross section of 10^{-16} cm^2 , one order of magnitude smaller than for the process observed on undoped TiO_2 (110) ($Q = 10^{-15} \text{ cm}^2$, Figure 5b). Both photodesorption processes were observed in previous studies on vacuum annealed rutile TiO_2 (110) crystals¹⁷. The relative ratio between these two processes and, thus, the shape of the photodesorption signal strongly depend on the morphology of the TiO_2 (110) surface. For example, O_2 photodesorption from a crystal which was Ar^+ sputtered and annealed at 900 K for a limited period of time (i.e. $t = 1-2$ hours) occurs preferentially via the slow decaying process with a cross section of 10^{-16} cm^2 . After

longer annealing times ($t > 3$ hours) the contribution of the fast decaying process with a cross section of 10^{-15} cm^2 dominates the overall shape of the photodesorption signal, which does not change with further annealing. Thus, the difference in the signals of Figure 35 is explained by the disordered surface structure of the N-implanted crystal, also indicated by the XTEM image in Figure 34.

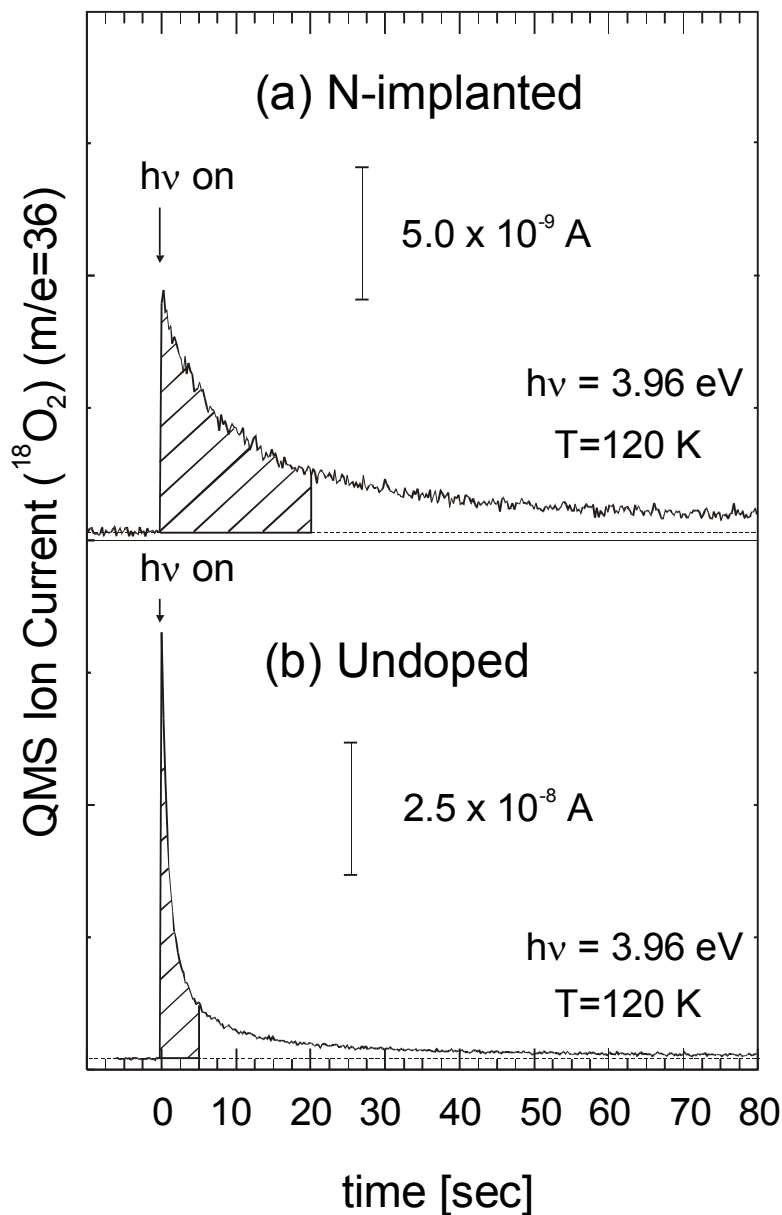


Figure 35: Time-dependent $^{18}\text{O}_2$ desorption signal for (a) a nitrogen implanted and (b) undoped $\text{TiO}_2(110)$ crystal. Total oxygen exposure was 1×10^{15} molecules cm^{-2} causing saturation coverage. The photon flux at

3.96 eV was 1×10^{15} photons $\text{cm}^{-2}\text{s}^{-1}$. The crosshatched areas show the integration range employed in measuring the photodesorption yield.

Action curves for the process of O_2 photodesorption were measured to determine the effect of nitrogen implantation on the spectral response of the TiO_2 (110) single crystals. Before each experiment the crystal was annealed to 900 K momentarily and a constant exposure (1×10^{15} molecules cm^{-2}) of O_2 was dosed after cooling down to 120 K. The relative yield (Y_{hv}) of photodesorbed oxygen as a function of the excitation energy, $h\nu$, was determined by ratioing the integral intensity of the photodesorption signal to the incident photon flux according to equation 7.2:

$$Y_{hv} = \frac{\int_0^{t_1} \Delta P_{\text{O}_2} dt}{\int_0^{t_1} F_{h\nu} dt} \quad (7.2)$$

For higher accuracy, the integration time for the slower decaying processes on N-implanted TiO_2 was 20 seconds, whereas for the undoped samples only the first five seconds were used (see cross-hatched areas in Figure 35). Both action curves in Figure 36 were normalized to the photodesorption yield measured at 4.1 eV in order to show differences in their energy dependence. It can be clearly seen that for the crystal exclusively sputtered with Ar^+ ions (and annealed to 900 K), the threshold energy for O_2 photodesorption is at about 3.0 eV. This value corresponds to the effective bandgap of bulk rutile and is in very good agreement with previous studies performed on TiO_2 (110) crystals, which were reoxidized in oxygen flux after sputter cleaning and then vacuum annealed to reproducibly produce surface defects^{3,12,17}.

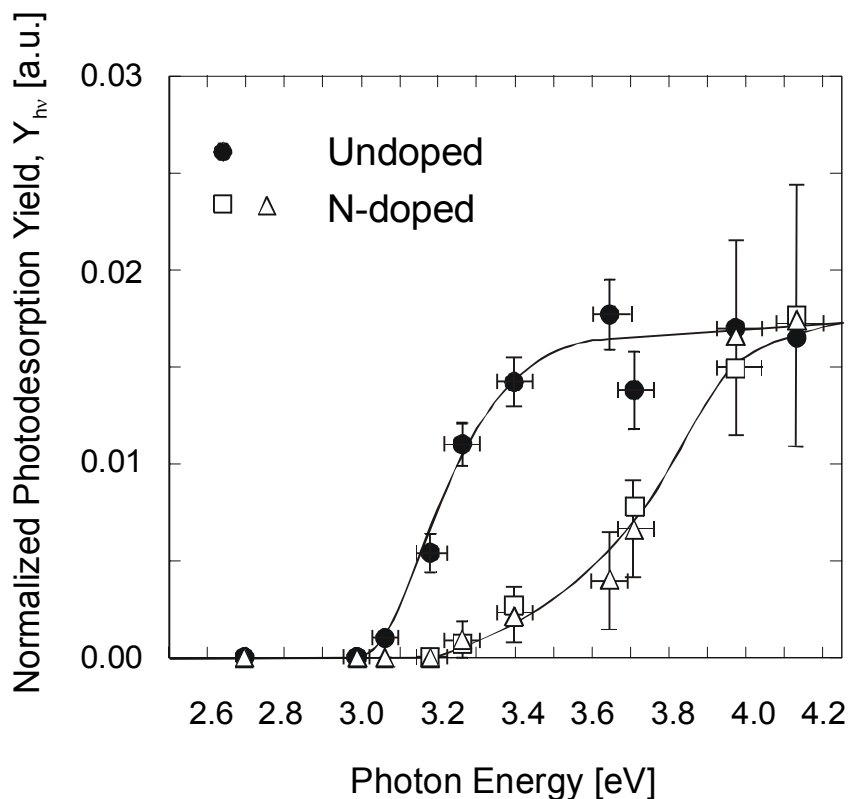


Figure 36: The photoaction curve for O_2 photodesorption from vacuum annealed $TiO_2(110)$ surfaces. The integrated photodesorption magnitude at each energy has been divided by the photon flux at each respective energy to obtain Y_{hv} . Both action curves shown here were normalized to the photodesorption yield measured at 4.1eV. Open squares and triangles represent values that were measured independently on two different nitrogen-doped single crystals.

When exactly the same sputter and annealing process was carried out with a $N_2^+ + Ar^+$ mixed ion beam, the action curve for O_2 photodesorption was dramatically shifted to the blue, as seen in Figure 36. The threshold energy at about 3.2 eV is shifted in the *opposite* direction to that reported by Asahi et al.^{36,131} for N-doped polycrystalline TiO_2 . Thus two profound differences are observed for TiO_2 (110) crystals containing N^- substitutional impurities, compared to identical crystals prepared without N^- incorporation:

1. The O_2 photodesorption cross section for the N^- implanted crystals decreases by a factor of 10, from 10^{-15} cm^2 to 10^{-16} cm^2 for 3.96 eV photons.
2. The threshold for O_2 photodesorption increases by 0.2 eV from a photon energy of 3.0 eV to 3.2 eV

In semiconductors, indirect interband transitions are characterized by a quadratic energy dependence of the optical absorption coefficient, α , near the absorption edge than is otherwise the case for direct transitions¹³⁷, which have a square-root energy dependence. The quadratic dependence is given in equation (7.3):

$$\alpha = B_i(h\nu - E_g)^2/h\nu \quad (7.3)$$

where B_i is the absorption constant for the indirect transition and E_g is the bandgap. Plots of $(O_2 \text{ photodesorption yield} \times h\nu)^{1/2}$ against the excitation energy, $h\nu$, shown in Figure 37 display a linear relationship for the first four data points of each curve. This suggests that the O_2 photodesorption processes from N-implanted and from undoped TiO_2 single crystals, with intercepts at the threshold energy of 2.97 and 3.15 eV respectively, are initiated by indirect band gap transitions in the substrate^{137,138}.

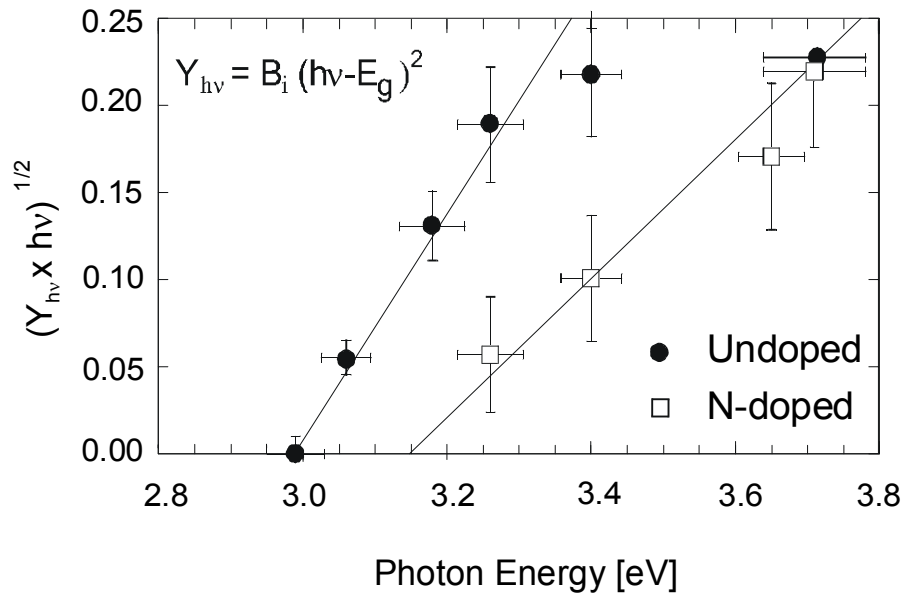


Figure 37: Plots of $(O_2 \text{ photodesorption yield} \times h\nu)^{1/2}$ vs. photon energy (eV) for undoped and nitrogen-implanted $TiO_2(110)$ crystals.

7.4. Discussion

Doping of polycrystalline powders and films of TiO₂ with anion impurities such as nitrogen^{36,130,131}, sulfur¹²⁹ and carbon¹²⁸ has been shown to be effective in lowering the threshold energy for photochemistry on the TiO₂ surface. This beneficial doping effect is explained by mixing of the or N-, S- and C- derived *p* states with the O 2*p* states leading to bandgap narrowing^{36,128,129,131}.

Asahi et al.^{36,131} have accomplished N doping by reactive sputtering of TiO₂ film targets in N₂/Ar gas mixtures, by high temperature treatment of TiO₂ powders in NH₃/Ar atmospheres and by oxidative annealing of TiN powder. In all cases, a noticeable new absorption range for light at energies less than the bandgap energy of 3.0 eV has been observed. The doped films were crystalline and XRD revealed the mixed structure of both rutile and anatase phases³⁶. N-doped powders produced by oxidation of polycrystalline TiN exhibited a homogeneous rutile phase¹³¹. The N(1s) core levels, measured with XPS, revealed three peak structures at binding energies at 402, 400 and 396 eV. Whereas the two features at higher binding energies were attributed to molecularly adsorbed nitrogen species, the nitrogen peak at 396 eV was assigned to substitutionally bound N⁻ species. On the basis of a quantitative correlation between photocatalytic activity and an increase of nitrogen component related to the 396 eV peak, these authors concluded that nitrogen ions which substitute O²⁻ in the TiO₂ lattice are the photoactive dopant species. In the present study, nitrogen doping was attained by sputtering atomically clean TiO₂ single crystal surfaces with mixtures of N₂⁺ and Ar⁺ ions. The SIMS profile proves that nitrogen was successfully implanted in the near surface region, 0 < x < 200 Å, and the XPS results exclusively revealed a N(1s) feature at 396.5 eV (Figure 31) due to substitutional atomic N⁻ species.

In general, ion bombardment of TiO₂ crystal surfaces leads to the amorphization and partial reduction of the near surface region, because oxygen ions are preferentially sputtered due to their lower binding energy³. In case of exclusive sputtering with noble gas ions, a state of constant concentration for all elements (Ti, O, Ar) and all oxidation states is reached after removal of a 100 Å thick layer¹³⁹. Subsequent annealing of the sputtered crystal to 900 K allows the epitaxial recrystallization of the amorphous and sputter-damaged area. Surface stoichiometry and structure are restored to bulk-like quality due to the diffusion of interstitial Ti ions from the surface into the bulk¹¹⁸. In the present study cross sectional TEM images reveal a more complex state of the near surface region. Monocrystallinity was not restored after sputtering with N₂⁺ and Ar⁺ ions and subsequent annealing under UHV conditions. This may be due to the presence of chemically-bound atomic nitrogen, which is then involved in the recrystallization process at elevated temperature. Nitrogen incorporation into the TiO₂ lattice causes changes in the lattice parameters (i.e. strain). These effects can be accommodated by the disorientation of small recrystallized grains on top and in between the monocrystalline structure of the crystal bulk (Figure 34). The following estimate was done to check if nitrogen-induced stress in the TiO₂ lattice could explain the observed band gap shift: according to the literature, the pressure dependence of the band gap position for an anatase TiO₂ single crystal¹⁴⁰ is 10 meV/GPa and no experimental value for TiO₂ in the rutile modification was found. However, SnO₂, which has the rutile structure and is also a wide band gap oxide semiconductor, has a value of 62 meV/GPa¹⁴¹. If we assume that these two values are the lower and upper limits for the rutile phase, the required stress to produce a band gap shift of 200 meV would be 20 and 3.2 GPa, respectively. The value for compressive strength, which corresponds to the maximum compressive stress for TiO₂ is 0.245 GPa for failure¹⁴². This is 1 order of magnitude smaller than the calculated 3.2

GPa for SnO₂ to produce a 200 meV offset and a factor of 80 smaller if the 10 meV/GPa value for anatase is used. For this reason, we exclude strain as a possible source for the observed blueshift.

The shift of the photodesorption threshold energy by 200 meV to the blue could easily be explained by the conversion of rutile to anatase³ by the nitrogen implantation and annealing procedure used here. In fact, it has been reported that by N⁺ implantation into polycrystalline TiO₂ films, a phase transformation of crystalline rutile to anatase occurred due to the relaxation of internal strain^{143,144}. In this study, XTEM images were acquired from samples of different parts of the nitrogen-implanted crystal. All of the crystalline regions that were analyzed by Fourier transforms were determined to be rutile. Not one grain was consistent with the structure of anatase. As a consequence of these observations, the volume fraction of any anatase phase if present must be very small and therefore should not contribute to the observed change in the optical properties.

Serpone et al.¹³⁸ suggested that the observation of blue-shifted thresholds, observed on small TiO₂ particles and taken as an evidence for a quantum size effect, are due to direct (Franck-Condon type) transitions in an otherwise indirect bandgap semiconductor. Although such direct transitions were noted for rutile TiO₂⁷⁰, this concept does not apply here. The action curves for undoped and N-implanted crystals display a quadratic dependence on the excitation energy, characteristic of indirect bandgap transitions in both cases (Figure 37).

A well known phenomenon associated with the optical properties of n-type semiconductors is the so-called “band filling mechanism” (Figure 38)¹⁴⁵. It is based on the effect of electron concentration on the location of the Fermi level, E_f.

Indirect-Undoped

Indirect-Doped

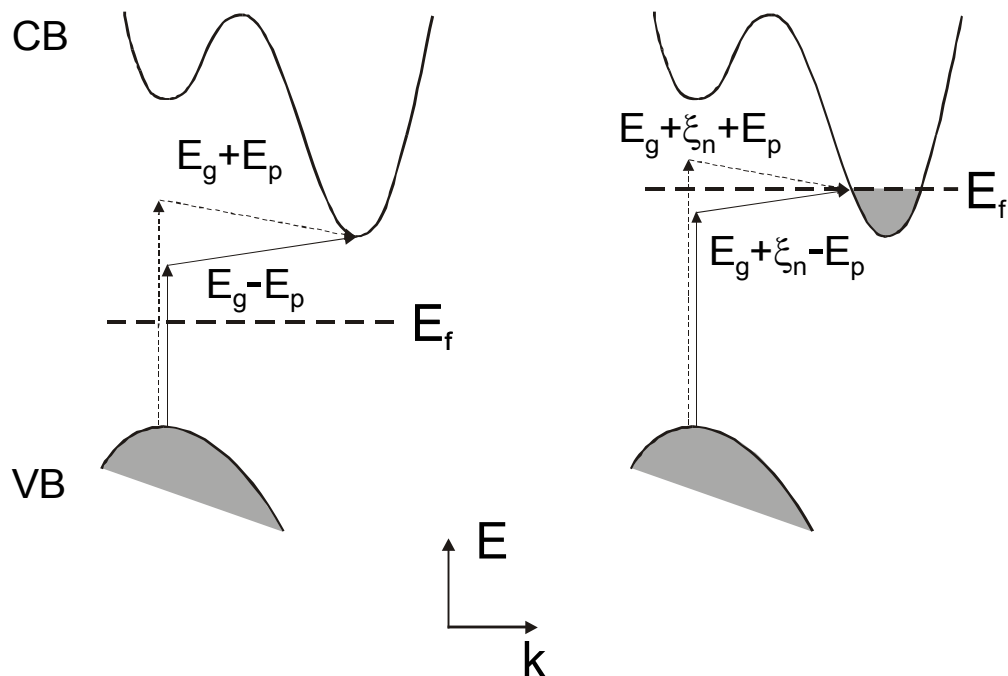


Figure 38: Schematic presentation of the effect of band filling on the photoexcitation threshold energy for a semiconductor with a band gap of E_g (adopted from ref. ¹⁴³). In this energy-momentum diagram for a degenerate n-type semiconductor, two-phonon assisted transitions ($E_g \pm E_p$) are shown to illustrate the usual photon absorption mechanism. If the semiconductor is heavily doped, the Fermi level, E_f , is inside the conduction band in an n-type material by a quantity ξ_n . Since the states below ξ_n are already filled, electronic transitions to states below $E_g + \xi_n$ are forbidden; hence, the absorption edge should shift to higher energies by a value equal to ξ_n .

For intrinsic or lightly doped semiconductors, such as vacuum-annealed and thermally-reduced TiO_2 , E_f is positioned within the bandgap and the semiconductor is said to be non-degenerate. When the electron concentration in the bulk is increased, e.g. by heavy n-type doping, the semiconductor becomes degenerate, and E_f lies above the bottom of the conduction band. As a consequence, some of the states within the conduction band (CB) are then filled, and electrons excited by a UV/Vis photon must go into higher levels in order to enter the CB, thus leading to a blueshift in optical absorption (Figure 38). For vacuum annealed TiO_2 crystals that are intrinsic n-type semiconductors, the local increase in partially reduced $\text{Ti}^{<4+}$ cations has a similar effect on

electron concentration and, thus, on the position of E_f . Although N is considered to be a shallow p-type dopant, wide band gap semiconductors such as ZnO, are difficult to p-dope using a pure nitrogen source alone. Because of ionic charge compensation, the N acceptors can easily be compensated by donor levels, which are related to additional oxygen vacancies and cations¹⁴⁶. Thus, we conclude, that the implantation of N^- ions into the rutile TiO_2 lattice, substituting O^{2-} ions, also increases the local concentration of electronically reduced Ti^{3+} states due to the monovalent oxidation state of the nitrogen anion. A maximum concentration of nitrogen of about 1 atomic % corresponds to a local concentration of 10^{20} cm^{-3} additional charge carriers in the photoactive near-surface region. Alternative charge compensation based on the presence of cation vacancies is unlikely, since the sputtering process creates an overall surplus of Ti cations, which then becomes depleted through annealing via the process of bulk-assisted oxidation¹¹⁸. In conclusion, we propose that the blueshift in the action curve for O_2 photodesorption is due to a band-filling mechanism based on the increase of the n-doping level of the TiO_2 crystal by N^- incorporation.

7.5. Conclusions

Reactive $N_2^+ + Ar^+$ sputtering and subsequent annealing at 900K in UHV of a (110) rutile TiO_2 single crystal leads to the implantation of atomic nitrogen within a range of 0-200 Å. The photochemical activity of N-implanted and undoped TiO_2 was investigated by means of O_2 photodesorption and the action curve revealed, opposite to a beneficial doping effect observed on polycrystalline materials^{36,131}, a blueshift compared to undoped crystals. This phenomenon is explained by the partial filling of the conduction band by electrons.

The changes in the optical properties due to the implantation of N^- into rutile single crystals may hold technological promise, since TiO_2 with its high dielectric constant is

extensively used in optical devices ³, and tuning of its electronic properties is also important for microelectronics. The presence of a band-filling mechanism caused by N⁻ dopant incorporation would imply that within the modified layer the local concentration of excess electrons can also be raised by UV light. As a result, the Fermi level and thus the reduction potential of the semiconductor material becomes a function of irradiation intensity and is adjustable by the photon flux ^{142,147}.

8. CHAPTER EIGHT: The Photochemical Activity of Nitrogen-Doped TiO₂(110) in Visible Light*

Abstract

TiO₂ (110) single crystals, doped with nitrogen by NH₃ treatment at 870 K have been found to exhibit photoactivity in the photon energy range down to 2.4 eV, which is 0.6 eV below the bandgap energy for rutile-TiO₂. The active dopant state of interstitial nitrogen responsible for this effect exhibits an N(1s) binding energy of 399.6 eV, and is due to a form of nitrogen probably bound to hydrogen, which differs from the substitutional nitride state with an N(1s) binding energy of 396.7 eV. Optical absorption measurements also show enhanced absorption down to 2.4 eV for the NH₃-treated TiO₂(110). A codoping effect between nitrogen and hydrogen is postulated to be responsible for the enhanced photoactivity of nitrogen-doped TiO₂ materials in the range of visible light.

8.1. Introduction

The photocatalytic and photoelectrochemical applications of semiconducting oxide materials provide a strong scientific incentive for ongoing research^{5,23,56}. Titanium dioxide, TiO₂, belongs to one of the most extensively used and investigated systems and has the advantages of being cheap, chemically stable and non-toxic. Other than the photocatalytic applications of TiO₂, including the degradation of organic pollutants in air and aqueous solutions, it is used for photovoltaic applications^{1,127} because it combines good electrical properties with excellent stability in many solvents over a wide pH range. However, because of

* Reproduced in part with permission from Oliver Diwald, Tracy L. Thompson, Tykhon Zubkov, Ed. G. Goralski, Scott D. Walck and John T. Yates, Jr. "Photochemical Activity of Nitrogen-Doped Rutile TiO₂ in Visible Light" *Journal of Physical Chemistry B*, **108** (2004) 6004-6008. Copyright 2004 American Chemical Society.

the rather high intrinsic bandgap of rutile TiO₂ (3.0 eV), only 4% of the incoming solar energy on earth's surface can be utilized. Therefore, considerable efforts have been made to extend the photoresponse of TiO₂-based systems further into the visible light region, using dopants.

Various transition metal cation dopants have been extensively investigated¹⁴⁸⁻¹⁵⁰. However the disadvantage of cationic dopants is that they can give rise to localized d-levels deep in the bandgap of TiO₂, which often serve as recombination centers for photogenerated charge carriers. Thus, anionic non-metal dopants, such as carbon¹²⁸, sulfur¹²⁹, and nitrogen¹³¹ may be more appropriate for extension of photocatalytic activity into the visible light region since the related impurity states are supposed to be close to the valence band maximum. Furthermore, the position of the conduction band minimum, which has to be kept at the level of the H₂/ H₂O potential, when TiO₂ is used for the photoelectrolysis of water into hydrogen and oxygen, is not affected¹⁵¹.

With respect to nitrogen-related dopants, Sato reported for the first time that calcining of mixtures of Ti(OH)₄ and ammonium salts leads to TiO₂-based materials that can be activated with visible light¹³⁰. He attributed this beneficial doping effect to NO_x impurities in the TiO₂ lattice. On the basis of a theoretical analysis, Asahi et al.³⁶ suggested that if nitrogen ions substitute for oxygen in the TiO₂ lattice, the corresponding N(2p) states are located above the valence band edge. By mixing of N(2p) states with O(2p) states, the band gap of the N-doped TiO₂ is reduced and the material should show photoactivity at energies below the intrinsic band gap edge (<3.0 eV). In fact, these authors have proven that films and powders of TiO_{2-x}N_x exhibit a dramatic improvement over pure titanium oxide in their optical absorption below 3.0 eV and the level of photocatalytic activity for visible light. Irie et al.¹⁵² measured higher quantum yields for the decomposition of gaseous isopropanol on TiO_{2-x}N_x with UV light than

with visible light and concluded that the nitrogen-induced effect allowing sub-bandgap excitation is due to an isolated N(2p) state rather than to narrowing of the bandgap. Lindgren et al.¹⁵³ confirmed by photoelectrochemical measurements that the nitrogen-created states are located close to the valence band maximum and that the conduction band edge remains unchanged by nitrogen doping.

Generally, polycrystalline N-doped samples have been produced by different preparative procedures: (1) reactive sputtering of TiO₂ targets with N₂/ Ar mixtures for films; (2) hydrolysis of NH_x/ TiO₂ mixtures or thermal treatment of TiO₂ in a NH₃ atmosphere for powder samples. In a recent single crystal study, we have shown that ion-implantation of atomically clean TiO₂ (110) surfaces with mixtures of N₂⁺ and Ar⁺ ions, followed by subsequent annealing under ultra high vacuum conditions, is an effective way to incorporate nitrogen into the TiO₂ lattice⁵³. X-ray photoelectron spectroscopy revealed exclusively a N (1s) feature at a binding energy of 396.6 eV which is attributed to substitutionally-bound nitride-nitrogen¹³¹. In contrast to expectations, these N-doped crystals, containing only nitride ions, exhibited a shift in the phototreshold energy of 0.2 eV to *higher* energy compared to undoped TiO₂(110), as measured by the photodesorption of molecular O₂⁵³.

In the present study, we have used another method to dope TiO₂(110) with nitrogen, and have found that the phototreshold energy can be shifted 0.6 eV in a *desirable* direction to *lower* energy. The new method of nitrogen doping involves high temperature treatment of TiO₂(110) with NH₃(g), and is observed to produce an additional subsurface N (1s) feature at 399.6 eV.

To determine the photoactivity in the threshold region of rutile (< 3eV), the photochemical reduction of Ag⁺_(aq) ions in aqueous solutions was measured⁴⁰⁻⁴². The capture of photogenerated electrons on the TiO₂ surface by Ag⁺ causes the deposition of metallic silver and

can, therefore, be directly used for quantification of the photoeffect on TiO₂. This was done for the first time by Fleischauer et al. who measured reaction rates and quantum efficiencies on ZnO and TiO₂ single crystal surfaces⁴⁰ by monitoring changes in the optical reflectivity due to the formation of metallic Ag. By means of atomic force microscopy, Farneth et al. used the photocatalytic reduction of Ag⁺ ions on polycrystalline TiO₂ films to investigate changes in the photoactivity of different rutile crystal faces^{41,42}. This method has been extended to assess the photoactivity of individual TiO₂ particles¹⁵⁴.

8.2. Experimental

Polished TiO₂(110) single crystal substrates (Princeton Scientific Corporation) were treated in a flow reactor system in an Ar gas atmosphere (1atm) at 870 K. Typical heating rates were 7 K min⁻¹. For doping, the Ar flow was replaced by NH₃ for five minutes, after the target temperature had been reached. Subsequently the crystals were kept in flowing argon for an hour at 870K and then cooled down in flowing argon over a time period of 2-3 hours. Optical absorption spectra were acquired with a Perkin Elmer Lambda 9 spectrophotometer.

For the silver reduction assay, doped and undoped crystal substrates were cleaved into slices of approximately 1 x 5 mm in size and then mounted pairwise on an optical microscope slide. Six to ten slices of the NH₃-treated and the blank crystal were assembled in two columns and immersed in an aqueous 0.1 N AgNO₃ solution which covered the sample surface to a depth of 3 mm. The incident UV light intensity at the position of the sample surface, depending on the photon energy, ranged between 1 - 4 mW cm⁻². Typical light exposure times were between 1 - 5 minutes, corresponding to photon fluxes of the order of 10¹⁷ photons cm⁻².

After sample exposure to light of defined energy and photon flux, the mounted crystals were rinsed, first in distilled water and then in ethanol. Remaining liquids were removed from the sample surface by blowing with dry air and subsequent drying in an oven for 40 min at 140°C in air.

Imaging of the silver deposits on the titanium dioxide surface was done using Atomic Force Microscopy (AFM). The instrument used is a Nanoscope IIIa DimensionTM 3100, from Digital Instruments. The probe tips used in this investigation were silicon nitride and were obtained from Veeco (model DNP-20). Images were collected in contact mode and were used to directly obtain information relating to the height and overall shape of the deposited silver clusters. Typical lateral scan frequencies were 1.5 Hz.

For quantification of the deposited silver, a flooding algorithm of the WSxM 4.0 software package (Nanotec Electronica S.L.) was used. The volume covered by silver clusters, per square centimeter, was taken as a measure of the quantity of deposited silver. Tip convolution effects as well as the volume contribution from the detected silver clusters below a threshold of 2 nm were neglected in this evaluation and errors due to these two simplifications tend to cancel each other. Values for the quantum yield were calculated as the number of Ag atoms produced per square centimeter, divided by the total number of photons per square centimeter impinging on the surface.

XPS measurements were carried out at the PPG Glass Technology Center. The XPS spectra were acquired with an ESCALAB Mk II (Vacuum Generators) spectrometer using unmonochromatized Mg K-alpha X-rays (240 W). Measurements by XPS and Ar⁺ sputtering steps (4 keV, I = 4 μA cm⁻²) were carried out in a high vacuum chamber with a base pressure of 10⁻⁸ Torr. The binding energy of the N(1s) peak was calibrated with respect to the O(1s) peak

from TiO₂ at 530.2 eV. The nitrogen concentration was estimated from the relative area intensities of the N(1s), Ti(2p) and O(1s) peaks. They were normalized using relative sensitivity factors in the Vacuum Generators software package.

8.3. Results and Discussion

8.3.1. Photoabsorption Spectrum

The absorption spectrum in Figure 39 reveals the fundamental absorption edge of rutile at 3.0 eV on both a nitrogen doped and an undoped rutile TiO₂(110) single crystal. However, the nitrogen doped crystal, produced via thermal treatment in an ammonia atmosphere, also has an increased optical absorption in the range of 2.4 - 3.0 eV. These crystals, once doped, are bluish-green in color while the undoped crystals are slightly yellowish in color, yet clear. The color of the nitrogen doped crystals is partially due to the bulk reduction of the crystal, since the thermal decomposition of NH₃ on the TiO₂ surface results in the evolution of molecular hydrogen which reduces the crystal electronically^{155,156}. In addition, the presence of the absorption band below the edge at 3 eV, indicates that nitrogen penetrates into the single crystal and effectively changes the electronic structure of the solid.

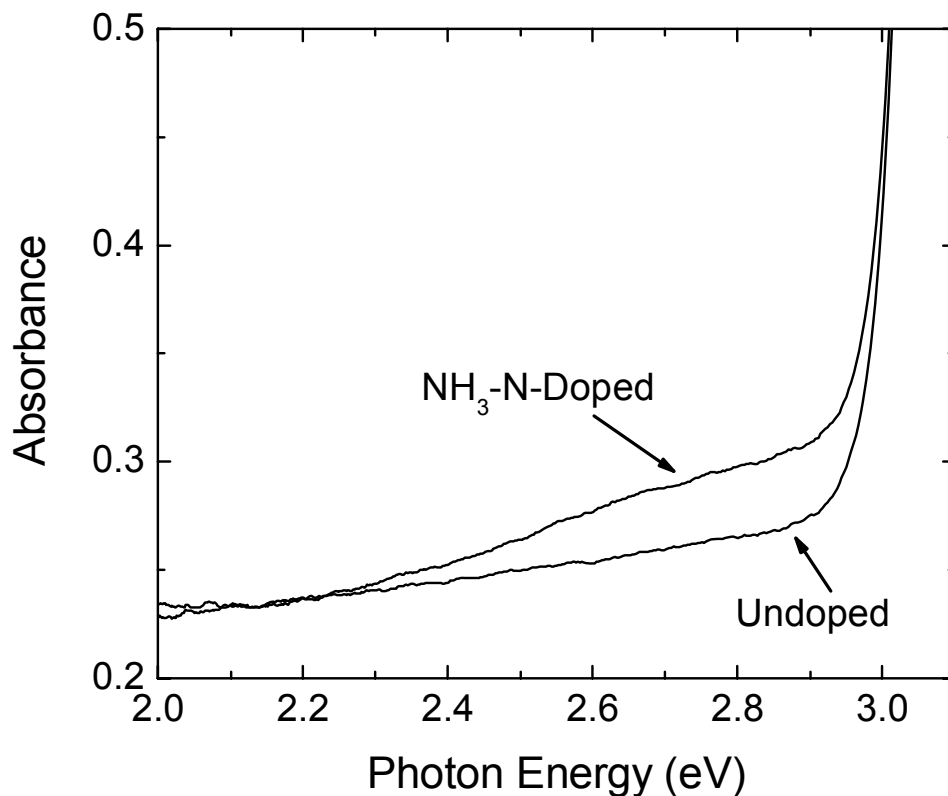


Figure 39: Absorption spectra of nitrogen-doped and undoped rutile TiO_2 single crystals measured at room temperature. The data have not been corrected for reflection loss.

8.3.2. Ag Deposition on the Surface of Doped and Undoped TiO_2 Crystals

For investigation of the photocatalytic activity in the near threshold region ($2.3 \leq h\nu \leq 3.0$ eV) the Ag deposition method was employed using defined numbers of photons passing through 10 nm windows in the optical filters. While unilluminated crystal surfaces exhibit only small noticeable changes before and after contact with the AgNO_3 solution (for quantification see Table I), Ag cluster deposition on the doped crystal surfaces was significant after exposure to visible light below $h\nu = 3.0$ eV. In Figure 40 a and b, typical topographic AFM images, obtained on samples after light excitation with $h\nu = 2.47$ eV, are presented.

Ag Photoreduction on $\text{TiO}_2(110)$
 $h\nu = 2.47 \text{ eV}$

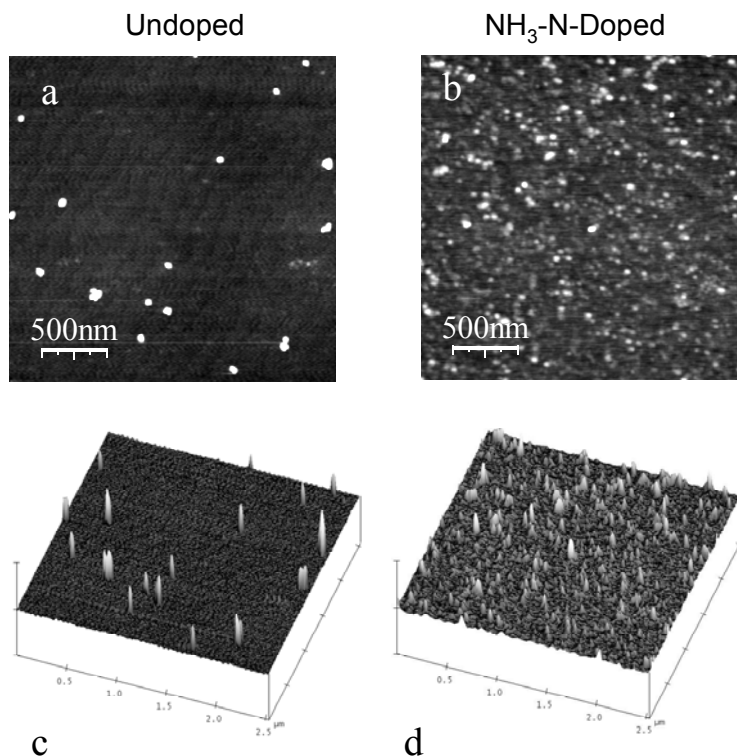


Figure 40: Contact-mode AFM images of silver deposits on the surface of undoped (images 'a' and 'c') and NH_3 -nitrogen doped (images 'b' and 'd') TiO_2 single crystals after photoreduction with $h\nu = 2.47 \text{ eV}$. Black-to-white vertical contrast in images a and b is 5 nm, whereas in images c and d, vertical contrast scale is 20 nm.

The contrast arises from vertical height differences on the surface, where black is low and white is high. Three-dimensional topographic reconstructions from the same data sets are displayed in Figure 40 c and Figure 40 d. It can clearly be seen that the doped and irradiated surface is homogeneously covered by Ag clusters with heights between 3 and 10 nm, whereas the bare surface of the undoped crystal contains only a limited number of clusters, inhomogeneously distributed. When the same experiment was performed with $h\nu = 2.98 \text{ eV}$ (Figure 41 a and b) the Ag deposition rate was dramatically enhanced and Ag clusters with average heights of 10 nm are imaged with the AFM.

Ag Photoreduction on $\text{TiO}_2(110)$
 $h\nu = 2.98 \text{ eV}$

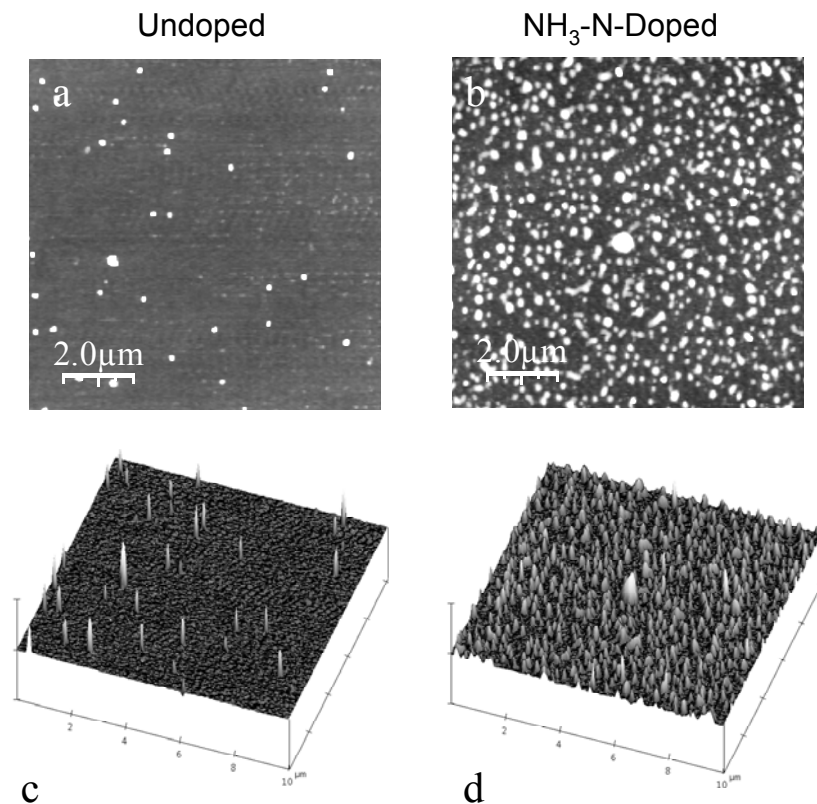


Figure 41: Contact-mode AFM images of silver deposits on the surface of undoped (a and c) and NH_3 -nitrogen-doped (b and d) TiO_2 single crystals after photoreduction with $h\nu = 2.98 \text{ eV}$. Black-to-white vertical contrast in panels a and b (2D images) is 10 nm, whereas the 3D representation in panels c and d have a vertical scale of 50 nm.

For quantification of the Ag concentration, the average volume cm^{-2} of these Ag clusters was derived from the AFM data. Based on 6-18 scans of different regions of every sample surface, the average concentration is shown in Table 2 as a function of photon energy. Assuming that each Ag atom originates from a photogenerated electron, the quantum yield¹⁵⁵ was calculated for the near threshold region ($< 3.0 \text{ eV}$) and plotted as a function of photon energy as shown in (Figure 42)¹⁵⁷. In the near threshold region ($< 3.0 \text{ eV}$), the concentration of deposited silver on the N-doped crystal was by a factor of 2 ($h\nu = 2.47 \text{ eV}$) to 4 ($h\nu = 2.98 \text{ eV}$) higher than for the undoped crystal, which proves the substantial photocatalytic activity of the NH_3 -treated crystal in

the visible light spectral range. The threshold photon energy for Ag deposition on the N-doped TiO₂(110) of about 2.4 eV is in good agreement with the optical absorption spectrum in Figure 39.

Table 2: Energy Dependence of Silver Deposition on Undoped and Nitrogen-Doped Rutile TiO₂ Single Crystals.

		Undoped TiO ₂ Crystal			Nitrogen-Doped TiO ₂ Crystal		
energy (eV)	number of photons (x 10 ¹⁷ cm ⁻²)	number of images	silver concentration (x 10 ⁻⁹ mol/cm ²)	standard deviation	number of images	silver concentration (x 10 ⁻⁹ mol/cm ²)	standard deviation
Dark	0	8	0.2	0.3	6	0.6	0.7
3.16	4.2	12	241.4	81.8	12	136.3	124.6
2.98	5.6	12	5.6	4.5	11	21.7	4.6
2.85	6.5	18	4.3	2.0	10	14.7	7.3
2.70	2.3	10	1.1	0.7	8	3.6	1.5
2.47	8.6	10	0.3	0.2	10	1.6	0.8
2.27	8.2	6	0.3	0.3	10	0.3	1.1

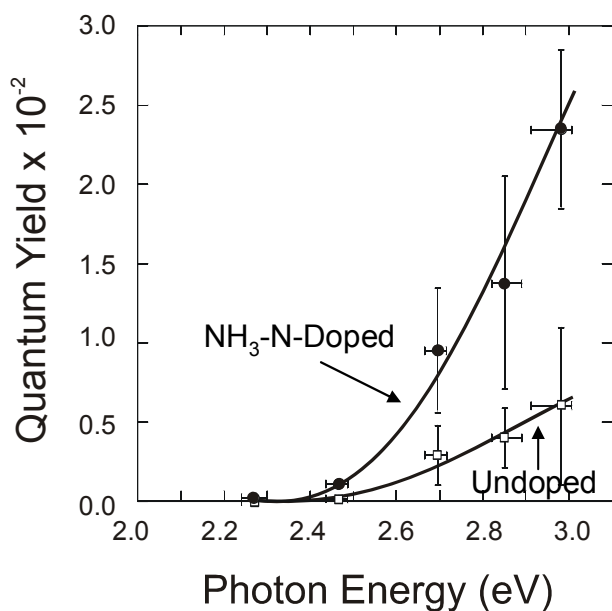


Figure 42: Action curve showing the quantum yield versus excitation energy for the photoreduction of silver on the surface of undoped and NH₃-nitrogen-doped TiO₂ single crystals. Error bars in the quantum yield are based on the standard deviation from measurements on 8-18 images from different regions of the crystal (see Table 2). Error bars in the photon energy correspond to the bandwidth of the interference filters used, where the location of the point is the band maximum of the respective filter transmission spectrum.

Higher rates for Ag deposition were observed after irradiation experiments with supra-bandgap photon energy (e.g. $h\nu = 3.16$ eV, Figure 43 a and c), leading to a much more complex topography of Ag deposits. Different from all sub-bandgap experiments, both doped and undoped TiO₂ surfaces produce large Ag islands with heights between 50-170 nm. The existence of much smaller clusters, as indicated by arrows in Figure 43, suggests that the large features emerge from the coalescence of many primary particles during photodeposition or during the drying procedure at 310 K.

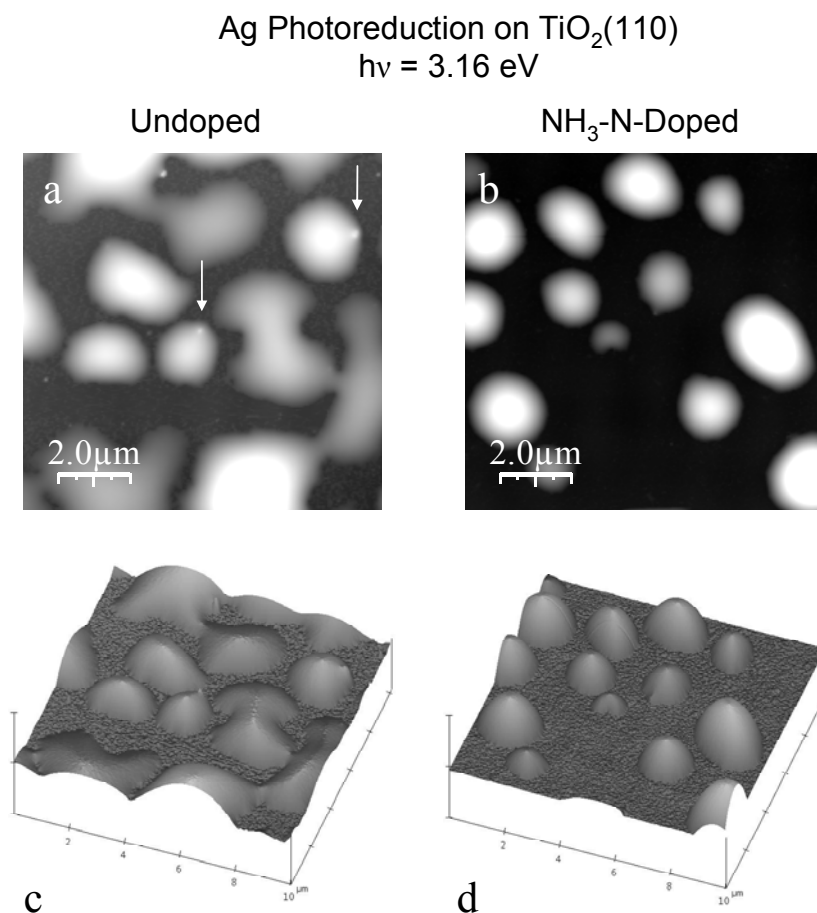


Figure 43: Contact-mode AFM images of silver deposits on the surface of undoped (a and c) and NH₃-nitrogen-doped (b and d) TiO₂ single crystals after photoreduction with $h\nu = 3.16$ eV. Black-to-white vertical contrast in panels a and b (2D images) is 100 nm, whereas the 3D representations in panels c and d have a vertical scale of 200 nm.

The average Ag concentration was determined to be $(2.41 \pm 0.8) \times 10^{-7}$ mol cm⁻² for an undoped crystal and $(1.36 \pm 1.25) 10^{-7}$ mol cm⁻² for the nitrogen-doped crystal. The large values for the standard deviations reflect the fact that on both sample surfaces some areas are uniformly coated, while others exhibit an inhomogeneous distribution of elevated features. The quantum yields at $h\nu = 3.16$ eV for the undoped and the doped samples are 0.35 and 0.2 respectively. These values are too high, considering that the (110) orientation of rutile TiO₂ is an order of magnitude less photochemically reactive than the (101) plane, for which quantum yields between 0.6 and 0.4 were reported^{41,42}. Together with the inhomogeneous distribution of silver, this points to the presence of autocatalytic reactions during Ag reduction with supra-bandgap energy light.

8.3.3. X-ray Photoelectron Spectroscopy

For chemical identification of the valence state of the dopant nitrogen, X-ray photoelectron spectroscopy (XPS) was employed. Surface analysis on doped and undoped TiO₂(110), showed an impurity XPS feature centered at 399.6 eV. UV treatment in air and/or removal of the first 5 Å of the surface by sputtering with Ar⁺ ions leads to the extensive depletion of these signals (Figure 44a). These traces of nitrogen must be attributed to surface contamination, probably originating from spurious NH₃ in the flow reactor chamber. Their presence only on the surface excludes their role in the enhanced optical activity in the range of visible light. However, after removal of 60 Å of TiO₂ by Ar⁺ sputtering, two N(1s) features at 399.6 and 396.7 eV are observed which indicates the presence of bulk nitrogen in two different chemical states. The total nitrogen concentration at 60 Å was determined to be about 0.6 atom %. The feature at 396.7 eV is generally known as the “nitride” peak and has been assigned to nitrogen anions, which substitute for oxygen in the TiO₂ lattice¹³⁴. As indicated by the smaller chemical shift, the nitrogen species associated with the feature at 399.6 eV carries less negative

charge than a nitride ion. The value for the binding energy agrees well with XPS data from NH_x -containing compounds¹⁵⁸ and suggests that the 399.6 eV N(1s) species is chemically bound to hydrogen.

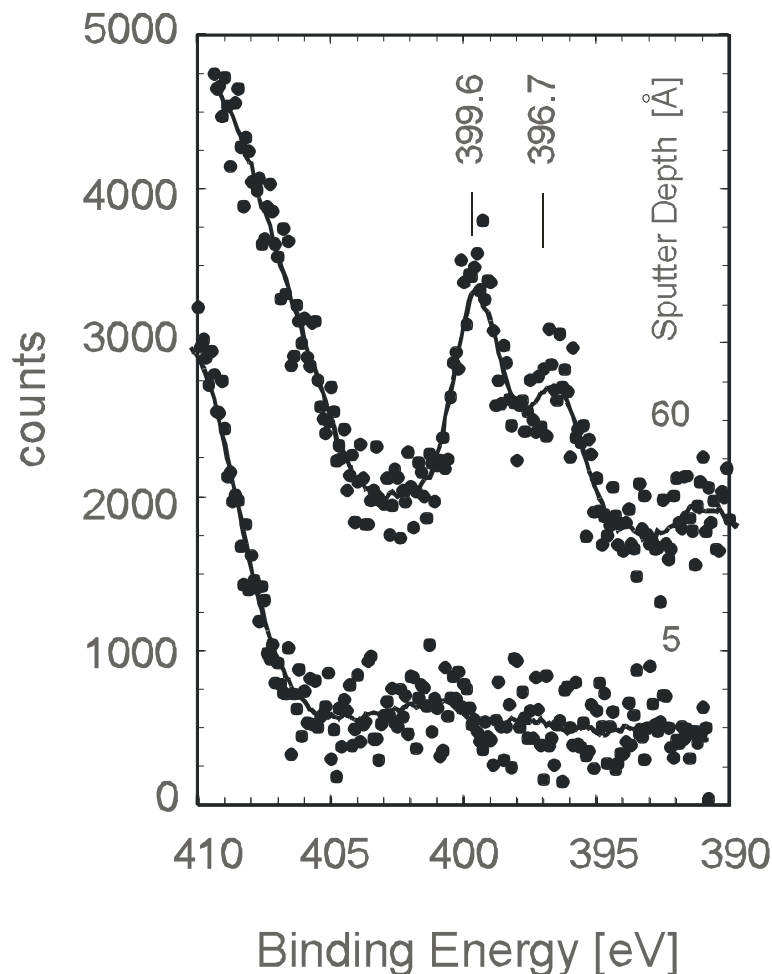


Figure 44: Nitrogen (N 1s) spectrum from a doped $\text{TiO}_2(110)$ crystal at two different Ar^+ sputter depths: a) 5 Å and b) 60 Å.

Our previous studies of nitrogen implantation into $\text{TiO}_2(110)$ have shown that the photochemical absorption edge is shifted 0.2 eV to *higher* energy and that the substitutional nitride ion with an N(1s) binding energy of 396.7 eV is the only subsurface dopant species present⁵³. This nitride species is probably also produced by the Ar ion sputtering method used to expose the subsurface region for XPS analysis in these experiments. This causes partial conversion into the nitride of nitrogen introduced by NH_3 doping at 870 K. We thus assign the

nitrogen state ($N(1s) = 399.6 \text{ eV}$) introduced by NH_3 as being responsible for the shift of the photochemical threshold down to about 2.4 eV . This form of nitrogen is most likely located in an interstitial site. This form of nitrogen dopant is probably bound to hydrogen. These results disagree with the conclusions of Asahi et al.³⁶, who reported that nitride ions which substitute for O^{2-} ions in the TiO_2 lattice are the necessary dopant species for TiO_2 photocatalysis in the visible light region.

8.3.4. Comparison of N-doping Effects in TiO_2 with those in ZnO

Although the effect of nitrogen doping in $TiO_2(110)$ is clearly shown in this work, the explanation for this effect is still somewhat under debate. The effect of doping in other wide bandgap semiconductors, like zinc oxide, for example, has recently also been studied. Zinc oxide is another n-type semiconductor, like TiO_2 , with an intrinsic bandgap of $E_g = 3.3 \text{ eV}$. In ZnO, nitrogen as a dopant should produce shallow acceptor levels within the bandgap. However, at this point in time, no one has successfully obtained p-type ZnO using a pure nitrogen source¹⁴⁶. On the other hand, co-doping of N in conjunction with H or Ga has been shown to be successful^{159,160}. The presence of donor dopants as suggested by Yamamoto¹⁶¹, has two consequences which may also apply to N:H doped TiO_2 . The first is an enhanced incorporation of acceptors because of their strong electrostatic attractive interaction leading to higher acceptor (N) incorporation in TiO_2 . The second consequence is the lowering of the acceptor energy level, bringing the level closer to the valence band. A hybridized state (N p-orbital and H s-orbital) is postulated to be formed in TiO_2 by analogy to ZnO. Both effects are beneficial for the enhanced optical absorption of ZnO and might also explain the photoactivity of N:H doped TiO_2 in the visible.

8.4. Conclusions

These findings, in conjunction with a recent investigation of nitrogen-implanted $\text{TiO}_2(110)$ ⁵³, indicate that nitrogen with an N(1s) binding energy of 399.6 eV is effective in reducing the threshold photon energy for photochemistry from 3.0 eV to 2.4 eV, a shift of 0.6 eV into the visible spectral region. This form of nitrogen can be introduced into the TiO_2 bulk using heat treatment in NH_3 at 870 K. This active nitrogen is likely to be interstitial and to be chemically-bound to hydrogen in the first few hundred Å below the TiO_2 surface. In contrast, substitutional nitrogen, in the form of implanted nitride species, is inactive for lowering the photochemical threshold energy below the bandgap energy of rutile TiO_2 ($E_g = 3.0$ eV). These findings are in contrast to current scientific opinion.

9. **CHAPTER NINE: Adsorption and Thermal Decomposition of 2-Chloro Ethyl Ethyl Sulfide on TiO₂ Surfaces[#]**

Abstract

The adsorption, desorption and oxidative decomposition of the 2-chloroethyl-ethyl sulfide molecule (2-CEES) has been investigated on the TiO₂(110) surface as well as on high area anatase and rutile powdered samples. A combination of measurement tools has been employed. It has been found that a monolayer of 2-CEES desorbs in the temperature range from 275 K to 400 K with an activation energy of 105 kJ/mol. Weak repulsive interactions are measured in the monolayer. The molecule may be oxidized both by Ti-OH groups on anatase or rutile, as well as by lattice oxygen in the TiO₂. Attack at the C-S bonds occurs as chloro-ethoxy and ethoxy groups are produced. At about 570 K these species further oxidize to form adsorbed COO and CO₃ species. The involvement of lattice oxygen in these reactions near 600 K has been observed by measurements of the background level in the infrared spectrum which may be used to measure the formation of trapped electron states at Ti³⁺ centers formed when adsorbate oxidation occurs by consumption of lattice oxygen. Upon heating to 900 K in vacuum, oxidation products on the TiO₂ surface are completely removed. Little difference in the reactivity patterns for anatase and rutile are found in this work.

[#] Reproduced in part with permission from Tracy L. Thompson, Dimitar A. Panayotov and John T. Yates, Jr. "Adsorption and Thermal Decomposition of 2-Chloro Ethyl Ethyl Sulfide on TiO₂ Surfaces" *Journal of Physical Chemistry B*, **108** (2004) 16825-16833. Copyright 2004 American Chemical Society.

9.1. Introduction

Titanium dioxide is currently utilized as a photoactive catalytic material for the destruction of organic molecules by photooxidation reactions driven by sunlight^{1,23,56,58,162}. The thermally-driven surface reactions which also occur on TiO₂ are therefore of importance in properly characterizing the full sequence of chemical events at work in the catalytic photooxidation chemistry of organic molecules. This approach has been exploited by Lin and co-workers in their recent studies on thermo- and photoreactivity of organic molecules on TiO₂¹⁶³⁻¹⁶⁵.

The 2-chloroethyl ethyl sulfide (2-CEES) molecule is a simulant for S-based mustard gas (HD) compounds which is widely used for laboratory experiments. It possesses both S-group functionality as well as Cl-group functionality, making its chemistry more complex than test molecules containing single reactive groups.

Only one study of 2-CEES thermal decomposition chemistry on a single crystalline surface has been published. This paper, by Zhou et al.¹⁶⁶ reported significant thermal decomposition of 2-CEES on the Pt(111) surface. The work reported here is the first to investigate the thermal decomposition of the 2-CEES molecule on TiO₂(110) and powdered TiO₂ surfaces. Previous work has studied the interactions of 2-CEES with TiO₂-SiO₂ and TiO₂ powders¹⁶⁷, where it was shown that 2-CEES binds to Ti-OH groups via both the chlorine and sulfur moieties in the molecule. The extent and nature of the thermal decomposition of 2-CEES was not investigated at that time.

The experiments described here combine two complementary approaches for the study of 2-CEES thermal decomposition on TiO₂. In the first, a TiO₂(110) rutile single crystal is employed, and both temperature programmed desorption mass spectrometry and Auger spectroscopy are combined to observe surface chemistry on this idealized single crystal surface

in an ultra high vacuum (UHV) apparatus. These experiments have the advantage of known levels of surface impurities, known crystal structure, and known surface defect density. Thermal desorption measurements for 2-CEES from $\text{TiO}_2(110)$ have been used to derive desorption rate parameters. In the second approach, transmission infrared spectroscopy has been employed using both anatase and rutile high area TiO_2 powders. These experiments have the advantage of being able to observe characteristic bond vibration frequencies for the 2-CEES adsorbate molecule, as well as the formation of new species during 2-CEES thermal decomposition. Generally the infrared experiments on high area powders are inferior to the single crystal experiments when desorption or reaction kinetics are to be measured because of interference by surface diffusion processes as molecules exit from the pore structure of the powder. However, because of the high surface area being investigated, small coverage of adsorbed reactant and product species may often be observed by the infrared method, leading to an understanding of the general reaction patterns of the adsorbate.

In this combined study, we find that strongly chemisorbed 2-CEES molecules decompose on TiO_2 while also thermally desorbing above about 275 K. It is found that lattice oxygen from the TiO_2 is a reactant producing oxygenated products containing R-O-C and R-C=O moieties in oxygenated compounds that eventually decompose and desorb. When Ti-OH groups are present, these oxidized species are observed to hydrogen bond to the 2-CEES molecule (through both the S and the Cl moiety, see earlier work ¹⁶⁷), and these hydrogen bonded Ti-OH groups then preferentially disappear as oxidation of the 2-CEES occurs in vacuum. Both the single crystal studies and the infrared studies suggest that cleanup of the TiO_2 occurs upon heating in vacuum to 900K.

9.2. Experimental

9.2.1. Ultrahigh Vacuum Studies on TiO₂(110)

The UHV chamber used for these experiments is described in Chapter Two of this thesis. The 2-CEES compound used in both the UHV and Transmission IR studies was obtained from Sigma-Aldrich (98%) and then transferred under nitrogen atmosphere into a glass bulb which was then attached to the gas line through which gas is admitted to the UHV chamber. The 2-CEES liquid was then further purified via several freeze-pump-thaw cycles. Traditionally, gases are dosed directly to the crystal surface by means of a capillary array molecular beam doser [⁵⁴] which minimizes gas exposure to the rest of the chamber, in turn allowing for faster pump down times and less spurious desorption from the inside walls of the chamber. However, it was found by a systematic study that the molecular beam doser behaves in an irreproducible manner due to adsorption effects in the capillary array when 2-CEES is dosed, and as a result, a backfilling method (using a leak valve) was employed for 2-CEES gas exposure to the crystal. When calculating the overall exposure of 2-CEES to the crystal surface, both the ion gauge sensitivity as well as the tail of the partial pressure of 2-CEES during pump down after exposure was considered. Thermal desorption measurements were carried out using a heating rate of 3.0 K/sec.

9.2.2. Transmission IR Studies on TiO₂ Powders:

9.2.2.1. IR cell and High Vacuum System

The transmission FTIR spectroscopic study of powder TiO₂ materials, anatase and rutile, was conducted in a stainless steel cell ¹⁶⁸, shown in Figure 45. The powdered TiO₂ samples are pressed into a flat tungsten grid ¹⁶⁹ and then attached firmly to a power/thermocouple feed-through via a pair of nickel leads. The temperature of the TiO₂ can be adjusted by electrical heating of the grid and by cooling with a liquid N₂ or with a dry ice – acetone mixture. A

programmable Honeywell digital controller operating off of feedback from a K-type thermocouple welded to the top of the grid assures temperature control with an accuracy of ± 1 K. The IR cell is connected to a stainless steel high vacuum system and is capable of working under a wide range of pressures (10^{-8} to ~ 760 Torr). Sample temperatures from 100 to 1500 K are routinely achieved. The stainless steel vacuum system is pumped simultaneously with a Pfeiffer Vacuum 60 L/s turbo-molecular pump and a Varian 20 L/s ion pump which allow a base pressure of 1×10^{-8} Torr to be achieved routinely. The base pressure was measured by the ionization current within the ion pump. Reactant gas pressure was measured by a MKS capacitance manometer (Baratron, type 116A, range 10^{-3} - 10^3 Torr).

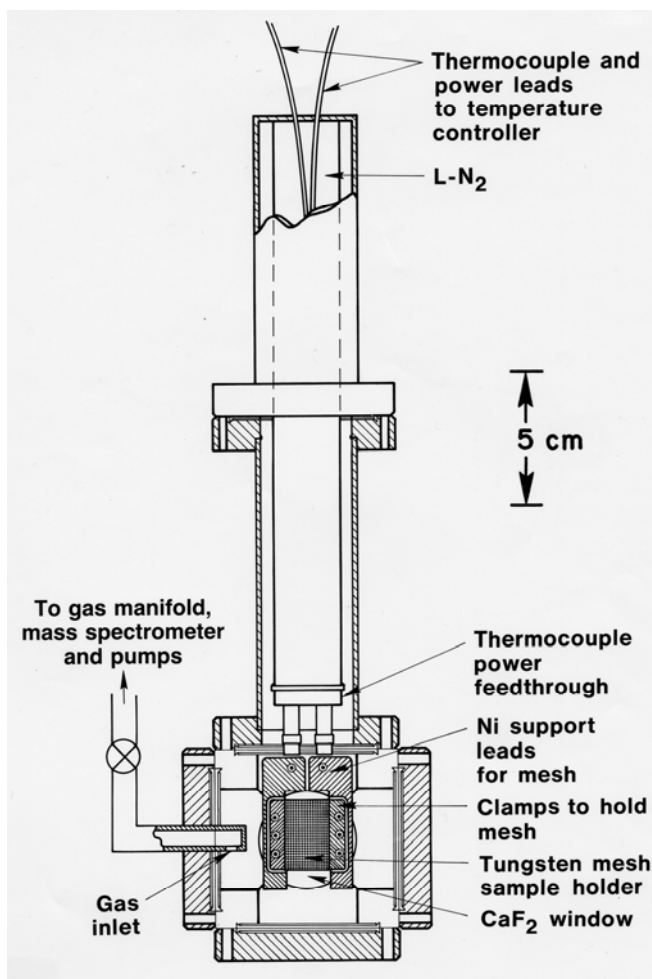


Figure 45: Schematic of high vacuum apparatus used for infrared studies of TiO₂ powders.

The IR cell is aligned to the IR beam using a computer-controlled translation system (Newport Corporation) with $\pm 1 \mu\text{m}$ accuracy^{167, 170} in both the horizontal and vertical positions.

Infrared spectra were obtained on a nitrogen-gas purged Mattson Fourier transform infrared spectrometer (Research Series I) equipped with a liquid N₂ cooled HgCdTe detector. The accumulation of spectra within the infrared region 4000 - 500 cm⁻¹ was made in the ratio mode at a resolution of 4 cm⁻¹. WinFIRST software supplied by Mattson was used for setting the spectrometer and for spectra acquisition. For each spectrum, typically 2000 scans were acquired in order to ensure precise measurement of low absorbance bands with high S/N ratio.

9.2.2.2. TiO₂ Powder Materials

Two different TiO₂ powder materials, anatase and rutile, were simultaneously studied by transmission FTIR spectroscopy. The anatase TiO₂ (P-25) was the widely studied photoactive material, Degussa P25 and the rutile TiO₂ was supplied by the Knözinger laboratory, Institut für Materialchemie, Technical University, Vienna. The anatase TiO₂ is reported to be 99.5% pure TiO₂ having 70% anatase and 30% rutile, and a surface area of $\sim 50 \text{ m}^2 \text{ g}^{-1}$ ¹⁷¹. The average particle diameter by number count is 21 nm; 90% of the particles fall in the size range 9 – 38 nm. The particles exist as aggregates approximately 0.1 mm in diameter¹⁶². The rutile TiO₂ produced by the liquid hydrolysis of TiCl₄ has a surface area of $20 \text{ m}^2 \text{ g}^{-1}$ after thermal treatment in air at 823 K. According to X-ray powder diffraction it contains only the rutile phase. The anatase and rutile TiO₂ samples are hydraulically pressed at 12 000 psi into the middle and the bottom positions of the same tungsten grid as circular spots 7 mm in diameter, typically weighing 4 - 4.5 mg ($10.4 - 11.7 \text{ mg cm}^{-2}$). The third, top position of the grid is empty and it was used for reference background spectral measurements. This double-sample method involving different

samples on the same grid allows close comparisons to be made for anatase and rutile under precisely the same conditions of material preparation, gas exposure and temperature.

The oxygen used for the oxidation of annealed TiO₂ was obtained from VWSCO and was 99.8% pure.

9.2.2.3. TiO₂ Activation; 2-CEES Adsorption and Thermal Stability Experiments

The activation of anatase and rutile TiO₂ samples involved consecutive thermal pretreatment, oxidation and thermal reduction procedures. The fresh samples were heated in vacuum to the desired pretreatment temperature, 675 K, at a rate of 20 K min⁻¹ and held at temperature for 4 h, then cooled down to room temperature. Oxygen, at 6.2 Torr was introduced into the IR cell and the samples' temperature was increased to 675 K at a heating rate of 20 K/min. The duration of the oxidation period was 1 h.; after that the samples were cooled down to room temperature and O₂ was evacuated. The subsequent reduction procedure involved vacuum annealing at 822 K for 3 h, followed by cooling down to room temperature. The temperature for reduction of powder TiO₂ (822 K) is slightly lower than used for the preparation of the reduced single crystal TiO₂(110) surface (900K). The powdered TiO₂ samples, annealed in vacuum at 822K, retain some Ti-OH groups which are useful in binding 2-CEES to the surface, as shown previously¹⁶⁷. The reference IR spectra for oxidized and thermally reduced samples were acquired at room temperature.

The adsorption of 2-CEES on partially reduced and as well partially dehydroxylated surfaces of anatase and rutile TiO₂ samples was carried out at 255 K via several dosages of 2-CEES at increased pressures ranging from 5 to 25 mTorr. After the last dose the IR cell was evacuated to 2 x 10⁻⁸ Torr pressure. FTIR spectra were collected following each of the 2-CEES exposures as well as following evacuation.

The UHV experiments, where products were observed to desorb during temperature programming, were simulated by successive cycles of heating from 255 K to a particular temperature at 3 K/sec, just as was done on the single crystal substrate. Following this programmed heating; fast cooling down to 255 K and IR spectra measurements at 255 K were then made. These experiments were carried out under dynamic vacuum conditions. Cooling to 255 K, requiring < 30 s, was accomplished via a dry ice – acetone cooling mixture in the Dewar of the IR cell. In this manner, the collected information about the spectral changes for the adsorbed species on high area TiO₂ samples can be related to the information obtained by thermal programming and mass spectrometric measurements made on the TiO₂(110) crystal.

9.3. Results

9.3.1. TiO₂(110) Results

9.3.1.1. Adsorption, Desorption and Thermal Decomposition of 2-CEES on Reduced TiO₂(110)

The interaction between adsorbed 2-CEES and the single crystal TiO₂(110) surface was initially studied via low temperature adsorption (110K) and subsequent temperature programmed desorption (TPD). For these experiments, the main cracking product of 2-CEES, mass 75, was monitored due to the low intensity of the parent ion, mass 124. Figure 46 shows the TPD spectrum of 2-CEES from a reduced TiO₂(110) surface for exposures between 0 and 1.5 x 10¹⁵ molecules cm⁻². The monolayer of 2-CEES becomes saturated after gas exposures to the crystal of 7 x 10¹⁴ molecules cm⁻² and desorbs in a single first-order kinetic process with the rate maximum at approximately 350 K. At higher exposures, a second layer develops on top of the monolayer and desorbs at approximately 230 K. Multilayer formation occurs at even higher coverage, and desorption from the multilayer occurs at approximately 170 K. Due to the

approximate linearity of the coverage versus exposure plot (inset to Figure 46) we assume a unity sticking coefficient exists at the 110 K adsorption temperature. A slight discontinuity in the coverage versus exposure curve is observed as the second layer begins to form.

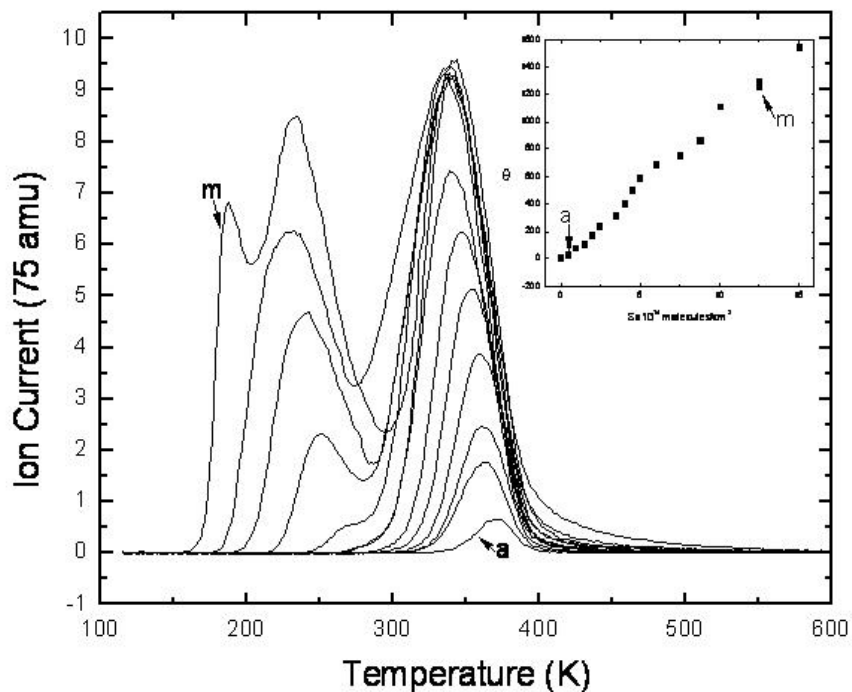


Figure 46: Thermal desorption spectra for 2-CEES adsorbed on TiO₂(110) for exposures ranging from 0 to 1.5×10^{15} molecules cm⁻². The inset depicts the coverage versus exposure behavior for this system.

The thermal desorption spectra for 2-CEES from the reduced TiO₂(110) surface were simulated for low coverage (between 5×10^{13} molecules cm⁻² and 3.5×10^{14} molecules cm⁻²) according to the Polanyi-Wigner equation for first-order desorption:

$$R_{des} = \nu^{\circ} \frac{1}{\beta} N \exp\left[-\frac{(E_{des}^{\circ} + E_{int} N)}{kT}\right] \quad (9.1)$$

Here R_{des} is the rate of desorption (dN/dt), N is the coverage, ν° is the frequency factor, β is equal to dT/dt , E_{des} is the desorption energy and E_{int} is the energy of the lateral interactions between adsorbed molecules. Figure 47 shows the results of the simulation where the zero-

coverage desorption energy, E_{des}° , was found to be 105 kJ mol^{-1} , the interaction energy is repulsive and measured to be -8 kJ mol^{-1} and the pre-exponential factor is on the order of $1 \times 10^{14} \text{ s}^{-1}$.

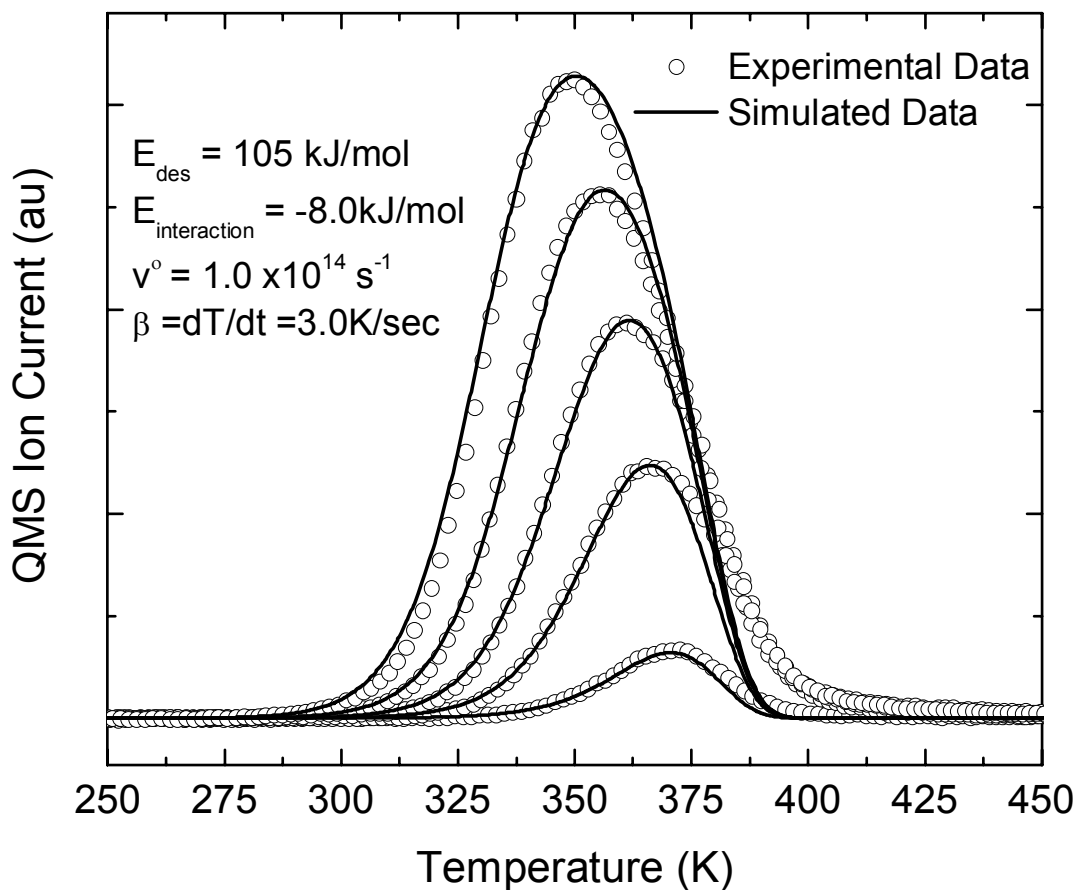


Figure 47: Simulated data versus experimental data for 2-CEES thermal desorption from $\text{TiO}_2(110)$ for low coverage ranging from 5×10^{13} to 3.5×10^{14} molecules cm^{-2} .

For 2-CEES adsorbed on the $\text{TiO}_2(110)$ surface, the parent molecule is completely desorbed by approximately 400 K, but at this temperature AES shows that significant thermal decomposition products remain on the crystal, giving Auger signals for S, Cl and C. Figure 48 displays the intensities of these 2-CEES decomposition products after heating to various

temperatures. The data shown in Figure 48 are initially normalized using AES intensities measured on the layer after 1 ML of 2-CEES exposure to the TiO₂(110) surface without any temperature ramping. The fact that these elements are observed beyond the 2-CEES desorption range is clear evidence for the partial thermal decomposition of 2-CEES during heating. Importantly, after TPD to temperatures of 900K, the surface becomes clean as all decomposition products are removed in vacuum (see insert to Figure 48).

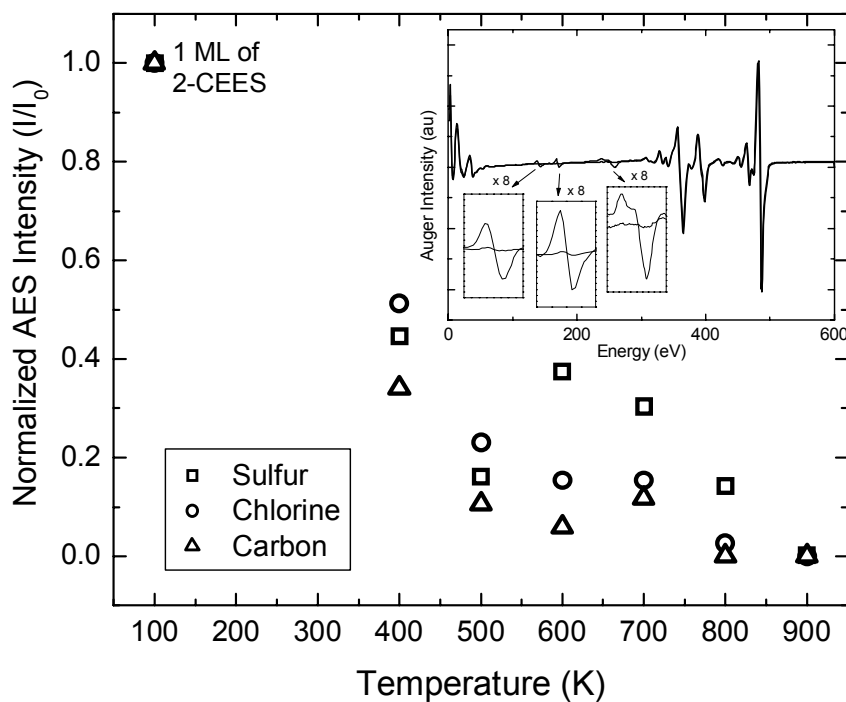


Figure 48: Change in surface coverage of S, Cl and C as a function of annealing temperature. Points are normalized to the amount of each element measured by Auger spectroscopy for 1 ML of 2-CEES (shown at 100 K). Inset shows two representative spectra for 1 ML of 2-CEES and for the same exposure after annealing momentarily to 900 K. The enlarged spectra show the same for the Auger regions for S, Cl and C.

Although complete assignment to all thermal decomposition products is not possible, some insight into possible products is presented in Table 3. Thermal decomposition products presented

in this table were measured by one of two methods. The presence of products was first crudely measured by analysis of the analog mass spectrum scan from mass 0 to mass 130, measured once every 5 seconds during temperature ramping of the crystal. Using this method, successive scans could be subtracted from one another to identify any changes, or lack thereof, for specific masses. Representative TPD spectra confirming that ethane and ethylene are produced are shown in Figure 49. Results in Table 3 provide evidence for the thermal decomposition of 2-CEES into hydrocarbon fragments, chlorinated hydrocarbon fragments, HCl, and oxygenated products. Because of the complexity of the products, we have not exhaustively studied their composition with the mass spectrometer.

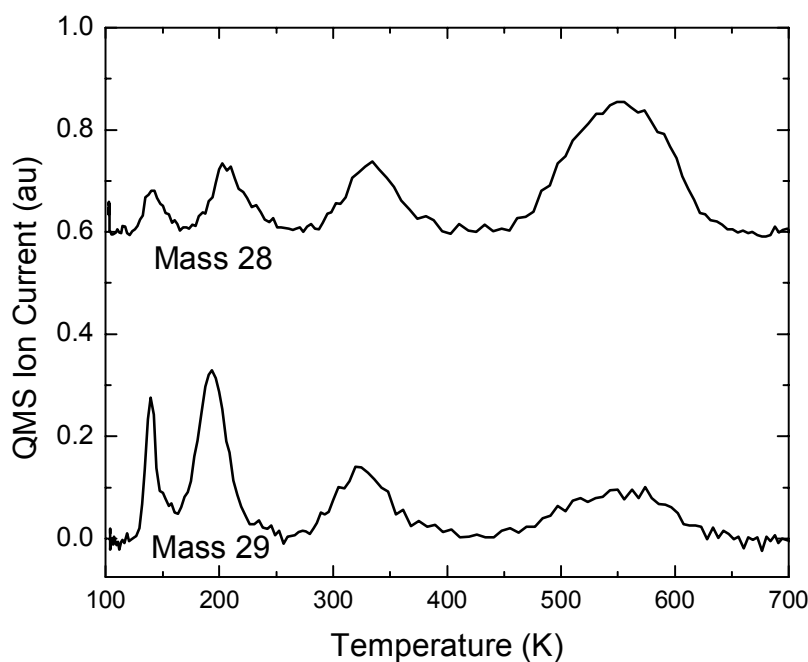


Figure 49: Representative thermal desorption spectra showing decomposition products from 2-CEES at masses 28 and 29, assigned to the thermal desorption of ethane and ethylene. Initial 2-CEES coverage = 1 ML.

Table 3: Evidence for thermal decomposition products of 2-CEES from TiO₂(110).

Name of Compound	Chemical Formula	Identification Based On...	Mass of Ion Fragment	Additional Remarks
<i>Ethane</i>	C ₂ H ₆	TPD: Peak at 550 K	30 (29 is main fragment)	Cracking pattern observed
<i>Ethylene</i>	C ₂ H ₄	TPD: Peak at 550 K	28	Cracking pattern observed
<i>Hydrogen Chloride</i>	HCl	TPD: Peak at 550-600K	36	Cracking pattern observed
<i>Chloroethane</i>	CH ₃ CH ₂ Cl	TPD: Peak at 200-250 K	64	Cracking pattern observed
<i>Formaldehyde (+ Ethane)</i>	H ₂ CO, (C ₂ H ₆)	TPD: Peak at 550K	30	Similar cracking pattern to ethane
<i>Acetaldehyde (+ Carbon Dioxide)</i>	CH ₃ CHO, (CO ₂)	TPD	44	Mass 44 also CO ₂ , mass 29 also seen for ethane, ethylene
<i>Methane (?)</i>	CH ₄	TPD	16	May also be from cracking of other products

9.3.2. Powdered TiO₂ Results

9.3.2.1. Adsorption of 2-CEES on Partially-Dehydroxylated TiO₂ Powders - Anatase and Rutile

Adsorption of 2-CEES on high area anatase and rutile powders at 255 K produces absorption bands which are characteristic of the adsorbed molecule. In addition, hydroxyl groups are modified by the low temperature adsorption. Difference spectra clearly show the modification of the hydroxyl groups on anatase and rutile surfaces, as seen in Figure 50 A.

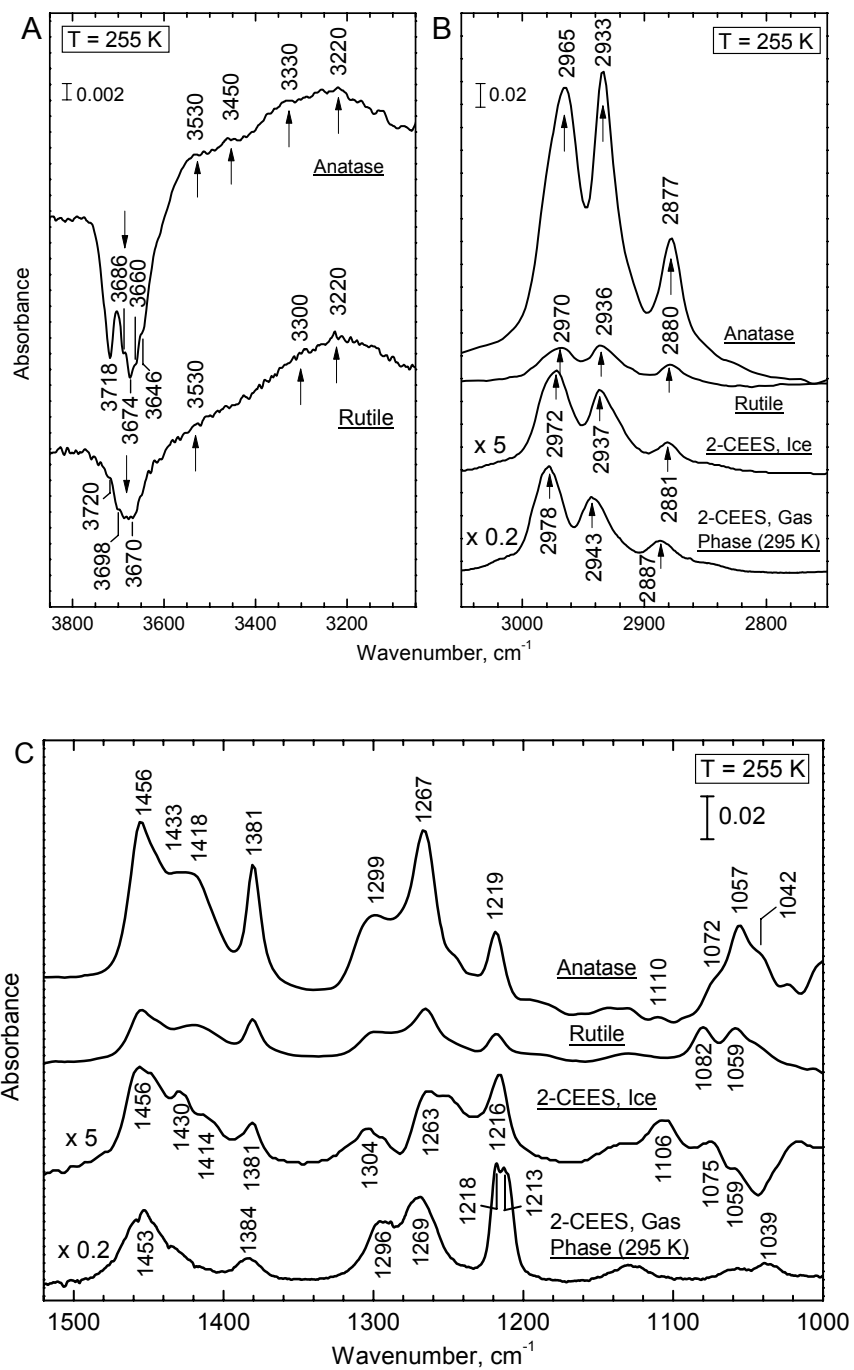


Figure 50: Difference IR spectra of 2-CEES adsorbed on TiO₂ anatase and rutile powders at 255K.

Here, the decrease in Ti-OH absorbance due to hydrogen bonding with 2-CEES are observed as several types of isolated Ti-OH groups in the 3700 cm^{-1} region are consumed, and are converted to lower frequency, spectrally-broadened Ti-OH species with frequencies in the 3500 cm^{-1} - 3200 cm^{-1} range. The hydrogen bonding of 2-CEES to Ti-OH groups has been reported previously ¹⁶⁷.

In Figure 50 b, a comparison is made in the alkyl stretching region for 2-CEES in four different physical conditions. The lower spectrum shows the reference spectrum for 2-CEES gas phase molecules, where intermolecular interactions are absent. Three alkyl modes are observed: The bands at 2978 cm^{-1} and 2943 cm^{-1} are assigned to the asymmetric $\nu(\text{CH}_2)_{\text{as}}$ and $\nu(\text{CH}_3)_{\text{as}}$ modes respectively ¹⁷²⁻¹⁷⁴, and the band at 2887 cm^{-1} is assigned to overtones of the $\delta(\text{CH}_2)_{\text{as}}$ and $\delta(\text{CH}_3)_{\text{as}}$ modes which are intensified by Fermi resonance ¹⁷². When 2-CEES condenses as an ice on a CaF_2 substrate, the spectrum shown in Figure 50 b is obtained. It may be seen that a red shift of 6 cm^{-1} is observed upon condensation into the ice. Adsorption on rutile and anatase gives alkyl stretching modes that are further red shifted from the gas by $7 - 10\text{ cm}^{-1}$. In addition, the adsorbed 2-CEES on both anatase and rutile exhibits an enhancement of intensity of the $\nu(\text{CH}_3)_{\text{as}}$ mode relative to the other two modes.

In Figure 50 C the spectral developments in the fingerprint region below 1500 cm^{-1} may be compared. The bands at 1453 cm^{-1} and 1384 cm^{-1} are assigned respectively to asymmetric and symmetric bending modes in CH_3 ^{174, 175} and the band or shoulder at 1430 cm^{-1} to the CH_2 scissor mode ^{172, 174}. The bands near 1296 cm^{-1} and 1269 cm^{-1} are assigned to CH_2 wagging modes ^{174, 175}, whereas the band at about 1220 cm^{-1} is assigned to the CH_2 wagging mode of the CH_2 groups near the S atom in the molecule ^{174, 175}. The bands in the 1070 cm^{-1} region are assigned to $\nu(\text{C-C})$ stretching modes ^{172, 174}. The mode assignment for 2-CEES is made in Table 4, using the gas phase frequencies.

Table 4: Vibration Frequencies (cm⁻¹) of 2-CEES: Gas, Ice and Species Adsorbed on TiO₂ Powders at 255K

Mode description	Gas (295K)	Ice, on CaF ₂	Adsorbed species		Literature Values
			Anatase	Rutile	
$\nu(\text{CH}_2)_{\text{as}}$	2978	2972	2965	2970	2971, 2956
$\nu(\text{CH}_3)_{\text{as}}$	2943	2937	2933	2936	2917
$\nu(\text{CH}_2)_{\text{s}}$, overtone of $\delta(\text{CH}_2)_{\text{as}}$ and $\delta(\text{CH}_3)_{\text{as}}$	2887	2881	2877	2880	2911, 2897, 2855
$\delta(\text{CH}_3)_{\text{as}}$ bent	1453	1456	1456	1456	1484
(CH ₂) scissor	1430	1430	1433	1433	1460
$\delta(\text{CH}_3)_{\text{s}}$ bent	1384	1381	1381	1381	1407
(CH ₂) wag	1296, 1269	1304, 1263	1299, 1267	1299, 1267	1294, 1266
S(CH ₂) wag	1218, 1213	1216	1219	1218	1218
$\nu(\text{C-C})_{\text{as}}$	~ 1040	1060	1070- 1040	1080- 1060	975

The hydrogen-bonded 2-CEES molecule is strongly held on the rutile and anatase surfaces. Evacuation to 2×10^{-8} Torr for 90 minutes at 255 K did not result in a loss of alkyl absorbance. Although the TiO₂(110) surface, discussed previously, did not have Ti-OH groups, the stability of the adsorbed layer observed on the high area TiO₂ surfaces is consistent with the beginning of thermal desorption of 2-CEES from TiO₂(110) only at about 275 K as shown in Figure 46 and Figure 47.

9.3.2.2. Thermal Activation of 2-CEES on High Area TiO₂- Anatase and Rutile

Anatase

Figure 51 shows the behavior of the infrared spectra as the high area anatase-TiO₂ containing chemisorbed 2-CEES is heated in vacuum. All spectra were measured after cooling back to 255 K. By observing the behavior of the associated hydroxyl groups (Figure 51 A) we see that at about 361 K, the hydrogen-bonded Ti-OH groups begin to disappear. This loss of associated Ti-OH absorbance is not correlated with the production of isolated Ti-OH groups, since little spectral change occurs in the difference spectra shown in the 3700 cm⁻¹ region. This behavior, observed from 361 K to ~ 514 K, suggests instead that associated Ti-OH groups are being consumed irreversibly by reaction with 2-CEES.

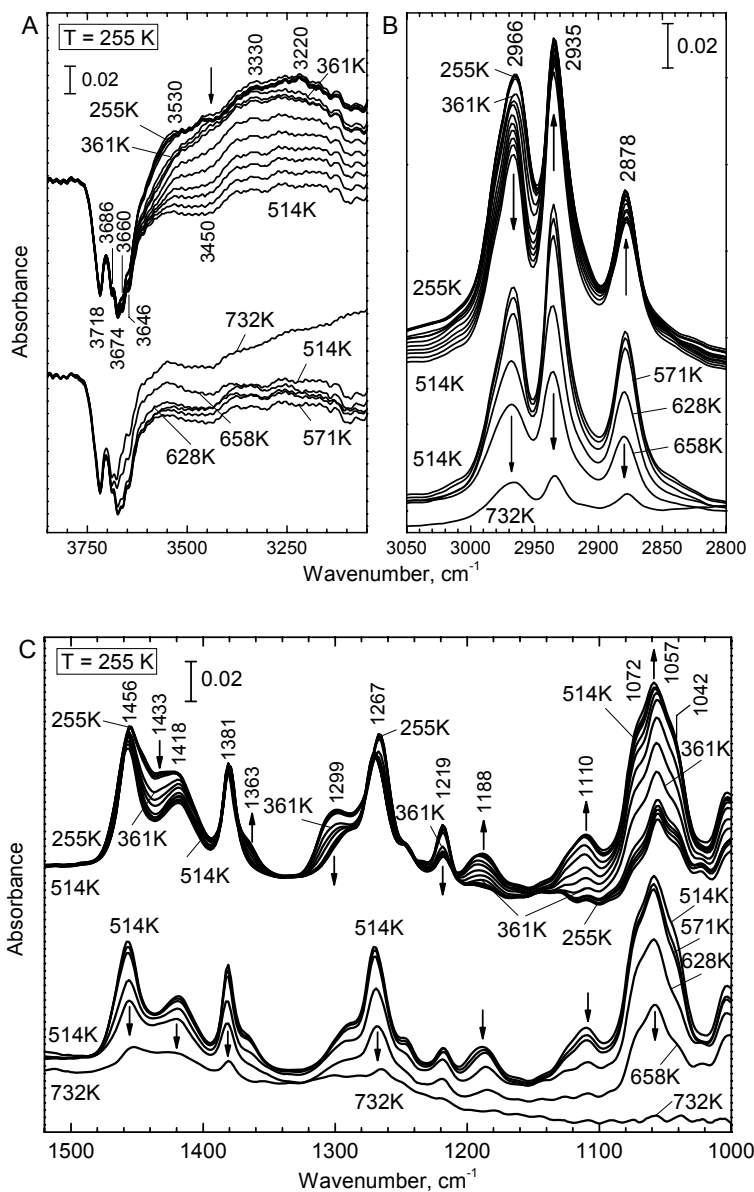


Figure 51: Difference IR spectra for 2-CEES/TiO₂ (anatase) during heating from 255 to 732 K.

The irreversible behavior of the surface species (2-CEES and associated Ti-OH) may also be seen by examining the behavior of the alkyl absorbance ratios in Figure 51 B. In the temperature range 255 K - 514 K, the two lower wavenumber $\nu(\text{CH}_2)_{\text{as}}$ and overtone $(\text{CH}_3)_{\text{as}}$ and $(\text{CH}_2)_{\text{as}}$ modes increase in peak absorbance while the high frequency mode $\nu(\text{CH}_2)_{\text{as}}$ decreases in peak absorbance. Since such changes in relative absorbance do not occur when the 2-CEES

coverage increases as it is adsorbed on TiO₂ (not shown), the intensity ratio change must be due to structural and configurational changes which are not related to coverage-dependent changes in the interactions between 2-CEES molecules. We believe this intensity ratio change is related to the onset of a chemical reaction between 2-CEES and the TiO₂ surface.

Figure 51 C shows similar evidence of the presence of a chemical reaction between 2-CEES and TiO₂ in the temperature range 255 K - 514 K. It may be seen that some spectral features in the fingerprint region decrease in absorbance, while others increase. Thus, the absorbance due to the CH₂ moieties decrease in magnitude. The band at 2966 cm⁻¹ (ν(CH₂)_{as}), at 1433 cm⁻¹ (CH₂ scissors), at 1299 cm⁻¹ (CH₂)_{wag}, and at 1219 cm⁻¹ (S-CH₂)_{wag} all decrease together in absorbance as the temperature is increased to 514 K. Interestingly, the absorbance of the (CH₃)_{sym} bending mode at 1381 cm⁻¹ is almost unchanged and the same is true for the (CH₃)_{as} bending mode at 1456 cm⁻¹ (the small changes being due to overlap with the 1433 cm⁻¹ mode which decreases in absorbance). These observations indicate that the CH₂ groups associated with both S and Cl are active in reaction with the TiO₂ surface, whereas the CH₃ group is not reactive up to about 514 K.

The increase in absorbance in the bands below 1200 cm⁻¹ is related to the production of C-O moieties which exhibit stretching frequencies in this range ^{163-165,172}. In particular, CH₃CH₂O-Ti and ClCH₂CH₂O-Ti species are indicated. The production of these ethoxy species by reaction with oxygen atoms from the TiO₂ substrate ^{163-165,172} is consistent with the development of enhanced absorbance due to CH₃- and -CH₂- groups in the alkyl absorbance region.

Above about 514 K, a parallel progressive change in all spectral features is observed, as all spectral features of the organic species decrease together. In addition, isolated Ti-OH groups begin to be regenerated above 514 K, as may be seen in Figure 51 A.

Rutile

As shown in Figure 52, the general behavior observed for anatase is also seen for rutile as adsorbed 2-CEES is thermally activated. Mode splitting of the C-O vibrations due to ethoxy species seems to be more evident for rutile than for anatase, and the regeneration of isolated Ti-OH groups on heating to 732 K does not seem to occur for rutile, where it is observed for anatase.

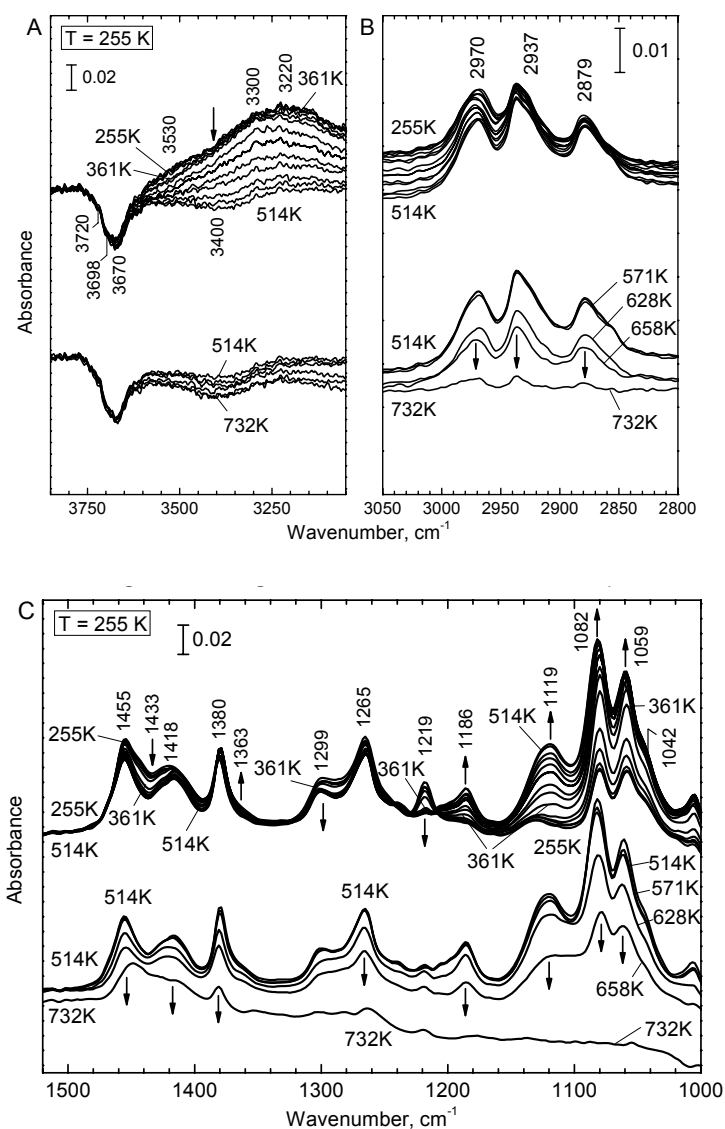


Figure 52: Difference IR spectra for 2-CEES/TiO₂ (rutile) during heating from 255 to 732 K.

Spectral Development in the Carbonyl and Carboxylate/Carbonate Spectral Regions-

Anatase and Rutile

As may be seen in Figure 53, small changes occur in the carbonyl region of the infrared spectrum as 2-CEES decomposes on both anatase- and rutile-TiO₂. For anatase (Figure 53 A), at about 378 K, a mixture of carbonyl modes at $\sim 1710\text{ cm}^{-1}$ and $\sim 1670\text{ cm}^{-1}$ are weakly observed.

On heating to 571 K, an increase in the spectral intensity throughout the region from $\sim 1730\text{ cm}^{-1}$ to $\sim 1650\text{ cm}^{-1}$ is observed. From 571 K to 732 K, carbonyl intensity decreases.

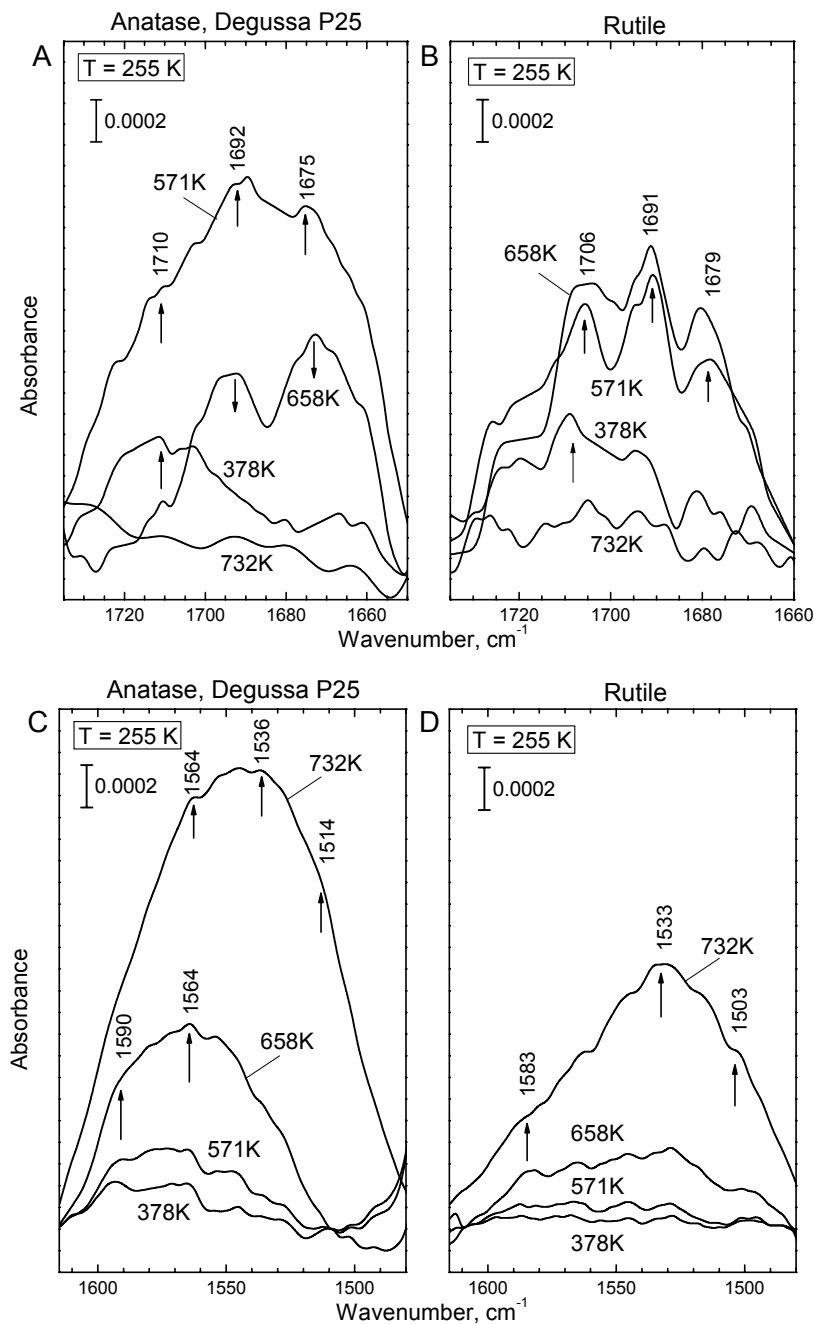


Figure 53: Difference IR spectra for carbonyl, carboxylate, and carbonate species formed during heating of 2-CEES/TiO₂ anatase and rutile powders.

For rutile (Figure 53 B), similar spectral developments are seen, with three carbonyl modes being resolved at the maximum carbonyl absorbance achieved by heating to 571-658 K. In the spectral region of carboxylate and carbonate absorbance, it is seen that the intensity of a broad infrared band increases monotonically up to 732 K for both anatase (Figure 53 C) and rutile (Figure 53 D). Thus we may say for both anatase and rutile-TiO₂ that carbonyl-containing surface species are produced by reaction of 2-CEES with TiO₂, and that these species are then further oxidized to carboxyl/carbonate species at the highest temperatures. These observations serve to strengthen the argument that oxygen-containing organic species are produced when 2-CEES thermally decomposes on TiO₂, and that lattice oxygen, from Ti-OH and also from TiO₂ participates in the oxidation process.

9.4. Discussion

The progression of the stages of oxidation of the 2-CEES molecule can be visualized from the combination of the mass spectrometric studies of the desorption of the molecule and some of its decomposition/oxidation products and the infrared studies of the species which are produced on the surface.

9.4.1. Molecular Desorption of 2-CEES

The thermal desorption studies shown in Figure 47 clearly show that 2-CEES desorption, occurring with an activation energy of $\sim 105 \text{ kJ mol}^{-1}$, is complete by about 400 K from a TiO₂(110) surface which has been reduced to produce oxygen anion vacancy sites and cationic sites which may be described as Ti³⁺ sites in the surface and the bulk. Auger studies indicate (Figure 48) that species containing S, Cl and C remain on the surface as a result of decomposition of a fairly large fraction of the monolayer of 2-CEES adsorbed. These

decomposition products are removed by heating to 900 K, and the adsorptive capacity of the TiO₂ is restored for 2-CEES.

9.4.2. Reaction of 2-CEES with TiO₂

Infrared investigations, shown in Figure 50 – Figure 53, performed on both anatase and rutile high area TiO₂ powders, are very revealing in showing in a general manner the functionalities which are consumed and produced when chemisorbed 2-CEES on TiO₂ is heated in vacuum.

The infrared studies have used TiO₂ which contains isolated Ti-OH groups at fairly low coverage. In agreement with previous work, some 2-CEES molecules are hydrogen bonded to these Ti-OH groups¹⁶⁷, while other 2-CEES molecules probably are chemisorbed on TiO₂ surface sites which do not possess Ti-OH groups.

At temperatures near 361 K, Ti-OH groups hydrogen bonded to 2-CEES molecules are irreversibly consumed as oxidation of 2-CEES begins to occur. It is likely that O moieties, present in the Ti-OH groups are most reactive toward 2-CEES. In the temperature range from ~ 361 K to ~ 541 K, CH₃CH₂O-Ti and ClCH₂CH₂O-Ti species are produced as C-S bonds in the 2-CEES molecule are broken. Near 550 K, processes involving the liberation of C₂H₆, C₂H₄, HCl and ClCH₂CH₃ are observed with the mass spectrometer as these decomposition products are evolved from TiO₂(110). At the same temperature, the CH₃CH₂O-Ti and ClCH₂CH₂O-Ti species begin to decompose, and carbonyl and carboxylate/carbonate species begin to form. By about 732 K almost all C-O bonds and C-H bonds have been broken and infrared modes corresponding to these bonds are almost completely removed from the spectrum.

Since no oxygen from the gas phase is present in these experiments, it must be lattice oxygen in the TiO₂ which participates in the 2-CEES stepwise oxidation. Based on the infrared

evidence, Ti-OH oxygen is most active, but OH groups cannot be involved in all of the oxidation pathways since the TiO₂(110) crystal surface, which is highly reactive in causing 2-CEES oxidative degradation, does not contain Ti-OH groups.

Wu et al.¹⁶⁴ have found that the surface hydroxyl groups of TiO₂ (Degussa P25) enhance the thermal decomposition of C₂H₅I molecule (previously hydrogen bonded to the OH-groups) to produce surface C₂H₅O_(a) ethoxy species at temperatures below 470 K in vacuum. Farfan-Arribas and Madix¹⁷⁶ have established that the defective TiO₂(110) surface is capable of strong adsorption of aliphatic alcohols at room temperature producing alkoxide and hydroxide groups. The alkoxide groups bound in a bridging oxygen vacancy (R-O_(b)) underwent reactions to produce the corresponding aldehydes, alkenes, and alcohols at temperatures above 550 K. On this basis, it is likely that ethoxy and chloroethoxy groups are also stabilized on TiO₂ when C-S bonds break in the 2-CEES molecule.

Figure 54 a is a summary of the thermal processes observed by mass spectrometric observation of desorption products from TiO₂(110) containing 1 ML of 2-CEES, and from the infrared measurements on anatase and rutile high area substrates. The temperature ranges for desorption and for formation and consumption of surface intermediates is schematically shown, along with the measurement of the peak absorbance at 2966 cm⁻¹ which is a general measure of the coverage of alkyl groups of all types on the surface. We find that ethoxy-species formation begins below 300 K, and that ethoxy species decomposition begins at about 570 K and that COO and CO₃ formation begins at about the same temperature.

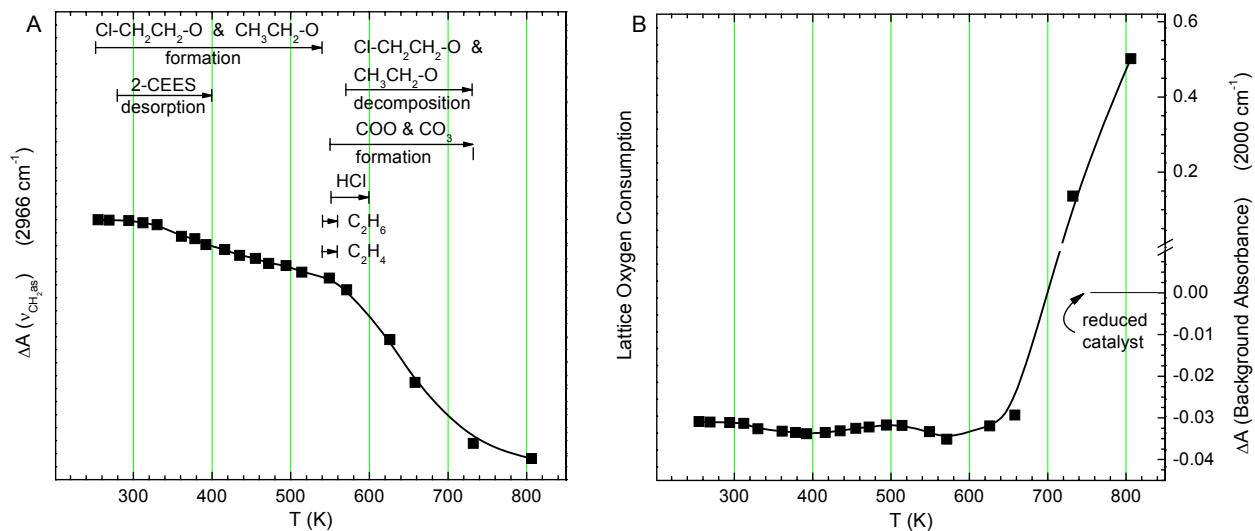


Figure 54: Schematic of the thermal processes observed and the formation of products upon heating of 2-CEES on $TiO_2(110)$ and TiO_2 anatase and rutile powders in vacuum.

A very interesting measurement of the shift of the background in the infrared measurements is shown in Figure 54 B, where the background was measured (at 2000 cm^{-1}) where interfering vibrational modes from surface species are not present. This background intensity is caused by the formation of electron traps near the conduction band edge by the loss of lattice oxygen, and the effect has been well studied by others^{86,177-179} as well as by ourselves^{180,181}. The traps may be thought of as Ti^{3+} centers formed upon loss of lattice O. Excitation of trapped electrons from these centers into the conduction band results in infrared absorption over a broad spectral range as infrared-induced electronic transitions occur to a continuum of conduction band electronic states. For the purposes of this paper, the changes in the absorbance of the infrared background may be used to monitor the consumption of lattice oxygen atoms by the formation of oxidized products from 2-CEES oxidation by TiO_2 . Figure 54 B shows that lattice oxygen begins to be consumed near $\sim 600 \text{ K}$, the temperature where ethoxy species begin to be decomposed and where COO and CO_3 species begin to be formed near $570 - 620 \text{ K}$. This is also the temperature where significant rapid consumption of surface species contributing to alkyl

absorbance at 2966 cm^{-1} begins to occur by a distinct final oxidation process, as shown in Figure 54 A.

These results suggest that TiO_2 should be an effective catalyst for thermal oxidation of the 2-CEES molecule under conditions where oxygen is resupplied to the catalyst from the gas phase, by the Mars-Van Krevlen oxidation mechanism.

9.5. Conclusions

The following results have been obtained in chemisorption studies of 2-chloroethyl ethyl sulfide on TiO_2 and the subsequent thermal oxidation using only lattice oxygen from TiO_2 .

1. 2-CEES adsorbs as a monolayer which desorbs starting at $\sim 270\text{ K}$ with an activation energy of 105 kJ mol^{-1} . Multilayers, desorbing at lower temperatures may be adsorbed on top of the monolayer.

2. A portion of the 2-CEES monolayer is oxidized by Ti-OH groups (if present on partially dehydroxylated TiO_2). In addition, lattice oxygen from TiO_2 participates in 2-CEES oxidation at temperatures above $\sim 570\text{ K}$.

3. The 2-CEES molecule produces $\text{ClCH}_2\text{CH}_2\text{-O-Ti}$ and $\text{CH}_3\text{CH}_2\text{-O-Ti}$ (ethoxy species) by bond scission of C-S bonds.

4. Ethoxy species convert to COO and CO_3 species above $\sim 550\text{ K}$.

5. By 900 K , all oxidation products are liberated and clean TiO_2 is formed in vacuum.

6. Only minor differences in the reactivity patterns of anatase- and rutile- TiO_2 is found in this work.

10. CHAPTER TEN: Photodecomposition of Adsorbed 2-Chloro Ethyl Ethyl Sulfide on TiO₂: Involvement of Lattice Oxygen⁺

Abstract

The photodecomposition of chemisorbed 2-chloroethyl ethyl sulfide (2-CEES) on the TiO₂ surface was investigated using several experimental methods involving both a rutile TiO₂(110) surface and powdered P-25 Degussa TiO₂. It is found that photo-oxidation of 2-CEES occurs in the absence of gas phase oxygen. The oxygen for this process is supplied by the TiO₂ lattice. For UV irradiation in the range 3.0 eV-5.0 eV, two simultaneous photodecomposition pathways are measured, one fast process with a measured cross section of $7.4 \times 10^{-19} \text{ cm}^2$ and one slow process with a measured cross section of $5.4 \times 10^{-20} \text{ cm}^2$. These two photodecomposition pathways probably involve different modes of binding of the 2-CEES molecule to sites on the TiO₂(110) surface. Aldehydic adsorbed products are observed to be produced by UV-irradiation and are measured by surface-sensitive IR spectroscopy. In addition, adsorbed carboxylates and carbonates are also produced. GC-MS studies of the gas phase photodecomposition products produced in the absence of O₂ also indicate the production of similar oxygenated products upon UV irradiation of 2-CEES over TiO₂ powder, as well as many products characteristic of free radical initiated processes on the TiO₂ surface. We postulate that free radical species, produced from the 2-CEES molecules by electron or hole attack, are able, in a sequence of reactions, to extract lattice oxygen from the TiO₂ photocatalyst surface.

⁺ Reproduced in part with permission from Tracy L. Thompson, Dimitar A. Panayotov, John T. Yates, Jr. Igor Martyanov and Kenneth Klabunde "Photodecomposition of Adsorbed 2-Chloroethyl Ethyl Sulfide on TiO₂: Involvement of Lattice Oxygen" *Journal of Physical Chemistry B*, **108** (2004) 17857-17865. Copyright 2004 American Chemical Society.

10.1. Introduction

The level of interest in the study of photocatalysis over metal oxide materials, specifically titanium dioxide, has grown significantly over recent years, sparked by the use of these materials for environmental cleanup. Materials like titanium dioxide are generally inexpensive, non-toxic and renewable as catalysts, and for these reasons, are becoming more widespread in their range of applications^{56,182}. Titanium dioxide shows promise in this area using sunlight for activation, and has been shown to photo-oxidize a number of pollutants effectively^{162,183}.

Traditionally, the study of photocatalysis over titanium dioxide involves either co-adsorption of molecular oxygen with an adsorbed molecule, or photocatalysis is done under a partial pressure of oxygen. In these instances, molecular oxygen is thought of as an active electron scavenger which effectively accepts electrons available at the surface when the oxide is reduced via thermal treatment, or by electron-hole pair creation with UV light²³. In the results presented here, we look specifically at the interaction of UV radiation with an adsorbed organic molecule (2-chloroethyl ethyl sulfide, 2-CEES) in the *absence* of gas phase or adsorbed molecular oxygen. The UV activated surface alone activates the organic molecule, causing it to dissociate. It has been reported that photocatalytic decomposition of acetic^{184,185} and formic¹⁸⁶ acids, and CH_2Cl_2 ¹⁶⁵ in the absence of gas phase O_2 can proceed on the TiO_2 surface under low-intensity UV light exposure, utilizing lattice oxygen as a reactant. In addition, CH_3CN photochemistry on TiO_2 has been shown to produce adsorbed NCO species¹⁸⁷.

The 2-CEES molecule chosen for this work is regularly used as a simulant for the chemical agent, mustard gas. The 2-CEES molecule differs from the actual chemical agent in that it carries only one chlorine atom, compared to the dichloride species which is mustard gas. A relatively small amount of research has been done regarding the interaction of this molecule with

surfaces. The photo-oxidation of 2-CEES over titanium dioxide or mixed $\text{TiO}_2\text{-SiO}_2$ has been investigated recently^{188,189}.

Panayotov et al. have recently studied the adsorption as well as photooxidation of 2-CEES on mixed $\text{TiO}_2\text{-SiO}_2$ powders^{167,189}. The 2-CEES binds via hydrogen bonding through both the chlorine moiety as well as the sulfur atom in the molecule to surface Si-OH groups in the $\text{TiO}_2\text{-SiO}_2$ mixed oxide. Similar surface bonding to Ti-OH groups is observed for TiO_2 surfaces¹⁶⁷. In addition, the photo-oxidation capabilities (involving $\text{O}_2(\text{g})$) of the mixed oxide catalyst towards 2-CEES as well as diethyl sulfide (DES) are reported¹⁸⁹. For both 2-CEES and DES in the presence of oxygen and UV light, a combination of partially oxidized and fully oxidized products was found on the surface. Martanyov and Klabunde also report clear evidence for a photooxidation reaction of 2-CEES in the presence of oxygen gas and propose a mechanism for photo-oxidation which involves the presence of the surface hydroxyl radical¹⁸⁸. Vorontsov et al. has also suggested possible routes for the photooxidation of a similar molecule (DES)^{175,190}.

The results presented hereafter are from a combined study utilizing ultra-high vacuum techniques where experiments are conducted with an atomically-clean single crystal $\text{TiO}_2(110)$ sample, as well as high vacuum conditions where polycrystalline TiO_2 powder is probed using transmission infrared spectroscopy and GC-MS chemical analysis. The use of a single crystal under well defined UHV conditions allows for very accurate control of adsorbate exposures, as well as complete control of the surface preparation. For studies on structurally undefined TiO_2 surfaces, infrared spectroscopy and GC-MS product analysis from powdered TiO_2 give chemical insight into the bond-breaking and bond-formation steps associated with the photochemistry.

10.2. Experimental

The experimental results presented in this manuscript were carried out in three separate apparatuses. Ultrahigh vacuum studies of a TiO₂(110) crystal have been combined with transmission IR studies and GC-MS product analysis studies of TiO₂ powder.

10.2.1. Ultra High Vacuum Study of 2-CEES on TiO₂(110)

Experiments involving the photodepletion of 2-chloroethyl ethyl sulfide over TiO₂(110) were carried out in a stainless steel ultra high vacuum (UHV) chamber described in Chapter Two of this thesis.

For photochemical measurements on TiO₂(110) single crystals, the full arc of the lamp was used in order to obtain maximum power for these experiments. The measured power in the photon energy range 3.0 eV – 5.0 eV during the experiment was 63 mW cm⁻². The “low” light power setting, obtained by adjusting the condensing lens on the lamp, allowed for a power density of 10.7 mW cm⁻². The total photon flux is measured during each light exposure by reflecting 9.6 % of the light beam directly to a power meter (Thorlabs, model D10MM). Power densities obtained from this power meter were cross checked against a thermopile (Oriel, Model 71751) and were found to be within 10% of one another. In order to obtain the approximate photon flux incident on the crystal surface, the average wavelength of the complete lamp irradiance profile was estimated by integration of the lamp profile versus wavelength for energies greater than the bandgap of TiO₂ in the range from 3.0 eV to 5.0 eV. This corresponds to an approximate photon flux for the high power setting of 1.02×10^{17} photons cm⁻² s⁻¹ and 1.73×10^{16} photons cm⁻² s⁻¹ for the low power setting.

2-CEES (98%) used in both the UHV and Transmission IR studies was obtained from Sigma-Aldrich and further purified via several freeze-pump-thaw cycles. Exposures of 2-CEES to the TiO₂(110) surface was done via backfilling the UHV chamber to pressures of 4×10^{-8}

mbar for various times. When calculating the overall exposure of 2-CEES to the crystal surface, both the ion gauge sensitivity as well as the contribution of the partial pressure of 2-CEES measured after ending gas admission were considered. The ion gauge sensitivity for 2-CEES is not available in the literature, and therefore an average sensitivity of several similar molecules was taken¹⁹¹. The sensitivity ratio $I^+(2\text{-CEES})/I^+(\text{N}_2) = 2.6$ was employed. Thermal desorption measurements were carried out using a heating rate of 3.0 K sec^{-1} .

10.2.2. Transmission IR Studies on TiO₂ Powder

10.2.2.1. TiO₂ Powder Material

The TiO₂ powder employed for this work is the commonly studied photoactive TiO₂ material (Degussa P25). Both the IR and the GC-MS studies used this material. The P-25 TiO₂ powder¹⁷¹ is reported to be 99.5% pure TiO₂ (70% anatase and 30% rutile) having a surface area of $50 \pm 15 \text{ m}^2 \text{ g}^{-1}$. The average particle diameter by number count is 21 nm where 90% of the particles fall in the size range from 9 – 38 nm. The particles exist as aggregates which are approximately 0.1 mm in diameter¹⁶². For the IR studies, the TiO₂ sample is hydraulically pressed into the tungsten grid as a circular spot 7 mm in diameter, typically weighing 4 - 4.5 mg ($10.4 - 11.7 \text{ mg cm}^{-2}$). The samples and the grid support assembly are then placed into the dual beam IR-UV photoreactor and evacuated.

10.2.2.2. High Vacuum System and UV Photoreactor for IR Studies

The details of the experimental setup and photoreactor used for the gas-phase photodegradation of 2-CEES on powder TiO₂-based materials have been published elsewhere¹⁹². The experimental setup consists of four main units: (i) high vacuum system with gas-vapor-

delivery module; (ii) dual beam IR-UV photoreactor; (iii) transmission FTIR spectrometer; and (iv) 350W Hg arc lamp as an ultraviolet light source.

The stainless steel vacuum system is pumped simultaneously with a Pfeiffer Vacuum 60 L/s turbomolecular pump and a Varian 20 L/s ion pump. The base pressure reached after 24 h baking of system while pumping with both pumps is $\sim 10^{-8}$ Torr, as measured by the ionization gauge. The pressure of reactant gases and vapors was measured with a MKS capacitance manometer (Baratron, type 116A, range 10^{-3} - 10^3 Torr).

The dual beam IR-UV photoreactor used in these experiments has been described previously¹⁹². The stainless steel photoreactor is capable of working under a wide range of pressures (10^{-8} to ~ 1000 mbar) and temperatures (100 to 1500 K)¹⁹³. The powdered TiO₂ sample is pressed hydraulically at 12000 lbs in⁻² into the openings of a flat tungsten grid¹⁶⁹ (0.0508 mm thick, with 0.22 mm² square holes, obtained from Buckbee-Mears, St. Paul, MN). The grid is held rigidly to a power/thermocouple feedthrough via a pair of nickel clamps and is oriented at a 45° angle to both the IR and the UV beams. The sample temperature is measured using a type-K thermocouple spot-welded to the top-center region of the grid. The sample is uniformly heated using the electrical resistance of the tungsten grid. The power leads and the type-K thermocouple leads pass through a re-entrant Dewar and are connected to a power supply controlled by a Honeywell digital controller. Two different cooling agents (liquid N₂ or a mixture of dry ice + acetone) were used to fill the Dewar and cool the sample. The dry ice + acetone mixture was utilized in the experiments carried out at 255 K. The accuracy of the temperature control was ± 1 K. The central, middle and the lower positions on the tungsten grid are used as sample spots. The TiO₂ sample pressed onto the lower spot serves as a direct measure of the reproducibility between experiments. The upper position on the grid is empty and is used for the background

absorbance measurements in the same experiment. Different positions on the same grid can be aligned to the IR beam using a computer-controlled translation system¹⁶⁸ (Newport Corporation) with $\pm 1 \mu\text{m}$ accuracy in both the horizontal and vertical directions.

Infrared spectra were obtained with a nitrogen-gas purged Mattson Fourier transform infrared spectrometer (Research Series I) equipped with a liquid N_2 cooled HgCdTe detector. All scans in the infrared region from 4000 to 500 cm^{-1} were made in the ratio mode at a resolution of 4 cm^{-1} . Typically, 2000 scans were accumulated in each spectrum to ensure measurement of low absorbance bands with high signal-to-noise ratio. WinFIRST software supplied by Mattson was used for setting the spectrometer and for spectra acquisition.

The UV light source employed here is a high-pressure 350W Hg arc (Oriel Corp.) lamp similar to that used in the single crystal work. The lamp is equipped with a water filter to remove the IR radiation. The UV light beam was focused onto the sample through a sapphire window. The intensity of the UV radiation on the sample was 370 mW cm^{-2} in the energy range of 3.0 eV-5.0 eV.

10.2.2.3. TiO_2 Activation; 2-CEES Adsorption and Photodecomposition Experiments

Consecutive oxidation and thermal reduction procedures are applied for initial activation of a fresh TiO_2 sample. The TiO_2 sample was heated in vacuum to the desired pretreatment temperature, 675 K, at a rate of 20 K min^{-1} , and then treated in vacuum at this temperature for 4 h followed by cooling to room temperature. Oxygen gas at 8.2 mbar was introduced into the cell and the temperature was raised again to 675 K at the same rate. After 1 h of oxidation, the sample was cooled to room temperature and O_2 was evacuated. At this point, the reference spectra for the oxidized sample were acquired. After that, the sample was reduced in vacuum at 822 K for 3 h then cooled to room temperature and the reference spectra for the thermally

reduced sample were taken. The powdered TiO₂ samples, annealed in vacuum at 822 K, retain some isolated Ti-OH groups which are useful in binding 2-CEES to the surface, as shown previously¹⁶⁷. The reference IR spectra for oxidized and thermally reduced samples were acquired at room temperature.

The photodecomposition of adsorbed 2-CEES was implemented after exposure to 0.20 mbar 2-CEES at 255 K.

10.2.3. GC-MS Studies on TiO₂ Powder

Quantitative analysis of the products forming on the surface of TiO₂ Degussa P25 was carried out as follows. First, ca. 200 μL of the suspension of TiO₂ in acetone (40 g L⁻¹) was deposited on the wall of a quartz cell equipped with a high vacuum valve. After drying at 323 K in air, the traces of organics on the surface of TiO₂ were burned off in air with a full arc of a 1000W Hg(Xe) lamp. Later ca. 20 μL of 2-CEES was added and frozen by immersing the cell in liquid nitrogen followed by evacuation to 10⁻⁴ mbar. Three freeze-pump-thaw cycles were employed to ensure thorough deoxygenation. Following this purification, the cell was sealed and transferred to conduct the photoreaction in the absence of O₂.

A 1000W Hg(Xe) lamp (Oriel) was used to carry out the photoprocess. Before reaching the sample, the light was passed through a water filter and a set of color filters (#57396, 59062 from Oriel) to eliminate IR radiation. The intensity of the light was ~ 70 mW cm⁻² with the UV spectral range being 3.1 eV - 4.0 eV.

After 60 minutes, the illumination was interrupted. The gas in the cell was equilibrated with one atmosphere of argon gas. Identification of reaction products was carried out using a GC-MS (QP5000 from Shimadzu) equipped with a capillary column (XTI-5, Rastek Corp.). During the analysis, the temperature of the column was programmed (1 minute at 313 K; ramp to

593 K at 40 K/min; and 4 minutes at 593 K). Nonvolatile products were extracted from the surface of the TiO₂ powder with liquid acetonitrile and analyzed in a similar way but with an appropriate cut-off time. To enhance thermal stability and volatility of some of the products in the extract, initial derivatization was done at 323 K for 60 minutes with a mixture of bis(trimethylsilyl)trifluoroacetamide with trimethylchlorosilane (BSTFA/TMCS, 99:1, Supelco) and then identified through a similar analytical approach in a separate set of experiments.

10.3. Results

10.3.1. Single Crystalline TiO₂

10.3.1.1. Thermal Desorption of 2-CEES from TiO₂(110)

The thermal chemistry of 2-CEES adsorbed on TiO₂(110) is thoroughly discussed elsewhere⁵³. Briefly, in adsorption experiments beginning at 110 K, it was found that 2-CEES thermally decomposes during the thermal desorption of the parent 2-CEES molecule in the temperature range from 110 K to 800 K. Auger analysis of the surface after the thermal desorption of the parent 2-CEES molecule by heating to a temperature of 500 K shows that the surface is contaminated with S, Cl and C. From these results, we estimate that approximately 20% of the initial coverage of 2-CEES is thermally decomposed upon heating to 500 K⁵³.

10.3.1.2. Photodecomposition of 2-CEES on TiO₂(110) in Vacuum

Figure 55 shows the result of the exposure of UV light to the adsorbed 2-CEES/TiO₂(110) system. For these experiments an initial coverage of 0.5 ML was used. After adsorption of 2-CEES at 110K, the crystal was exposed to full arc irradiation ($63 \text{ mW cm}^{-2} = 1.02 \times 10^{17} \text{ photons cm}^{-2} \text{ s}^{-1}$) for a certain time period, followed by temperature programmed desorption (TPD) to monitor the change in the amount of adsorbed 2-CEES due to

photodecomposition. The major mass spectrometer cracking product of the 2-CEES molecule at 75 amu was monitored. Experiments were also done using a lower light power setting ($10.7 \text{ mW cm}^{-2} = 1.73 \times 10^{16} \text{ photons cm}^{-2} \text{ s}^{-1}$) in order to more accurately measure the photodecomposition effect at lower light fluences. During UV exposure, the crystal temperature increased no more than 5K. The inset to Figure 55 shows an example of the actual TPD data where there is evidence of a large decrease in the amount of remaining 2-CEES after 60 seconds ($6.1 \times 10^{18} \text{ photons cm}^{-2}$) of exposure to UV light as compared to measurements made on the non-irradiated surface. For increasing UV exposure times, the amount of adsorbed 2-CEES decreased monotonically. The decrease in 2-CEES coverage was fit to a double exponential decay rate as shown in Figure 55. Total cross sections for both the fast and slow photodecomposition process were measured to be $Q_{\text{fast}} = 7.4 \times 10^{-19} \text{ cm}^2$ and $Q_{\text{slow}} = 5.4 \times 10^{-20} \text{ cm}^2$ and the fitted curve corresponds to these two parallel processes. Upon completion of thermal desorption to 900 K, the surface became clean and its ability to adsorb 2-CEES was fully restored.

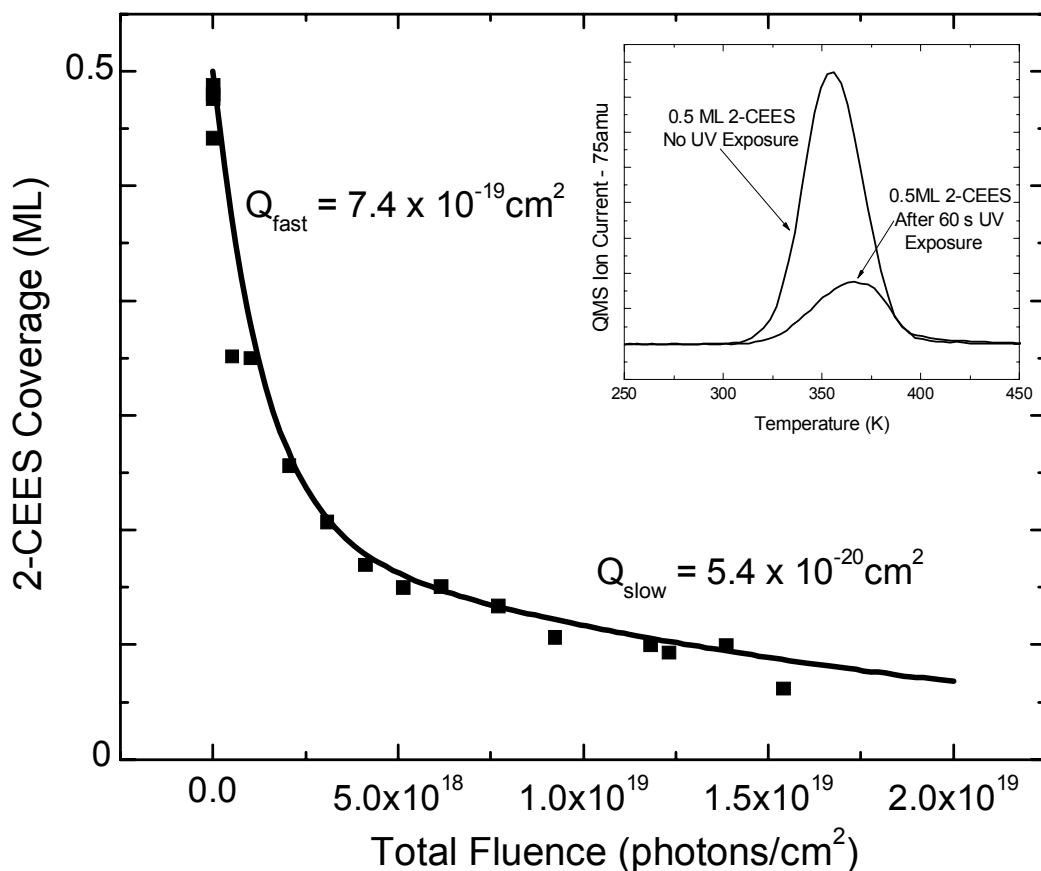


Figure 55: Measurement of the decrease in the TPD peak area of adsorbed 2-CEES with increasing photon fluence. Fitting of the experimental data shows two simultaneous processes which occur, each with a different cross section.

The measurements of the two photodecomposition cross sections for 2-CEES are confounded by a small thermal decomposition process which occurs during the TPD measurement. The 20% thermal decomposition that occurs during each measurement has a direct effect on the measured coverage¹⁹⁴. However, this effect does not influence our evaluation of the magnitude of the total measured cross sections for the photo-induced decomposition of 2-CEES in the two processes found in this work.

In order to ensure that the 2-CEES molecule was in fact decomposed, and not just photo-desorbed, an experiment was done by monitoring mass 75 during the initial exposure to UV using direct line-of-sight sampling by the mass spectrometer. Results of that experiment are shown in Figure 56a where there is no photodesorption signal detected above the noise level. Figure 56b shows the expected photodesorption signal for 0.03 monolayers of 2-CEES. The assumed photodesorption cross section for this simulation is $7.4 \times 10^{-19} \text{ cm}^2$, consistent with the measurements in Figure 55. The comparison of Figure 56a and Figure 56b clearly show that much less than 0.03 ML photodesorption of the 2-CEES molecule occurs. We therefore conclude that the photodepletion effect is indeed due almost exclusively to UV-induced photodecomposition of the 2-CEES molecule.

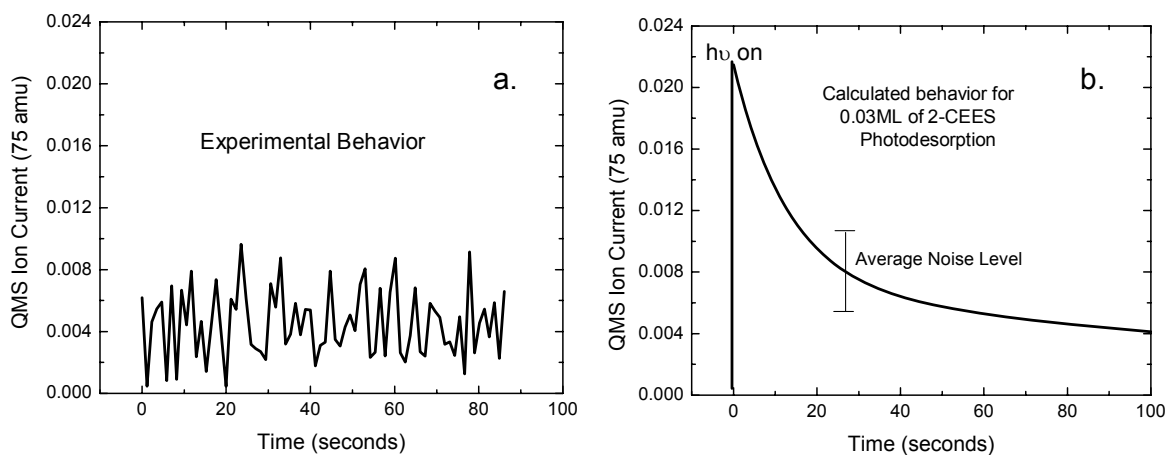


Figure 56: a) Measurement of the lack of observed photodesorption of the parent 2-CEES molecule. b) Simulated curve for the expected photodesorption of 2-CEES. The simulation intensity is for the desorption of 0.03 ML of 2-CEES, corresponding to a photodesorption cross section of $4.4 \times 10^{-20} \text{ cm}^2$.

10.3.2. Powdered TiO₂ Results-IR Spectroscopy

10.3.2.1. Adsorption of 2-CEES on TiO₂ Powder

The adsorption of 2-CEES on TiO₂ Degussa P25 powder is discussed elsewhere¹⁹⁴. Briefly, it was found that adsorption of 2-CEES on high area anatase powder at 255 K produces IR absorption bands in the regions of both the stretching (3000 – 2700 cm⁻¹) and the deformation (1500 – 1000 cm⁻¹) modes which are characteristic of the adsorbed molecule. In addition, all types of isolated Ti-OH groups^{110,194-196} interact via hydrogen bonding with the adsorbed 2-CEES molecule¹⁹⁴. The loss of isolated Ti-OH groups during 2-CEES adsorption is accompanied by the production of a number of types of associated Ti-OH groups which exhibit lower OH stretching frequencies. The hydrogen bonding of 2-CEES to Ti-OH groups keeps the molecule strongly bonded to the TiO₂ surface and it is not desorbed at 255 K under dynamic high vacuum conditions, as reported previously¹⁹⁴. It is likely that 2-CEES also bonds to other sites on the partially-dehydroxylated TiO₂ surface studied here, as found on the TiO₂ single crystal.

10.3.2.2. IR Measurements of 2-CEES Photodecomposition on TiO₂ Powder

Illumination of 2-CEES-covered TiO₂-powder with polychromatic UV light (3.0 eV – 5.0 eV, P = 370 mW cm⁻²) at 255 K in vacuum causes a pronounced increase in the background IR absorbance of the TiO₂ over the entire region from 3000 to 1000 cm⁻¹. Subtraction of the spectrum before the beginning of irradiation from the excited state spectrum produces a structureless broad IR background absorption which increases with time of UV illumination. Selected background spectra measured as a function of the UV exposure time for the 2-CEES/TiO₂-powder system are presented in Figure 57. This physical phenomenon, absorption of light due to mobile charge carriers, was first observed for silicon^{197,198} and germanium^{199,200}.

Theories on the transport process for conduction electrons have also been developed²⁰¹⁻²⁰³. The change in the background IR absorption is caused by the formation of electron traps and their filling by electrons near the conduction band edge due to the loss of lattice oxygen. This effect has been well studied by others^{85,86,177-179,204,205} as well as by ourselves^{180,181,194}. A broad and structureless IR absorption has also been reported for TiO₂ after UV excitation and is assigned to continuous charge carrier transitions into the conduction band specific to semiconductors^{85,86,177,178}. The signal growth with a $\sim \nu^{-1.5}$ law is usually observed for electronic interband transitions, where acoustic phonons provide the required momentum¹⁴⁵. We have recently reported that during continuous UV irradiation of TiO₂ powder in the mW cm⁻² range, photogenerated electrons are either trapped at localized sites giving paramagnetic Ti³⁺ centers, or are excited to the conduction band, giving EPR-silent conduction band electrons which may be observed by their structureless IR absorption⁵⁹ as seen in Figure 57. The EPR measurements show that under high vacuum conditions, the majority of photoexcited electrons enter the conduction band⁵⁹.

Background Spectral Changes due to Lattice Oxygen Loss during 2-CEES Photodecomposition on TiO₂

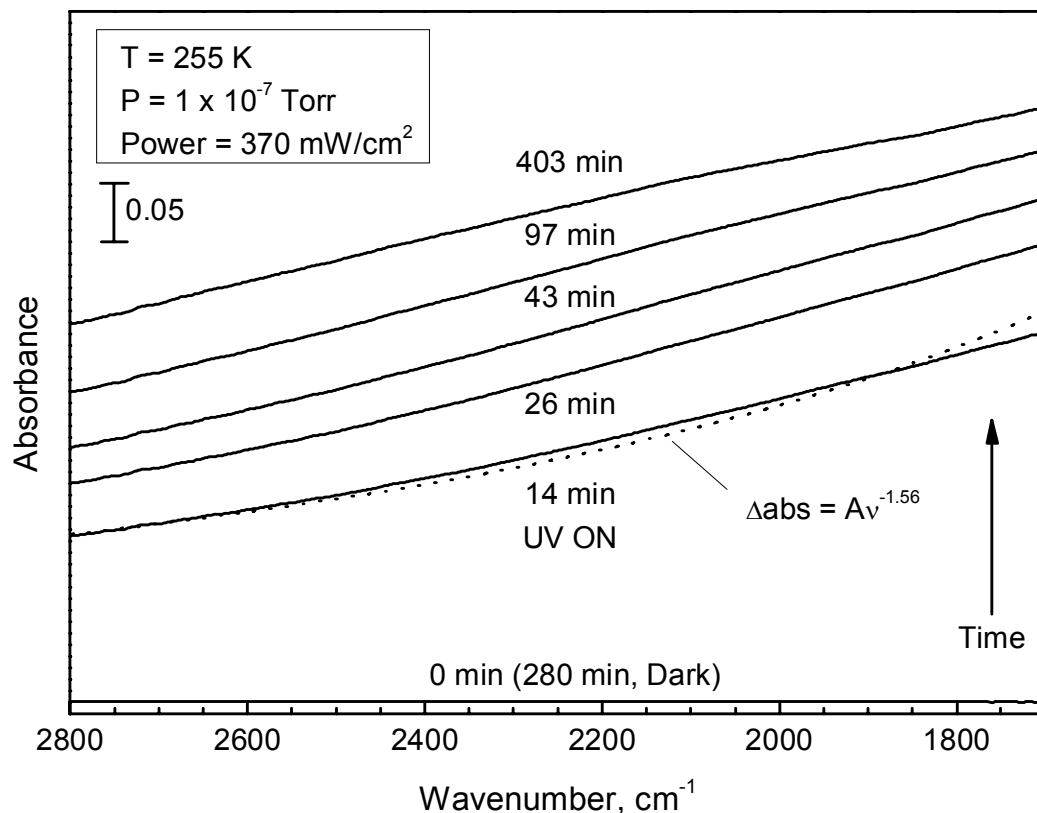


Figure 57: Change in the IR absorbance due to the loss of lattice oxygen as a function of UV exposure during 2-CEES decomposition. The depicted increase in the background IR absorbance signifies the presence of mobile electrons in the conduction band as a result of UV excitation.

Thus, the increase in the background absorbance during UV irradiation of TiO₂ covered by adsorbed 2-CEES (as shown in Figure 57) can be attributed to loss of lattice oxygen and to the concomitant photoexcitation of electrons into the trap sites produced near the conduction band edge.

10.3.2.3. Photodecomposition of 2-CEES on TiO₂ Powder in Vacuum

Figure 58 shows the kinetics of absorbance change due to alkyl group depletion as a result of the exposure to UV light of the 2-CEES /TiO₂-powder system. During UV exposure, the sample temperature was controlled and did not exceed 255 K. The total photodecomposition of 2-CEES, estimated on the basis of the integrated alkyl absorbance within the range 3010 – 2820 cm⁻¹, was about 5 % of the initial 2-CEES coverage.

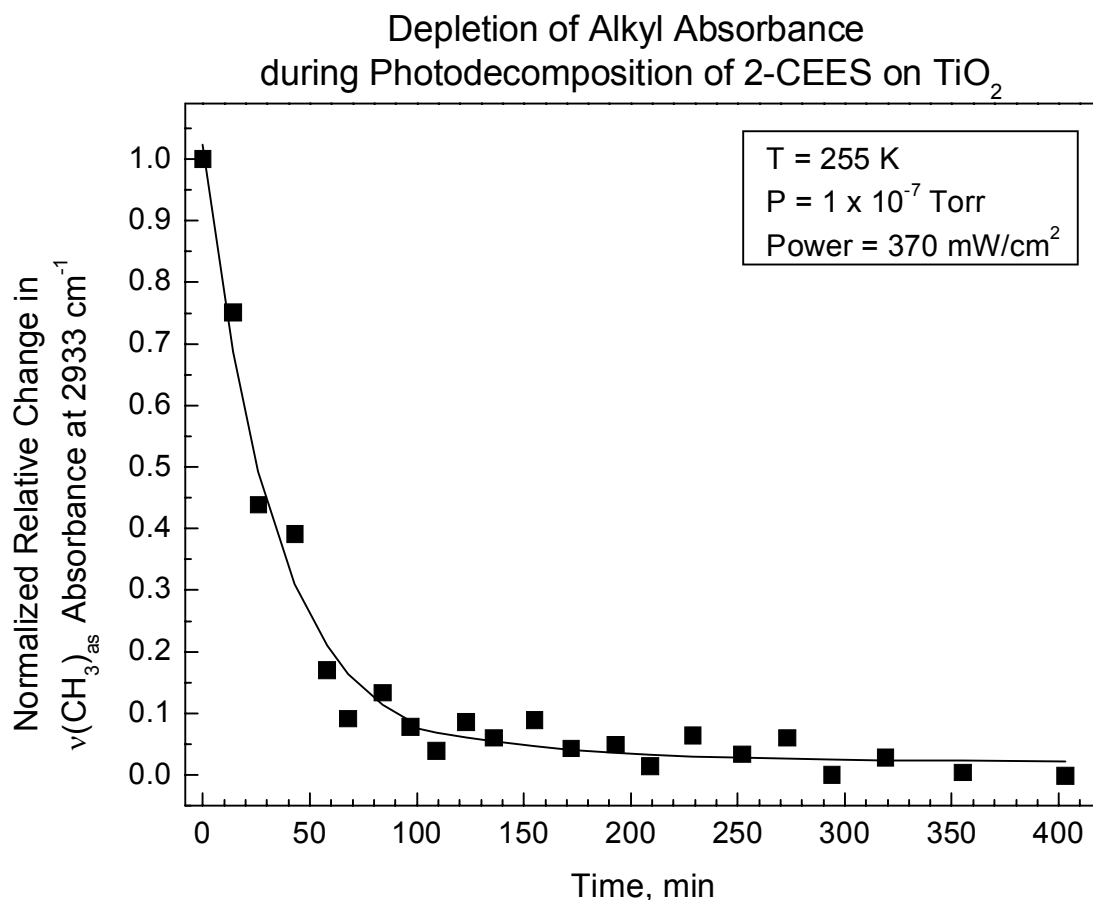


Figure 58: Loss of alkyl absorbance with increasing UV exposure measured by IR spectroscopy during 2-CEES photodecomposition.

10.3.2.4. Formation of Oxidized Products During Photodecomposition of 2-CEES

The formation of oxidized products and their hydrogen bonding to surface Ti-OH groups is observed during UV-exposure of 2-CEES on TiO₂ powder in vacuum as shown in Figure 59.

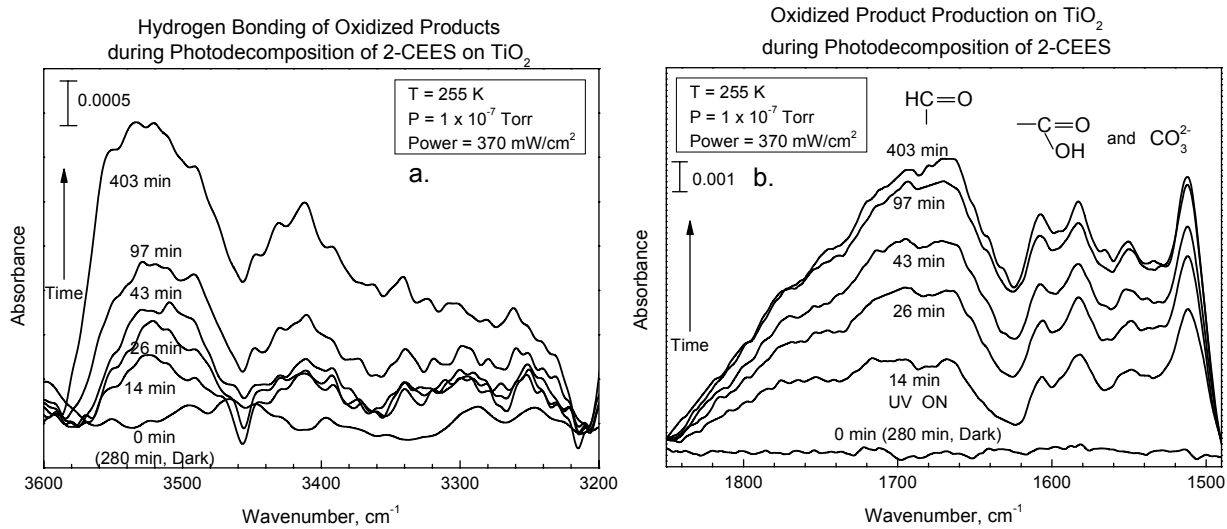


Figure 59: Formation of hydrogen-bonded and oxygen-containing products with increasing UV exposure during 2-CEES photodecomposition.

The difference spectra in Figure 59a and Figure 59b show the growth of IR features due to (a) associated Ti-OH groups; and (b) carbonyl stretching modes respectively. The broad IR absorption band centered at 1680 cm^{-1} (Figure 59b) is attributed to various carbonyl stretching modes due to aldehyde species, while the IR features below 1620 cm^{-1} are due to various carboxylate and carbonate species. As the oxidized products are formed, they are hydrogen bonded to surface Ti-OH groups that produce the broad IR absorption in the region from 3600 to 3200 cm^{-1} (Figure 59a) where hydroxyl groups associated with oxidation products are reported to absorb^{110,194,195}. The changes in the spectrum of adsorbed 2-CEES reveal the photodissociation process of the parent 2-CEES molecule. Analogous spectral changes to those presented in Figure 59 have recently been reported for the photocatalytic oxidation of 2-CEES in the presence of O_2 on $\text{TiO}_2\text{-SiO}_2$ powder¹⁸⁹. Aldehydes are the primary gas products for 2-CEES¹⁸⁸ and DES¹⁹⁰ photocatalytic oxidation in the presence of $\text{O}_2(\text{g})$ on TiO_2 powder. As our photoillumination experiments with 2-CEES/ TiO_2 -powder system are performed under high vacuum conditions at a base pressure of 1×10^{-7} Torr, i.e. in absence of gas phase oxygen, oxidized products can be

produced only at the expense of the TiO_2 lattice oxygen. The removal of lattice oxygen due to supra-bandgap photoexcitation of the TiO_2 powder containing chemisorbed 2-CEES is detected indirectly by the changes in the background IR absorption of the catalyst sample as shown in Figure 57. Therefore, the oxidative photodegradation of 2-CEES adsorbed on TiO_2 involves the lattice oxygen of TiO_2 .

10.3.2.5. Selected Kinetics Results for 2-CEES Photodecomposition Using Infrared Absorbances

Figure 60 shows the rates of photodecomposition as observed from the changes in infrared absorbances during photodecomposition of 2-CEES on TiO_2 at 255 K.

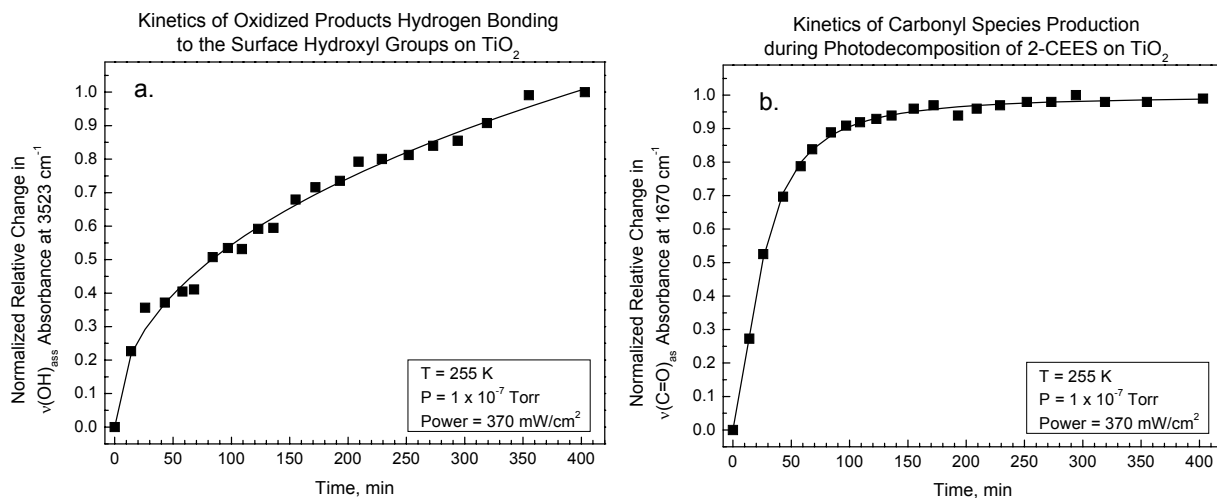


Figure 60: Measured kinetics for the formation of products as a result of UV radiation for both hydrogen bonded and other oxygenated products.

Figure 60a presents the kinetics for the growth in intensity of hydrogen bonded hydroxyls as measured by the absorbance at 3523 cm^{-1} (Figure 59a). The kinetics of aldehyde species production is shown in Figure 60b and is measured by the absorbance at 1670 cm^{-1} . A comparison of the kinetics of aldehyde species formation (Figure 60b) with that for 2-CEES

depletion (Figure 58) clearly reveals the correspondence between the two processes; as 2-CEES is photodecomposed, aldehyde species are produced with approximately the same kinetics ($\tau_{1/2} \approx 25$ min.). This correlation implies that the photodepletion of 2-CEES is directly related to the formation of aldehydes, i.e. the oxidative photodegradation of 2-CEES involving lattice oxygen is the main photocatalytic process on the TiO₂ surface. The kinetics of hydrogen-bonded species production (Figure 60a) is retarded compared to the formation of the aldehyde products, possibly because some of these products originate from subsequent oxidation steps beyond the aldehyde stage.

10.3.2.6. Absence of Reactivity after Switching from UV Illumination to Dark Conditions

The results presented in Figure 61 show that after switching off the UV source, no further spectral changes are observed for 70 min under dark conditions in vacuum. This means that no further thermal processes take place at 255 K, and thus, the photooxidation of 2-CEES by lattice oxygen is not likely to involve a thermal process at 255 K that operates in parallel with the photodecomposition process. It was also found that under dark conditions no further changes in the background IR absorption take place (not shown), i.e. the background does not relax to the state measured before UV irradiation. This implies that at 255 K in vacuum the photoexcited electrons in TiO₂ remain trapped in the conduction band (separated from holes) after discontinuation of UV illumination.

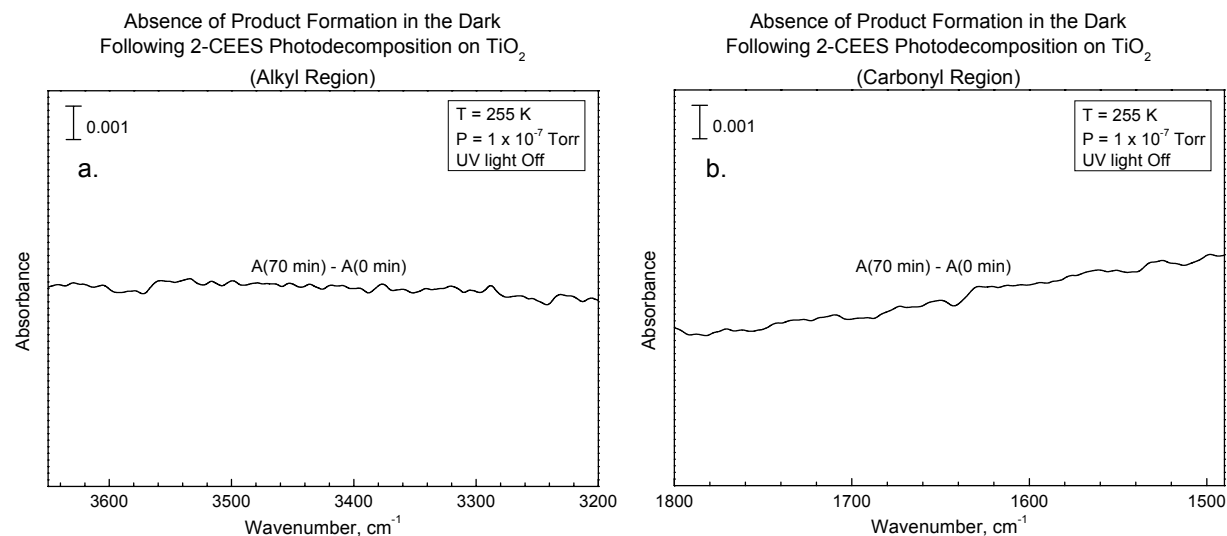


Figure 61: Absence of additional 2-CEES degradation in the dark.

10.3.3. Powdered TiO₂ Results- GC-MS Studies

In contrast to the oxidation of 2-CEES over TiO₂ in air, the illumination of the TiO₂ containing 2-CEES in an oxygen-free environment resulted in the sample's color change from white to light blue. The light blue color is characteristic of the production of slightly reduced TiO₂ as lattice oxygen depletion from the bulk occurs during photoreaction.

The set of the products detected in the gas phase and their relative amounts (measured in terms of total ion current measured by the MS detector) are given in Table 5.

Table 5: Relative Amounts of the Products of the Photoreaction of 2-CEES on TiO₂ Detected in the Gas Phase

PRODUCT		%
Hydrogen chloride	HCl	16
Carbon dioxide	CO ₂	15
Ethylene	C ₂ H ₄	10
Chloroethylene	ClCHCH ₂	1.3
Acetaldehyde	CH ₃ C(O)H	8.5
Chloroethane	ClCH ₂ CH ₃	3.7
Ethanethiol	CH ₃ CH ₂ SH	18
Dichloromethane	CH ₂ Cl ₂	12
Ethyl methyl sulfide	CH ₃ CH ₂ SCH ₃	3
1,2-Dichloroethane	ClCH ₂ CH ₂ Cl	0.4
Ethyl vinyl sulfide	CH ₃ CH ₂ SCHCH ₂	9.8

Diethyl disulfide	CH ₃ CH ₂ SSCH ₂ CH ₃	1.7
1,2-Bis(ethylthio) ethane	CH ₃ CH ₂ SCH ₂ CH ₂ SCH ₂ CH ₃	0.6

Two oxygen-containing products including acetaldehyde (CH₃C(O)H) and carbon dioxide (CO₂) were found to be formed and released in the gas phase during the photoreaction. The production of these two gas phase products correlate well with the observation by IR spectroscopy of aldehyde groups and carbonate groups formed on the TiO₂ surface (Figure 59b). Other gaseous products of the photodecomposition reaction were found to be oxygen free.

Additionally, five products were detected in the extract from the TiO₂ after the photoreaction (Table 6). Two of these five products also contain oxygen derived from the TiO₂ lattice.

Table 6: Relative Amounts of the Products of the Photoreaction of 2-CEES on TiO₂ Detected in Acetonitrile Extract

PRODUCT		%
Chloroethyl ethyl disulfide	ClCH ₂ CH ₂ SSCH ₂ CH ₃	16
1,2-Bis(ethylthio) ethane	CH ₃ CH ₂ SCH ₂ CH ₂ SCH ₂ CH ₃	55
1-[(2-chloroethyl)thio]-2-(ethylthio) ethane	ClCH ₂ CH ₂ SCH ₂ CH ₂ SCH ₂ CH ₃	28
bis[2-(ethylthio)ethyl] ether	CH ₃ CH ₂ SCH ₂ CH ₂ OCH ₂ CH ₂ SCH ₂ CH ₃	1
2-Hydroxyethyl ethyl sulfide*	CH ₃ CH ₂ SCH ₂ CH ₂ OH	—

10.4. Discussion

10.4.1. Photodecomposition of 2-CEES on TiO₂(110)

The use of an atomically clean single crystal of TiO₂ provides an opportunity to observe photoprocesses on the surface which is not covered by other chemical species. Our studies

* This compound was detected only after derivatization as 2-[trimethylsiloxy]ethyl ethyl sulfide ((CH₃)₃SiOCH₂CH₂SCH₂CH₃).

indicate that the clean TiO₂ surface exhibits a high efficiency for inducing the photodecomposition of the 2-CEES molecule. The depletion of the molecule occurs via two parallel processes exhibiting cross sections of 7.4 x 10⁻¹⁹ cm² and 5.4 x 10⁻²⁰ cm². These cross sections are in the range often observed for the photochemical destruction of molecules on metal and semiconductor surfaces^{206,207}. The photochemical destruction process is induced by electron-hole pair formation in the semiconductor and is due to the action of either photogenerated electrons or photogenerated holes. In the case of photogenerated electrons, electron attachment processes to adsorbed molecules are often observed in other surface-mediated photochemical systems^{206,208-210}, and the temporary negative ion produced then decomposes, via a reaction schematically shown in equation 10.1.



The R• species, a reactive free radical, can then participate in other chemical steps where it reacts with other RX or R• species.

A hole generated by electron-hole pair formation in TiO₂ may abstract an electron from an adsorbed species to produce a radical cation. As shown in equation 10.2, the radical cation may also undergo subsequent reaction steps.



In addition to the scission of chemical bonds in an adsorbed molecule induced indirectly by electrons or holes photo-produced in the substrate, it is also possible to induce photodesorption for certain molecules chemisorbed on TiO₂ as has been reported previously^{17,55}. Our experiments, shown in Figure 56, indicate that the photodesorption channel is non-existent or of very low cross section for the 2-CEES molecule on TiO₂. The measurements in Figure 56

suggest that if photodesorption does occur, the cross section for the process must be below $\sim 10^{-20}$ cm^2 .

The direct photoexcitation of an adsorbed molecule by absorption of a photon may also induce chemical decomposition. To evaluate the probability of a direct photochemical process, we measured the UV absorbance of a solution of 2-CEES in n-hexane. In the photon energy range from 3.2 eV to 5.0 eV, we measure an average photoabsorption cross section of 2.8×10^{-21} cm^2 . Assuming a quantum efficiency of unity, we calculate that a maximum of $\sim 5\%$ of the 2-CEES monolayer could be decomposed by *direct* UV excitation (photon fluence = 2×10^{19} cm^{-2} ; 2-CEES coverage equivalent to that in the single crystal studies $\approx 5 \times 10^{14}$ 2-CEES molecules cm^{-2}). On this basis, we conclude that the major contribution to the overall photodecomposition of 2-CEES is substrate mediated.

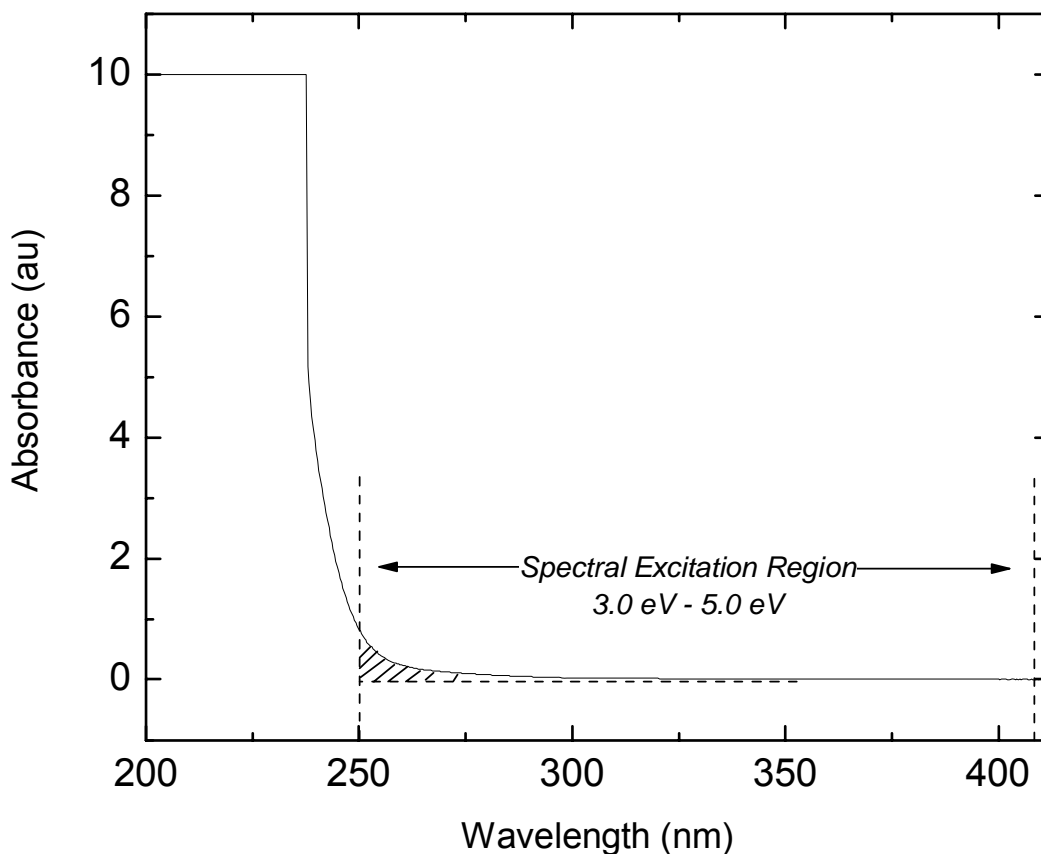


Figure 62: UV absorbance spectra for 2-CEES diluted in n-hexane. The absorbance at wavelengths above 250 nm may be used to estimate the fraction of incident radiation absorbed by 2-CEES on the TiO₂(110) crystal.

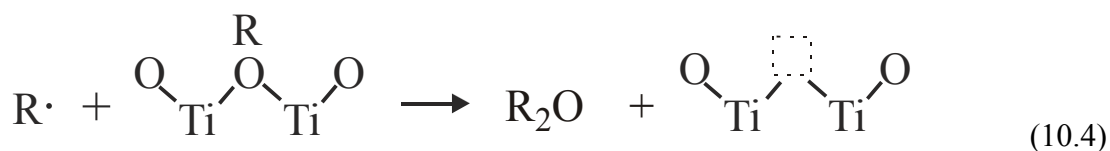
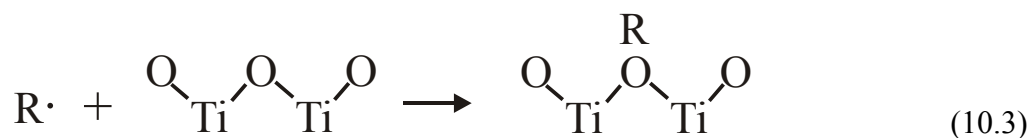
10.4.2. Reaction of Lattice O in TiO₂

A key finding in this work is that in the absence of O₂, the 2-CEES molecule is photooxidized. For this to happen, lattice oxygen must be involved. The presence of high cross section photoreaction processes on TiO₂(110), which contains no Ti-OH groups, indicates that the photoreactions of 2-CEES occur without the involvement of Ti-OH groups. Furthermore, when Ti-OH groups are present on the surface, the IR results indicate that they are not consumed in the reaction, and that instead they form hydrogen bonds with the reaction products (Figure

59a; Figure 60a). Therefore, under photochemical excitation conditions, these results indicate that the lattice oxygen in TiO₂ is labile when an organic molecule such as 2-CEES is photodecomposed by capture of an electron or a hole. Product yield studies, using GC-MS analysis, further indicate that the oxygenated gas phase products, CO₂ and CH₃C(O)H, and a surface-bound alcoholic product, are formed at ~300 K. Another ether-type product remains on the TiO₂ surface (Table 5). The production of these products is consistent with the observation by infrared spectroscopy of surface carbonate (CO₃²⁻) formation, surface carboxylate (COOH) and surface aldehyde (HCO) formation at 255 K under anaerobic photodecomposition conditions over powdered TiO₂ (Figure 59b).

One might postulate that UV irradiation of TiO₂ could generate oxygen anion vacancy defects, and the liberated oxygen might be a reactive oxidant species. However, careful STM measurements made previously²¹¹ indicate that UV radiation is inactive for producing surface oxygen vacancy defects on TiO₂(110).

We therefore postulate that reactive organic species, made either by hole attack or electron attachment processes with the 2-CEES molecule, are responsible for the abstraction of lattice oxygen from TiO₂. These reactive organic species are most likely free radical species. The reaction may be schematically written as in equation 10.3 and 10.4:



Thermochemical arguments involving single alkyl (R[•]) radical attack on TiO₂(s) and producing a gas phase RO species lead to highly unfavorable endothermic processes. However, multiple radical attack reactions producing R₂O species may be exothermic and favorable. Most of the products of the photodecomposition of 2-CEES, shown in Table 5 and Table 6 can only be formed by multiple step elementary processes induced photochemically. A similar radical-induced lattice oxygen abstraction process has been observed for CN radicals produced photochemically on TiO₂ where adsorbed NCO species were produced¹⁸⁷. In addition to multiple radical abstraction processes, the production of carbene species which attack lattice oxygen with favorable thermodynamics is possible, leading for example to aldehyde and CO₂ formation.

Further evidence for the removal of lattice oxygen by the photoprocess studied here may be found in the behavior of the infrared background during 2-CEES photodecomposition in the absence of O₂. Figure 57 shows that the photoreaction is accompanied by a significant increase in the IR background. This effect is due to the removal of O atoms from the lattice which leads to the capture of electrons near the conduction band edge. These electrons may be observed by their broadband IR absorbance as a result of electronic excitations occurring into the continuum set of levels available to trapped electrons near the conduction band edge^{145,201-203}. Indeed, annealing of TiO₂, which also results in oxygen depletion from the surface, and the concomitant trapping of electrons in the conduction band, is accompanied by a similar enhancement in the IR background absorbance^{59,85,86,177,180,194}.

10.4.3. Radical Production by Anaerobic Photodecomposition of 2-CEES on TiO₂.

Many of the products shown in Table 5 and Table 6 are likely to be formed by multiple free radical reactions. For example, the S-S bond in the diethyl disulfide product clearly results from a particular C-S bond cleavage process at the chlorinated ethyl group of the 2-CEES

reactant, followed by recombination of the radical products. Similarly, the ethane thiol product must originate from the cleavage of the same C-S bond. Photochemical radical processes resulting in C-C, C-Cl and C-H bond scission are also indicated by the products observed as listed in Table 5 and Table 6.

10.4.4. Connection to Photooxidation Chemistry on TiO₂

During photooxidation processes on TiO₂, it is believed that molecular O₂ acts as an electron scavenger. Thus, photoreduction processes involving the organic molecule might not be observed in the presence of O₂ due to competition by O₂ for electrons. Therefore, the comparison of the oxidation products obtained under anaerobic conditions with those obtained in the presence of molecular oxygen^{188,189} is informative. The comparison shows that products such as ethyl vinyl sulfide (CH₃CH₂SCHCH₂) and HCl are produced primarily in the absence of O₂. These particular products may therefore result from electron transfer from TiO₂ rather than from hole-induced effects, since O₂ inhibits their formation.

10.5. Conclusions

The anaerobic photochemical reaction of 2-chloroethyl ethyl sulfide (2-CEES) on the TiO₂ surface has been studied using a combination of measurement techniques designed to understand photophysical and photochemical phenomena. The following results have been obtained:

1. Photooxidation of 2-CEES occurs on the TiO₂ surface in the absence of added molecular oxygen; the source of the oxygen is the TiO₂ lattice.

2. For UV irradiation in the energy range 3.0 - 5.0 eV, two photoreaction processes occur on TiO₂(110) in parallel with cross sections of $7.4 \times 10^{-19} \text{ cm}^2$ and $5.4 \times 10^{-20} \text{ cm}^2$.

Photodesorption is not observed and the upper limit of the cross section for 2-CEES photodesorption is $\sim 10^{-20} \text{ cm}^2$.

3. Indirectly excited photoprocesses which cause the scission of C-S, C-C, C-Cl, and C-H bonds are inferred from the many products observed. These products are associated molecules, most likely produced by a sequence of free radical steps induced when electrons and holes are photogenerated in the TiO_2 and transferred to adsorbed 2-CEES molecules.

4. Direct photoexcitation of the adsorbed 2-CEES molecule in the photon energy range 3.0 - 5.0 eV is excluded on the basis of the minor UV absorbance of the molecule in this range.

5. It is postulated that lattice oxygen extraction from TiO_2 is caused by multiple free radical attack processes on the TiO_2 surface, where free radical species are generated by electron and hole interaction with the adsorbed 2-CEES molecule. Using more than a single free radical to attack the TiO_2 can lead to favorable thermodynamics for oxygen extraction from $\text{TiO}_2(\text{s})$.

11. CHAPTER ELEVEN: The Photoactivation of TiO₂: A Review[∞]

11.1. Introduction

The photoactivation of TiO₂ has received enormous attention from scientists and engineers in the last decade. This interest has been generated because of the confluence of several extraordinary developments: (1) The major success of the Grätzel solar cell^{151,212,213}, employing TiO₂ as the active semiconductor. Here TiO₂ has been modified to enhance its efficiency in producing electrical energy; (2) The use of TiO₂ as a medium for environmental cleanup through activation of the photooxidation of organic pollutants on self-cleaning surfaces. This work has been stimulated by many Japanese workers, leading to a revolution in Japan now spreading westward through a wide variety of TiO₂-based technological innovations²; (3) The development of hydrophilic surfaces activated by solar energy^{214,215}; and (4) The recent discovery that TiO₂-based self cleaning surfaces also exhibit antimicrobial activity useful in the home and the hospital^{2,216}.

During the period encompassing these technological developments the pace of scientific research on photochemistry on TiO₂ surfaces has doubled and redoubled in periods of about 5 years as may be seen from the survey shown in Figure 63.

[∞] Reproduced with permission from Tracy L. Thompson and John T. Yates, Jr. "The Photoactivation of TiO₂: A Review", submitted for publication *Chemical Reviews* (2006). Copyright 2006 American Chemical Society.

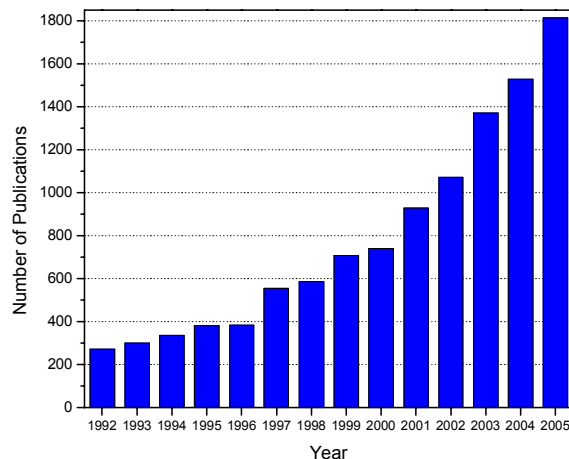


Figure 63: Annual number of papers published where “TiO₂ or titanium dioxide” and “photo-” are mentioned, beginning in 1992 through November of 2005. Literature search was done using ISI’s Web of Science (www.isiknowledge.com).

This review encompasses several scientific themes which underpin our increasing understanding of TiO₂ as a photoactive semiconducting material. The review builds upon an earlier review entitled "Photocatalysis on TiO₂ Surfaces - Principles, Mechanisms and Selected Results"²³, that is now 11 years old. In the current review, topics of particular concern are: (1) The role of both surface and bulk defects and bulk impurities in influencing the photosensitivity of TiO₂; (2) The recombination of charge carriers in TiO₂; (3) The transfer of charge from photoexcited TiO₂ to molecules bound to the TiO₂ surface; (4) New insights into the photoexcitation of TiO₂ afforded by detailed studies of the photodesorption of chemisorbed O₂; and (5) The origin of the photo-induced hydrophilicity of TiO₂. Primarily, experiments involving the use of surface science methods are included since it is through the tight control and careful measurement of surface properties that insight into fundamentals governing photochemistry on TiO₂ surfaces may be gained with some certainty. Numerous surface studies of TiO₂ at the atomic level of detail attest to the additional complexity of compound semiconductor surfaces compared to metals or elemental semiconductors.

11.2. Properties of TiO₂ Materials

Other comprehensive reviews dealing with the structure of TiO₂ materials exist^{3,72}. A brief synopsis will be presented here in order to facilitate a more complete understanding of the following sections in this review.

11.2.1. Bulk Structure

Titanium dioxide can exist in one of three bulk crystalline forms: rutile, anatase and brookite. Diebold³ has reviewed the basic structural characteristics of both anatase and rutile materials; the brookite structure is not often used for experimental investigations. In addition, Henrich and Cox⁴ present a generalized discussion of the bulk structures of many metal oxide crystals. Both the rutile and anatase crystal structures are in distorted octahedron classes⁵. In rutile, slight distortion from orthorhombic structure occurs where the unit cell is stretched beyond a cubic shape. In anatase, the distortion of the cubic lattice is more significant, and thus the resulting symmetry is less orthorhombic. Figure 64 depicts the distorted octahedral symmetries characteristic of rutile (left) and anatase (right).

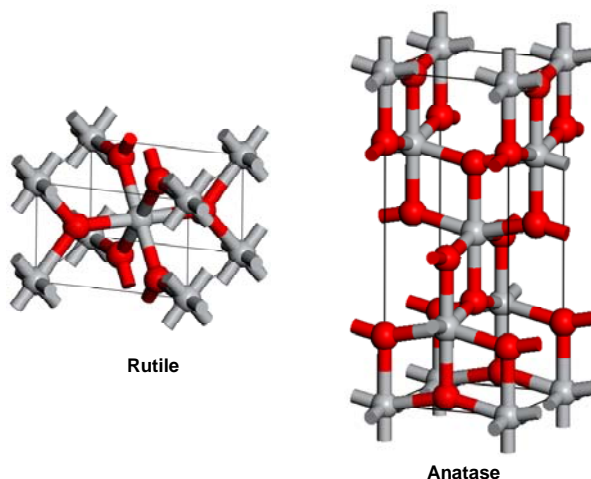


Figure 64: Bulk crystal structure of rutile (left) and anatase (right). Titanium atoms are grey and oxygen atoms are red.

11.2.2. Surface Structure of TiO₂(110)

The surface structure of the rutile TiO₂(110) has been well characterized, as it is the most commonly investigated titania crystal face. The surface consists of rows of bridging oxygen atoms that lie above the in-plane surface. The rows of bridging oxygen atoms are located directly on top of 6-fold coordinated Ti rows. The 6-fold coordinated Ti rows exist in the same plane as 5-fold coordinated Ti atoms. The rows of 5- and 6- fold Ti atoms are separated by rows of in-plane oxygen atoms. A model of the stoichiometric surface depicting all four types of surface atoms is shown in Figure 65.

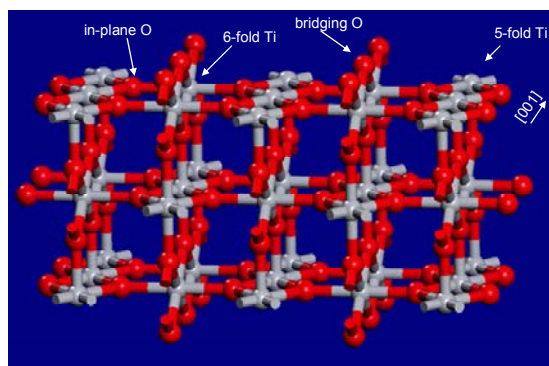


Figure 65: Surface structure of the stoichiometric TiO₂(110)-(1x1) surface depicting the 2 different types of titanium and oxygen atoms present.

The detailed structure of the TiO₂(110) surface has been investigated by *ab-initio* theoretical methods²¹⁷, by surface X-ray diffraction (SXRD)²¹⁸, and very recently by low energy electron diffraction²¹⁹. The surface O atoms and the surface Ti atoms are expected to be in distorted positions relative to the bulk. The extent of the lattice relaxation measured by SXRD and calculated theoretically differs by about 0.3 Å (O) and 0.1 Å (Ti). Recent LEED I/V measurements, and analysis involving adjustable self consistent phase shifts²¹⁹ have eliminated this discrepancy and show that an O atom outward relaxation of about 0.1Å occurs, accompanied by an outward Ti atom relaxation of about 0.25 Å²¹⁹.

11.2.2.1. Measuring Defects: TiO₂(110) – (1 x 1)

The photoactivity of the TiO₂(110) surface is critically dependent on the presence of defects in the surface region of the crystal substrate. These defects, known to be oxygen vacancies located in the bridging oxygen rows, can be created by thermal annealing^{3,15,16} or by ion sputtering¹⁰, and have been previously quantified using He ion scattering^{7,11}, scanning tunneling microscopy^{3,12,220}, as well as by XPS^{7,10,14,19,20}, UPS¹⁹, EELS²⁰ and EPR spectroscopy^{6,59,74}. The presence of these defects changes the electronic structure of the material. Defect characterization, as well as the induced electronic structural changes associated with defect sites is discussed thoroughly by Diebold³.

Very recently it has been found that STM images of oxygen defects may be influenced by the dissociation of traces of water vapor present in ultrahigh vacuum systems, causing the defect to adsorb a hydroxyl group. This finding is completely consistent with other earlier studies of the interaction of oxygen vacancy defect sites to produce water dissociation and surface hydroxyl groups^{22,221,222}. While both the defect and the hydroxyl group are bright by STM, the hydroxyl group is brighter than the defect^{223,224}. This has caused a reinterpretation of earlier work^{123,124} to be necessary, where the role of hydroxyl groups was not recognized. A clear distinction between the defect STM images and the hydroxylated defect images has been correctly recognized by Thornton et al.²²³, who have additionally shown that the hydroxylated defects may be converted to non-hydroxylated defects using electron pulses from the STM tip.

The coverage of surface defects that are created by thermal annealing can be analyzed through the adsorption and subsequent thermal desorption of CO₂ from the TiO₂(110) surface^{15,22}. On the stoichiometric TiO₂(110) surface, CO₂ adsorbs at regular Ti⁴⁺ sites on the surface of the crystal ($E_{\text{des}} = 48.5 \text{ kJ mol}^{-1}$). The coverage dependent thermal desorption spectra

for CO₂ adsorbed at these sites consists of a single peak near 160 K. Upon thermal annealing to temperatures near 600 K, defect formation on the TiO₂(110)-(1 x 1) surface begins to occur and these defective surfaces are often called reduced surfaces. The presence of defects on the partially reduced surface can be detected using CO₂ as a probe molecule: CO₂ preferentially adsorbs on defect sites at low coverages²². At higher coverage, when defects are present, CO₂ adsorbs on both defect sites ($E_{\text{des}} = 54.0 \text{ kJ mol}^{-1}$) and on regular sites. The thermal desorption profile for CO₂ from TiO₂(110) consists of a 2 peak pattern characteristic of the quantity of defects present as the annealing temperature is increased. A comparison of the thermal desorption spectra for CO₂ from an oxidized TiO₂(110) surface to the same for a reduced TiO₂(110) surface is shown in Figure 66. This method serves as a simple quantitative measure of the surface defect density on TiO₂(110) single crystalline substrates.

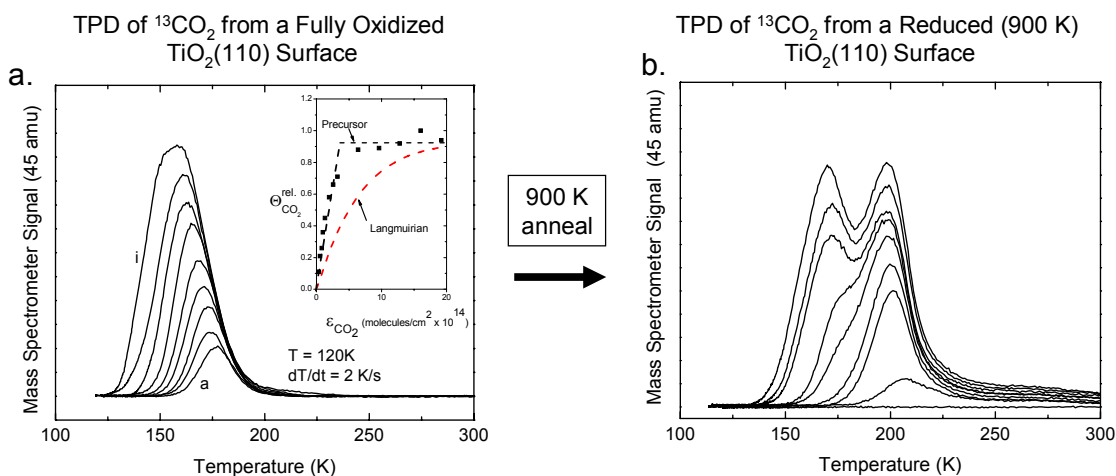


Figure 66: Comparison of the thermal desorption spectra for CO₂ from an oxidized stoichiometric surface to the CO₂ desorption from a reduced (900K, 1hr) surface. CO₂ preferentially adsorbs at defect sites on the reduced surface. The inset to (a) shows the coverage (θ) versus exposure (ϵ) data for CO₂ adsorbed on the oxidized surface: a mobile precursor mechanism describes the adsorption process. Reproduced with permission from Reference¹⁵. Copyright 2003 American Chemical Society.

Various quantitative studies of the coverage of defects versus annealing temperature show that the defect coverage reaches a maximum of about 10% of a monolayer when the TiO₂(110) surface is heated to $\sim 900 \text{ K}$ ⁷. This value is maintained even with additional heating

due to the diffusion of titanium interstitial atoms from the surface region of the crystal to regions deeper within the bulk of the TiO_2 ^{9,118}. This process establishes an equilibrium concentration of oxygen vacancies that is maintained even with extensive annealing at temperatures at or below 900 K as described by Henderson^{9,118}.

11.2.2.2. Extensive Defect Formation: $\text{TiO}_2(110)$ - (1 x 2)

With more extensive annealing above $\sim 1100\text{K}$, a (1 x 2) reconstruction of the $\text{TiO}_2(110)$ surface occurs. The conversion between the slightly defective surface (1 x 1) and the (1 x 2) reconstruction is seen in Figure 67. The (1 x 2) surface consists of a cross link structure as well as a single link structure. On the right side of Figure 67, a diagram of the cross link and single link features is presented and has been described by Stone et al¹¹⁶. The atomic nature of the (1 x 2) surface structure has been debated in the past. For a detailed overview of the (1 x 2) surface reconstruction and the models presented to describe this surface, the authors refer the reader to Reference ³, which includes references to the majority of research done on this surface. Since the publication of Reference ³, the (1 x 2) structures proposed by Pang et al.¹²¹ and by Onishi et al.²²⁵ are both accepted models: based on crystal preparation procedures, the description of the (1 x 2) structure by either one of the “added row” models may be appropriate.

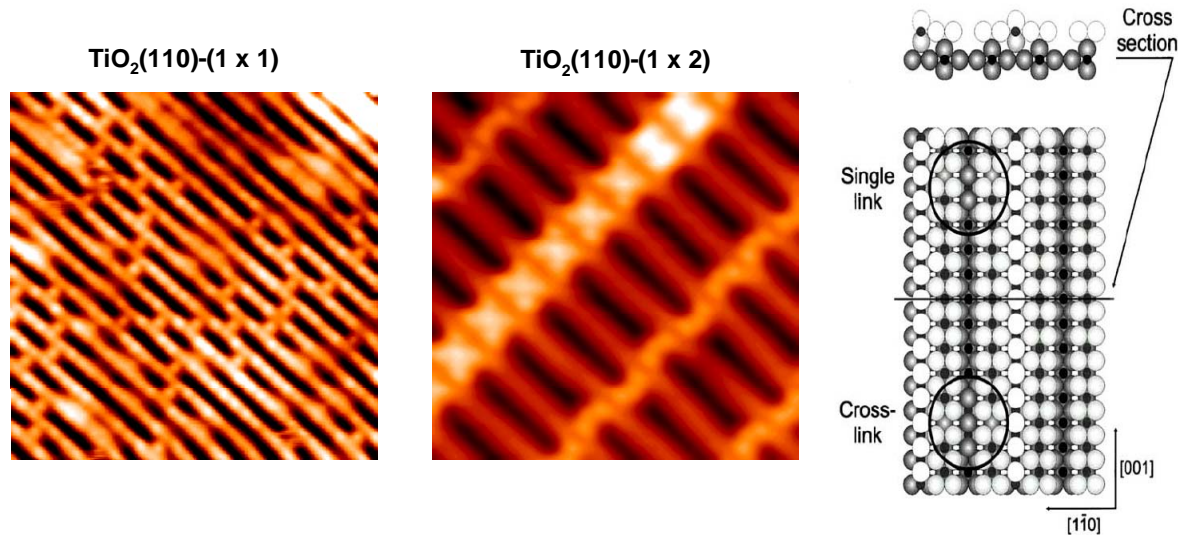


Figure 67: STM images of the reduced $\text{TiO}_2(110)-(1 \times 1)$ surface (left) and the extensively reduced $\text{TiO}_2(110)-(1 \times 2)$ surface (right). The (1×2) surface reconstruction forms after extensive annealing at temperatures near 1100 K. The (1×2) surface exhibits both single link and cross-link features, shown schematically in the ball model on the right hand side of the figure. Reprinted with permission from Reference ²²⁶. Copyright 2003 Elsevier B.V.

The (1×2) reconstructed surface does display differing behavior in the presence of UV light when compared to the (1×1) surface, which is unaffected by UV irradiance²¹¹. When exposed to high photon fluxes of UV light, extensive line defect formation was shown to occur on the (1×2) surface. No effect was seen under the same conditions for the (1×1) surface.

11.3. Excitation of Charge Carriers

The excitation of charge carriers (electron hole pairs) for TiO_2 materials occurs when the substrate material is exposed to photons of energy higher than the bandgap for TiO_2 . The sections below address possible mechanisms for lowering the threshold energy for substrate excitation, a topic that has received considerable research interest. Secondly, this section presents an overview of strategies that have been developed for monitoring the presence of excited charge carriers using either infrared (IR) spectroscopy or electron paramagnetic resonance (EPR) spectroscopy.

11.3.1. Lowering the Threshold Energy for Excitation

Due to the inherent relatively large bandgap characteristic of TiO₂ materials, a great deal of research has focused on lowering the threshold energy for excitation in order to utilize a larger fraction of visible light for conversion to photochemical energy.

There has been a great deal of interest recently on the use of both nonmetal, as well as transition metal doping as will be addressed below.

11.3.1.1. Nitrogen Doping

The idea of doping titanium dioxide materials with nitrogen and other anionic species was first presented by Asahi et al. in 2001³⁶. They reported theoretical results where they have substituted C, N, F, P or S for oxygen atoms in the titania lattice. Results of density of states (DOS) calculations for anatase TiO₂ suggest that substitutional type doping (interstitial type doping, or a mixture of both substitutional and interstitial type were both found to be ineffective) using nitrogen is effective due to the mixing of nitrogen 2p states with oxygen 2p states, thus causing a significant decrease in the width of the overall bandgap. Similar calculated results were also obtained for S-doping, however, S-doping is not commonly employed due to its large ionic radius. Asahi et al. further investigated the use of nitrogen as a substitutional dopant experimentally through characterization of TiO_{2-x}N_x films. The doped material, made by sputtering TiO₂ films with N₂/Ar mixtures³⁶, was found to consist of both anatase and rutile grain structure, and was shown to absorb light below 500nm. The photocatalytic activity of the films was analyzed by measuring the decomposition rates for the photooxidation of methylene blue as a function of photon energy in addition to the measurement of the photodecomposition of gaseous acetaldehyde³⁶. All of the films showed enhanced photocatalytic activity in the visible light region. The films exhibit N 1s XPS features at 396, 400 and 402 eV binding energy. The

authors of this work claim that the nitrogen species responsible for the overall bandgap narrowing effect exhibits the 396 eV N 1s binding energy. Similar doped powders that did not show the 396eV XPS feature also did not show enhanced photocatalytic activity³⁶.

Recently, a study was published that more clearly investigated the origin of the band gap narrowing by nitrogen doping. In that work³⁹, doping of the TiO₂(110) crystal was done in a high temperature flow reactor where the crystal could be simultaneously heated and exposed to NH₃ gas at high temperature³⁹. After treatment, the crystal was subjected to XPS analysis where a pair of N(1s) features were revealed, one at 396.5 eV (seen previously and assigned to substitutionally bound N⁻) and one at 399.6 eV, which has been attributed to an N⁻H complex interstitially bound in the TiO₂ lattice³⁹. The 2 feature XPS spectrum observed for the NH₃ treated samples is comparable to that presented by Asahi et al. ³⁶. However, in Asahi's work, the authors claim that the N 1s XPS feature at 396.5eV (attributed to be substitutionally bound N⁻) is related to the photo threshold energy decrease observed, whereas the work in reference ³⁹ finds that the 399.6 eV N(1s) state due to N⁻H species is the active dopant. A comparison of the XPS spectra from the doped material presented by Asahi ³⁶ and of the NH₃ doped material presented by Diwald et al.³⁹ is shown in Figure 68.

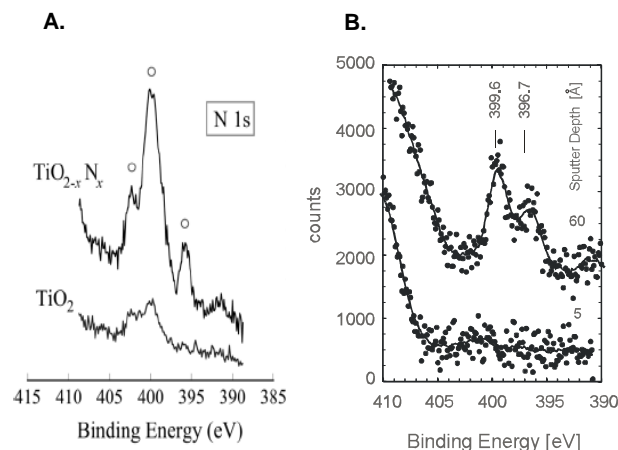


Figure 68: Comparison of the N (1s) XPS data presented (A) by Asahi et al.³⁶ and (B) by Diwald et al.³⁹.

Figure A: Reprinted with permission from Reference ³⁶. Copyright 2001 AAAS. (www.sciencemag.org).

Figure B: Reprinted with permission from Reference ³⁹. Copyright 2004 American Chemical Society.

A novel test, developed by Fleischauer et al.⁴⁰⁻⁴², was employed by Diwald et al.³⁹ to determine the photoactivity of the $\text{N}^{\cdot\cdot}\text{H}$ doped crystal as a function of photon energy. The results yielded a significant decrease of 0.6 eV in the photothreshold energy needed for substrate excitation. This test involved the photoreduction of $\text{Ag}^+(\text{aq})$ ions to form Ag° deposits on the TiO_2 crystal surface. The surface, once exposed to UV, was then imaged using atomic force microscopy (AFM) which was used to evaluate the density and size of Ag° clusters produced photolytically. A representative comparison of the AFM images of the NH_3 -doped and undoped crystals exposed to UV radiation at 2.47 eV are shown in Figure 69. It should be noted that this effect of $\text{N}^{\cdot\cdot}\text{H}$ doping has been studied for a photoreduction reaction, not for a photooxidation reaction. A summary of the results of these studies is shown in Figure 70 where it may be seen that an ~ 0.6 eV decrease in the photothreshold is seen for the $\text{N}^{\cdot\cdot}\text{H}$ doped TiO_2 crystal compared to undoped TiO_2 .

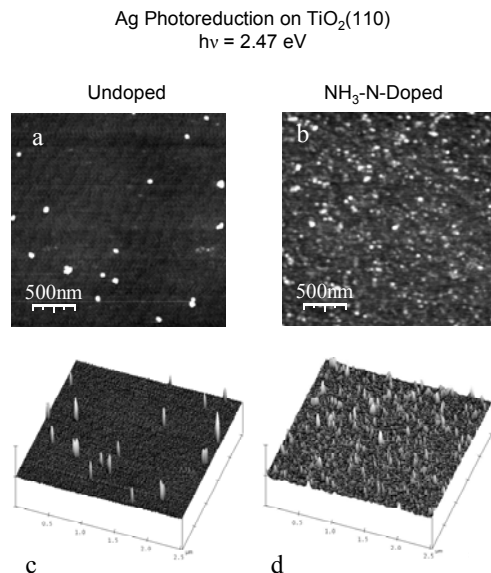


Figure 69: AFM images of Ag clusters deposited on (a) undoped and (b) NH₃-doped TiO₂ rutile single crystals. Reprinted with permission from Reference ³⁹. Copyright 2004 American Chemical Society.

Prior to the work done where NH₃ was used as a dopant³⁹, doping of TiO₂(110) was also attempted by Diwald et al.⁵³ using a high energy ion gun (in UHV) in order to implant the TiO₂(110) using a N₂/Ar⁺ mixture⁵³. After 3.0 keV N₂⁺ implantation, the crystal was annealed extensively, allowing diffusion of implanted N atoms further into the bulk of the crystal. The crystal photoactivity was then tested using the photodesorption of adsorbed O₂ at varying photon energies. XPS, TEM and SIMS were also used to examine the nature and depth of the implanted nitrogen species. Results of this work showed an *increase* in the photothreshold energy, opposite to that observed by others. The XPS data for the ion implanted surface show a single 396.5 eV N(1s) feature attributed to substitutional nitrogen, assigned as N⁻, and therefore suggesting that substitutionally bound N⁻ alone is not responsible for the decrease in the photothreshold of TiO₂(110) as suggested by Asahi et al³⁶. Work done by Burda et al.⁴⁴ on nitrogen-doped TiO₂ nanoparticles reports substitutionally bound nitrogen as the active dopant species, in agreement with Asahi³⁶. This work however, differs from that of Asahi in that the measured N 1s XPS

feature exhibits a binding energy near 400 eV, and no peak is measured at or near 396 eV as found by Asahi³⁶. Other authors also report N 1s XPS features for nitrogen doped titania at 400 eV⁴⁵, yet assignment of this species remains an issue. Burda et al. reports that the substitutional type nitrogen species responsible for the observed increase in the measured photocatalytic activity in the visible region is due to N-O type bonding as reported in Reference⁴⁶. Thus, while Diwald et al.³⁹ and Burda et al.⁴⁴ agree that a nitrogen species with an N 1s binding energy near 400 eV is an active dopant, the assignment of its chemical nature differs.

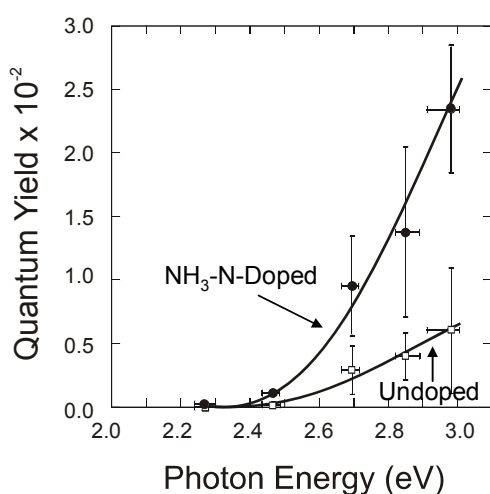


Figure 70: Comparison of the photoactivation of undoped versus NH₃ doped TiO₂(110) single crystals. The points shown here were measured using the photoreduction of Ag as measured by AFM and reported in Reference³⁹. Reprinted with permission from Reference³⁹. Copyright 2004 American Chemical Society.

Hoffmann et al.³⁷ have also extensively investigated the effect of nitrogen doping on titania materials. That work focused on investigating the photo-oxidation of organics over N-doped materials prepared using a method earlier reported by Burda and Gole³⁸. Hoffmann et al.³⁷, report results suggesting that organic molecules like methylene blue, commonly employed by others to monitor photo-oxidative processes, may be uninformative as to the actual activity of the TiO₂. It is likely that photo-oxidation of methylene blue and other dyes occurs thru direct excitation and degradation by UV or VIS illumination. These dyes are oxidized with or without

the presence of TiO_2^{37} , and may give false results when used to investigate photooxidation chemistry on TiO_2 .

Recent calculations have addressed the variances in the photoactivity measurements⁴⁷ using density functional theory to consider both anatase and rutile-type samples which have been substitutionally doped with nitrogen. The conclusions of this work are profound. For anatase samples, substitutional N-doping results in a decrease in the photon energy necessary to excite the material; for rutile TiO_2 materials, the opposite effect is observed, and is attributed to the contraction of the valence band and the stabilization of the N 2p state thus causing an overall increase in the effective bandgap in agreement with the work of Diwald et al⁵³. For anatase TiO_2 , substitutionally bound nitrogen atoms create localized occupied electronic states (N 2p in character) above the top of the O 2p valence band. The creation of this occupied electronic state has also been shown experimentally^{48,49}. As a result, the mechanism for photoexcitation of N-doped anatase is most probably direct excitation of electrons from the N 2p state located within the bandgap of the TiO_2 , into the conduction band. The measured inter-band gap density of states have been postulated to reduce the rate of electron-hole pair generation which may readily occur without the presence of these states⁴⁸. A schematic diagram explaining this effect for anatase and rutile is shown in Figure 71 where for rutile TiO_2 the suppression of the top of the valence band is observed for N doping. Similar calculations recently presented by other authors⁵⁰ agree with the work presented by Selloni et al⁴⁷.

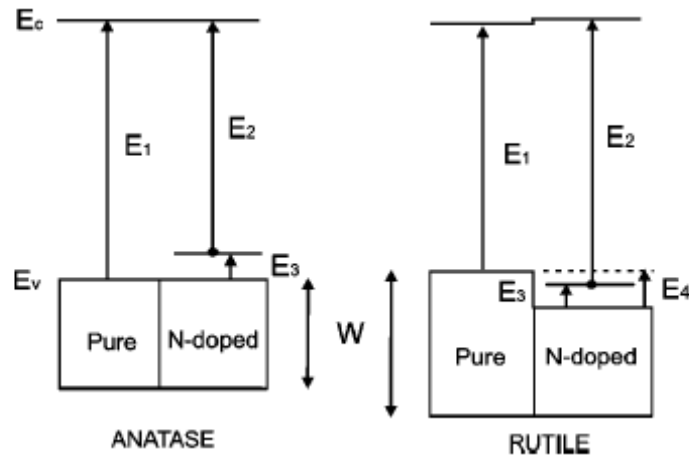


Figure 71: Comparison of the calculated electronic structures for N-doped anatase and rutile TiO_2 as described by Selloni et al⁴⁷. Reprinted with permission from Reference ⁴⁷. Copyright 2004 American Physical Society.

The difference in the dopant states for substitutional- versus interstitial- type impurities in anatase TiO_2 was investigated both experimentally using electron paramagnetic resonance spectroscopy (EPR) and XPS, and theoretically using DFT calculations⁵¹. This recent work⁵¹ reveals a distinct N 1s XPS feature at 400 eV, but the authors note that preparation methods and differing experimental conditions can drastically affect the nature of the measured XPS signals. In addition, the authors also point out the probability that the observed XPS feature ascribed to N 1s transitions may originate from the presence of any number of differing nitrogen species. Although the EPR characterization of the nitrogen species in the anatase material considered in this work is inconclusive, the theoretical findings show very distinct differences in the calculated electronic structure for substitutional versus interstitial type nitrogen. Both types of impurities are found to add localized states within the bandgap. For substitutional type nitrogen, these states are located 0.14 eV above the valence band, and for interstitial type nitrogen species (referred to as N-O) the localized states are calculated to lie 0.73 eV above the valence band. In addition,

these calculations have also found that there is a large decrease in the formation energy for oxygen vacancies as a result of additional nitrogen atoms in the lattice. Therefore, oxygen vacancies are most probably induced by N-doping of TiO₂. This work, while quite useful in realizing the actual electronic nature of doped titania materials, fails to address the actual observed change in the photocatalytic activity as a result of impurity addition.

In summary, there is a great deal of literature existing on the topic of nitrogen doping of TiO₂ materials, most of which agrees that the addition of nitrogen to the lattice of TiO₂ results in increased photocatalytic activity at lower photon energies. Theoretical results have also clearly illustrated that the addition of either substitutionally or interstitially bound nitrogen species result in localized N 2p states that are discrete levels above the valence band, in contrast to past reports which suggested valence band broadening. Table 1 (see Chapter One) presents a compilation of the literature dealing with nitrogen doping on TiO₂.

11.3.1.2. Carbon Doping

In addition to investigations of TiO₂ doping with nitrogen as discussed above, carbon has recently received considerable interest as a non-metallic dopant in TiO₂ materials. Carbon was first investigated as a substitutional-type dopant in TiO₂ by Khan et al.¹²⁸ where the authors studied the band-gap energy through measurement of the efficiency of water splitting similar to the method first used by Honda and Fujishima¹. The material studied in this work was chemically modified TiO₂ synthesized using flame pyrolysis of a Ti metal sample, an ill-defined material compared to single crystalline TiO₂. Carbon was incorporated during the pyrolysis process that was carried out in the presence of combustion products (CO₂ and H₂O)¹²⁸. The resulting TiO₂ film was characterized by x-ray diffraction (XRD) and found to be mainly rutile. Measurements of the photocurrent at varying applied voltages show increased activity for the

carbon-doped films when compared to undoped materials that were fabricated using the same method. A significantly reduced bandgap of 2.32 eV is reported for the carbon-doped material, compared to 3.0 eV for undoped rutile. The proposed mechanism for this action is band-gap narrowing¹²⁸.

Since the initial experimental investigation of carbon-doped TiO₂, other authors have investigated carbon doping in TiO₂ both experimentally²²⁷⁻²²⁹ and theoretically^{50,230}. Sakthivel and Kisch have shown that carbon incorporation in TiO₂ causes a 4-5 fold increase in activity for the degradation of 4-chlorophenol by UV light compared to nitrogen-doped TiO₂ materials. The preparation method for the samples presented in reference²²⁷, although similar to that presented by Khan et al.¹²⁸, results in carbon containing species, either elemental adventitious carbon, or carbonate species. This finding is in contrast to that presented by Khan¹²⁸ who report the presence of substitutionally bound carbon. Tachikawa et al.²²⁸ investigated carbonate-species doped TiO₂ (anatase) and found that although UV-induced charge carriers are generated more readily for carbonate-doped TiO₂, no evidence for enhanced photo-oxidation chemistry is measured. The authors attribute this finding to a possible decrease in the mobility of the photogenerated holes which participate in the photooxidation step. This may be directly related to significant trapping of charge carriers that occurs upon photoexcitation, and is directly dependent on the incoming photon flux and the density of impurity sites (which may act as trapping sites) in the surface or the bulk of the material²⁶.

Very recent theoretical work is aimed at understanding the theory of the action of carbon-type dopants in both anatase and rutile forms of TiO₂²³⁰. The authors investigated the effect of both substitutional and interstitial type carbon dopants in the anatase and rutile forms of TiO₂. The stability of the dopant species as a function of oxygen partial pressure was investigated. In

addition, the electronic structure of each material after the addition of either substitutional or interstitial type dopants was calculated. For both rutile and anatase TiO₂, it is found that the same general trends are realized for both substitutional and interstitial type of carbon dopants as a function of the oxygen partial pressure. At low partial pressures of oxygen, substitutional type doping of carbon atoms substituting for oxygen atoms is favored. In addition, the formation energy for oxygen vacancies decreases with the presence of the carbon dopant. At high partial pressures of oxygen, both interstitial and substitutional (where carbon binds to titanium atoms) carbon dopants are present. For both anatase and rutile, the presence of both types of carbon dopants causes the formation of localized occupied band gap states that vary in energy based on the dopant type, the presence or absence of oxygen vacancies, and the background partial pressure of oxygen. The presence of these states gives rise to the decreased energy necessary for excitation of either material, as reported experimentally.

11.3.1.3. Transition metal dopants

Doping with transition metal ions including Cr²³¹, V²³², Fe^{233,234}, Pb²³⁵, Cu²³⁶ and others has been investigated. Doping with these metal ions has shown both positive and negative effects on the photocatalytic activity of TiO₂, where a number of authors claim that although metal ion doping should decrease the photothreshold energy of TiO₂, the metal ion may also serve as a recombination center for electrons and holes, thus diminishing the overall activity of the photocatalyst²³⁷. Karvinen et al.²³⁸ have theoretically investigated the role of transition metal dopants in both anatase and rutile TiO₂ models. For anatase TiO₂, the addition of Ti³⁺, V³⁺, Cr³⁺, Mn³⁺ and Fe³⁺ caused significant bandgap narrowing; however, for the rutile system, no effect was found²³⁸. Hoffmann et al.^{148,237} have investigated a great number of metal ion dopants in TiO₂ with the specific aim to measure the photoactivities of the resulting material. A mixture of

both positive and negative effects was reported. In general, doping with metal ions has not been investigated to the extent that non-metal dopants have been studied.

11.3.2. Monitoring Charge Carrier Excitation and Recombination

Recent work done by Berger et al.⁵⁹ reported the detection of mobile charge carriers by either electron paramagnetic resonance spectroscopy, or by infrared spectroscopy. These tools complement each other quite well for studies of this nature. In this work, it was shown that under continuous UV-illumination, photogenerated electrons are either trapped at localized states within the bandgap (Ti^{3+} centers) where they are measured by EPR spectroscopy, or they are promoted to the conduction band where they are unable to be detected by EPR, but are able to be easily measured by IR spectroscopy. Photoexcited hole species are able to be detected also using EPR, and are measured as O^- species, which originates from lattice O^{2-} ions. Using these methods, the lifetime of the photoexcited electrons and holes can be measured and is found to be on the order of hours at low temperature ($T = 90 \text{ K}$). At room temperature, the recombination process is much faster, and the photogenerated electrons and holes recombine rapidly. Figure 72 illustrates the detection of photogenerated electrons and holes via either EPR or IR spectroscopy.

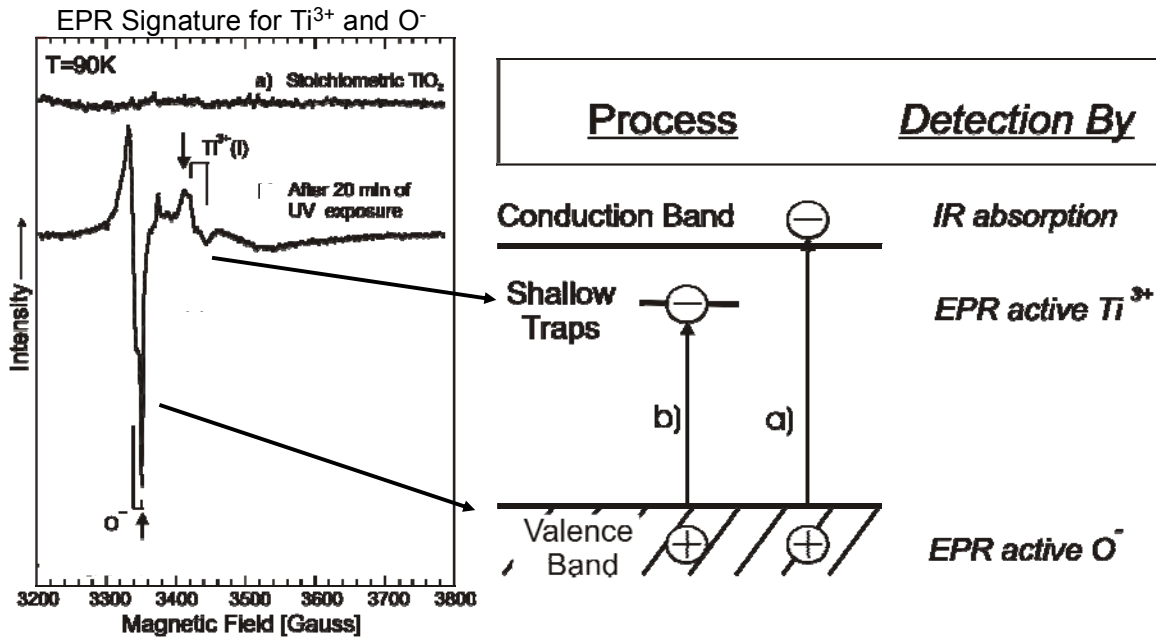


Figure 72: Characteristic EPR signature for photogenerated electrons and holes in fully oxidized anatase TiO_2 . Right hand schematic shows the location of the conduction band electrons (detected by IR spectroscopy), electrons trapped at shallow trap sites (EPR detection) and charge carrier holes present in the valence band (EPR detection). Reprinted with permission from Reference ⁵⁹. Copyright 2005 American Chemical Society.

11.3.3. IR Spectroscopy as a Tool for Monitoring CB Electrons

The energetic promotion of electrons from the valence band to the conduction band in semiconductors can occur in a number of ways. As discussed earlier, promotion of electrons via UV irradiation with photons greater than the bandgap energy leaves electrons in the conduction band where, at low temperature, they may be stored for long periods of time. For a mixed oxide material ($\text{TiO}_2\text{-SiO}_2$), Payanotov et al.¹⁸⁰ have observed the presence of conduction band electrons produced upon thermal annealing in vacuum. The same is observed for pure TiO_2 , unmixed with SiO_2 ²³⁹. This effect is directly related to the thermally activated production of defects within the material as the time and/or temperature of the annealing process increases. The shallow-trap defect site (probably Ti^{3+}) then provides electrons to the conduction band by

thermal excitation from the defect state at the temperature of the measurement (476 K), as shown schematically in Figure 73.

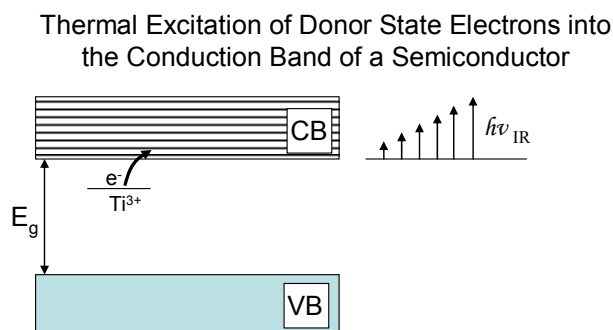


Figure 73: Schematic diagram depicting the thermally-activated charge injection of electrons from shallow trap sites into a continuum of states in the conduction band of this wide-band gap semiconductor.

This process is sometimes referred to as “metallization” of the semiconductor. Free carriers (electrons) promoted to the conduction band behave approximately as delocalized electrons in an infinite-walled three dimensional box. The high density of states provides a continuum of electronic excitations resulting in an increase in the featureless background of the infrared spectrum as excitations of many energies in the infrared region combine to produce the broadband background absorption. This phenomenon is called Drude absorption, as found in metals²⁴⁰. In semiconductors, detection of excitation between delocalized conduction band electron states is done by infrared absorption spectroscopy, and a broad structureless absorption increase is measured, as shown in Figure 74. The description of these delocalized electrons, their coupling to phonons, and the formation of polarons as a result of lattice distortion, are topics beyond the scope of this review. Hoffmann and co-workers^{86,177} have detected transient and persistent diffuse reflectance infrared signals due to the population of conduction band electrons upon irradiation of TiO_2 powders with supra bandgap light, where the baseline IR absorption for

TiO₂ rises immediately upon UV irradiation⁵⁹. In addition, the observed response partially recovers in the dark and fully recovers upon addition of oxygen.

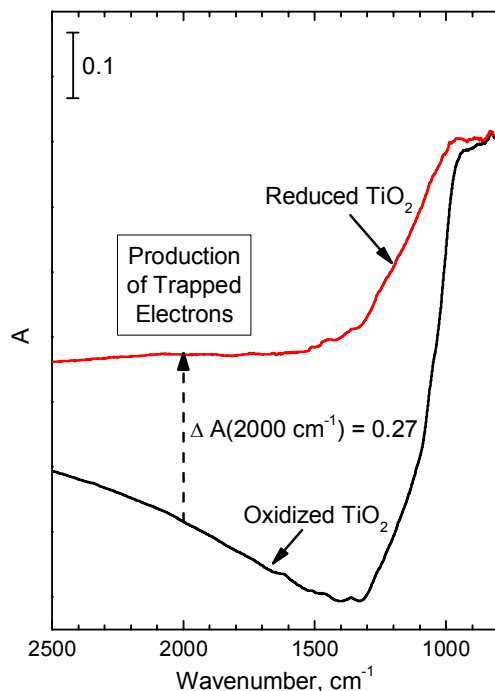


Figure 74: IR absorbance spectra for oxidized and reduced TiO₂. Trapped electrons are measured by the increase in the background absorbance measured at 2000 cm⁻¹.

Detection of photo-produced conduction band electrons by IR spectroscopy was also earlier reported by Yamakata et al.²⁴¹ where the authors measure the excitation of Pt/TiO₂ materials activated by short time scale laser pulses. Here, as in work presented by Berger et al.⁵⁹, the transient IR absorbance over a wide range of wavenumbers (3000-900 cm⁻¹) is monitored before, during and after the photo-excitation step. Yamakata et al.²⁴¹ observe a peak in the IR absorbance at time = 0 (onset of 10 ns laser pulse) and measure a decay in the absorbance intensity to 8% of the original value over a time period of 1 microsecond at 323 K. The reported decay kinetics for photogenerated electrons after excitation is shown to be first-order, which is in

contrast to results presented by these authors for work done on $\text{TiO}_2(110)$ at 110K where second-order recombination kinetics are inferred. (See section Chapter 3 and reference ²⁶.) The explanation presented by Yamakata et al. for this result is the following: in colloidal TiO_2 particles, where only low concentrations of electron-hole pairs accumulate, the kinetic rate law is first-order in nature, whereas when higher concentrations of electron-hole pairs are present, the kinetic rate law is second-order in nature²⁴².

Early work done on the detection of trapped electrons in the conduction band as measured by IR spectroscopy was reported by Baraton et al.²⁴³. The authors report the use of TiO_2 as a sensor material for oxidizing or reducing agents. In the presence of an oxidizing agent, electrons are removed from the conduction band by the adsorbate, thus decreasing the background IR absorbance. The opposite effect was measured for reducing agents that inject electrons into the conduction band, thus increasing the background IR absorbance²⁴³. This work demonstrates the use of metal oxide materials for gas sensors using IR spectroscopy as a detection tool.

11.3.3.1. EPR

Electron paramagnetic resonance spectroscopy (EPR) is widely employed for the detection of photoexcited charge carriers in metal oxide materials. Early work on the use of EPR for the study of UV induced effects on TiO_2 materials has been studied extensively and reported in review format^{244,245}. Work done by Howe and Grätzel⁷⁷ reports on the trapping of photogenerated electrons and holes in the bulk and surface region of hydrated anatase TiO_2 polycrystalline material at very low temperatures (4.2 K). Electrons are trapped at low temperatures at localized Ti^{4+} sites (to produce Ti^{3+}) within the bulk of the material, and holes are trapped as lattice oxide ions (O^-) below the surface. As mentioned above and reported by

Berger et al.⁵⁹ the photogenerated electrons and holes exhibit a lifetime of hours at 90 K. A direct linear correlation between the concentration of photogenerated electrons (Ti^{3+} species) and holes (O^- species) measured by EPR spectroscopy on polycrystalline anatase TiO_2 exists and is depicted in Figure 75. The deviation from linearity suggests that at high UV light intensities a fraction of photogenerated electrons are transferred to the EPR-silent conduction band (due to the finite concentration of Ti^{3+} electron-trap defect sites), where they can be measured using IR spectroscopy as discussed in Section 3.2.1.

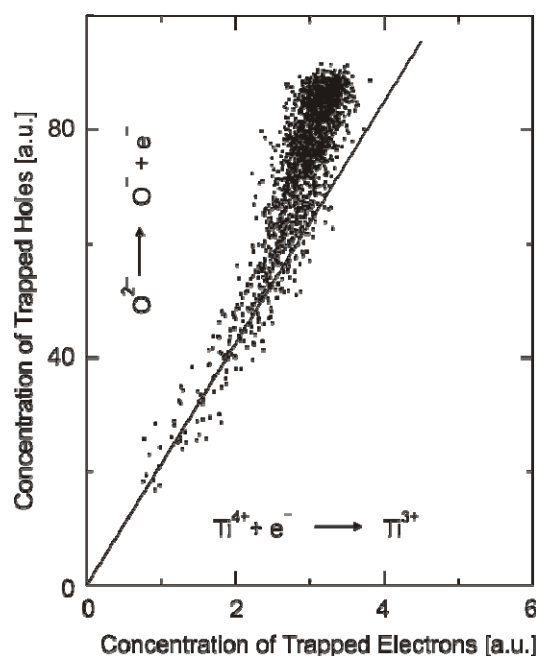


Figure 75: Correlation between the concentration of trapped electrons and trapped holes as observed by EPR spectroscopy of photoexcited TiO_2 . At high UV light intensity, trapped electrons are excited into the conduction band (EPR silent). As a result, the concentration of trapped electrons is not equal to the concentration of trapped holes and a break in the linear correlation occurs. Reprinted with permission from Reference⁵⁹. Copyright 2005 American Chemical Society.

For reduced samples, where oxygen vacancies are created in the bulk of the material, the EPR signal is identical to that of trapped (Ti^{3+}) photogenerated electrons that are created in the presence of UV irradiation: Ti^{3+} signals are clearly measured in each case. However, for reduced TiO_2 , the EPR signal intensity is enhanced by a factor of 25 suggesting a greater concentration of thermally produced electrons after annealing the TiO_2 to 950 K when compared to the

concentration of photogenerated trapped electrons observed for oxidized TiO₂. Little to no signal is observed for O⁻ holes in thermally-reduced TiO₂. When the reduced material is further exposed to sub-bandgap UV irradiation, a photobleaching effect occurs where all the characteristic electron and hole EPR signatures are eliminated. This effect can be explained by the ionization of trapped electrons located in inter-bandgap states⁵⁹.

11.4. Recombination of Excited Electrons and Holes

11.4.1. Shockley-Read-Hall Recombination At Trap Sites

The concentration of charge carriers upon UV excitation in any semiconductor is reduced by the inherent recombination process which may occur, leading to the destruction of active electron-hole pairs. For TiO₂, this action can be explained by the Shockley-Read-Hall model for nonradiative recombination which describes the capture of mobile electrons and/or holes at trap sites within the semiconductor^{24,25}. Once trapped, the electron (or hole) is then annihilated via recombination with holes from the valence band (or electrons from the conduction band). The active sites for electron or hole trapping may vary and are usually described as defect states within the crystal due to interstitial atoms, defect states, or grain boundaries and the like. In the Shockley-Read-Hall mechanism, as schematically depicted in Figure 76, four transition processes may occur: 1) electron capture; 2) electron emission; 3) hole capture; 4) hole emission. This model assumes that the semiconductor is non-degenerate and that the density of trap sites is relatively small compared to the majority carrier density present in the material. For a TiO₂(110) single crystal the concentration of hole-trapping sites was estimated by Thompson et al.²⁶ to be on the order of $2.5 \times 10^{18} \text{ cm}^{-3}$, which is equivalent to an atomic fraction of 3×10^{-5} of the bulk atomic sites in the crystal.

Shockley-Read-Hall Recombination: Possible Transition Processes

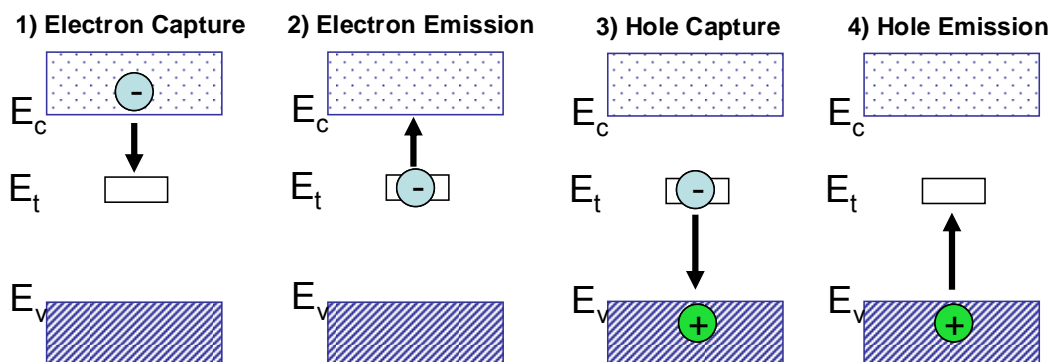
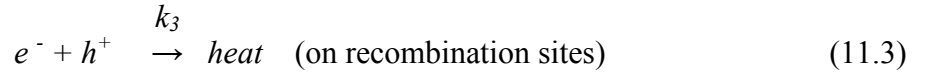
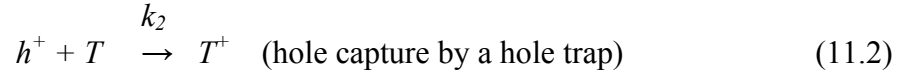
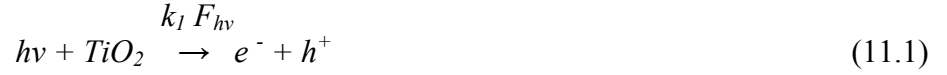


Figure 76: Schematic diagram showing the 4 electronic transition processes that may occur for the charge carrier recombination as described by Reference ²⁵.

11.4.2. Kinetics of Recombination

Very recently, the kinetic processes by which photochemistry on TiO_2 is governed was investigated using a simple surface photochemical reaction, namely the photon induced desorption of molecular oxygen from $\text{TiO}_2(110)$ ²⁶. It is known that oxygen molecules are adsorbed at oxygen-vacancy defect sites^{8,55,107} in the surface and that they become negatively charged as O_2^- species^{63,64,104}. This will be discussed in greater detail in section 5.1. In order to study the relative activity of photogenerated charge carriers, the effect of the incident light intensity on the rate of photodesorption of O_2 was investigated. This work builds on that of other authors who have reported a correlation between reaction rate or photo-oxidation rate to the square root of the incident light intensity²⁷⁻³². Those experiments are less refined than the work presented in Reference ²⁶ that involves carefully controlled studies of a simple photoprocess that occurs in ultrahigh vacuum on a planar single crystal of TiO_2 with known surface structure³, known surface defect density⁷, and in the absence of solvents and surface-bound chromophores. In addition, the photon flux and photon energy are well known. Thus, quantification of the rate of a well-defined photoprocess compared to the photon flux received by the planar single crystal

surface can be accurately made in this model system involving a TiO₂(110) single crystal. A kinetic model was developed and is presented below and in Reference ²⁶:



After hole trap filling by reaction (11.2) and assuming a fast equilibrium is established between the e-h pair formation (step 11.1) and the recombination (step 11.3), the rate of O₂⁻(a) photodesorption will be, according to the steady state approximation:

$$-d[O_2^-(a)]/dt = k_4[O_2^-(a)] \left[\frac{k_1}{k_3} \right]^{1/2} F_{hv}^{1/2} \quad (11.5)$$

where the recombination process (step 3) is second-order in the hole concentration, [h], leading to a desorption rate containing the factor F_{hv}^{1/2}. This assumes that at steady state conditions, [e-] ≈ [h⁺] = constant. The linear correlation between the yield of photodesorbing oxygen and the square-root of the incident light intensity is shown in Figure 77.

$^{18}\text{O}_2$ Initial Photodesorption Yield – $\text{TiO}_2(110)$

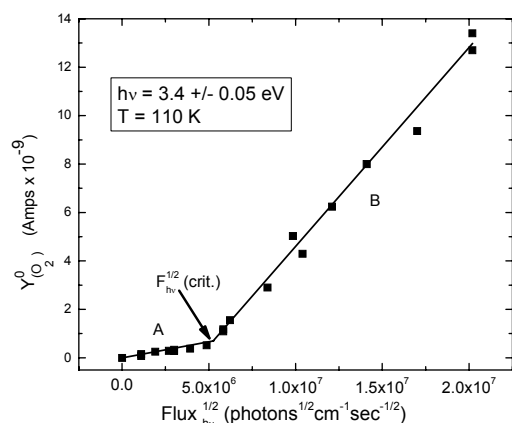


Figure 77: Yield of photodesorbing oxygen for increasing photon flux. A linear correlation between the yield of photodesorbing oxygen and the square-root of the photon flux proves that the recombination process is second-order. Reprinted with permission from Reference ²⁶. Copyright 2005 American Chemical Society.

11.4.3. Evidence for Trap Filling – Photodesorption of O_2

From equation 11.5, the instantaneous rate of photodesorption is measured for the initial pulse height of $^{18}\text{O}_2$ that desorbs from the $\text{TiO}_2(110)$ surface as supra band gap light is exposed to the crystal face. The initial photodesorption pulse is termed the initial yield of photodesorbing oxygen, $Y_{\text{O}_2}^0$. Figure 77 shows the dependence of $Y_{\text{O}_2}^0$ on the magnitude of $F_{h\nu}^{1/2}$. Two linear branches with differing slopes, A and B, are measured. Branch A corresponds to a photodesorption process of low efficiency where significant hole trapping results in a lower probability for photogenerated holes to reach the surface. In branch B, the large concentration of photogenerated holes saturates the hole trapping centers and in this region of high $F_{h\nu}$, there is an increase in the number of holes that are able to reach the surface. As shown in Figure 78, about each trapping site (T) there is a spatial range in which photogenerated holes produced in this region will, on average, reach the T-site and become trapped. Photogenerated holes not trapped at T-sites will reach the surface, where the holes can produce O_2 photodesorption with a

probability governed by the factors $F_{hv}^{1/2}$ and $[k_1/k_3]^{1/2}$ in the series of experiments at constant $[O_2^-]$.

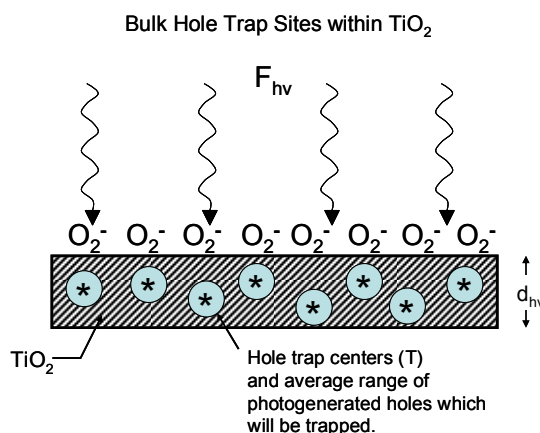


Figure 78: Schematic diagram showing the active range of sites for hole trapping. Reprinted with permission from Reference ²⁶. Copyright 2005 American Chemical Society.

Most studies of the photochemical filling of trap states have concerned electron trapping. When an electron trap becomes filled the Fermi level crosses the energy level of the trap and the trap becomes inactivated for further electron capture. This trap saturation effect can enhance the lifetime of photogenerated charge carriers and can improve the quantum yield of carriers at higher light intensities⁸⁰. These ideas may also apply to hole trapping in TiO₂, as demonstrated in Figure 77.

Trap filling has been observed in semiconducting silicon substrates^{79,96} and has also been suggested for rutile single crystals⁷⁰, polycrystalline TiO₂ electrodes⁸⁰ and ZnO nanoparticles⁹⁴. The saturation of deep trap levels results in enhanced carrier mobility and carrier lifetime. Schwarzburg⁸⁰ finds similar results to that presented in Figure 77; however the authors investigate charge carrier mobility via transient photocurrent measurements. An inflection point in the measured photocurrent due to the saturation of deep trap levels was reported there⁸⁰. Nelson et al.⁸⁴ reports that multiple trapping events may occur at a broad energetic distribution of trap states located within the bandgap region. This broad exponential energy distribution of trap

states is responsible for the large range of measured recombination times⁸⁴. Ghosh et al. also report a large number of possible trapping sites for electrons or holes at differing energy levels throughout the bandgap⁷⁰.

11.4.4. Electron and Hole Scavengers on TiO₂ Surfaces

The recombination rate of excited electrons and holes directly impacts the reaction rate for any photochemical process which occurs on the substrate. The rate of recombination is affected by a number of factors including charge trapping (discussed above), the chemisorption or physisorption of target molecules and the incident light intensity among others. Often, a sacrificial electron or hole scavenger is used to decrease the recombination rate, and in turn, to increase the lifetime of the other charge carrier. This technique is commonly employed for photochemical systems involving metal oxide semiconductors like TiO₂.

Perhaps the most referenced electron scavenger used to prolong the lifetime of photogenerated holes is adsorbed molecular oxygen, which readily accepts an electron to become the superoxide ion as discussed by Anpo¹⁰⁴. Using absorption spectroscopy, Panayotov et al.⁵⁹ and others^{177,246} have observed the loss of thermally excited conduction band electrons to adsorbed O₂, forming O₂⁻. For photoproduced holes, commonly employed scavenger molecules include methanol^{26,66,69,247-249}, propanol²⁵⁰, ethanol²⁴⁷, glycerol²⁵¹ and surface hydroxyl groups²⁵².

11.5. Charge Transfer to Adsorbed Species

Interfacial charge transfer between photoactivated semiconductor surfaces and adsorbate molecules is centrally important for understanding of photochemical processes. The following section will address the interactions between adsorbed oxygen and TiO₂. In addition section 5.2 addresses the role of the adsorbate electrophilicity on the efficiency of charge transfer.

11.5.1. Oxygen Chemisorbed on TiO₂ Surfaces

The interaction between adsorbed O₂ and TiO₂ surfaces has been extensively studied on polycrystalline as well as single crystalline substrates both theoretically⁶²⁻⁶⁴ and experimentally^{8,104,253}. This section of this review addresses only very recent studies that report on the charge transfer processes that occur between the photoexcited TiO₂ substrate material and the adsorbed O₂ species.

It is well known that neutral O₂ molecules adsorb as O₂⁻ on TiO₂ surfaces¹⁰⁴ where electrons are available in the conduction band or from localized Ti³⁺ sites as measured by EPR spectroscopy¹⁰². Electrons are promoted to the conduction band or to localized Ti³⁺ sites when the sample is reduced (oxygen vacancies are present), or when the sample is activated with UV light above the TiO₂ bandgap. Electron transfer from the conduction band to adsorbed O₂ can be monitored using IR spectroscopy⁵⁹ where the decrease in the background IR absorbance is attributed to the loss of conduction band electrons to form the surface O₂⁻ adsorbate.

11.5.1.1. Fractal Kinetics for Charge Transport to Chemisorbed Oxygen during Photodesorption

Recently, work done by these authors has investigated the charge transfer kinetics for photogenerated hole transfer from the surface region of a TiO₂(110) single crystal to an adsorbed O₂ molecule. The photodesorption of O₂ from TiO₂(110) surfaces has been investigated in the past by a number of authors both experimentally^{55,60,61,107} and theoretically⁶². As discussed in Section 11.4.3, the rate for O₂ photodesorption depends linearly on the square root of the incident light intensity²⁶. The O₂ photodesorption process is affected by charge carrier trapping and the subsequent saturation of traps as described²⁶. The mechanism for the photodesorption of adsorbed O₂⁻ from TiO₂(110) is based on the activation of

the adsorbed O_2^- by a photogenerated hole that results in the neutralization of the oxygen molecule, and finally, the desorption of the neutral species⁶². The detailed reason for O_2 photodesorption when charge transfer occurs is currently unknown. When continuous UV irradiation is employed as the excitation source, the O_2 photodesorption from $TiO_2(110)$ can be observed over a time scale of hundreds of seconds as shown in Figure 79. Previous work^{55,60} has fit the O_2 photodesorption curve to a multiexponential function: the presented model described the presence of 3 types of adsorbed oxygen species (α_1 , α_2 and β), each exhibiting its own cross section for photodesorption. The results presented in reference²⁶ and ²⁵⁴ have reconsidered this model for photodesorption. The new findings suggest that it is appropriate for the O_2 photodesorption process to be described as a fractal kinetic process, as discussed below and in reference²⁵⁴.

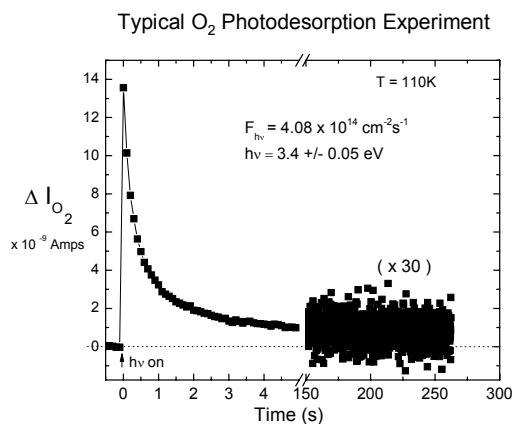


Figure 79: Oxygen photodesorption experiment for O_2 on $TiO_2(110)$. Significant desorption is still measured even after 200 seconds. Reprinted with permission from Reference²⁵⁴. Copyright 2006 American Chemical Society.

When one considers the rate of the photodesorption of O_2 from $TiO_2(110)$ according to the equations presented in Section 11.4.2, the following expression can be derived:

$$-\frac{d[\theta_{O_2}]}{dt} = -k_4 [O_2^-(a)] \left(\frac{k_1}{k_3} \right)^{1/2} \cdot F_{hv}^{1/2} \quad (11.6)$$

where the rate of change in the photodesorption of oxygen is related to the product of the rate constants. As shown in Figure 80, the product of the rate constants describing the hole excitation, hole recombination with electrons and hole transfer to adsorbed O_2^- is plotted against the relative coverage of adsorbed oxygen. The resulting plot depicts a drastic decrease in the rate constant term, $k_4(k_1/k_3)^{1/2}$, by a factor in excess of 100 over the time period of the photodesorption measurement. The change in the rate constant term during this experiment can be explained by a fractal rate law, where the rate constant, k_4 , varies as a function of coverage. The constants k_1 and k_3 are likely to be unvarying in the experiment, being determined by the solid-state properties of the TiO_2 .

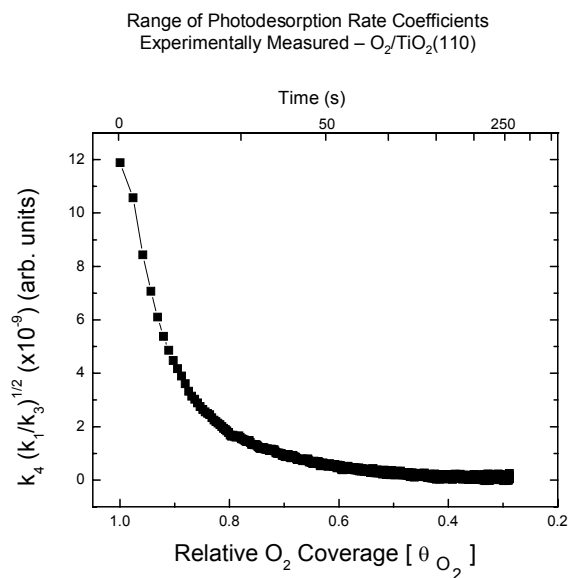


Figure 80: Plot of $k_4(k_1/k_3)^{1/2}$ for the photodesorption of oxygen from TiO_2 as a function of the remaining O_2 coverage. Reprinted with permission from Reference ²⁵⁴. Copyright 2006 American Chemical Society.

A model for the large decrease in k_4 during the O_2 photodesorption process involving a fractal kinetic rate law is described by Kopelman^{33,34,108}. In a fractal kinetic process, reactions are described with a rate coefficient, as opposed to a rate constant. The rate coefficient varies as the reaction progresses *through time* according to the following equation:

$$k_4 = k_4^0 t^{-h} \quad (11.7)$$

or

$$\ln k_4 = -h \ln t + \text{const.} \quad (11.8)$$

Figure 81 shows a scaling plot used to describe the fractal character of O₂ photodesorption from TiO₂(110) surfaces where the exponential coefficient, h , used to describe this process is found to be on the order of 0.50. According to Kopelman, the magnitude of h provides insight into the dimensionality of the fractal process that occurs on the surface. For values of h near 0.50, the fractal percolation process is characterized as being one-dimensional.

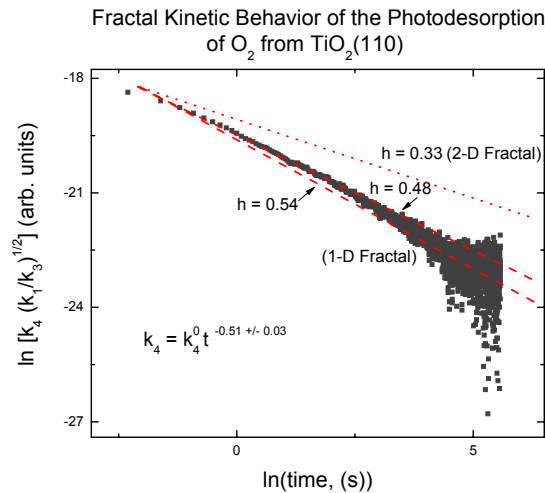


Figure 81: Scaling plot which describes the fractal kinetic behavior for O₂ desorption from TiO₂(110). The scaling factor, h , for this fit suggests that electron transport across the TiO₂(110) surface may be one-dimensional. Reprinted with permission from Reference ²⁵⁴. Copyright 2006 American Chemical Society.

Figure 82 schematically represents the postulated one-dimensional electron transport route that occurs across the surface of defective TiO₂(110). The defective TiO₂ surface has excess electrons centered at oxygen vacancies, as described earlier in this review. However, recent work by Vijay et al.³⁵ has suggested that the electrons associated with the oxygen vacancy are somewhat delocalized, thus creating a large so called ‘charge cloud’ of electron density

around the vacancy site. These charge clouds may interact with one another, providing a network of available routes for charge transfer. This network, which becomes more interconnected as the coverage of oxygen adsorbed at vacancies *decreases*, may serve to neutralize photoproduced holes. As a result, the value for k_4 will decrease as the coverage of interconnected charge clouds increases while the photodesorption process proceeds.

Schematic of Electron Transport via O-Vacancy Defect Sites, Leading to a Decreasing O_2 Photodesorption Rate Constant as Coverage Decreases

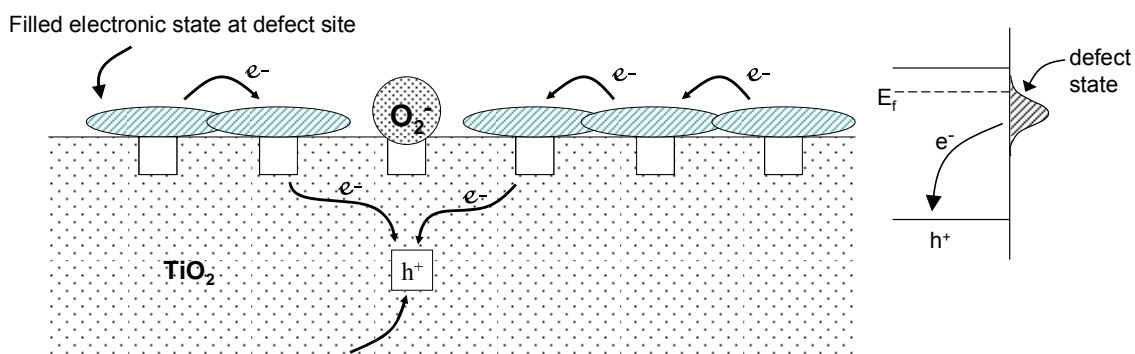


Figure 82: Diagram of the electronic charge clouds associated with oxygen vacancy sites on the reduced $TiO_2(110)$ surface. Percolation through the charge clouds at unoccupied vacancies is postulated to be one-dimensional. Reprinted with permission from Reference ²⁵⁴. Copyright 2006 American Chemical Society.

11.5.2. The Role of Adsorbate Electrophilicity on Charge Transport

As described in section 11.3.2.1, infrared spectroscopy can be employed to investigate the excitation of charge from the valence band into the conduction band for TiO_2 and mixed TiO_2-SiO_2 materials. For polycrystalline TiO_2 , it has been shown that electrons are trapped in the conduction band upon either thermal or photon excitation where they reside for long times if the temperature is sufficiently low⁵⁹. The conduction band is depopulated by warming the sample or by charge transfer from the conduction band to adsorbates on the surface.

Panayotov et al.¹⁸⁰ have investigated this charge transfer process on TiO_2-SiO_2 powdered material, where the charge transfer from the conduction band to two different adsorbate

molecules is compared. There it was found that efficient charge transfer occurs exclusively between the TiO₂ surface and an adsorbate molecule with an electrophilic moiety. No observable charge transfer occurred with a similar molecule with the electrophilic moiety removed. The adsorbate molecules employed for this work were 2-chloroethyl ethyl sulfide (2-CEES) and diethyl sulfide (DES). These molecules have the same chemical structure, except that the 2-CEES molecule has a chlorine atom on one terminus of the molecule. The charge transfer processes measured in that work is recorded as a change in the level of IR background absorbance, which is directly related to the concentration of trapped electrons in the conduction band of the TiO₂-SiO₂ mixed oxide. Figure 83 shows the change in the background IR absorbance versus the pressure of the admitted adsorbate gas. For the 2-CEES molecule, a clear decrease in the concentration of trapped electrons in the conduction band is observed as efficient charge transfer occurs from the substrate to the adsorbate. For adsorbed DES, no change in the level of trapped electrons is observed. The authors attribute this effect to the large electronegativity of the chlorine atom¹⁸⁰ and to direct electron transfer to the Cl atom in the molecule. Similar effects were also observed by Hoffmann et al.^{86,177} and Yamakata et al.¹⁷⁸. Panayotov et al.⁹⁷ also later investigated the same effect with TiO₂ as the substrate material rather than the TiO₂-SiO₂ mixed oxide. In that work, the same effect is measured. For both 2-CEES and ethyl chloride (not shown), efficient electron transfer occurs from trapped electrons in the conduction band to the Cl atom in the adsorbate molecule. Adsorbed DES does not accept electrons from the conduction band of the TiO₂. Upon charge transfer from the conduction band to either 2-CEES or ethyl chloride, ethoxy groups are formed as the reduction product for the charge transfer process⁹⁷.

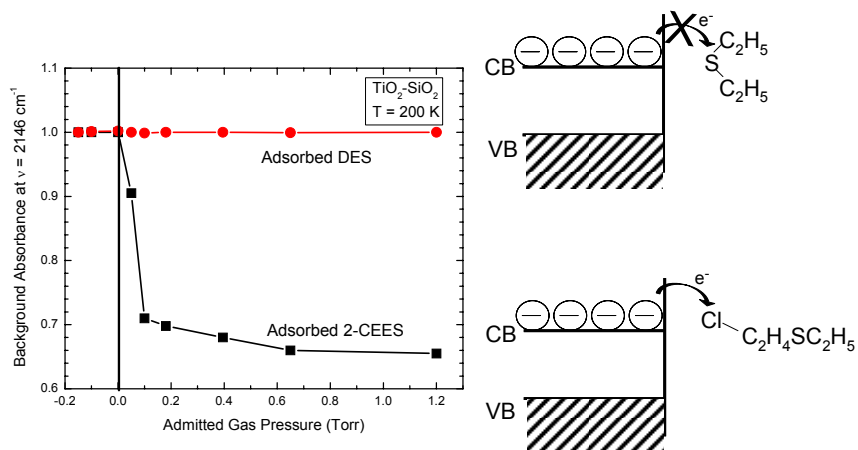


Figure 83: Preferential charge transfer from the conduction band of TiO₂ to molecules adsorbed through an electrophilic moiety. Reproduced in part from Reference¹⁸⁰. Copyright 2003 Elsevier B.V.

11.6. UV-Induced Hydrophilicity of TiO₂

11.6.1. Introduction

In addition to the photo-oxidative effect observed on TiO₂ surfaces and in suspensions of TiO₂ colloids, TiO₂ surfaces have been more recently studied with the aim to understand the UV-induced hydrophilicity effect first reported by Fujishima et al. in *Nature* (1997)²¹⁴. In that report, it was shown that the wettability of TiO₂ surfaces studied under ambient atmospheric conditions is controlled by exposure to UV light, where an apparent contact angle of the pre-irradiated TiO₂ surface was measured to be ~ 72°. After irradiation, angles of 0 – 1° were reported. This study investigated both polycrystalline films and single crystal (rutile and anatase) samples, thus concluding that the observed UV-induced hydrophilicity was an inherent property of TiO₂, and did not change based on the character of the specific type of TiO₂ material. In that work²¹⁴, Fujishima et al. propose that the UV light generates oxygen vacancies which were postulated to be active sites for water dissociation. The single crystal TiO₂ surface was observed to be

composed of both hydrophilic and hydrophobic domains (microscopic in size) as measured using frictional force microscopy. The authors proposed that the hydrophilic domains dominate the overall macroscopic interaction between the surface and the macroscopic water droplet. One year later, the same authors published a full paper including additional measurements yet still proposing the same UV-induced defect model (production of surface Ti^{3+} ions by UV)²¹⁵. In that work, the authors report evidence of the production of both hydrophilic and oleophilic domains in agreement with their earlier work. The hydrophilic domains are attributed to defect sites where dissociative water adsorption occurs and the physical reason for the development of domain structures was unexplained. The remainder of the surface is said to be oleophilic. However, the authors did recognize that hydrocarbon layers are measurable contaminants on the surface of the TiO_2 films which they investigated but they claim the hydrophilicity effect on TiO_2 is governed by UV-induced defect production. Photooxidation of hydrocarbons present in their experiments in the ambient atmosphere is considered by those authors to be an independent process unrelated to UV-induced hydrophilicity²¹⁵.

Since the publication of those early papers^{214,215}, a large amount of work has been done in order to elucidate the mechanism for the UV-induced hydrophilicity effect. Until recently, when the mechanism was clearly defined by workers in this laboratory²⁵⁵, this effect has been debated and a number of mechanisms have been proposed, most of which will be discussed in the next section. However, even without a clear understanding of this phenomenon, a large number of commercial products have been developed based on this technology, including windows and mirrors which are self-cleaning and anti-fogging. As a result, this area of metal oxide surface photochemistry has generated broad interest.

Below, we address the most commonly used techniques for measuring hydrophilic effects on TiO₂ and review a number of proposed mechanisms and experiments found in the literature. In addition, some very recent experimental results clarifying the dominant mechanism of photoinduced hydrophilicity will be presented.

11.6.2. Contact Angle Measurements

The most commonly employed and direct method for measuring surface hydrophilicity or hydrophobicity is through analysis of the water contact angle. Contact angle measurements are most simply done using the sessile drop method which has been extensively reviewed by Neumann and Good²⁵⁶, and is briefly explained here. The sessile drop method involves the placement of a droplet of liquid onto a horizontal surface and measuring the contact angle, either directly, or through analysis of a digital image of the droplet on the surface. The solid-liquid interaction at the surface obeys Young's equation as:

$$\gamma_{LV} \cos \theta = \gamma_{SV} - \gamma_{SL} \quad (11.9)$$

where γ_{LV} is the surface tension between the interface between the water droplet and the surrounding atmosphere, γ_{SV} is the surface tension between the surface and the surrounding atmosphere, γ_{SL} is the surface tension between the surface and the liquid and θ is the contact angle as shown in Figure 84. At the three-phase interface, the vector forces balance is described by equation 11.9. The measurement of droplet contact angles on a surface often involves a large variability of reported angles, and such measurements should be considered as qualitative indicators that may vary drastically with experimental conditions, including atmospheric humidity, surface contamination and/or droplet contamination, among others²⁵⁷. Additionally, contact angle measurements below 10°, signifying a superhydrophilic surface, are especially hard to analyze due to the inability to measure such low contact angles.

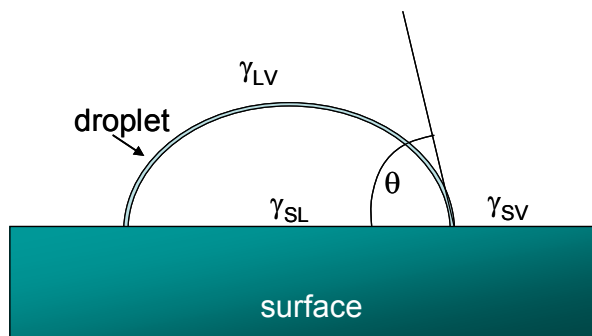


Figure 84: Diagram of the vector forces present at the solid-liquid interface. The measured contact angle (θ) is shown.

Reported contact angle measurements on titania surfaces have traditionally used a method which involves pre-irradiation of the surface in ambient air, followed by droplet placement on the surface, and then contact angle measurement. The general consensus of a great deal of work done by a number of different groups²⁵⁸⁻²⁶⁵ using this experimental protocol is that a gradual decrease in the measured contact angle occurs with increasing pre-illumination time in the air. A very recent report²⁵⁵, described in a later section, uses a technique that involves direct UV-irradiation *during* contact angle measurement, and records consecutive digital images thus enabling one to watch in real time the contact angle changes with increasing UV-illumination time. The use of this method for contact angle analysis has shown surprisingly that *sudden wetting* occurs at a critical UV exposure time. The *in situ* method shows an instantaneous wetting of the TiO_2 surface by the water droplet after some critical time period for UV illumination²⁵⁵. Further details of these measurements will be presented in Section 11.6.3.3. In contrast, all contact angle measurements made in ambient air show a gradual decrease in contact angle with increasing irradiation time, and this effect is attributed to the occurrence of continuous contamination of the surface by hydrocarbon molecules present at ppm levels in the ambient air, making such measurements ineffective for mechanistic studies of the origin of the hydrophilicity effect.

11.6.3. Proposed Models

When surveying the massive amount of literature dealing with the UV-induced hydrophilicity effect on TiO₂ surfaces, three possible mechanisms have been proposed as discussed below.

11.6.3.1. UV-Induced Defect Production

First proposed by Fujishima et al.^{214,215} at the time of the discovery of the photo-induced wetting effect, this model involves the production of Ti³⁺ ions at the surface as a result of oxygen atom ejection from the lattice. This model has since been also proposed by a number of additional authors^{258-261,266}. The defects, known as oxygen vacancies or Ti³⁺ sites, when produced on the surface by thermal activation are known to cause water dissociation^{22,221,222}, and thus for the production of adsorbed –OH species, which are known to be hydrophilic in nature. As a result, this was a first logical explanation for the UV induced hydrophilicity effect.

The UV-induced defect formation postulate was directly and quantitatively investigated and results have been reported by Mezhenny et al²¹¹. In that work, the STM was used to probe TiO₂(110) surfaces which have been irradiated extensively with known fluxes of 1.6 – 5.6 eV UV photons under atomically-clean conditions in ultra-high vacuum. Both the (1 x 1) and (1 x 2) surfaces were investigated both before and after UV irradiation. The result of this study was starkly conclusive. For the (1 x 1) surface, statistical counting of defect sites present on the surface revealed that *no* additional defects are formed with UV irradiation ($h\nu \geq 3.0$ eV) with $> 5 \times 10^{24}$ photons cm⁻². Figure 85 shows representative STM images of the TiO₂ surface before UV-irradiation and after UV exposure to $> 5 \times 10^{24}$ photons cm⁻². Statistical counting of oxygen vacancies (imaged as bright spots) revealed no statistically significant difference in the vacancy defect concentration before or after UV-illumination for these very high irradiation fluences. For

the (1 x 2) surface, which is produced by high temperature thermal annealing³, the *upper limit* of the cross section for defect formation was measured to be on the order of $10^{-23.5\pm 0.2}$ cm². The highly-reduced (1 x 2) surface is not representative of a TiO₂ surface in ambient conditions. This demonstrated insensitivity of TiO₂(110) to UV irradiation indicates that, using the average power levels reported in the literature for the UV-induced hydrophilicity effect to be seen, one would have to irradiate a TiO₂ surface for many days in order to produce the defect density necessary to cause a macroscopic change in the wetting characteristics of the surface. This work therefore provides conclusive evidence at the atomic level that the UV-induced defect formation postulate is incorrect. In addition, recent DFT calculations presented by Bouzoubaa et al.²⁶⁷ show the energy of formation of an O vacancy defect to be on the order of ~ 7 eV for rutile surfaces, confirming that UV irradiation at significantly lower photon energies cannot be responsible for vacancy formation.

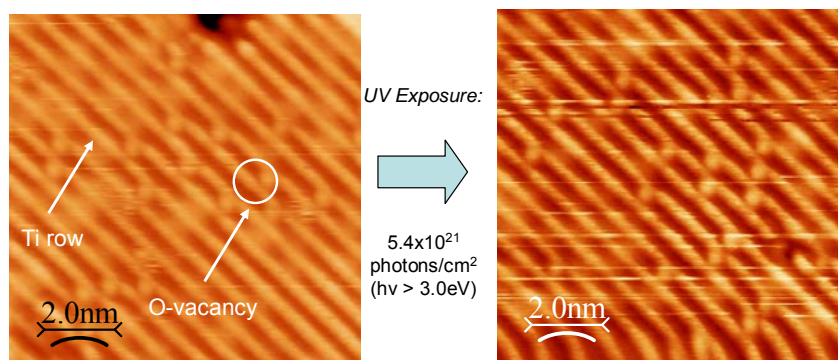


Figure 85: STM images of the partially reduced TiO₂(110)-(1x1) surface before and after UV irradiation. No additional defect formation is observed as a result of UV irradiation, negating the proposed UV induced hydrophilicity model that suggests otherwise.

11.6.3.2. UV-Induced Rupture of Ti-OH Bonding

A second model proposed by Sakai et al. in 2003²⁶², suggests that the UV-induced hydrophilicity effect is due to surface modifications, which in the presence of H₂O, lead to an

increased surface coverage of Ti-OH groups. This model was proposed on the basis of XPS, IR and electrochemical measurements. The authors explain this effect in the following way: -OH groups that are bound in 2-fold coordination to Ti atoms are converted by H₂O adsorption into two -OH groups that are singly coordinated each to their own Ti atom. Further XPS investigations done by Gao et al.²⁶⁸ suggest a similar mechanism where Ti-OH groups are converted into Ti-OH groups that are associated with dangling bonds.

Recent experiments have been done which suggest that the mechanisms suggested in References^{262,268} are invalid²⁵⁵. These experiments involve the use of a powdered TiO₂ sample which has been exposed to UV light under high vacuum conditions in order to study how UV light affects chemisorbed H₂O or Ti-OH bonds found on the TiO₂ surface. IR measurements were made after 200 minutes of sample irradiation ($h\nu = 3.82$ eV, 1.76×10^{21} photons cm⁻²), and no spectral changes were observed in the 3800-3000 cm⁻¹ hydroxyl stretching region, suggesting that no changes occur in the surface bonding character of Ti-OH groups and of adsorbed H₂O molecules due to UV illumination²⁵⁵. These spectroscopic measurements are shown in Figure 86. These experiments were done on a cooled TiO₂ sample (T = 153 K) to avoid heating by the UV lamp.

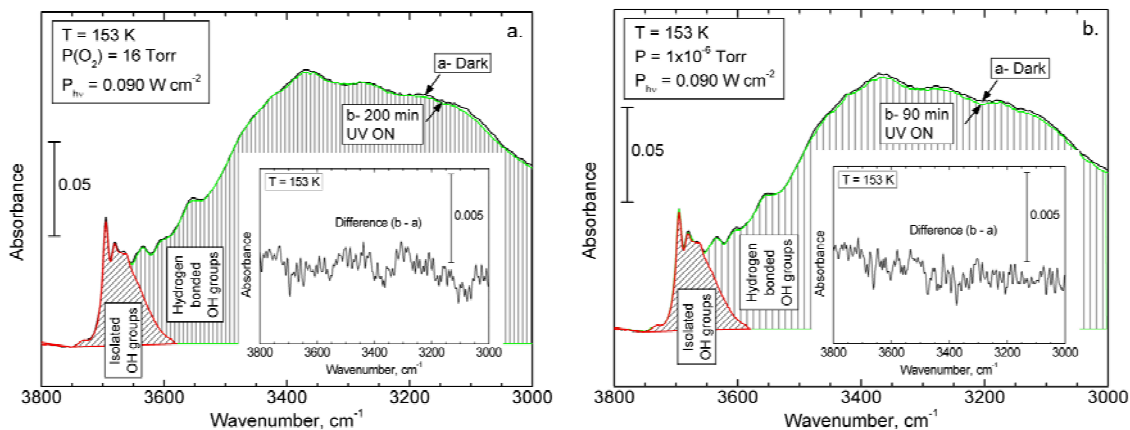


Figure 86: IR absorption spectra for –OH groups on TiO₂ both before and after UV irradiation in O₂ and in vacuum. No observed change in the spectrum due to OH groups is measured. Reprinted with permission from Reference ²⁵⁵. Copyright 2005 American Chemical Society.

11.6.3.3. Photooxidation of Hydrophobic Contaminant Layers

A third model for the UV-induced hydrophilicity effect on TiO₂ simply involves the removal of a hydrophobic hydrocarbon monolayer by photooxidation. The atomically clean TiO₂ surface produced is hydrophilic.

Work done by Wang et al.²⁶⁹ has employed sum frequency generation (SFG) as a surface sensitive technique to investigate wettability effects on nanoparticulate anatase TiO₂ films. This work notes that the as-prepared surface, while appearing to be clean when investigated using Fourier transform infrared spectroscopy (FTIR), contains trace hydrocarbon layers as measured using SFG as would be expected in any experiment conducted in an ambient atmosphere. While not proven directly, these authors suggest that the UV-induced photocatalytic removal of hydrocarbons is the explanation for the wettability effect.

The photocatalytic removal of adsorbed hydrocarbons was first postulated as the *sole cause* for the hydrophilicity effect on TiO₂ in 2003^{268,270}. However, no firm experimental proof has verified this postulate until recently. Zubkov et al.²⁵⁵ directly investigated the UV-induced

wettability phenomenon through careful study of an atomically clean rutile (110) single crystal surface, prepared in ultrahigh vacuum followed by surface characterization (Auger spectroscopy and LEED), and then exposure to a water droplet for contact angle measurements *in situ*, under highly controlled atmospheric purity conditions. The ultra-high vacuum system used was designed especially for these measurements on a TiO₂(110) crystal and utilized a preparation and analysis chamber, connected to a pressurizable ultrahigh vacuum experimental chamber (used for water droplet measurements) through a sliding seal as shown in Figure 87. Included in the design of the atmospheric chamber is a special non-contaminating syringe inlet for deposition of a droplet of highly purified water. The overpressure in the chamber keeps airborne contaminants from entering the chamber as the water droplet is deposited on the surface by a syringe needle injected through a small open tube. The chamber is pressurized with a slight overpressure of 99.9999% pure oxygen gas which was saturated with purified H₂O vapor. During some experiments, known quantities of *n*-hexane in the ppm range were added to simulate typical hydrocarbon contamination levels in an ambient atmosphere. As a result, this approach eliminates all potential contaminants that may have had a drastic effect in all experiments performed in ambient air as presented previously in the literature. The method then quantitatively adds known levels of hydrocarbon to observe the effect on the UV-induced wettability of the TiO₂(110) surface.

Apparatus for Wetting Studies

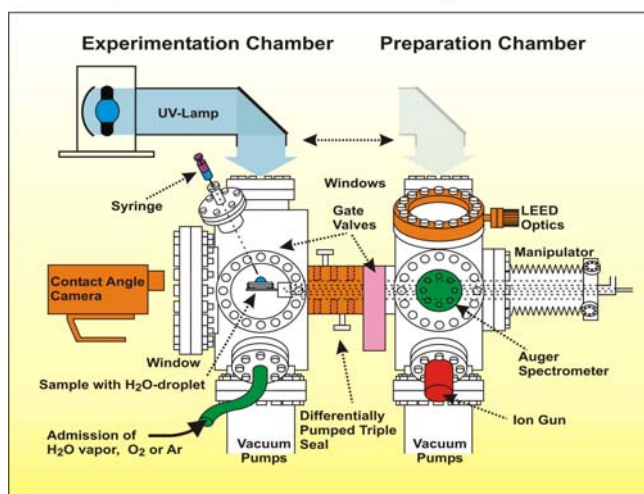


Figure 87: Diagram of the apparatus used for in situ measurements of the water contact angle on $\text{TiO}_2(110)$. Reprinted with permission from Reference ²⁵⁵. Copyright 2005 American Chemical Society.

In the studies conducted by Zubkov et al., contact angle measurements on an atomically clean $\text{TiO}_2(110)$ surface were carried out using controlled ppm levels of a model hydrocarbon, *n*-hexane, to artificially contaminate the surface. In Figure 88, it is shown that upon droplet introduction to the $\text{TiO}_2(110)$ surface in an atmosphere consisting of 1 atmosphere of pure $\text{O}_2(\text{g})$ and 120 ppm of hexane, a contact angle of $\sim 21^\circ$ is measured. After irradiation for up to 154 seconds, the contact angle remains essentially unchanged.

Typical H₂O Contact Angle Showing Sudden Onset of Wetting of TiO₂(110)

P_{O₂} = 1 atm; hexane = 120 ppm

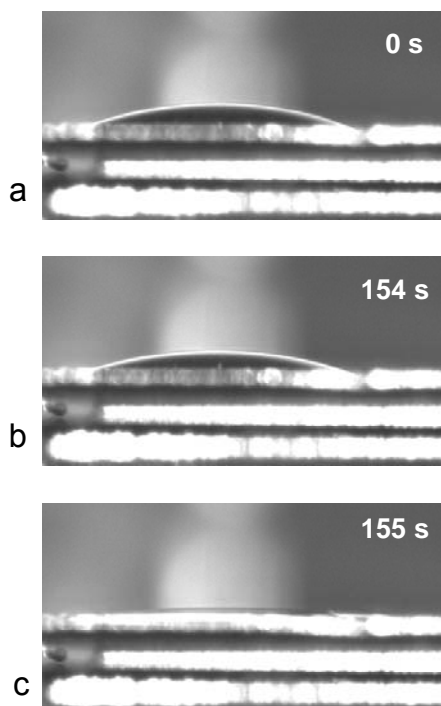


Figure 88: a) Water droplet on unirradiated TiO₂ in mixed O₂ + hexane atmosphere. b) The same water droplet after 154 seconds of UV exposure. c) Sudden and complete wetting of the water droplet on the TiO₂ surface after 155 seconds. Reprinted with permission from Reference ²⁵⁵. Copyright 2005 American Chemical Society.

At 155 seconds, the water droplet suddenly wets the surface, resulting in a contact angle below 10°. The same experiment was done using varied ppm atmospheric concentrations of hexane in O₂ exposed to the surface. At zero hexane exposure, upon irradiation, the droplet wets the surface almost immediately. A strong correlation between the steady-state coverage of adsorbed hexane in equilibrium with gaseous hexane, and the irradiation time required for sudden droplet wetting is found, demonstrating the dominant role of hydrocarbon contamination. Data for various levels of hexane exposure are shown in Figure 89 where one can see, in each case, evidence for sudden wetting after a finite induction time which is proportional to the hexane concentration in O₂ at 1 atmosphere.

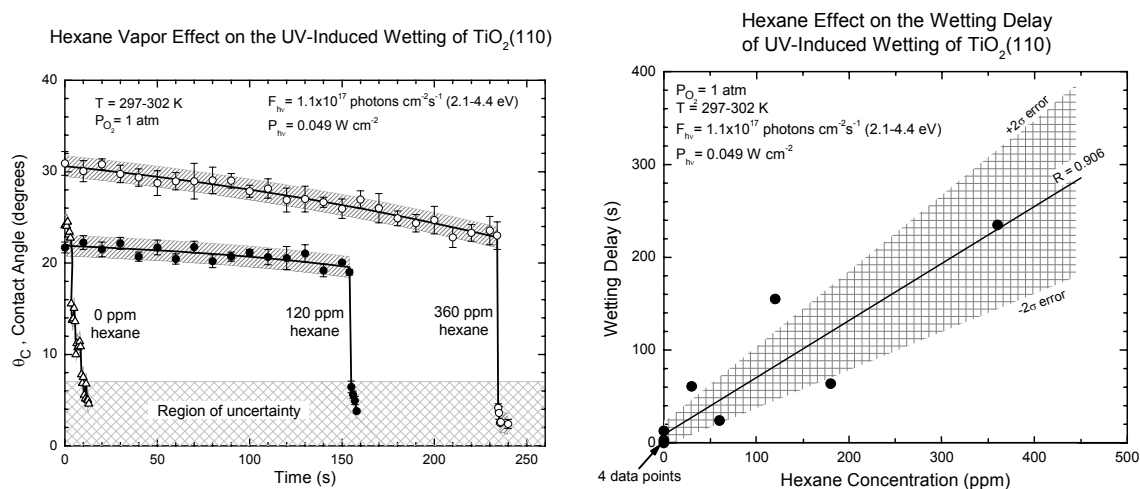


Figure 89: Measured contact angles for water droplets on the TiO₂ surface exposed to varying levels of hexane. The induction period before complete wetting increases with increasing hexane partial pressure as shown in the right hand side. Reprinted with permission from Reference ²⁵⁵. Copyright 2005 American Chemical Society.

In these experiments at 300 K, the hexane gas is in equilibrium with adsorbed hexane in a single monolayer, producing a steady state hexane coverage. When UV-induced photooxidation of the transient layer of adsorbed hydrocarbon occurs, the equilibrium is disturbed by increasing the rate of loss of adsorbed hexane due to photooxidation, and the hexane coverage in the unwet regions of the crystal slowly decreases. At the point where the coverage of adsorbed hexane reaches a critical value near zero monolayers, droplet wetting suddenly occurs. A schematic picture of this effect is shown in Figure 90. In this model, the hydrocarbon layer under the droplet is more slowly oxidized because of screening of this interfacial region from O₂ by the droplet.

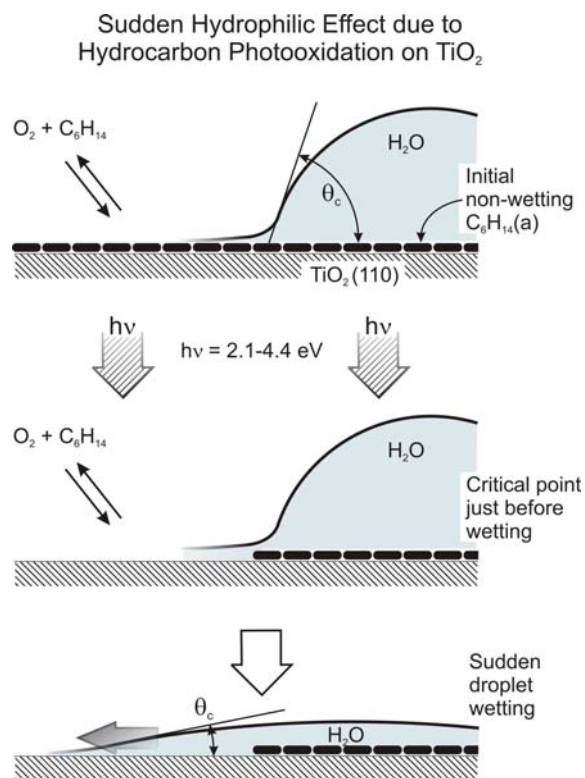


Figure 90: Diagram showing the mechanism for the measured photoinduced hydrophilicity effect on TiO_2 surfaces. Reprinted with permission from Reference²⁵⁵. Copyright 2005 American Chemical Society.

These experiments support a model for the UV-induced hydrophilicity effect on TiO_2 surfaces where the photooxidation of adsorbed organic contaminants is the dominant factor leading to a hydrophilic surface.

11.7. Summary and Outlook

This review has selectively dealt with a number of topics having to do with the photoexcitation of TiO_2 , emphasizing recent measurements and theory which are based on modern methods of investigation. In most cases, we have connected what has been discovered by physical measurement of the photoexcitation of TiO_2 to its photochemical behavior. At the present time, we are just entering a stage of understanding the photoexcitation of TiO_2 which is beginning to connect to well-known principles of semiconductor physics, based on modern

theory and modern surface science experiments at the atomic level of resolution. It is apparent that rather amazing technological developments using the photoexcitation of TiO₂ have moved far beyond our basic understanding of the electronic and chemical processes which occur when TiO₂ is excited by light. It is likely that the rapid growth of research on this topic will continue as new TiO₂-based technologies continue to stimulate the field.

11.8. Acknowledgements

We would like to thank a number of colleagues, friends and co-workers for their invaluable suggestions and discussions: Professor Hovorje Petek, Dr. Oliver Diwald, Dr. Tykhon Zubkov, Professor Clemens Burda, Dr. Cristiana Di Valentin, Dr. Horia Metiu and Dr. Mitko Panayotov. The authors would like to thank Mr. Peter Maksymovych for his help with figure design and for his STM images. We acknowledge with thanks the support of this work by the DoD Multidisciplinary University Research Initiative (MURI) program administered by the Army Research Office under Grant DAAD 19-01-0-0619.

APPENDIX

APPENDIX A

New Concepts about TiO₂-Based Photocatalysis: Surface Defects, Oxygen and Charge Transfer[∞]

A. Introduction

We report studies of photochemistry on TiO₂ surfaces using the methods of surface science. This work combines physical and chemical measurements which are focused upon the electronic excitation of the semiconductor, the transfer of trapped electrical charge to adsorbed species, and the fate of these species. A number of reviews of the photophysics and photochemistry which occurs with TiO₂ are available^{23,56,58}. In addition, the surface behavior of TiO₂ has been extensively studied following various thermal and chemical treatments, and a recent excellent review has been published³.

This contribution is a review of recent published work in the field as well as a report of related studies which have been done in the authors' laboratory, woven together to reflect current understanding in a rapidly changing area.

TiO₂ is of great interest because of its ability to catalyze the photooxidation of organic molecules. TiO₂ mediated photooxidation may be used for environmental remediation, where toxic materials at low concentrations are photocatalytically converted, in a series of chemical steps, to harmless oxidation products such as CO₂ and H₂O. The photocatalytic activity of TiO₂ has been recognized since the pioneering studies of water reduction through photoexcitation of TiO₂ by Honda and Fujishima in 1972¹.

[∞] Reproduced in full with permission from Tracy L. Thompson and John T. Yates, Jr. "TiO₂-based photocatalysis: surface defects, oxygen and charge transfer" *Topics in Catalysis*, **35** (2005) 197-210. Copyright 2005 Elsevier, B. V.

It is now recognized that oxygen vacancy defects on the surface of TiO_2 play an essential part in governing the adsorption of O_2 , where O_2 molecules seek the vacancy defect sites for non-dissociative adsorption, producing the superoxide species, O_2^- . This takes place by O_2 interaction with surface Ti^{3+} sites which are produced by thermal reduction of the surface by removal of surface O^{2-} anions.

Adsorbed O_2 molecules can also act as electron scavengers when electron-hole pair creation occurs by photoexcitation in the TiO_2 , also producing superoxide O_2^- species. Adsorbed O_2^- may then interact with photogenerated holes, which results in the desorption of $\text{O}_2(\text{g})$. Finally, the adsorbed O_2 , when excited by electron-hole pair production in the TiO_2 , acts as an oxidizing agent for organic molecules on the surface of the TiO_2 .

Because of the grand challenge to efficiently utilize sunlight to photoexcite TiO_2 , many workers have used the electronic doping of TiO_2 by foreign atoms to reduce the photothreshold energy below the bandgap of undoped TiO_2 (3.0 eV). In this report/review, we discuss the use of nitrogen dopant for this purpose, showing that a favorable reduction of the photothreshold energy (< 3.0 eV) occurs when $\text{N}^{\text{III}}\text{H}$ species are introduced into the TiO_2 lattice by chemical means involving high temperature exposure to NH_3 . In contrast to $\text{N}^{\text{III}}\text{H}$ doping, nitrogen atoms, substitutionally introduced by ion implantation as N^{V} , cause the photothreshold energy to move to higher energies (> 3.0 eV).

The understanding of the excitation of TiO_2 by photons has recently been enhanced by EPR and IR studies of the production of trapped electrons and holes in the semiconductor. In addition, the transfer of trapped charge to sufficiently electrophilic molecules adsorbed on the TiO_2 surface has been observed by EPR and IR spectroscopy, and a brief report of this work concludes this report.

B. Results and Discussion

i. Defect Creation and Detection on TiO₂(110)

Defects on the TiO₂(110) surface are easily created by electron bombardment, sputtering, or simply by thermal annealing the surface to high temperatures. Thermally-created defects have been recognized extensively in the literature as point defects that exist as oxygen vacancy sites located within the bridging oxygen rows of the TiO₂(110)-(1 x 1) surface. The creation of these defects has a profound effect on the electronic properties of the surface. Macroscopically, the presence of oxygen vacancies creates an overall reduced state of the TiO₂ crystal, both in the bulk and in the surface. Upon the annealing, the creation of defects within the bulk is associated with the creation of color centers and Ti³⁺ interstitial ions¹¹⁸, and an overall reduced stoichiometry as a result of the loss of oxygen atoms. This effect occurs on the surface as well, where the presence of an oxygen vacancy site leaves an exposed Ti⁺³ ion which may be visualized as a Ti⁴⁺ ion associated with a somewhat localized electron. It has been shown by many authors that this site is an active adsorption site for adsorbates, and that interesting chemistry may occur at this Ti³⁺ site. The stoichiometric state of the surface can be regained by annealing the crystal in a flux of oxygen to high temperature¹¹⁷. This treatment has been studied by scanning tunneling microscopy (STM) and shown to completely re-oxidize exposed Ti⁺³ atoms as well as interstitial titanium ions that diffuse from the bulk to the surface during annealing^{9,117,271}. This treatment causes the incorporation of oxygen into the surface layers of the TiO₂ resulting in the addition of layers of TiO₂ to the surface²⁷². The lack of surface defects as a result, leaves the surface relatively inactive chemically. The process of reduction and oxidation of the surface layers is reversible, although extensive annealing of the crystal leads to high concentrations of Ti³⁺ interstitials, extensive bulk oxygen loss and the formation of

crystallographic shear planes ⁶. While annealing in O₂ oxidizes surface vacancies, the high concentration of thermally created defects remaining within the bulk may lead to eventual inactivity as a photocatalyst and to irreversible changes to the electronic structure of TiO₂(110). Further experimental details on this issue and its critical importance to the overall surface morphology and overall activity of the crystal can be found in the literature ^{6,117,222,272,273}.

Recently, it was shown that the presence or absence of thermally-created defect sites can be easily probed with the temperature programmed desorption (TPD) technique ¹⁵. This probe involves the adsorption of a test molecule, namely CO₂, to either the reduced or oxidized surface of the crystal. The subsequent CO₂ thermal desorption from the crystal (reduced or oxidized) provides insight into the overall reduction state of the crystal. Previously, the adsorption of CO₂ on defective TiO₂ was considered by M. Henderson ²². There, a two peak thermal desorption spectrum was measured and attributed to CO₂ bound to the regular sites on the surface, as well as the defective Ti⁺³ (oxygen vacancy) sites. This concept was then applied by Thompson et al. ¹⁵ to the oxidized surface and to surfaces of varying defect density produced by thermal annealing. The results of this set of experiments showed the following: CO₂ chemisorbs on defect sites within the TiO₂(110) surface with a significantly higher binding energy (54.0 kJ mol⁻¹) than on regular sites (48.5 kJ mol⁻¹). Annealing the oxidized surface to temperatures near 600 K creates low coverage of defects while annealing at 900 K causes the fraction of defect sites to reach a maximum. The difference in the CO₂ TPD spectra observed for the oxidized surface and for the surface produced at 900 K is presented in Figure 91. The inset, showing a departure from Langmuirian adsorption kinetics, indicates that at 120 K, CO₂ adsorbs by a mobile-precursor mechanism.

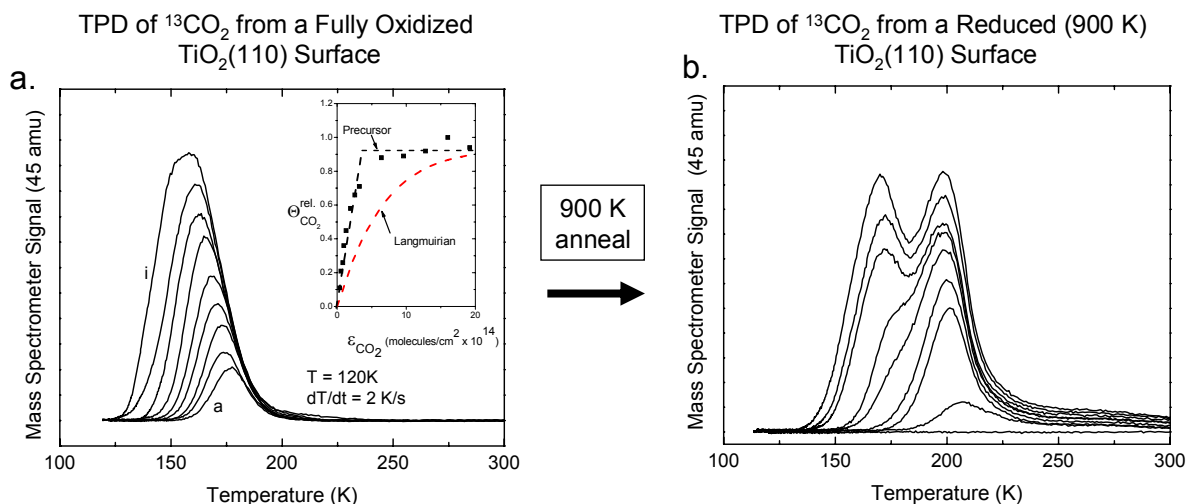


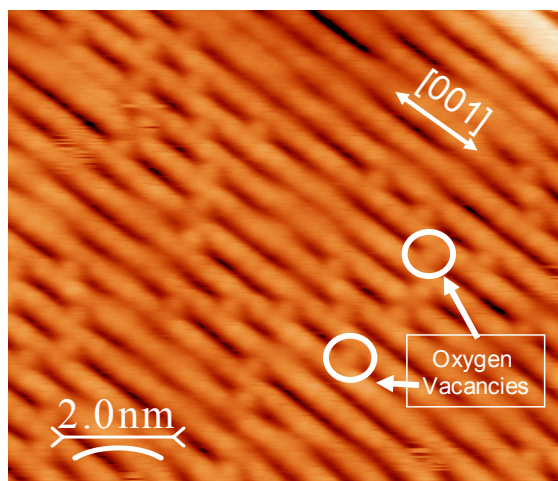
Figure 91: CO_2 TPD from oxidized (left) and reduced (right) $\text{TiO}_2(110)$ surfaces. Inset to Figure 91a shows a departure from Langmuirian kinetics, proving that CO_2 adsorbs through a mobile precursor mechanism. Figure 91a and b are taken from Reference ¹⁵.

Other work previously done in this laboratory also exploits an adsorbate specific test in order to determine the presence or absence of vacancies. Lu et al. ¹⁶ were able to clearly show that by adsorbing a test molecule on the defective surface as well as on a fully stoichiometric surface and comparing the results of temperature programming, one can observe the reactivity of thermally-created defect sites and can measure their relative population. Specifically in that work, thermally-created defect sites were shown to be active for the reduction of $^{13}\text{CH}_2\text{O}$ to $^{13}\text{C}_2\text{H}_4$ and ^{15}NO to $^{15}\text{N}_2\text{O}$. Experiments performed using a more simple adsorbate, O_2 , were reported by Lu et al. ^{55,60} where it was shown that the presence of defects is necessary for the UV-induced photodesorption of molecular oxygen. Later work done by Rusu et al. ¹⁰⁷ showed that the intensity of photodesorbing oxygen has a direct correlation to the defect density on the thermally annealed $\text{TiO}_2(110)$ surface. Also, a combination of temperature programmed desorption and electron energy loss spectroscopy has been used by Henderson et al. ⁸ to show that molecular oxygen does not adsorb between 100 and 300 K on the fully-oxidized surface

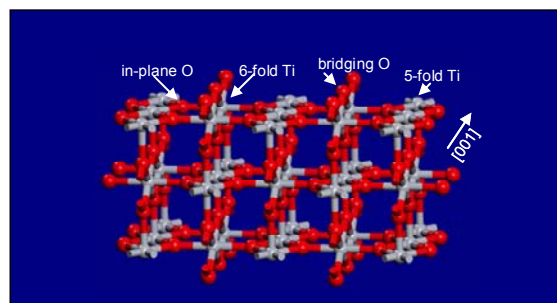
which does not contain vacancies. However, when vacancies are present, oxygen adsorbs both in a molecular and an irreversible dissociative manner, depending on the exposure of oxygen and on the adsorption temperature. This behavior has been recently confirmed by theoretical methods²⁷⁴. Because the chemistry of oxygen is critical to the observed photocatalytic activity of TiO₂ surfaces, more related work will be presented in the following section.

While the use of chemical methods to detect oxygen vacancies on TiO₂ has the advantages of being straightforward, it cannot give the information necessary to analyze the surface morphology and structural changes that may occur with the production of defects. For this reason, the use of tools such as scanning tunneling microscopy (STM) and other imaging techniques has greatly enhanced the understanding of the structure of thermally-created defects on the TiO₂(110) surface. Much work has been done by a number of different groups with STM to better understand the nature of surface defects^{12,120,220}.

a) STM Image of the Reduced (900 K) $\text{TiO}_2(110)-(1 \times 1)$ Surface



b) $\text{TiO}_2(110)-(1 \times 1)$



c) $\text{TiO}_2(110)-(1 \times 2)$

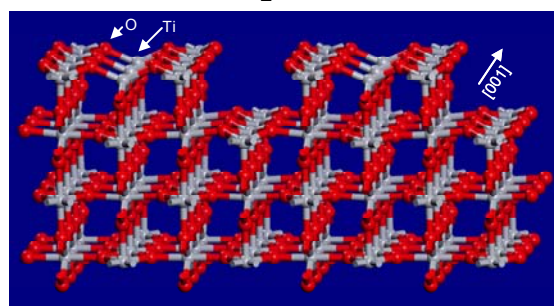


Figure 92: (a) STM image showing the point defects (oxygen vacancies) on the $\text{TiO}_2(110)$ surface. Image taken from Reference ²¹¹. (b) Structural diagram of the $\text{TiO}_2(110)-(1 \times 1)$ surface. (c) Structural diagram of the $\text{TiO}_2(110)-(1 \times 2)$ surface presented by Pang et al. ¹²¹.

Figure 92 shows a representative image of the $\text{TiO}_2(110)-(1 \times 1)$ surface that has been thermally annealed to 900 K ²¹¹. This image clearly shows rows of titanium atoms, imaged as bright lines, and rows of bridging oxygen atoms, imaged as dark lines using a positive sample bias to detect empty states. Oxygen vacancies are shown as bright spots within the rows of bridging oxygen atoms (a titanium atom is seen at an oxygen vacancy). A recent comprehensive review by Diebold discusses in great detail the STM images of defect sites on titania ³.

Because the interaction of UV light is critical to the use of TiO_2 as a photocatalyst, it is necessary to understand any changes in the surface that may occur as a function of UV irradiation. This effect was studied by Mezhenney et. al. ²¹¹ where STM was used to determine the effect of UV light on the defect density of the $\text{TiO}_2(110)$ surface. In that work, no evidence was found to suggest that additional defects were formed in the presence of UV light (1.6 eV –

6.2 eV; 0.9 W cm^{-2} for $h\nu > 3.0 \text{ eV}$) on the $\text{TiO}_2(110)$ -(1 x 1) surface. This work would have been sensitive to a cross section of $Q > 10^{-24} \text{ cm}^2$ for the photo production of defect sites. However, for the highly-reduced state of the surface, where the (1 x 2) reconstruction of $\text{TiO}_2(110)$ is present, UV light had a significant effect. It was shown that high photon fluences of broadband UV irradiation were responsible for the propagation of long “line defects” observed as rows of oxygen atom loss in the $\langle 001 \rangle$ direction. The exact nature of these UV-induced long line defects is not currently understood; however this result plays an important role when considering photo-processes that may occur on the defective surface in the presence of UV light. Even here, the cross section for defect production by UV light is only $10^{-23.5 \pm 0.2} \text{ cm}^2$.²¹¹

The work presented in this section has focused mainly on the thermal creation of defects in the $\text{TiO}_2(110)$ surface. However, it is important also to consider the nature of defects created by other means. The presence of defects, as shown by a number of methods, has a direct effect on the electronic structure of the surface and bulk. Some very recent work by Onda et al.¹³ using two-photon photoemission spectroscopy (2PPE) gives insight into defect production on the $\text{TiO}_2(110)$ surface. 2PPE is a valuable tool for the measurement of the work function change as a result of the influence of defects or the presence of adsorbates. This work considers defects created by 3 different methods: 1) thermal annealing; 2) electron bombardment; and 3) Ar^+ sputtering. Figure 93a shows the drastic changes in the work function of $\text{TiO}_2(110)$ as a result of defect generation by the three methods listed above. A band energy diagram showing the 2PPE excitation process and the energy distribution for photoemitted electrons is shown in Figure 93b. As may be seen in Figure 93b, as the final state energy of the 2PPE cutoff decreases, the work function Φ , decreases. The decrease in work function occurs as O^{2-} ions are removed from the surface. Also the intensity of the 2PPE spectra will increase as the defect concentration increases

and the work function decreases. From Figure 93a, it is clear to see that the surface prepared by Ar^+ sputtering creates the greatest defect density (lowest surface oxygen concentration), and the lowest work function where a decrease of ~ 1.0 eV is observed.

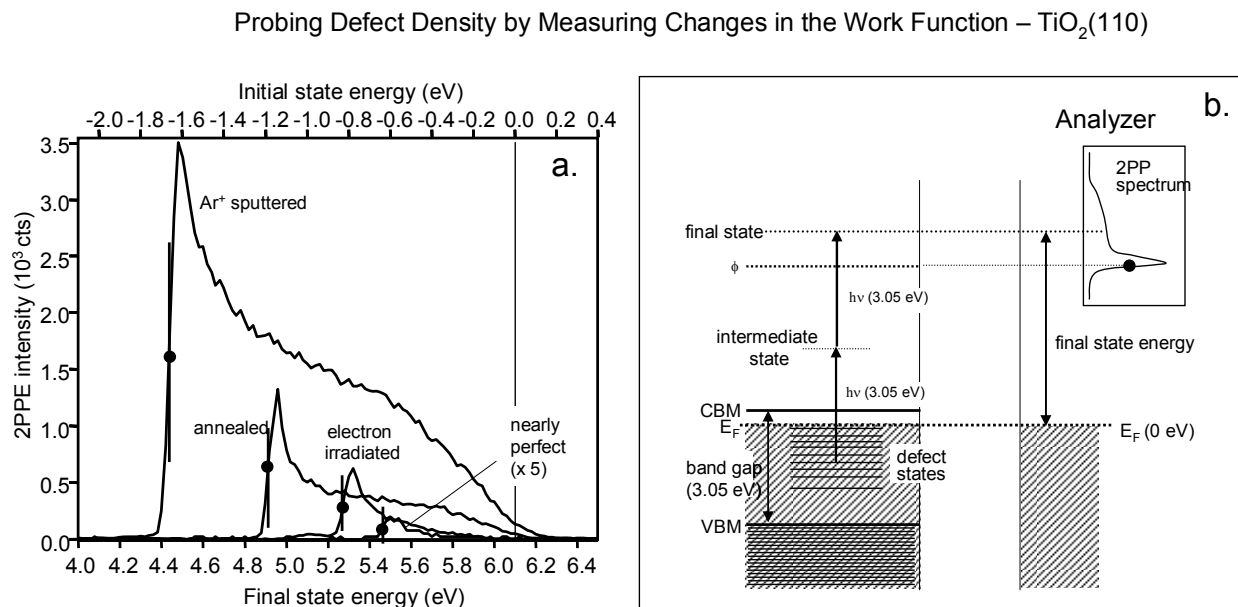


Figure 93: Figure 93a shows the 2PPE spectra for $\text{TiO}_2(110)$ with varying defect densities. Figure 93b is a representative band energy diagram depicting the 2PPE process. The figure has been slightly modified from reference ¹³.

More information was obtained in this study by using the same method to again probe the change in work function to each surface (with different defect density/ defect type) when oxygen and water were adsorbed. The adsorption of oxygen even at low temperature on the electron-irradiated surface heals most of the surface defects, but the same effect is not observed for annealed and Ar^+ sputtered surfaces. These measurements suggest that electron irradiated surfaces contain only surface bridging oxygen vacancies, which are healed by exposure to molecular oxygen, whereas annealed and Ar^+ sputtered surfaces contain surface bridging oxygen vacancies as well as other defects, proposed to be subsurface defects or more “highly reduced surface species”. These sorts of defects are not healed by addition of oxygen at low temperature.

A mechanism for formation of oxygen vacancies created by electron bombardment was presented by Knotek and Feibelman²⁷⁵ where they postulate and explain O^+ ejection from the TiO_2 surface as a result of electron stimulated desorption. The Knotek-Feibelman mechanism applies directly to high energy electron-induced processes. This work serves to provide insight into the interatomic Auger processes which may be useful in considering other processes that may occur on TiO_2 . In their model, shown schematically in Figure 94, holes are initially created in the $Ti(3p)$ core level (Step 1 in Figure 94) by energetic electron bombardment (e^-). Because no valence electrons on Ti^{4+} cations exist, the main route for the $Ti(3p)$ hole decay is an interatomic Auger process by which the 2 electrons necessary for the hole decay originate from a surface oxide ion. The O^{2-} lattice ion has filled states that exist at higher energies than the core $Ti(3p)$ hole. These electrons may be removed by a “double-Auger” process (Step 2 in Figure 94) where the $Ti(3p)$ hole is filled and 2 Auger electrons are ejected. The result produces an O^+ ion which is energetically repelled in a Coulomb explosion (Step 3 in Figure 94). This mechanism is consistent with the findings of Onda¹³ and others¹⁴ where ESD is observed to create only oxygen vacancies.

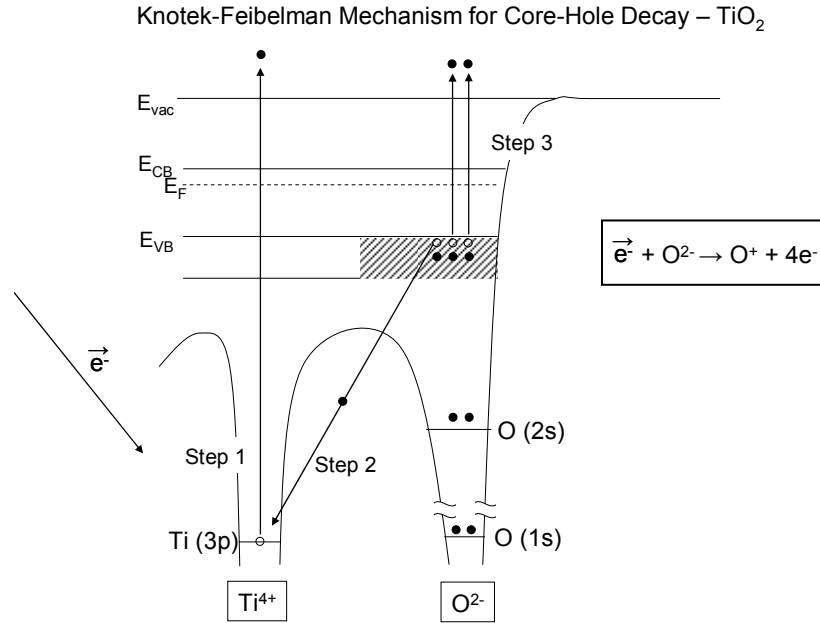


Figure 94: Band energy diagram depicting the Knotek-Feibelman mechanism for core hole Auger decay after electron bombardment^{275,276}, leading to O⁺ ejection (Electron Stimulated Desorption, ESD).

The comparison of the nature of electron beam induced defects and Ar⁺ sputtering induced defects has also been presented by Wang et al.^{14,19} where they show that the addition of water to both types of defective surfaces results in very different situations. For electron beam irradiated surfaces, the addition of water completely heals defects; however, defects still remain upon water addition to the Ar⁺ sputtered surface¹⁹. Similar conclusions were reached by Pan et al.⁷ when they compared the fully-oxidized, vacuum-annealed surface to an Ar⁺ sputtered surface of TiO₂(110) using low energy ion scattering (LEIS) and X-ray photoelectron spectroscopy (XPS).

ii. Molecular Oxygen Adsorption on Defective TiO₂

The interaction of O₂ with TiO₂ is important for a number of reasons. Molecular oxygen is the oxidizing reagent for many photooxidation processes which are catalyzed by TiO₂. Photooxidation on TiO₂ surfaces forms the basis for a major technology where TiO₂ is used for environmental cleanup processes, driven either by the UV component of sunlight, or by artificial

UV irradiation. In addition, molecular oxygen is an electron scavenger at TiO₂ surfaces, and in the presence of scavenging oxygen molecules, the photogenerated holes, which ultimately drive surface photooxidation processes, experience longer lifetimes due to the reduction of their recombination rate with electrons.

Adsorbed oxygen molecules also provide a method for the investigation of photochemistry on TiO₂ surfaces. As presented in the last section, the adsorption and successive thermal desorption or photodesorption of O₂ can give insight into the concentration of surface defects on the TiO₂(110) surface¹⁰⁷. In addition to this, the adsorption and photodesorption of oxygen can serve as a method for determining the UV photoactivation threshold energy for TiO₂ surfaces.

Because the reduced TiO₂ surface has a localized electron density at or near exposed Ti³⁺ atoms, molecular oxygen adsorbs readily at these sites⁸. Evidence from electron paramagnetic resonance spectroscopy reveals that adsorbed oxygen on reduced titania powders exists as the superoxide species, O₂⁻¹⁰⁴. This effect has also been investigated and confirmed theoretically where results show the formation of O₂⁻ upon adsorption⁶⁴. In addition to the natural charge exchange experienced by O₂ from Ti³⁺ defect sites, UV light produces excited electrons in TiO₂ which also may be scavenged by adsorbed O₂, making O₂⁻ surface species.

The production of electron-hole pairs (resulting from UV excitation) can cause the capture of a hole by O₂⁻(a), and as a result, neutral molecular oxygen is photodesorbed. This process is shown schematically in Figure 95.

Schematic Diagram for the Photo-Induced Desorption of O_2 from $TiO_2(110)$

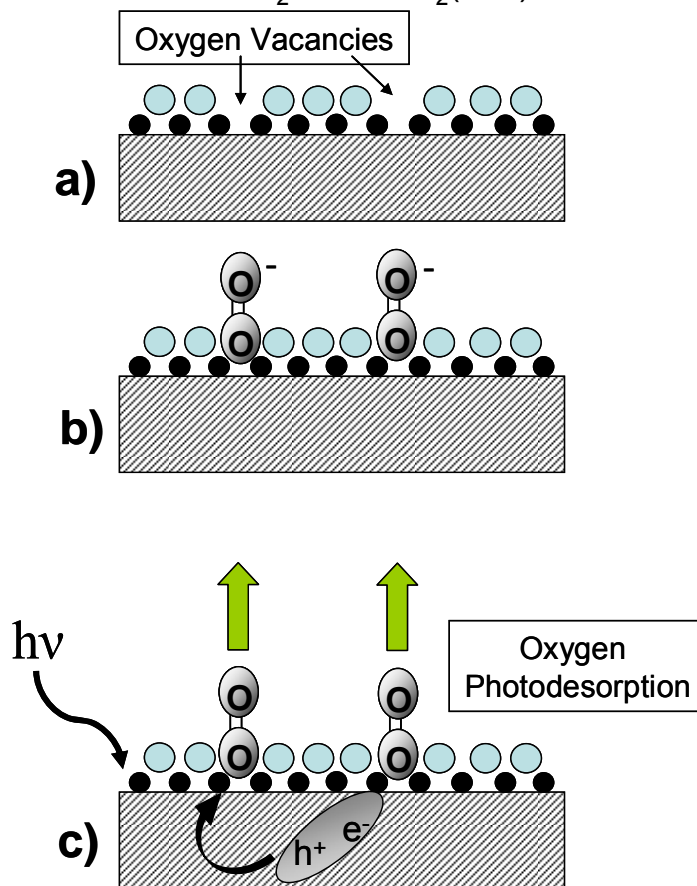


Figure 95: Schematic diagram showing the mechanism for O_2 adsorption and photo-induced desorption from a defective $TiO_2(110)$ surface.

The explanation for this desorption mechanism relies on the electronic structure of the reduced TiO_2 which is an n-type semiconductor that undergoes upward band bending upon oxygen addition to the surface. As a result, holes can readily migrate to the surface, and in turn neutralize the adsorbed O_2^- species²⁷⁷. The effect of the neutralization (hole capture) and subsequent photodesorption of oxygen into the gas phase is directly related to the ability to create electron-hole pairs, which occurs when the TiO_2 is excited with energies at or above the bandgap energy. For this reason, the photodesorption of oxygen from TiO_2 has been shown to be photon-energy dependent⁵⁵. Figure 96 is consistent with earlier findings⁵⁵, clearly showing the onset of oxygen

photodesorption at the known bandgap of rutile TiO_2 , (3.0 eV). Recent work has focused on theoretically explaining the UV induced phenomena of O_2 photodesorption from a reduced $\text{TiO}_2(110)$ surface ⁶². The authors present results of *ab initio* Hartree Fock calculations that consider the reduced $\text{TiO}_2(110)$ using a cluster model. They confirm the mechanism in which hole-capture induces photodesorption of O_2 from TiO_2 . In addition, they present a theoretical O_2 photodesorption yield (also shown in Figure 96) versus photon energy that is consistent with the work originally presented by Lu et al. ⁵⁵, and with the results of Figure 96. In addition to the primary O_2 photodesorption process beginning near 3.0 eV, the theoretical studies suggest that other O_2 photoexcitation processes must occur due to deviations in the onset energy and shape of the experimental desorption versus photon energy profile for O_2 photodesorption from $\text{TiO}_2(110)$ compared to that calculated ⁶².

O₂ Photodesorption Yield versus Photon Energy:
Experimental versus Theoretical Results - Reduced TiO₂(110)

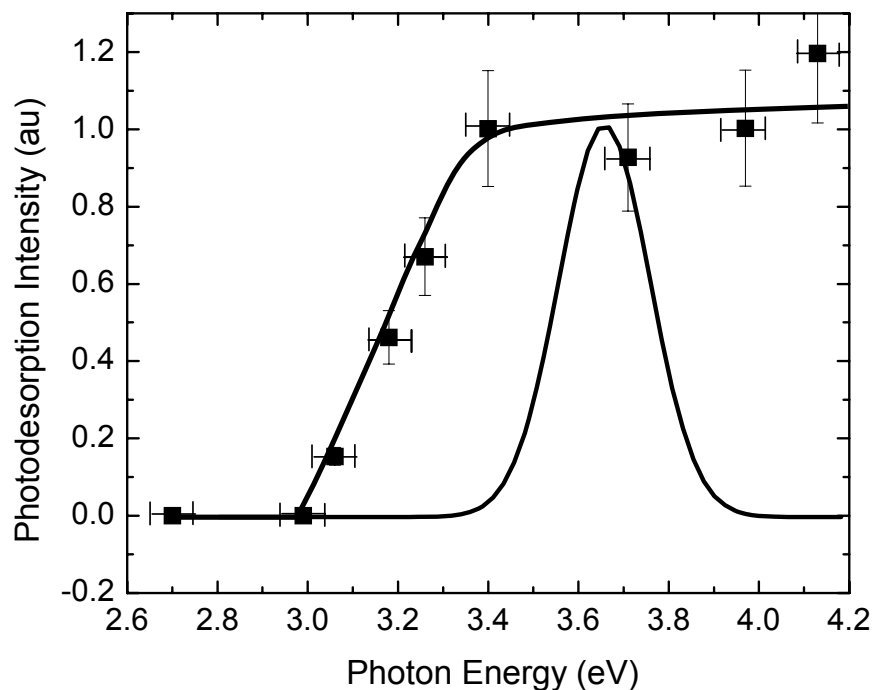


Figure 96: Experimental data for O₂ photodesorption yield versus photon energy (shown as ■) and the theoretical results for the same process⁶².

The UV induced photodesorption of O₂ from TiO₂ has been shown to be first-order in photon flux and O₂ coverage, and careful analysis of the photodesorption signals show clear evidence for at least 2 photodesorption channels for O₂ from TiO₂⁶⁰. The two channels are deconvolved based on their respective cross sections where the α -channel undergoes slower photodesorption ($Q = \sim 10^{-17} \text{ cm}^{-2}$) and the β -channel undergoes faster photodesorption ($Q = \sim 10^{-15} \text{ cm}^{-2}$). It was found that the α -O₂ species can irreversibly convert to the β -O₂ species upon mild thermal activation (300 K). This observation suggests that α -O₂ species can convert to β -O₂ species either by a chemical change at the O₂ adsorption site, or by migration to another TiO₂ site, where the species changes chemically. Lu et al.⁶⁰ defined the 2 species in the following

way: the first channel (α) has the ability to photooxidize CO into CO₂ and has a lower photodesorption cross section than the second species (β) which does not play a role in CO oxidation and is observed to only photodesorb. The authors of this work propose that the 2 photodesorption channels for adsorbed oxygen may be explained by the presence of both a superoxide type O₂ (O₂⁻), which has been confirmed by a number of authors^{8,64}, as well as a peroxy type O₂ (O₂²⁻). Although the O₂²⁻ types have not been spectroscopically investigated (peroxy species are not paramagnetic, thus unobservable by EPR), their presence is likely due to the availability of somewhat delocalized electrons near defect sites, readily available for transfer to adsorbates. The thermal conversion of α -O₂ to β -O₂ may be observed clearly by studies of the kinetics of photodesorption as the O₂-saturated surface is annealed from 105 K to 350 K, as shown in Figure 97. For O₂ adsorbed at 105 K, a photodesorption curve exhibiting a long tail (and hence a low photodesorption cross section ($Q_{\alpha} \approx 10^{-17} \text{ cm}^2$)) is measured. As the adsorbed oxygen is annealed to higher temperatures in sequential experiments, the desorption tail becomes sharper, and measurements of its shape yield a higher photodesorption cross section ($Q_{\beta} \approx 10^{-15} \text{ cm}^2$)⁶⁰. When the adsorbed O₂ species are used to photooxidize coadsorbed CO, it is seen that the α -O₂ species are singularly active for CO₂ formation, as shown by the sequence of CO₂ photoproduction plots in the right-hand side of Figure 97. Here, it may be seen that the thermal conversion of α -O₂ to β -O₂ leads to the termination of reactivity with CO, and the CO₂ photoproduction rate drops to zero.

The α -O₂ → β -O₂ Thermal Conversion Process – Relation to CO Photooxidation to CO₂

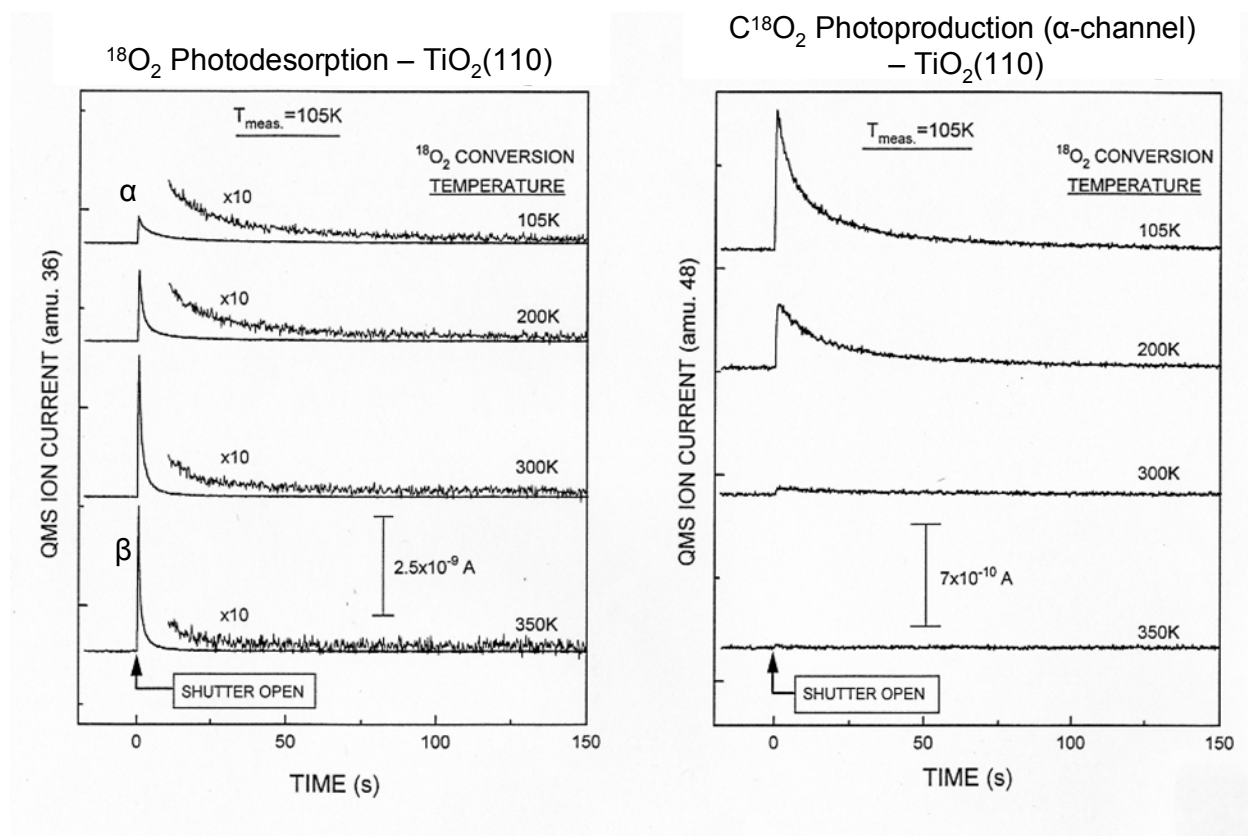


Figure 97: Data for O₂ photodesorption and the correlation to the CO₂ yield from CO oxidation as a result of the presence of α -type O₂. Figure taken from reference ⁵⁵.

Perkins et al. have combined photodesorption studies of O₂ with thermal desorption studies ⁶¹. They find multiple states of adsorbed O₂ which exhibit differing cross sections, but one state observed (which desorbs at ~ 400 K) cannot be related to the α -O₂ species or the β -O₂ species shown in Figure 97, because both either convert or desorb by 400 K ^{55,60}.

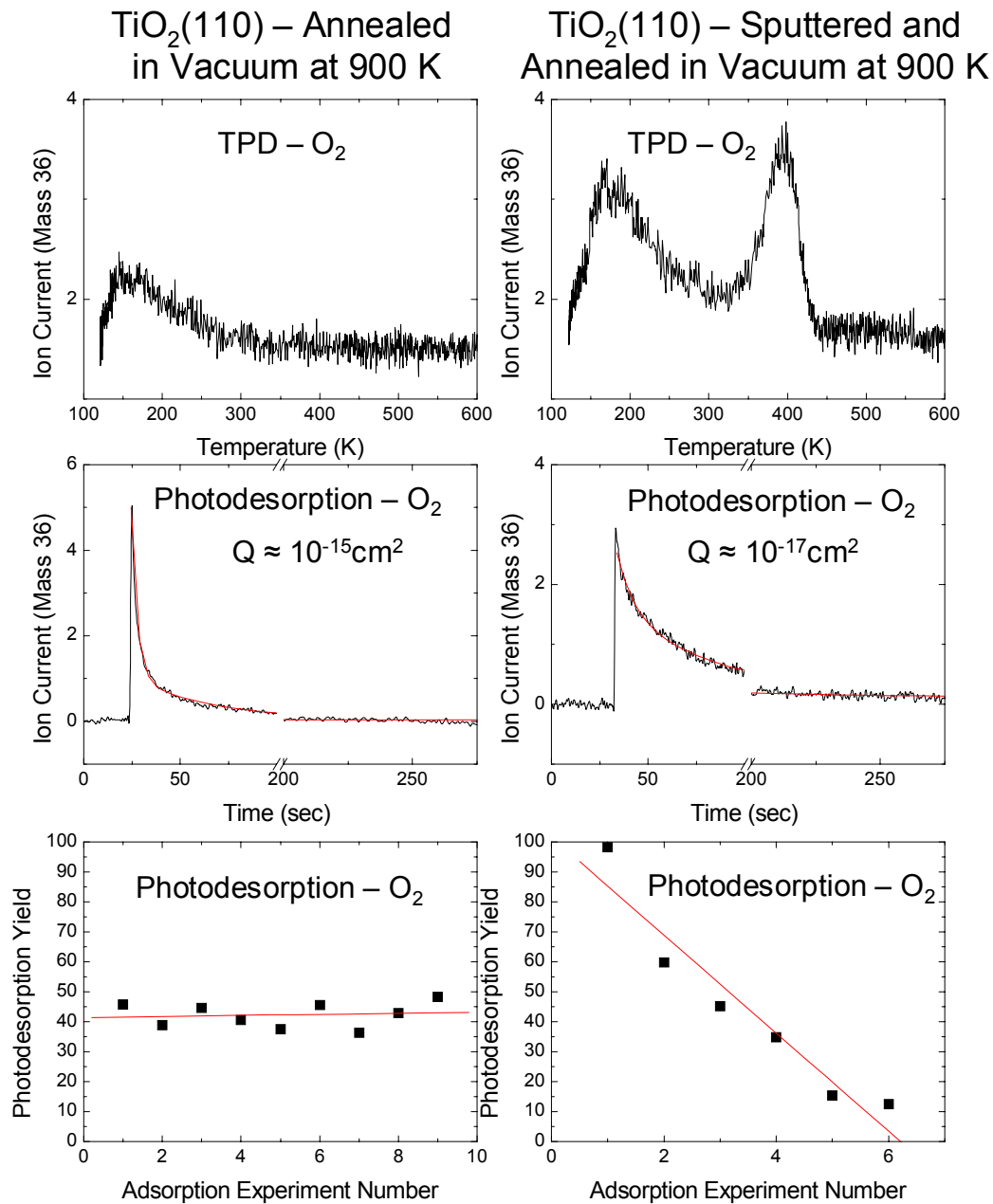


Figure 98: Data for the thermal- and photo- desorption behavior for $\text{TiO}_2(110)$ surfaces prepared either by annealing in vacuum, or by sputtering and annealing.

Figure 98 illustrates the role of different surface preparations for the $\text{TiO}_2(110)$ surface in producing differing photodesorption and thermal desorption properties of adsorbed O_2 . In the left hand part of Figure 98, three experiments are shown for a surface which has been annealed in O_2

and then made defective by annealing in vacuum at 900 K. Three properties are measured: (1) a low temperature O₂ thermal desorption process is observed; (2) O₂ photodesorbs with a high cross section ($Q \approx 10^{-15} \text{ cm}^2$); (3) repeated adsorption of O₂ does not remove sites capable of photodesorbing O₂. In contrast to the behavior shown in the left part of Figure 98, a crystal which has been ion bombarded and then annealed at 850 K in vacuum shows entirely different behavior: (1) both low and high temperature O₂ thermal desorption processes are present; (2) O₂ photodesorbs with a low cross section ($Q \approx 10^{-17} \text{ cm}^2$); (3) repeated adsorption of O₂ leads to depletion of sites capable of photodesorbing O₂, suggesting the dissociative adsorption of O₂. These results illustrate that surface preparation methods leading to different types of defective TiO₂(110) surfaces play a significant role in controlling both the thermal- and photo- desorption behavior of O₂. At this point, based on the cumulative work of a number of different authors, using different measurement techniques, considering both experimental and theoretical approaches, we can collectively conclude the following about the nature of chemisorbed O₂ on TiO₂(110):

(1) O₂ is adsorbed both molecularly and dissociatively on the reduced TiO₂(110) surface. For $T < 150 \text{ K}$, O₂ adsorbs predominantly in a molecular fashion. For $T > 150 \text{ K}$, O₂ predominantly adsorbs dissociatively, thus filling oxygen vacancies with O adatoms. The ratio of molecular versus dissociative adsorption may be greatly affected by surface preparation.

(2) Once adsorbed, the most stable configuration is O₂⁻, where the O₂ molecule accepts an electron from the reduced TiO₂ surface^{59,104}. However O₂²⁻ and O₂⁰ may also exist⁶⁴. More work should be done to clarify this hypothesis.

iii. O₂-Mediated Vacancy Diffusion on TiO₂(110)

A beautiful STM study of the diffusion of oxygen vacancy defects on TiO₂ was recently published¹²³. In this study, it was found that upon adsorption of molecular O₂ on a defective TiO₂(110) surface, localized vacancy defect sites appear to move along the $\langle 1\bar{1}0 \rangle$ direction even at low temperature (180 - 250 K). The reported mechanism for this phenomenon involves (step 1) the dissociative adsorption of O₂, where a single O adatom fills the vacancy site, and the remaining oxygen adatom proceeds to extract a lattice oxygen atom from the surface, regenerating adsorbed O₂, and leaving a new vacancy site in its place (steps 2 and 3). The proposed mechanism is schematically illustrated in Figure 99.

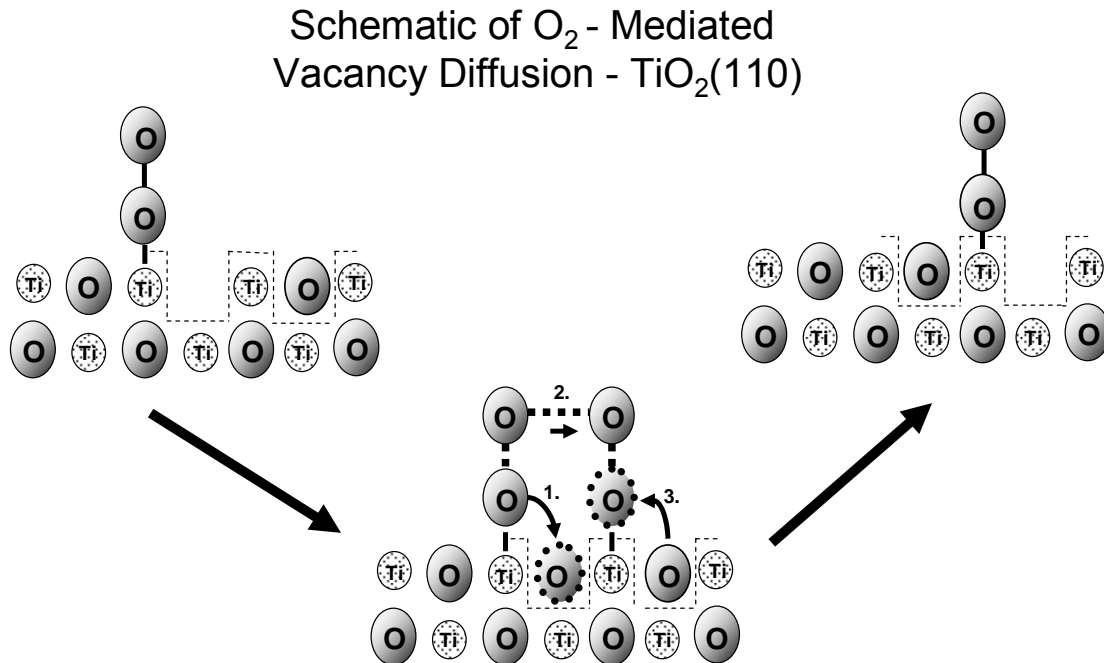


Figure 99: Schematic diagram presented by Besenbacher et al. for the mechanism for O₂ mediated vacancy diffusion on TiO₂(110)¹²³.

In order to verify the O₂-mediated vacancy migration mechanism proposed from the STM studies, in which ¹⁸O₂ isotopic exchange with the lattice ¹⁶O in Ti¹⁶O₂ would be expected, both O₂-photodesorption and O₂-thermal desorption measurements have been performed on surfaces

prepared identically to that in the STM experiments^{123,278}. Figure 100 shows the results for both photo- and thermal desorption measurements where no evidence is seen for isotopic mixing in either experiment. More details pertaining to the results from this work can be found in reference²⁷⁹.

Negative Observation of $^{18}\text{O}_2 + \text{Ti}^{16}\text{O}_2$ Isotopic Exchange

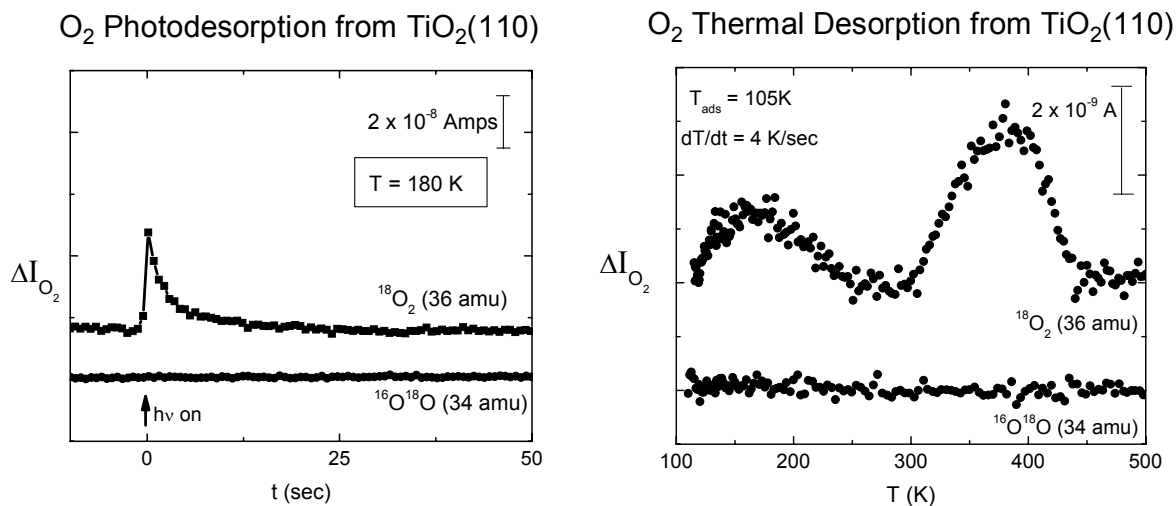


Figure 100: Isotopic mixing experiment for the photo- and thermal-desorption of $^{18}\text{O}_2$ adsorbed on $\text{Ti}^{16}\text{O}_2(110)$. No isotopic mixing is observed²⁷⁹.

These measurements indicate that the mechanism suggested for O₂ mediated vacancy diffusion¹²³ should be reexamined.

iv. Extension of the Phototreshold of TiO₂ into the Visible: Doping of TiO₂

The use of TiO₂ as a photo-activated environmental clean-up agent has elicited much interest in the prospect of lowering the phototreshold energy of TiO₂, thus lowering the energy needed for electronic activation of the solid. Currently, only ~5% of the solar energy supplied at earth's surface can be utilized by TiO₂ (bandgap 3.0 eV)¹⁸². A common research goal is to extend this region to lower wavelengths, in turn increasing the activity of TiO₂ in natural

sunlight. The dependence of the yield of photochemical processes on photon energy has recently been utilized to examine the role of doping of TiO₂ to modify its response to radiation⁵³.

Doping with transition metal ions including Cr²³¹, V²³², Fe^{233,234}, Pb²³⁵, Cu²³⁶ and others has been investigated. Doping with these metal ions has shown both positive and negative effects on the photocatalytic activity of TiO₂, where a number of authors claim that although metal ion doping should decrease the phototreshold energy of TiO₂, the metal ion may also serve as a recombination center for electrons and holes, thus diminishing the overall activity of the photocatalyst. In addition, non-metal dopants such as C¹²⁸, S^{280,281} and N^{131,282} have also been experimentally studied. Recent work done by Asahi et al.³⁶ has suggested that doping with nitrogen shows a clear, beneficial shift of the threshold for photocatalytic activity to lower energies. Doping with nitrogen (or other non-metals) is advantageous to doping with metal ions because nitrogen can easily be incorporated into the surface by annealing the sample in a nitrogen-containing gas flux, or by ion implanting nitrogen into the TiO₂. A number of groups have studied the effect of N-doping in TiO₂. The main conclusion reached by most authors has been that N-doping indeed has a positive effect on lowering the phototreshold energy for TiO₂. Most of this work, however has been done with either anatase TiO₂, or mixed anatase/rutile TiO₂ powder systems. We have chosen a more controlled nitrogen doping experiment involving a single crystal rutile TiO₂(110) substrate.

Doping of the TiO₂(110) crystal was done in a high temperature flow reactor where the crystal could be simultaneously heated and exposed to NH₃ gas at high temperature³⁹. After treatment, the crystal was subjected to XPS analysis where 2 N(1s) features were revealed, one at 396.5 eV (seen previously and assigned to substitutionally bound N⁻) and one at 399.6 eV, which we attribute to an N[·]H complex interstitially bound in the TiO₂ lattice. A novel test, developed

by Fleishauer et al.⁴⁰⁻⁴², was used to determine the photoactivity of the N[·]H doped crystal as a function of photon energy, and the results yielded a significant decrease of 0.6 eV in the photothreshold energy needed for substrate excitation. The 2 feature XPS spectrum observed for the NH₃ treated samples is comparable to that presented by Asahi et al.³⁶. However in that work, the authors claim that the N(1s) XPS feature at 396.5 eV (attributed to be substitutionally bound N⁻) is responsible for the photo threshold energy decrease observed, whereas the work of reference³⁹ find that the 399.6 eV N(1s) state due to N[·]H species is the active dopant.

Doping of TiO₂(110) was also attempted using a high energy ion gun (in UHV) in order to implant the TiO₂(110) using a N₂/Ar⁺ mixture⁵³. After 3.0 keV N₂⁺ implantation, the crystal was annealed extensively, allowing diffusion of implanted N atoms further into the bulk of the crystal. The crystal photoactivity was then tested using the photodesorption of adsorbed O₂ at varying photon energies. XPS, TEM and SIMS were also used to examine the nature and depth of the implanted nitrogen species. Results of this work showed an *increase* in the photothreshold energy, opposite to that observed by others. The XPS data for the ion implanted surface show a single 396.5 eV N(1s) feature attributed to substitutional nitrogen, as N⁻, therefore suggesting that substitutionally bound N⁻ alone is not responsible for the decrease in the photothreshold of TiO₂(110) as observed for N[·]H species³⁹. The increase in the photothreshold energy of TiO₂ for N⁻ doping is attributed to the deposition of charge in the low levels of the conduction band (also known as the band-filling mechanism), causing higher energy photons to be needed to excite into the conduction band.

The results from these two experiments are summarized in Figure 101 which clearly depicts both the unfavorable shift to higher photothreshold energy due to N⁻ implantation, and

the favorable shift to lower energies due to N-H incorporation via chemical doping. The respective N(1s) XPS features are shown as insets.

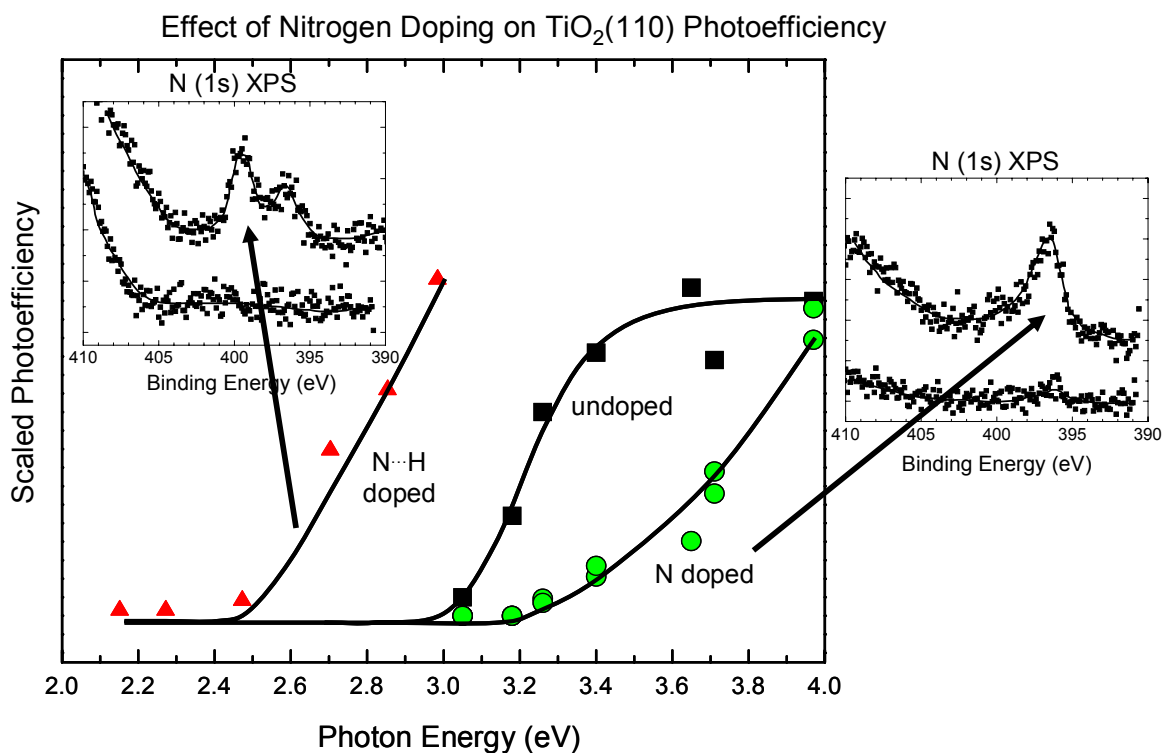


Figure 101: Change in the photothreshold energy $\text{TiO}_2(110)$ doped by N_2^+ implantation or by high temperature NH_3 treatment. XPS data for either doping situation is also presented^{39,53}.

Very recent theoretical work done by Di Valentin et al.⁴⁷ has confirmed very different photoactivity results for anatase and rutile TiO_2 that were doped with substitutionally bound nitrogen. For anatase samples, the presence of substitutionally bound nitrogen causes a decrease in the absorption band edge, while in rutile, the opposite (increase in absorption band edge) is observed. While the explanation for the effect reported in reference⁵³ differs from that presented by Di Valentin and co-workers⁴⁷, the drastic difference in the behavior of anatase and rutile may partially explain the experimental differences measured by Asahi and others³⁶ (mainly using anatase) and our work^{39,53} (rutile single crystal) for implanted nitrogen doping.

v. Spectroscopic Detection of Electrons, Holes and O_2^- Superoxide Species on UV-Irradiated TiO_2 : Observing Charge Transfer to Adsorbed Molecules

In a recent combined study utilizing both electron paramagnetic resonance spectroscopy (EPR) and infrared spectroscopy (IR), it was shown that photoactive electrons and holes created by UV-generated charge separation can be measured in stoichiometric TiO_2 . Using EPR, holes are detected by the observation of O^- which originates from lattice oxygen O^{2-} ions upon UV excitation. The UV-generated electrons can either be excited into the conduction band where they are observed by IR spectroscopy, or they can be trapped at Ti^{3+} centers lying below the conduction band and are measured there by EPR spectroscopy. Figure 102 depicts a schematic diagram showing the UV-induced formation of electron-hole pairs, and the measurement techniques used for detection as well as the characteristic EPR signature for Ti^{3+} (electrons) and O^- (holes).

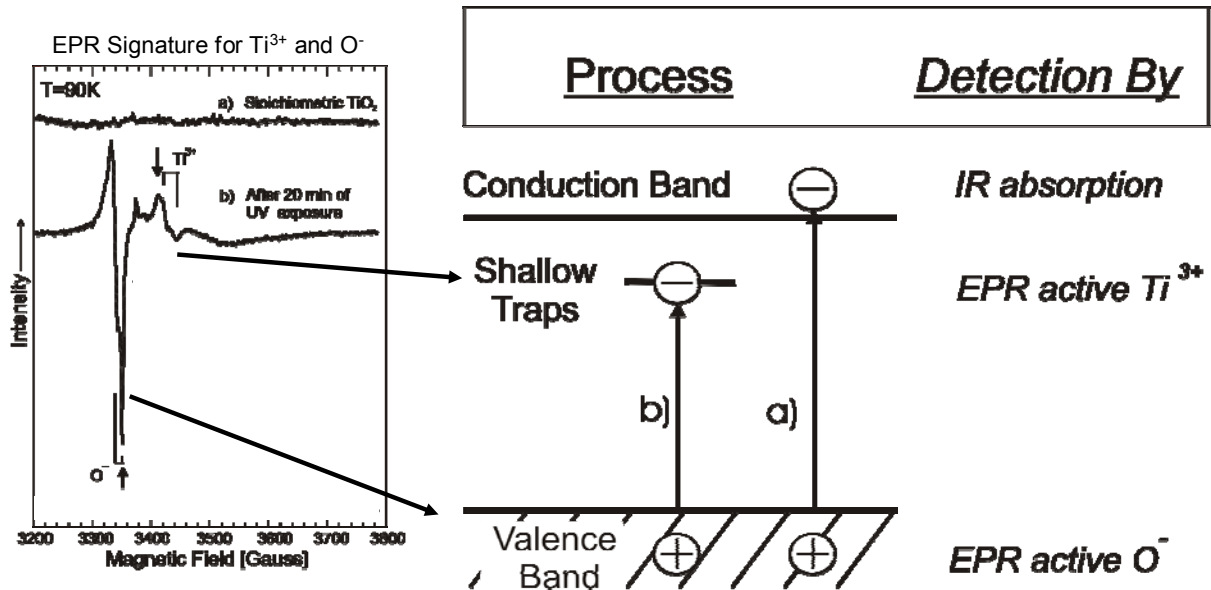


Figure 102: EPR signatures for photogenerated Ti^{3+} (electrons) and O^- (holes). Image on the right side is a schematic diagram for the UV-induced generation of electron-hole pairs and the respective measurement method utilized for their detection ⁵⁹.

The process depicted in Figure 102 is a result of excitation via UV radiation at 90 K; however, the measured lifetimes of electrons and holes has a direct correlation to the temperature during excitation. It was shown that raising the sample temperature from 90 K to 140 K, caused a drastic decrease in the EPR signal due to electrons trapped at Ti^{3+} sites within the bandgap. At this temperature, it is clear that significant recombination occurs (via a low activation energy process, $E_a \approx 0.01$ eV), although photoexcitation of electrons to the conduction band is clearly still observed at this temperature. In addition, the presence of UV-generated holes is still measured at 140 K. At temperatures near 298 K, neither photogenerated holes nor electrons are measured, due to the rapid recombination of electron-hole pairs.

Additional experiments were done to investigate the effect of the addition of gas phase O_2 during UV radiation ($T = 140$ K). There is was found that O_2 serves as a direct electron scavenger, producing O_2^- species adsorbed on the surface as a result of the acceptance of conduction band electrons. The EPR signature of O_2^- is shown in Figure 103. Here the spectral features of O_2^- are superimposed on the O^- (hole) spectrum, and a simulation of both O^- and O_2^- species is seen to generate the experimental spectrum. The concentration of holes measured during this process were equal to the concentration of O_2^- species measured, suggesting that the majority of electrons created via charge separation were promoted to the conduction band, and transferred to adsorbed O_2 as O_2^- .

O₂ (a) as an Electron Scavenger:
Production of O₂⁻ (ads.)

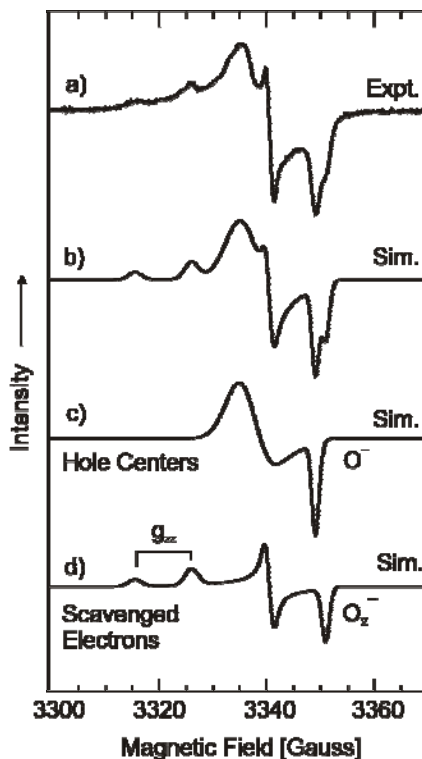


Figure 103: Characteristic EPR signature for O₂ adsorbed as O₂⁻ on TiO₂⁵⁹.

Conduction band electrons created upon UV-generation of electron hole pairs in anatase TiO₂ have been measured as a change in the background absorbance of the IR signal⁸⁵. Figure 104a shows a schematic representation of UV-generated electrons that reside for long lifetimes in the conduction band. Figure 104b depicts the actual measured change in the IR absorbance from 0 seconds of irradiation to 1200 seconds of irradiation. The IR absorbance due to conduction band electrons occurs as a result of the continuum of final states available to conduction band electrons which lead to broad band absorbance. In accordance to EPR measurements for the addition of oxygen to UV-irradiated TiO₂, the effect of oxygen on the background IR absorbance after completion of UV radiation was also investigated⁵⁹. In this case, adsorbed oxygen works as an effective electron scavenger, removing electrons from the

conduction band to form the superoxo species, O_2^- , and subsequently lowering the background IR absorbance⁵⁹.

Trapped Conduction Band Electrons Detected by Changes in Background IR Absorbance

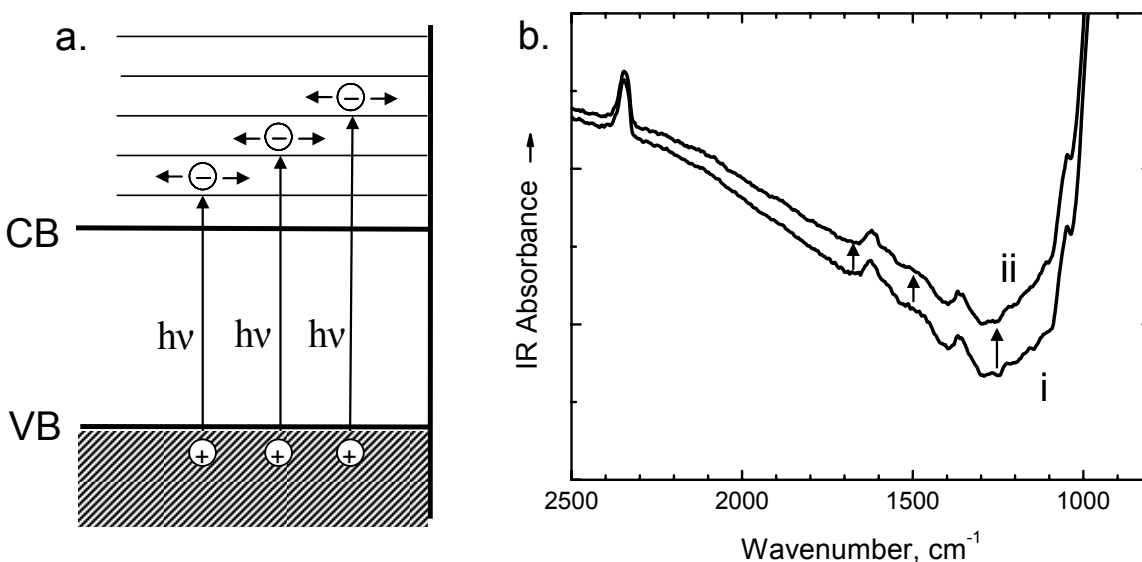


Figure 104: (a) Diagram showing the photoexcitation of electrons into a continuum of states within the conduction band. (b) IR background absorbance change for (i) 0 seconds and (ii) 1200 seconds irradiation by UV light ($3.0 \text{ eV} \leq h\nu \leq 6.2 \text{ eV}$)⁵⁹.

Another example of charge transfer from TiO_2 was seen for organic type adsorbates on powdered TiO_2 samples, as measured by IR spectroscopy¹⁸⁰. There it was shown that for 2 chemically similar adsorbates, charge transfer exclusively occurred to the more electrophilic adsorbate, whereas little to no charge transfer occurred to a less electrophilic molecule. Figure 105 shows the results from this work where at the start, conduction band electrons are observed as a result of reduction of the TiO_2 surface by thermal annealing at 900 K.

Preferential Electron Transfer: TiO₂ CB Electrons to Electrophilic Molecules

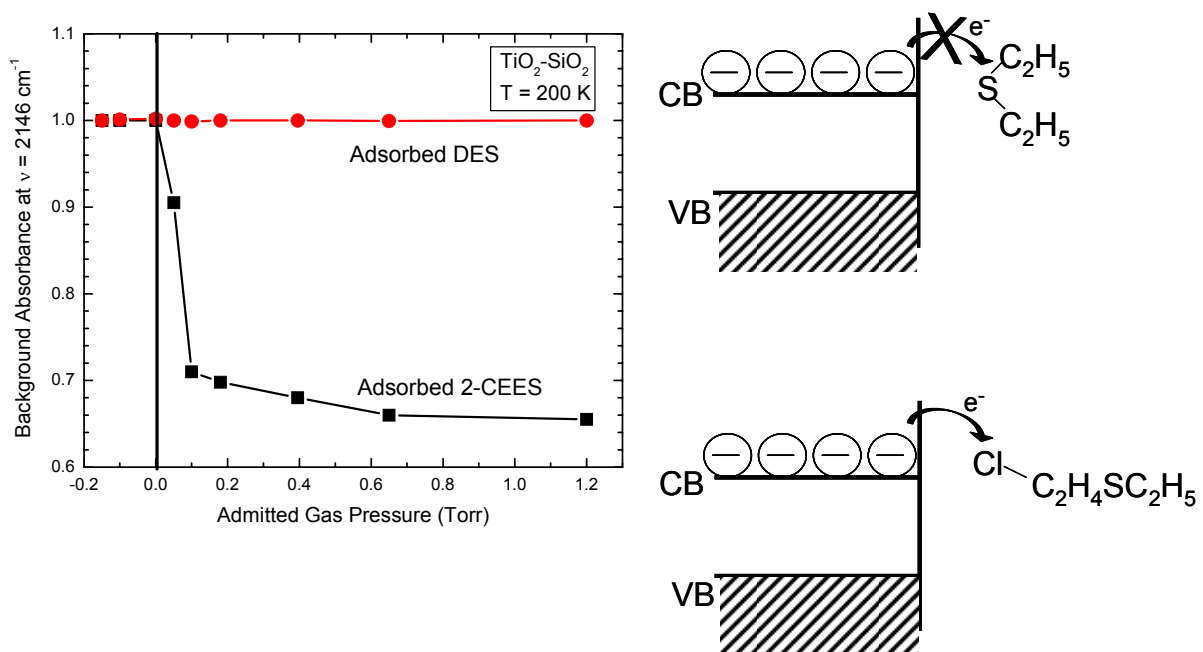


Figure 105: Selective electron scavenging by more electronegative molecules. The figure represents the preferential charge transfer through the electronegative chlorine molecule and lack of charge transfer to the less electronegative molecule¹⁸⁰.

Upon addition of 2-chloroethyl ethyl sulfide (2-CEES, bound in two ways through the S and Cl moiety), direct electron transfer occurs, causing the background IR absorbance (measure of available conduction band electrons) to decrease. In contrast, the same experiment was done using diethyl sulfide (DES, analog to 2-CEES, but no Cl present). Adsorption of DES produces no change in the background absorbance, signifying lack of charge transfer to the less electrophilic molecule. These results suggest that electron transfer from the conduction band of TiO₂ to an adsorbed molecule is dependent on the nature of the surface bonding functionality within a molecule. Possibly a critical electronegativity of the bonding functionality is needed to effect charge transfer.

C. Summary

This paper is both a summary of previously-reported studies of the TiO₂ surface as a photocatalyst as well as a report of recent studies. A number of specific issues are treated and a coherent picture of the behavior of TiO₂ surfaces is beginning to emerge. The specific issues are summarized briefly below:

(1). Anion vacancy defects can be created by three means and these have been studied on the TiO₂(110) surface. Vacancy creation occurs by the use of thermal annealing above about 600 K, by electron bombardment, and by ion bombardment. Differences in the types of defects are observed, with ion bombardment being most aggressive in making both surface vacancy defects as well as bulk defects. In contrast, electron bombardment is shown to produce oxygen vacancies which are localized in the surface region. Ultraviolet photons with energies above the bandgap energy (3.0 eV) have been shown to be ineffective in producing vacancy defect sites on stoichiometric TiO₂(110).

(2). Defects can be detected by chemical means using CO₂ as an adsorbate. Slightly higher desorption activation energies are observed for CO₂ from vacancy defect sites than from non-defective TiO₂(110) surface sites. Undissociated molecular oxygen is also adsorbed at oxygen vacancy defect sites, and photodesorption of the oxygen can occur from these sites. Also, both formaldehyde and NO are specifically adsorbed at defect sites undergo specific chemistries as a result of the chemical nature of the defect.

(3). Surface defect sites may be detected by physical means using either work function or EPR methods. The work function of TiO₂ decreases as oxygen vacancies are formed by thermal treatment, electron bombardment, and by ion bombardment. EPR is able to detect the hole states (as O⁻ centers) and the localized electrons (as Ti³⁺ states). Thermally activated recombination of

the localized electrons with holes occurs near 140 K. Both states are observed either when TiO₂ powders are heated or when photoexcitation occurs.

(4). Electrons promoted either photochemically or thermally to the conduction band of TiO₂ may be detected by IR spectroscopy. Here, electrons are electronically excited over a wide range of IR photon energies and thereby cause an overall increase in the background of the IR spectrum of the TiO₂.

(5). Recent STM studies have demonstrated that vacancies in the TiO₂(110) surface are caused to migrate by the presence of adsorbed O₂. A mechanism which must involve adsorbate oxygen isotopic mixing with the lattice oxygen atoms has been proposed, but all experiments designed to detect isotopic mixing in either thermally-desorbing or photodesorbing O₂ have been unsuccessful, suggesting that the proposed mechanism of oxygen-mediated vacancy diffusion on the surface must be reexamined.

(6). Doping of TiO₂(110) by nitrogen has been shown to result in different shifts of the photothreshold. NH₃ doping, in which N^{···}H species are postulated to occupy interstitial sites, causes the photothreshold to shift 0.6 eV toward the visible. Nitrogen ion implantation, which is postulated to cause N⁻ substitutional doping, causes the photothreshold to shift towards the ultraviolet.

(7). Charge transfer from both Ti³⁺ sites and from the conduction band to adsorbate molecules has been observed using both EPR and IR methods. The adsorbed superoxide species, O₂⁻, has been detected by EPR when molecular oxygen is present on the surface. Loss of electrons trapped in the conduction band of TiO₂, to sufficiently electrophilic molecules has been detected by IR spectroscopy, and it has been shown that the Cl moiety is responsible for charge transfer into a bifunctional organic molecule containing both Cl and S atoms.

APPENDIX B

UV Lamp Calibration and Photon Flux Calculation

UV Source:

The UV Lamp employed for all photochemistry experiments presented in this thesis is a 500 W Hg Arc Lamp (model 6285, Oriel Corporation). The lamp is used in conjunction with an IR blocking water filter (Oriel) and interference filters of varying wavelength (Andover Corporation). Each filter has a transmission gap of ± 5 nm. The lamp housing is equipped with an adjustable iris (typical iris diameter setting = 0.8 cm -1.2 cm) to change the size of the light beam incident on the sample, and a shutter to facilitate timed UV exposures to the sample. The lamp housing itself contains a spherical reflector positioned behind the UV lamp (internal to the housing) and also a series of quartz condenser lenses (external to housing, see Figure 107) used to collimate and focus the light beam. The irradiance profile of the 500 W Lamp is shown in Figure 106.

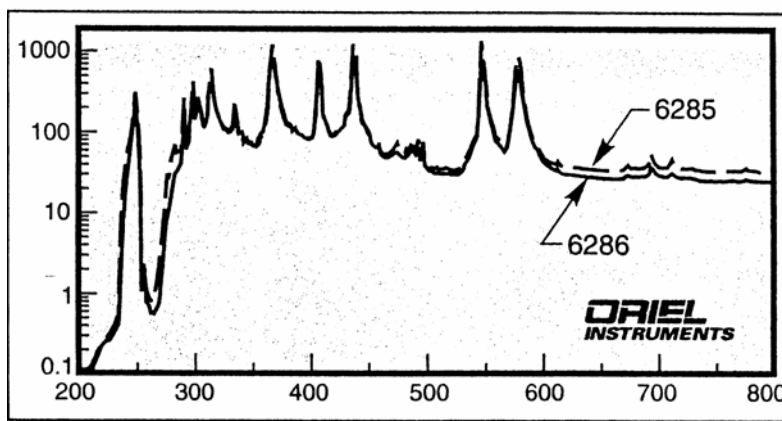


Figure 106: Irradiance profile for 500 W Hg Arc Lamp Model 6285 employed for photochemical experiments presented in this thesis.

Photon Flux Calibration

A measurement of the UV power density is necessary to calculate the exact photon flux incident on the crystal surface. The power density is measured using a photodiode (EG&G, now PerkinElmer Optoelectronics, HUV-4000B) that has been cross calibrated against an absolute thermopile detector (ThermoOriel, Thermopile element # 71751) as described below: the calibration of the photodiode against the thermopile detector is done at each photon energy used in the course of the presented experiments. The photodiode is used in conjunction with a neutral density filter for all reported experiments. This filter limits the lamp input into the photodiode to prohibit saturation of the photodiode sensor. The experimental configuration used for the calibration procedure mimics that used in each photochemistry experiment. The thermopile is placed where the sample would be located. The placement of the lamp, thermopile (absolute detector) and photodiode is shown schematically in Figure 107.

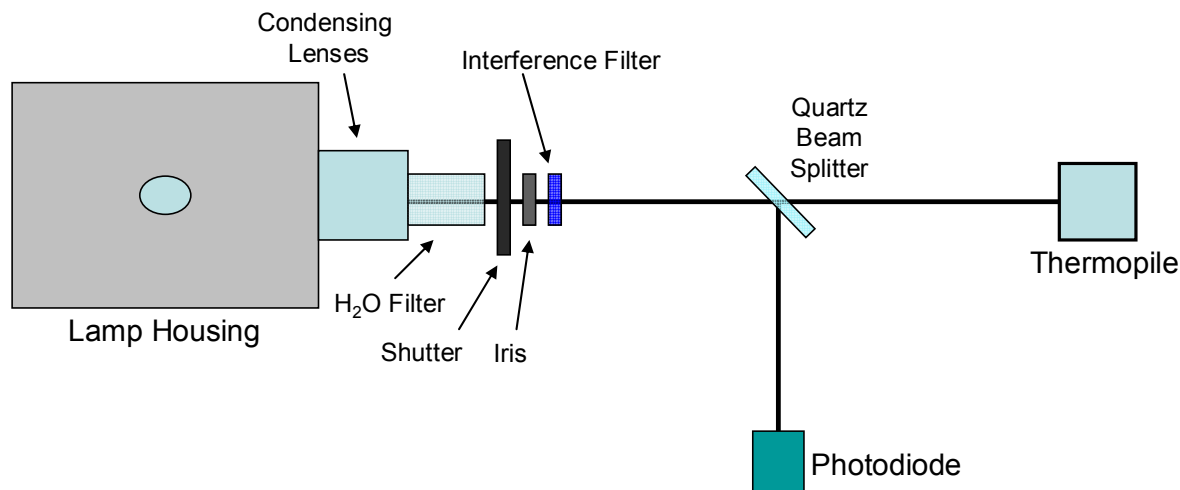


Figure 107: Geometrical position of the various components of the UV Lamp, Quartz Beam Splitter, Thermopile and Photodiode used for lamp calibration measurements.

The distance between the absolute thermopile detector and the lamp aperture is the same as the distance between the lamp and the crystal during all photochemistry experiments. The

photodiode and beam splitter distances also correspond as such. Calibration of the photodiode at each photon energy is done by interchanging the position of the thermopile and photodiode in order to determine the calibration factor (a ratio of output voltages), B , for each interference filter. Data for the calibration factor, B , versus photon energy are shown in Figure 108. The data presented in Figure 108 take into account that only 9.6% of the UV intensity is recorded by the photodiode due to the reflectivity of the quartz beam splitter. The 9.6% reflectivity characteristic of the quartz beam splitter is measured using the absolute thermopile detector positioned in the path of the transmitted beam and then also in the path of the reflected beam. Both thermopile positions are equidistant from the quartz beam splitter. The ratio of the two measured thermopile voltages was taken to determine the reflection properties of the quartz beam splitter.

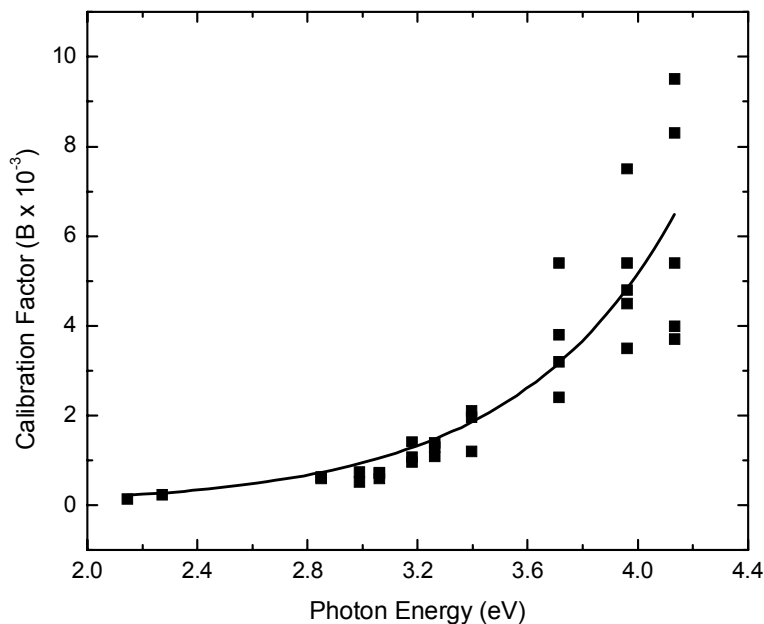


Figure 108: Calibration data for the photodiode used in conjunction with the thermopile at varied photon energies.

A large scatter in measured values for the calibration factor at high photon energies is due to noise inherent to the photodiode when measuring voltages as a result of the high transmission of the interference filters used at those energies. The values obtained from this curve are then used according to the following set of simple equations to derive the photon flux incident on the crystal. First the measured output of the photodiode (V) is recorded and converted to absolute terms using the calibration data above:

$$V_{pd} \cdot B = V_{tp} \quad (\text{B.1})$$

where V_{pd} is voltage recorded by the photodiode and V_{tp} is the thermopile voltage. The calculated voltage value (V_{tp}) is then divided by the responsivity (40 V / W for this particular thermopile) of the thermopile and the active area of the thermopile detector ($1.5 \times 10^{-4} \text{ cm}^2$). The resulting value is the power density, P (W cm^{-2}). The obtained value for the power density must be further corrected for the angle of incidence of the UV light to the sample (60°). The corrected power density is then used to calculate the total photon flux at the crystal surface according to:

$$F = \left(\frac{\lambda}{hc} \right) \cdot P \quad (\text{B.2})$$

where F is the total photon flux ($\text{photons} \cdot \text{cm}^{-2} \cdot \text{s}^{-1}$), λ is the wavelength (m), h is Planck's constant ($\text{J} \cdot \text{s}$), c is the speed of light ($\text{m} \cdot \text{s}^{-1}$) and P is the power density ($\text{W} \cdot \text{cm}^{-2}$).

APPENDIX C

Calculation of the UV Penetration Depth in TiO₂

In order to determine the penetration depth of UV photons which are exposed to the surface of TiO₂, the UV-VIS transmission spectra of TiO₂ films of varying thickness were measured, and are shown in the Figure 109 below.

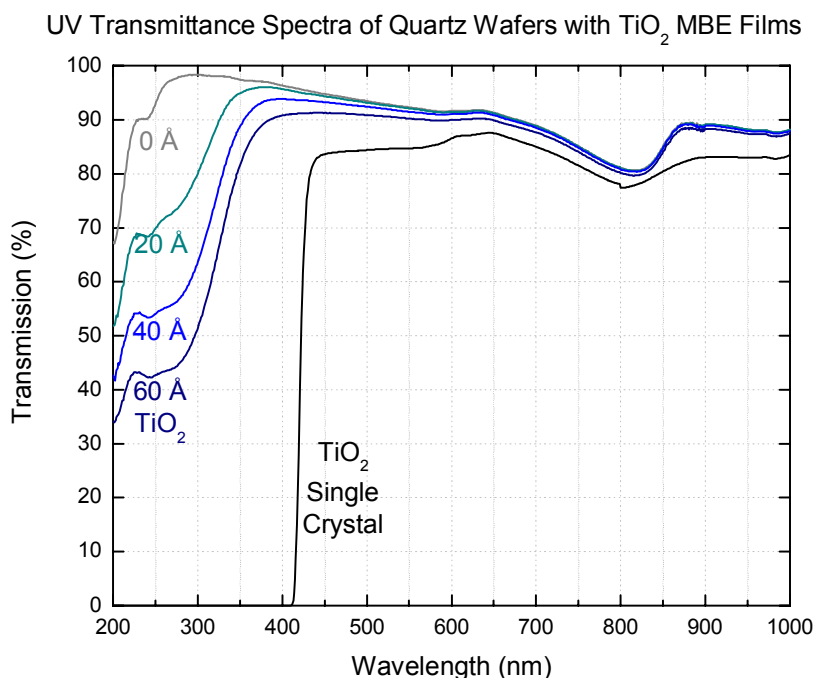


Figure 109: UV transmittance data for a TiO₂(110) single crystal (1mm thickness) and TiO₂ films of varying thickness.

From these data, the measured transmittance was plotted (shown in Figure 110) versus the film thickness in order to determine the slope according to the equations shown below. The films were made in the laboratory of Professor Darrell Schlom by Venu Vaithyanathan using a calibrated molecular beam epitaxy source. Using this method, films of varying thickness can be made with Angstrom accuracy.

$$\frac{I}{I_o} = e^{-z/\lambda} \quad (C.1)$$

$$-\ln \frac{I}{I_o} = \left(\frac{1}{\lambda}\right) \cdot z \quad (C.2)$$

$$1/\lambda = 0.0096 \text{ \AA}^{-1}$$

$$\lambda = 103 \text{ \AA} \text{ (at 312 nm)}$$

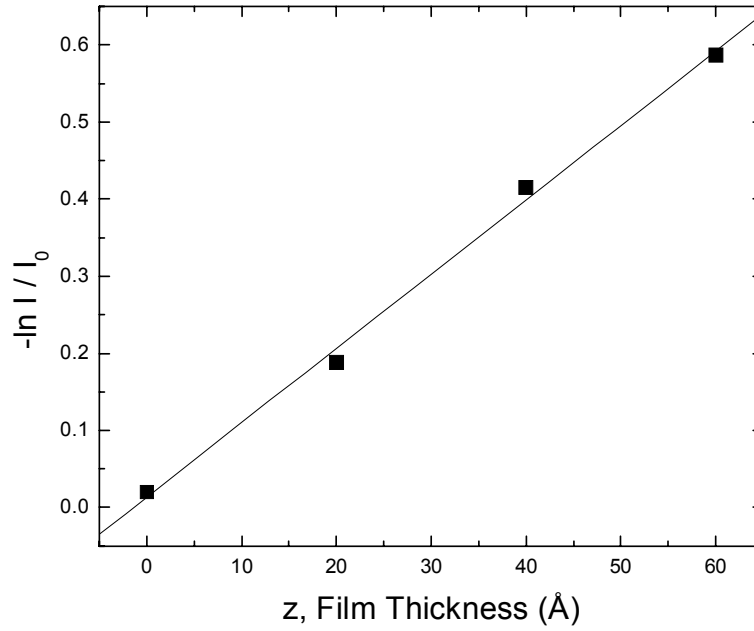


Figure 110: Measured UV transmission through TiO₂ films of varying thickness at 312 nm.

APPENDIX D

Calibration of the Molecular Beam Doser for Accurate Gas Exposure

For all experiments reported in this document unless otherwise stated, accurate gas exposures to the single crystal surface were done using a microcapillary array beam doser. The use of such a doser is superior over less accurate gas exposure techniques (ie: backfilling) for a number of reasons. Primarily, less gas is exposed to the vacuum system and subsequently adsorbed on the walls of the vacuum chamber. Therefore, lower pressures can be reached in shorter times after gas dosing. In addition, less gas exposure lowers the probability of impurity desorption from the walls of the vacuum chamber that may in turn adsorb onto the single crystal surface. The molecular beam doser is calibrated in an absolute manner thru measurement of the gas conductance through a pinhole aperture as described hereafter.

The design for the microcapillary array beam doser is shown in Figure 111. The main components of the doser are the pinhole aperture (7 μm diameter) and the microcapillary array. Once the gas passes through the aperture, it is randomized in direction by the shim stock baffle. Finally, the gas stream passes through the microcapillary array. The microcapillary array consists of fused glass capillaries 10 μm in diameter and 500 μm in length.

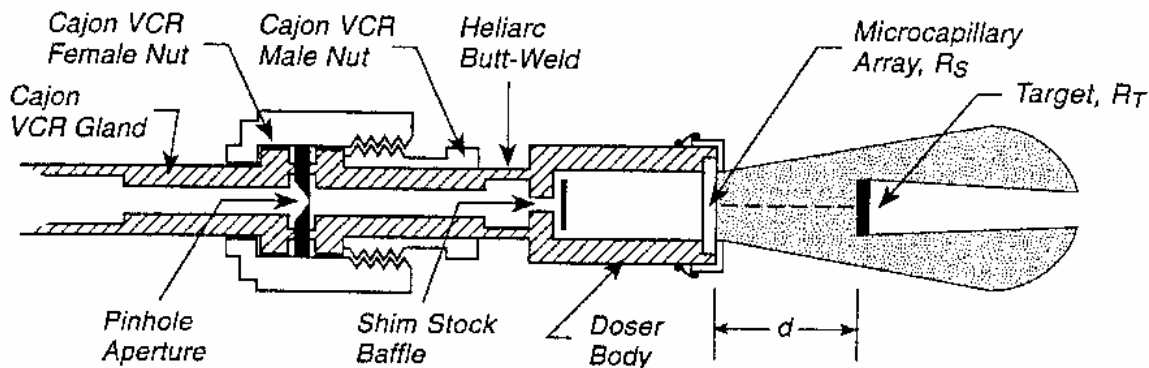


Figure 111: Schematic diagram of the design of the microcapillary array beam doser used for accurate gas exposures to a single crystal surface. Figure taken from Reference ⁵⁴.

The conductance of the pinhole aperture of the microcapillary array beam doser is calibrated by measuring the pressure drop of Ar(g) in the gas handling line with a 0 to 10 torr Baratron capacitance monometer. A gas handling system with known volume was used to fill the beam doser. Calibration measurements were done at room temperature.

The calibration of the conductance of the pinhole aperture is done using the ideal gas law:

$$PV = nRT \quad (\text{E.1})$$

where P is the gas pressure in the gas handling system, V is the volume of the gas handling system, n is the number of moles of the gas, R is the gas constant and T is the temperature.

Equation E.1 can be differentiated with respect to time to give:

$$\frac{dP}{dt} = \left(\frac{RT}{V} \right) \frac{dn}{dt} \quad (\text{E.2})$$

The decrease in the number of moles of gas, (dn/dt), is then related to the rate of pumping through the pinhole aperture, which depends on the back pressure in the gas line. The flow rate of gas molecules is proportional to the pressure, hence

$$\frac{dn}{dt} = -B \cdot P \quad (\text{E.3})$$

Therefore,

$$\frac{dP}{dt} = \left(\frac{RT}{V} \right) (-B \cdot P) \quad (\text{E.4})$$

or,

$$\frac{d \ln P}{dt} = \left(\frac{RT}{V} \right) (-B) \quad (\text{E.5})$$

Figure 112 plots $\Delta(\ln P)$ as a function of dosing time. The slope of this curve can be measured and then used to determine the conductance of the pinhole aperture. The measured gas flux is 2.5×10^{14} molecules torr⁻¹ sec⁻¹ for Ar(g).

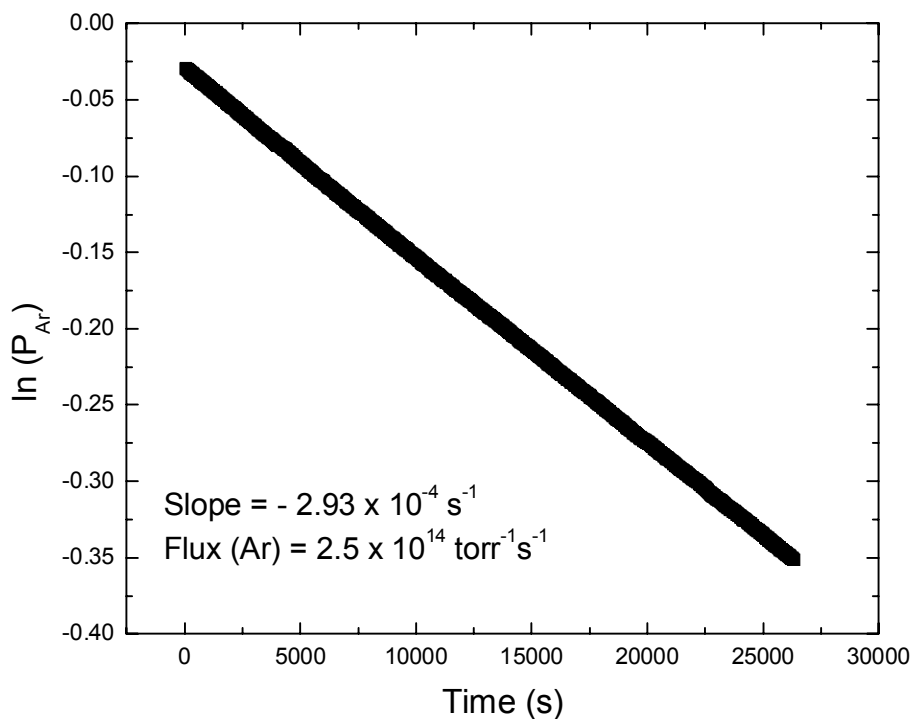


Figure 112: Calibration of the capillary array molecular beam doser for Ar(g).

The amount of the exposed gas that is actually intercepted by the crystal is calculated through consideration of the known geometry of the diameter of the doser (R_S), the diameter of the

crystal (R_T) and the distance between them (d). Figure 113 depicts the variation in the actual intercepted flux of gas by the crystal with respect to the acceptance angle of the crystal. For a crystal with dimensions of 1 cm^2 , $R_S / R_T \sim 1$. For the experiments presented here, the approximate angle of acceptance of the single crystal was 27 %. As such, the amount of gas intercepted by the crystal is $\sim 32 \%$ of the measured gas exposure. The resulting flux intercepted by the crystal is then equal to $8.0 \times 10^{13} \text{ molecules torr}^{-1} \text{ sec}^{-1}$ for Ar(g) .

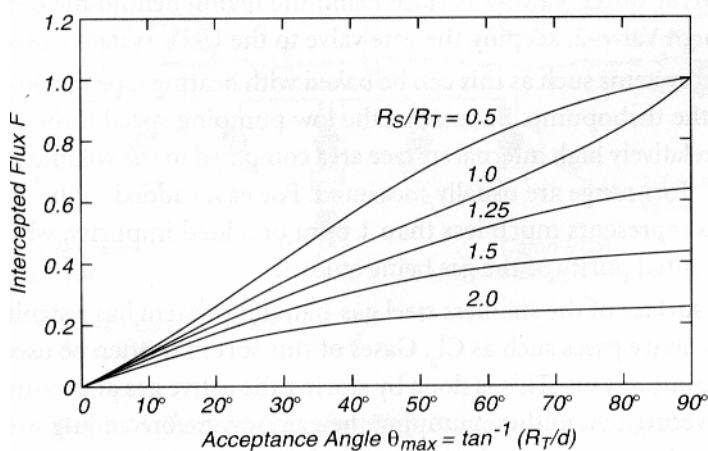


Figure 113: Percent of gas flux intercepted by a crystal for varying geometrical arrangements. Figure reproduced from Reference ¹²⁵.

APPENDIX E

List of Publications (in Ascending Chronological Order)

1. S. Mezhenny, P. Maksymovych, **T.L. Thompson**, O. Diwald, D. Stahl, S.D. Walck, J.T. Yates, Jr. "STM Studies of Defect Production on the $\text{TiO}_2(110) - (1 \times 1)$ and $\text{TiO}_2(110) - (1 \times 2)$ Surfaces Induced by UV Irradiation" *Chem. Phys. Lett.* **369** (2003) 152-158.
2. **Tracy L. Thompson**, Oliver Diwald, John T. Yates, Jr. "The Thermal Desorption of CO_2 as a Probe for Monitoring the Defect Density on $\text{TiO}_2(110)$ ". *J. Phys. Chem. B.*, **107** (2003) 11700-11704.
3. O. Diwald, **T.L. Thompson**, E. Goralski, S. Walck, J.T. Yates, Jr. "The Effect of Nitrogen Doping on the Photoactivity of $\text{TiO}_2(110)$ Rutile Single Crystals". *J. Phys. Chem. B.*, **108** (2004) 52-57.
4. Oliver Diwald, **Tracy L. Thompson**, Tykhon Zubkov, Ed Goralski, Scott Walck and John T. Yates, Jr. "Photochemical Activity of Nitrogen-Doped Rutile TiO_2 in Visible Light" *J. Phys. Chem. B.* **108** (2004) 6004-6008.
5. **Tracy L. Thompson**, Oliver Diwald and John T. Yates, Jr. "Molecular Oxygen Mediated Vacancy Diffusion on $\text{TiO}_2(110)$ – New Studies of the Proposed Mechanism" *Chem. Phys. Lett.* **393** (2004) 28-30.
6. **Tracy L. Thompson**, Dimitar Panayotov and John T. Yates, Jr. "Adsorption and Thermal Decomposition of 2-Chloroethyl Ethyl Sulfide on TiO_2 Surfaces" *J. Phys. Chem. B.* **108** (2004) 16825-16833.
7. T. Berger, M. Sterrer, O. Diwald, E. Knözinger, D. Panayotov, **T. L. Thompson** and J. T. Yates, Jr. "Light Induced Charge Separation in Anatase TiO_2 Particles" *J. Phys. Chem. B.* **109** (2005) 6061-6068.

8. **Tracy L. Thompson**, Dimitar Panayotov and John T. Yates, Jr. “The Photodecomposition of Adsorbed 2-Chloroethyl Ethyl Sulfide (2-CEES) on TiO₂: The Involvement of Lattice Oxygen” *J. Phys. Chem. B.* **108** (2004) 17857-17865.
9. Tykhon Zubkov, Dirk Stahl, **Tracy L. Thompson**, Dimitar Panayotov, Oliver Diwald and John T. Yates, Jr. “Ultraviolet Light-Induced Hydrophilicity Effect on TiO₂(110)-(1x1). Dominant Role of the Photooxidation of Adsorbed Hydrocarbons Causing Wetting by Water Droplets”, *J. Phys. Chem. B.* **109** (2005) 15454-15462.
10. **Tracy L. Thompson** and John T. Yates, Jr. “TiO₂-Based Photocatalysis: surface defects, oxygen and charge transfer”, *Top. Catal.* **35** (2005) 197-210.
11. **Tracy L. Thompson** and John T. Yates, Jr. “Monitoring Hole Trapping in Photoexcited TiO₂ Using a Surface Photoreaction” *J. Phys. Chem. B.* **109** (2005) 18230. *note: Feature Article.
12. **Tracy L. Thompson** and John T. Yates, Jr. “Fractal Kinetics in a Surface Photochemical Process-O₂ Photodesorption from TiO₂(110)”, *J. Phys. Chem. B.*, accepted for publication, 2006.
13. **Tracy L. Thompson** and John T. Yates, Jr. “Photoactivation of TiO₂ Surfaces” *Chem. Rev.*, invited article, submitted, 2006.

BIBLIOGRAPHY

- (1) Honda, K.; Fujishima, A. *Nature* **1972**, *238*, 37-38.
- (2) Fujishima, A.; Hashimoto, K.; Watanabe, H. *TiO₂ Photocatalysis: Fundamentals and Applications*; BKC, Inc.: Tokyo, 1997.
- (3) Diebold, U. *Surf. Sci. Rep.* **2003**, *48*, 53-229.
- (4) Henrich, V. E.; Cox, P. A. *The Surface Science of Metal Oxides*; Cambridge University Press: Cambridge, 1994.
- (5) *Photocatalysis: Fundamentals and Applications*; Serpone, N.; Pilezzetti, E., Eds.; Wiley-Interscience: New York, 1989.
- (6) Li, M.; Hebenstreit, W.; Diebold, U.; Tyryshkin, A. M.; Bowman, M. K.; Dunham, G. G.; Henderson, M. A. *J. Phys. Chem. B* **2000**, *104*, 4944-4950.
- (7) Pan, J. M.; Maschhoff, B. L.; Diebold, U.; Madey, T. E. *J. Vac. Sci. Technol. A* **1992**, *10*, 2470-2476.
- (8) Henderson, M. A.; Epling, W. S.; Perkins, C. L.; Peden, C. H. F.; Diebold, U. *J. Phys. Chem. B* **1999**, *103*, 5328-5337.
- (9) Henderson, M. A. *Surf. Sci.* **1995**, *343*, L1156-L1160.
- (10) Petigny, S.; Mostefa-Sba, H.; Domenichini, B.; Lesniewska, E.; Steinbrunn, A.; Bourgeois, S. *Surf. Sci.* **1998**, *410*, 250-257.
- (11) Pan, J. M.; Maschhoff, B. L.; Diebold, U.; Madey, T. E. *Abstr. Pap. Am. Chem. Soc.* **1991**, *202*, 172-Coll.
- (12) Diebold, U.; Lehman, J.; Mahmoud, T.; Kuhn, M.; Leonardelli, G.; Hebenstreit, W.; Schmid, M.; Varga, P. *Surf. Sci.* **1998**, *411*, 137-153.
- (13) Onda, K.; Li, B.; Petek, H. *Phys. Rev. B* **2004**, *70*, 045415 1-11 .
- (14) Wang, L. Q.; Baer, D. R.; Engelhard, M. H. *Surf. Sci.* **1994**, *320*, 295-306.
- (15) Thompson, T. L.; Diwald, O.; Yates Jr., J. T. *J. Phys. Chem. B* **2003**, *107*, 11700-11704.
- (16) Lu, G. Q.; Linsebigler, A.; Yates Jr., J. T. *J. Phys. Chem.* **1994**, *98*, 11733-11738.
- (17) Linsebigler, A.; Lu, G. Q.; Yates Jr., J. T. *J. Phys. Chem.* **1996**, *100*, 6631-6636.
- (18) Henderson, M. A.; Otero-Tapia, S.; Castro, M. E. *Faraday Discuss.* **1999**, 313-329.

- (19) Wang, L. Q.; Baer, D. R.; Engelhard, M. H.; Shultz, A. N. *Surf. Sci.* **1995**, *344*, 237-250.
- (20) Göpel, W.; Anderson, J. A.; Frankel, D.; Jaehnig, M.; Phillips, K.; Schafer, J. A.; Rocker, G. *Surf. Sci.* **1984**, *139*, 333-346.
- (21) Kolasinski, K. *Surface Science: Foundations of Catalysis and Nanoscience*; John Wiley and Sons Ltd.: London, 2002.
- (22) Henderson, M. A. *Surf. Sci.* **1998**, *400*, 203-219.
- (23) Linsebigler, A. L.; Lu, G. Q.; Yates Jr., J. T. *Chem. Rev.* **1995**, *95*, 735-758.
- (24) Li, S. S. *Semiconductor Physical Electronics*; Plenum Press: New York, 1993.
- (25) Shockley, W.; Read Jr., W. T. *Phys. Rev.* **1952**, *87*, 835-842.
- (26) Thompson, T. L.; Yates Jr., J. T. *J. Phys. Chem. B* **2005**, *109*, 18230-18236.
- (27) Egerton, T. A.; King, C. J. *J. Oil Col. Chem. Assoc.* **1979**, *62*, 386.
- (28) Cunningham, J.; Hodnett, B. K. *J. Chem. Soc., Faraday Trans.* **1981**, *77*, 2777-2801.
- (29) Kormann, C.; Bahnemann, D. W.; Hoffmann, M. R. *Environ. Sci. Technol.* **1991**, *25*, 494-500.
- (30) Peral, J.; Domenech, X.; Ollis, D. F. *J. Chem. Technol. Biotech.* **1997**, *70*, 117-140.
- (31) D'Oliveira, J.-C.; Al-Sayyed, G.; Pichat, P. *Environ. Sci. Technol.* **1990**, *24*, 990-996.
- (32) Okamoto, K.; Yamamoto, Y.; Tanaka, H.; Itaya, A. *Bull. Chem. Soc. Jpn.* **1985**, *58*, 2023-2028.
- (33) Kopelman, R. *Science* **1988**, *241*, 1620-1626.
- (34) Kopelman, R. Diffusion-controlled Reaction Kinetics. In *The Fractal Approach to Heterogeneous Chemistry: Surfaces Colloids and Polymers*; Avnir, D., Ed.; John Wiley and Sons: New York, 1989; pp 295-309.
- (35) Vijay, A.; Mills, G.; Metiu, H. *J. Chem. Phys.* **2003**, *118*, 6536-6551.
- (36) Asahi, R.; Morikawa, T.; Ohwaki, T.; Aoki, K.; Taga, Y. *Science* **2001**, *293*, 269-271.
- (37) Mrowetz, M.; Balcerski, W.; Colussi, A. J.; Hoffmann, M. R. *J. Phys. Chem. B* **2004**, *108*, 17269-17273.

- (38) Gole, J. L.; Stout, J. D.; Burda, C.; Lou, Y.; Chen, X. *J. Phys. Chem. B* **2004**, *108*, 1230-1240.
- (39) Diwald, O.; Thompson, T. L.; Zubkov, T.; Goralski, E. G.; Walck, S. D.; Yates, J. T. *J. Phys. Chem. B* **2004**, *108*, 6004-6008.
- (40) Fleischauer, P. D.; Alan Kan, H. K. A.; Shepard, J. R. *J. Am. Chem. Soc.* **1972**, *94*, 283-285.
- (41) Hotsenpiller, P. A. M.; Bolt, J. D.; Farneth, W. E.; Lowekamp, J. B.; Rohrer, G. S. *J. Phys. Chem. B* **1998**, *102*, 3216-3226.
- (42) Lowekamp, J. B.; Rohrer, G. S.; Hotsenpiller, P. A. M.; Bolt, J. D.; Farneth, W. E. *J. Phys. Chem. B* **1998**, *102*, 7323-7327.
- (43) Diwald, O.; Thompson, T. L.; Goralski, E. G.; Walck, S. D.; Yates, J. T. *Journal of Physical Chemistry B* **2004**, *108*, 52-57.
- (44) Chen, X.; Burda, C. *J. Phys. Chem. B* **2004**, *108*, 15446-15449.
- (45) Sato, S.; Nakamura, R.; Abe, S. *Appl. Catal. A-Gen.* **2005**, *284*, 131-137.
- (46) Chen, X.; Lou, Y.; Samia, A. C. S.; Burda, C.; Gole, J. L. *Adv. Func. Mater.* **2005**, *15*, 41-49.
- (47) Di Valentin, C.; Pacchioni, G.; Selloni, A. *Phys. Rev. B* **2004**, *70*, 085116 1 - 4.
- (48) Nakamura, R.; Tanaka, T.; Nakato, Y. *J. Phys. Chem. B* **2004**, *108*, 10617-10620.
- (49) Miyauchi, M.; Ikezawa, A.; Tobimatsu, H.; Irie, H.; Hashimoto, K. *Phys. Chem. Chem. Phys.* **2004**, *6*, 865-870.
- (50) Lee, J. Y.; Park, J.; Cho, J. H. *Appl. Phys. Lett.* **2005**, *87*, 011904 1-3.
- (51) Di Valentin, C.; Pacchioni, G.; Selloni, A.; Livraghi, S.; Giamello, E. *J. Phys. Chem. B* **2005**, *109*, 11414-11419.
- (52) Burda, C.; Lou, Y.; Chen, X.; Samia, A. C. S.; Stout, J. D.; Gole, J. L. *Nano Lett.* **2003**, *3*, 1049-1051.
- (53) Diwald, O.; Thompson, T. L.; Goralski, E. G.; Walck, S. D.; Yates Jr., J. T. *J. Phys. Chem. B* **2004**, *108*, 52-57.
- (54) Yates Jr., J. T. *Experimental Innovations in Surface Science*; AIP and Springer-Verlag: New York, 1998.
- (55) Lu, G. Q.; Linsebigler, A.; Yates Jr., J. T. *J. Chem. Phys.* **1995**, *102*, 4657-4662.

- (56) Hoffmann, M. R.; Martin, S. T.; Choi, W. Y.; Bahnemann, D. W. *Chem. Rev.* **1995**, *95*, 69-96.
- (57) Bahnemann, D. W.; Hilgendorff, M.; Memming, R. *J. Phys. Chem. B* **1997**, *101*, 4265-4275.
- (58) Fox, M. A.; Dulay, M. T. *Chem. Rev.* **1993**, *93*, 341-357.
- (59) Berger, T.; Sterrer, M.; Diwald, O.; Knözinger, E.; Panayotov, D.; Thompson, T. L.; Yates, J. T. *J. Phys. Chem. B* **2005**, *109*, 6061-6068.
- (60) Lu, G. Q.; Linsebigler, A.; Yates Jr., J. T. *J. Chem. Phys.* **1995**, *102*, 3005-3008.
- (61) Perkins, C. L.; Henderson, M. A. *J. Phys. Chem. B* **2001**, *105*, 3856-3863.
- (62) de Lara-Castells, M. P.; Krause, J. L. *J. Chem. Phys.* **2003**, *118*, 5098-5105.
- (63) de Lara-Castells, M. P.; Krause, J. L. *J. Chem. Phys.* **2001**, *115*, 4798-4810.
- (64) de Lara-Castells, M. P.; Krause, J. L. *Chem. Phys. Lett.* **2002**, *354*, 483-490.
- (65) See Appendix C for details of the measurement of the UV penetration depth for TiO₂ films.
- (66) Micic, O. I.; Zhang, Y. N.; Cromack, K. R.; Trifunac, A. D.; Thurnauer, M. C. *J. Phys. Chem.* **1993**, *97*, 13284-13288.
- (67) Choi, W. Y.; Hoffmann, M. R. *Environ. Sci. Technol.* **1997**, *31*, 89-95.
- (68) Yamakata, A.; Ishibashi, T.; Onishi, H. *J. Phys. Chem. B* **2002**, *106*, 9122-9125.
- (69) Yoshihara, T.; Katoh, R.; Furube, A.; Tamaki, Y.; Murai, M.; Hara, K.; Murata, S.; Arakawa, H.; Tachiya, M. *J. Phys. Chem. B* **2004**, *108*, 3817-3823.
- (70) Ghosh, A. K.; Wakim, F. G.; Addiss, P. R. *Phys. Rev. Lett.* **1969**, *184*, 979-988.
- (71) Yagi, E.; Hasiguti, R. R.; Aono, M. *Phys. Rev. B* **1996**, *54*, 7945-7956.
- (72) Hasiguti, R. R. *Annu. Rev. Mater. Sci.* **1972**, *2*, 69-92.
- (73) Chester, P. F. *J. Appl. Phys.* **1961**, *32*, 2233-2236.
- (74) Kingsbury Jr., P. I.; Ohlsen, W. D.; Johnson, O. W. *Phys. Rev.* **1968**, *175*, 1091-1098.
- (75) Aono, M.; Hasiguti, R. R. *Phys. Rev. B* **1993**, *48*, 12406-12414.
- (76) Micic, O. I.; Zhang, Y. N.; Cromack, K. R.; Trifunac, A. D.; Thurnauer, M. C. *J. Phys. Chem.* **1993**, *97*, 7277-7283.

- (77) Howe, R. F.; Grätzel, M. *J. Phys. Chem.* **1987**, *91*, 3906-3909.
- (78) deJongh, P. E.; Vanmaekelbergh, D. *Phys. Rev. Lett.* **1996**, *77*, 3427-3430.
- (79) Fabre, E.; Mautref, M.; Mircea, A. *Appl. Phys. Lett.* **1975**, *27*, 239-241.
- (80) Schwarzburg, K.; Willig, F. *Appl. Phys. Lett.* **1991**, *58*, 2520-2522.
- (81) Barzykin, A. V.; Tachiya, M. *J. Phys. Chem. B* **2002**, *106*, 4356-4363.
- (82) Barzykin, A. V.; Tachiya, M. *J. Phys. Chem. B* **2004**, *108*, 8385-8389.
- (83) Iwata, K.; Takaya, T.; Hamaguchi, H.; Yamakata, A.; Ishibashi, T. A.; Onishi, H.; Kuroda, H. *J. Phys. Chem. B* **2004**, *108*, 20233-20239.
- (84) Nelson, J.; Haque, S. A.; Klug, D. R.; Durrant, J. R. *Phys. Rev. B* **2001**, *6320*, 205321-205329.
- (85) Szczepankiewicz, S. H.; Moss, J. A.; Hoffmann, M. R. *J. Phys. Chem. B* **2002**, *106*, 7654-7658.
- (86) Szczepankiewicz, S. H.; Moss, J. A.; Hoffmann, M. R. *J. Phys. Chem. B* **2002**, *106*, 2922-2927.
- (87) Kopidakis, N.; Schiff, E. A.; Park, N. G.; van de Lagemaat, J.; Frank, A. J. *J. Phys. Chem. B* **2000**, *104*, 3930-3936.
- (88) Frank, A. J.; Kopidakis, N.; van de Lagemaat, J. *Coord. Chem. Rev.* **2004**, *248*, 1165-1179.
- (89) Kuznetsov, A. I.; Kameneva, O.; Alexandrov, A.; Bityurin, N.; Marteau, P.; Chhor, K.; Sanchez, C.; Kanaev, A. *Phys. Rev. E* **2005**, *71*, 021403 1 - 7.
- (90) Hurum, D. C.; Gray, K. A.; Rajh, T.; Thurnauer, M. C. *J. Phys. Chem. B* **2005**, *109*, 977-980.
- (91) Singh, J. *Physics of Semiconductors and Their Heterostructures*; McGraw-Hill, Inc.: New York, 1993.
- (92) Hasiguti, R. R.; Yagi, E. *Phys. Rev. B* **1994**, *49*, 7251-7256.
- (93) Karazhanov, S. Z. *Semicond. Sci. Tech.* **2001**, *16*, 276-280.
- (94) Hoyer, P.; Weller, H. *J. Phys. Chem.* **1995**, *99*, 14096-14100.
- (95) Haque, S. A.; Tachibana, Y.; Willis, R. L.; Moser, J. E.; Gratzel, M.; Klug, D. R.; Durrant, J. R. *J. Phys. Chem. B* **2000**, *104*, 538-547.
- (96) Ho, C. T.; Bell, R. O.; Wald, F. V. *Appl. Phys. Lett.* **1977**, *31*, 463-465.

- (97) Panayotov, D. A.; Yates, J. T. *Chem. Phys. Lett.* **2004**, *399*, 300-306.
- (98) Kamat, P. V. *Prog. React. Kinet.* **1994**, *19*, 277-316.
- (99) Mora-Sero, I.; Dittrich, T.; Belaidi, A.; Garcia-Belmonte, G.; Bisquert, J. *J. Phys. Chem. B* **2005**, *109*, 14932-14938.
- (100) Leng, W. H.; Zhang, Z.; Zhang, J. Q.; Cao, C. N. *J. Phys. Chem. B* **2005**, *109*, 15008-15023.
- (101) Finger, M.; Haeger, A.; Hesse, D. *Chem. Eng. Technol.* **2005**, *28*, 783-789.
- (102) Berger, T.; Sterrer, M.; Diwald, O.; Knozinger, E. *Chemphyschem* **2005**, *6*, 2104-2112.
- (103) Rasmussen, M. D.; Molina, L. M.; Hammer, B. *J. Chem. Phys.* **2004**, *120*, 988-997.
- (104) Anpo, M.; Che, M.; Fubini, B.; Garrone, E.; Giamello, E.; Paganini, M. C. *Top. Catal.* **1999**, *8*, 189-198.
- (105) Thompson, T. L.; Yates Jr., J. T. *Top. Catal.* **2005**, *35*, 197-210.
- (106) Yates Jr., J. T. The Thermal Desorption of Adsorbed Species. In *Methods of Experimental Physics*; Park, R. L., Ed.; Academic Press: New York, 1985; Vol. 22.
- (107) Rusu, C. N.; Yates Jr., J. T. *Langmuir* **1997**, *13*, 4311-4316.
- (108) Kopelman, R. *J. Stat. Phys.* **1986**, *42*, 185-201.
- (109) Markovits, A.; Fahmi, A.; Minot, C. *Theochem* **1996**, *371*, 219-235.
- (110) Tanaka, K.; White, J. M. *J. Phys. Chem.* **1982**, *86*, 4708.
- (111) Tanaka, K.; Miyahara, K.; Toyoshima, I. *J. Phys. Chem.* **1984**, *88*, 3504-3508.
- (112) Yanagisawa, Y.; Sumimoto, T. *Appl. Phys. Lett.* **1994**, *64*, 3343-3344.
- (113) Yanagisawa, Y. *Energ. Convers. Manage.* **1995**, *36*, 443-446.
- (114) Liao, L. F.; Lien, C. F.; Shieh, D. L.; Chen, M. T.; Lin, J. L. *J. Phys. Chem. B* **2002**, *106*, 11240-11245.
- (115) Göpel, W.; Rucker, G.; Feierabend, R. *Phys. Rev. B* **1983**, *28*, 3427-3438.
- (116) Stone, P.; Bennett, R. A.; Bowker, M. *New J. Phys.* **1999**, *1*, 1.1-1.12.
- (117) Li, M.; Hebenstreit, W.; Gross, L.; Diebold, U.; Henderson, M. A.; Jennison, D. R.; Schultz, P. A.; Sears, M. P. *Surf. Sci.* **1999**, *437*, 173-190.

- (118) Henderson, M. A. *Surf. Sci.* **1999**, *419*, 174-187.
- (119) Weinberg, W. H. In *Kinetics of Interface Reactions*; Grunze, M., Kreuzer, H. J., Eds.; Springer-Verlag: New York, 1987; pp 95.
- (120) Tanner, R. E.; Castell, M. R.; Briggs, G. A. D. *Surf. Sci.* **1998**, *413*, 672-681.
- (121) Pang, C. L.; Haycock, S. A.; Raza, H.; Murray, P. W.; Thornton, G.; Gulseren, O.; James, R.; Bullett, D. W. *Phys. Rev. B* **1998**, *58*, 1586-1589.
- (122) Diebold, U.; Anderson, J. F.; Ng, K. O.; Vanderbilt, D. *Phys. Rev. Lett.* **1996**, *77*, 1322-1325.
- (123) Schaub, R.; Wahlstrom, E.; Ronnau, A.; Laegsgaard, E.; Stensgaard, I.; Besenbacher, F. *Science* **2003**, *299*, 377-379.
- (124) Schaub, R.; Thostrup, R.; Lopez, N.; Laegsgaard, E.; Stensgaard, I.; Norskov, J. K.; Besenbacher, F. *Phys. Rev. Lett.* **2001**, *87*, 226104 1 - 4.
- (125) Winkler, A.; Yates Jr., J. T. *J. Vac. Sci. Technol. A* **1988**, *6*, 2929 - 2932.
- (126) Khan, S. U. M.; Akikusa, J. *Int. J. Hyd. Energy* **2002**, *27*, 863 - 868.
- (127) O'Regan, B.; Grätzel, M. *Nature* **1991**, *353*, 737 - 740.
- (128) Khan, S. U. M.; Al-Shahry, M.; Ingler, W. B. *Science* **2002**, *297*, 2243-2245.
- (129) Umabayashi, T.; Yamaki, T.; Itoh, H.; Asai, K. *Appl. Phys. Lett.* **2002**, *81*, 454-456.
- (130) Sato, S. *Chem. Phys. Lett.* **1986**, *123*, 126-128.
- (131) Morikawa, T.; Asahi, R.; Ohwaki, T.; Aoki, K.; Taga, Y. *Jap. J. Appl. Phys. 2-Lett.* **2001**, *40*, L561-L563.
- (132) Walck, S. D.; McCaffrey, J. P. *Mat. Res. Soc. Symp. Proc.* **1997**, *480*, 149.
- (133) Prior work done by sputtering with nitrogen alone showed that nitrogen was incorporated, but after postannealing, significant nitrogen loss was observed. Using a heavier ion in conjunction with nitrogen allows for a more persistent implantation of the dopant through utilization of the so-called "knock on effect".
- (134) Saha, N. C.; Tompkins, H. G. *J. Appl. Phys.* **1992**, *72*, 3072-3079.
- (135) The effects seen in the first 50 A are representative for the pre-equilibrium region of the sputtering process and are ascribed to SIMS-specific phenomena arising from primary ion mixing and the chemical enhancement of the secondary ion yield.

- (136) Roch, T., Institute for Solid State Electronics, Technical University of Vienna, private communication.
- (137) Mooser, E.; Pearson, W. B. In *Progress in Semiconductors*; Gibson, A. F., Ed.; John Wiley and Sons: New York, 1960; Vol. 5; pp 53.
- (138) Serpone, N.; Lawless, D.; Khairutdinov, R. *J. Phys. Chem.* **1995**, *99*, 16646-16649.
- (139) Wolff, M.; Schultze, J. W. *Surf. Int. Anal.* 1988, *12*, 93-95.
- (140) Ohta, S.; Sekiya, T.; Kurita, S. *Phys. Status Solidi B* 2001, *223*, 265-269.
- (141) Schweitzer, C.; Reimann, K.; Steube, M. *Solid State Commun.* 1999, *110*, 697-700.
- (142) Samsonov, G. V. *The Oxide Handbook*; IFI/Plenum: New York, 1973.
- (143) Fukushima, K.; Yamada, I. *Jap. J. Appl. Phys.* **1996**, *35*, 5790-5793.
- (144) Fukushima, K.; Yamada, I. *Nucl. Instrum. Methods Phys. Res. Sect.* **1996**, *112*, 116.
- (145) Pankove, J. I. *Optical Processes in Semiconductors*; Dover Publications: New York, 1975.
- (146) Lee, E. C.; Kim, Y. S.; Jin, Y. G.; Chang, K. J. *Phys. Rev. B* **2001**, *64*, 085120 (085121-085125).
- (147) Liu, C. Y.; Bard, A. J. *J. Phys. Chem.* **1989**, *93*, 3232-3235.
- (148) Choi, W. Y.; Termin, A.; Hoffmann, M. R. *Angew. Chem. Int. Ed.* **1994**, *33*, 1091-1092.
- (149) Herrmann, J. M.; Disdier, J.; Pichat, P. *Chem. Phys. Lett.* **1984**, *108*, 618-622.
- (150) Anpo, M.; Takeuchi, M. *J. Catal.* **2003**, *216*, 505-516.
- (151) Hagfeldt, A.; Gratzel, M. *Chem. Rev.* **1995**, *95*, 49-68.
- (152) Irie, H.; Watanabe, Y.; Hashimoto, K. *J. Phys. Chem. B* **2003**, *107*, 5483-5486.
- (153) Lindgren, T.; Mwabora, J. M.; Avendano, E.; Jonsson, J.; Hoel, A.; Granqvist, C. G.; Lindquist, S. E. *J. Phys. Chem. B* **2003**, *107*, 5709-5716.
- (154) Farneth, W. E.; McLean, R. S.; Bolt, J. D.; Dokou, E.; Barteau, M. A. *Langmuir* **1999**, *15*, 8569-8573.
- (155) Rekoske, J. E.; Barteau, M. A. *J. Phys. Chem. B* **1997**, *101*, 1113-1124.

- (156) This produces a broad optical absorption (from 0.5 eV to 2 eV) that is associated with electronically reduced defects in the bulk.
- (157) The accuracy of the quantum yield in Table 2 is dependent on the validity of the assumptions made, i.e., the neglect of tip convolution effects and neglect to quantify features below the 2-nm threshold. The AFM probe has a finite radius, therefore the lateral dimensions of small protruding features from the surface are systematically overestimated. Thus the values in Table 2 are an upper limit for the actual quantum yields.
- (158) Souto, S.; Alvarez, F. *Appl. Phys. Lett.* **1997**, *70*, 1539-1541.
- (159) Minegishi, K.; Koiwai, Y.; Kikuchi, Y.; Yano, K.; Kasuga, M.; Shimizu, A. *Jap. J. Appl. Phys. 2-Lett.* **1997**, *36*, L1453-L1455.
- (160) Joseph, M.; Tabata, H.; Kawai, T. *Jap. J. Appl. Phys. 2-Lett.* **1999**, *38*, L1205-L1207.
- (161) Yamamoto, T. *Thin Sol. Films* **2002**, *421*, 100-106.
- (162) Mills, A.; LeHunte, S. *J. Photoch. Photobio. A* **1997**, *108*, 1-35.
- (163) Wu, W. C.; Chuang, C. C.; Lin, J. L. *J. Phys. Chem. B* **2000**, *104*, 8719-8724.
- (164) Wu, W. C.; Liao, L. F.; Lien, C. F.; Lin, J. L. *Phys. Chem. Chem. Phys.* **2001**, *3*, 4456-4461.
- (165) Chen, M. T.; Lien, C. F.; Liao, L. F.; Lin, J. L. *J. Phys. Chem. B* **2003**, *107*, 3837-3843.
- (166) Zhou, X. L.; Sun, Z. J.; White, J. M. *J. Vac. Sci. Technol. A* **1993**, *11*, 2110-2116.
- (167) Panayotov, D.; Yates Jr., J. T. *J. Phys. Chem. B* **2003**, *107*, 10560-10564.
- (168) Mawhinney, D. B.; Rossin, J. A.; Gerhart, K.; Yates Jr., J. T. *Langmuir* **1999**, *15*, 4617-4621.
- (169) Ballinger, T. H.; Wong, J. C. S.; Yates Jr., J. T. *Langmuir* **1992**, *8*, 1676-1678.
- (170) Newport Corporation Motion Control 1997 Catalog, Section 5, p. 8.
- (171) Highly Dispersed Metallic Oxides Produced by Aerosil Process. In *Degussa Technical Bulletin Pigments*, 1990; Vol. 56; pp 13.
- (172) Wu, W. C.; Liao, L. F.; Shiu, J. S.; Lin, J. L. *Phys. Chem. Chem. Phys.* **2000**, *2*, 4441-4446.
- (173) Wong, J. C. S.; Linsebigler, A.; Lu, G. Q.; Fan, J. F.; Yates Jr., J. T. *J. Phys. Chem.* **1995**, *99*, 335-344.

- (174) Sosa, C.; Bartlett, R. J.; KuBulat, K.-H.; Pearson, W. B. *J. Phys. Chem.* **1989**, *2*, 577-588.
- (175) Kozlov, D. V.; Vorontsov, A. V.; Smirniotis, P. G.; Savinov, E. N. *Appl. Catal. B-Environ.* **2003**, *42*, 77-87.
- (176) Farfan-Arribas, E.; Madix, R. J. *J. Phys. Chem. B* **2002**, *106*, 10680-10692.
- (177) Szczepankiewicz, S. H.; Colussi, A. J.; Hoffmann, M. R. *J. Phys. Chem. B* **2000**, *104*, 9842-9850.
- (178) Yamakata, A.; Ishibashi, T.; Onishi, H. *J. Phys. Chem. B* **2001**, *105*, 7258-7262.
- (179) Ghiotti, G.; Chiorino, A.; Boccuzzi, F. *Surf. Sci.* **1993**, *287*, 228-234.
- (180) Panayotov, D.; Yates Jr., J. T. *Chem. Phys. Lett.* **2003**, *381*, 154-162.
- (181) Panayotov, D.; Yates Jr., J. T. *J. Phys. Chem. B* **2004**, *108*, 2998-3004.
- (182) Anpo, M. *Pure Appl. Chem.* **2000**, *72*, 1265-1270.
- (183) Anpo, M. *Catal. Sur. Jpn.* **1997**, *1*, 169-173.
- (184) Sclafani, A.; Palmisano, L.; Schiavello, M.; Augugliaro, V. *New J. Chem.* **1988**, *12*, 129-134.
- (185) Muggli, D. S.; Falconer, J. L. *J. Catal.* **1999**, *187*, 230-237.
- (186) Muggli, D. S.; Falconer, J. L. *J. Catal.* **2000**, *191*, 318-325.
- (187) Zhuang, J.; Rusu, C. N.; Yates Jr., J. T. *J. Phys. Chem. B* **1999**, *103*, 6957-6967.
- (188) Martyanov, I. N.; Klabunde, K. J. *Environ. Sci. Technol.* **2003**, *37*, 3448-3453.
- (189) Panayotov, D. A.; Paul, D. K.; Yates Jr., J. T. *J. Phys. Chem. B* **2003**, *107*, 10571-10575.
- (190) Vorontsov, A. V.; Savinov, E. V.; Davydov, L.; Smirniotis, P. G. *Appl. Catal. B-Environ.* **2001**, *32*, 11-24.
- (191) Nakao, F. *Vacuum* **1975**, *25*, 431-435.
- (192) Rusu, C. N.; Yates Jr., J. T. *J. Phys. Chem. B* **2000**, *104*, 1729-1737.
- (193) Basu, P.; Ballinger, T. H.; Yates Jr., J. T. *Rev. Sci. Inst.* **1988**, *59*, 1321-1329.
- (194) Thompson, T. L.; Panayotov, D. A.; Yates, J. T. *J. Phys. Chem. B* **2004**, *108*, 16825-16833.

- (195) Primet, M.; Pichat, P.; Matthieu, M.-V. *J. Phys. Chem.* **1971**, *75*, 1216-1219.
- (196) Hadjiivanov, K. I.; Klissurski, D. G. *Chem. Soc. Rev.* **1996**, *25*, 61- 69.
- (197) Becker, M.; Fan, H. Y. *Phys. Rev.* **1949**, *76*, 1531-1532.
- (198) Briggs, H. B. *Phys. Rev.* **1950**, *77*, 727-728.
- (199) Briggs, H. B.; Fletcher, R. C. *Phys. Rev.* **1953**, *91*, 1342-1346.
- (200) Harrick, N. J. *Phys. Rev.* **1956**, *97*, 491-492.
- (201) Kahn, A. H. *Phys. Rev.* **1955**, *97*, 1647-1652.
- (202) Spitzer, W. G.; Fan, H. Y. *Phys. Rev.* **1957**, *106*, 882-890.
- (203) Meyer, H. J. G. *Phys. Rev.* **1958**, *1958*, 298-308.
- (204) Baratron, M.-I.; Merhari, L. *Scripta Mater.* **2001**, *44*, 1643-1648.
- (205) Baratron, M.-I.; Merhari, L. *Euro. Cer. Soc.* **2004**, *24*, 1399-1404.
- (206) Lamont, C. L. A.; Conrad, H.; Bradshaw, A. M. *Surf. Sci.* **1993**, *287*, 169-174.
- (207) Zhou, X. L.; White, J. M. Photodissociation and Photoreaction of Molecules Attached to Metal Surfaces. In *Laser Spectroscopy and Photo-Chemistry on Metal Surfaces*; Dai, H.-L., Ho, W. K., Eds.; World Scientific Publishing Co.: River Edge, NJ, 1995; Vol. 5; pp 1141-1240.
- (208) Roop, B.; Lloyd, K. G.; Costello, S. A.; Campion, A.; White, J. M. *J. Chem. Phys.* **1989**, *91*, 5103-5114.
- (209) Marsh, E. P.; Gilton, T. L.; Meier, W.; Schneider, M. R.; Cowin, J. P. *Phys. Rev. Lett.* **1988**, *61*, 2725-2728.
- (210) Holbert, V. P.; Garrett, S. J.; Stair, P. C.; Weitz, E. *Surf. Sci.* **1996**, *346*, 189-205.
- (211) Mezhenny, S.; Maksymovych, P.; Thompson, T. L.; Diwald, O.; Stahl, D.; Walck, S. D.; Yates Jr., J. T. *Chem. Phys. Lett.* **2003**, *369*, 152-158.
- (212) Grätzel, M. *Nature* **2001**, *414*, 338-344.
- (213) Grätzel, M. *J. Photoch. Photobio. C* **2003**, *4*, 145-153.
- (214) Wang, R.; Hashimoto, K.; Fujishima, A.; Chikuni, M.; Kojima, E.; Kitamura, A.; Shimohigoshi, M.; Watanabe, T. *Nature* **1997**, *388*, 431-432.
- (215) Wang, R.; Hashimoto, K.; Fujishima, A.; Chikuni, M.; Kojima, E.; Kitamura, A.; Shimohigoshi, M.; Watanabe, T. *Adv. Mater.* **1998**, *10*, 135-+.

- (216) Sunada, K.; Kikuchi, Y.; Hashimoto, K.; Fujishima, A. *Environ. Sci. Technol.* **1998**, *32*, 726-728.
- (217) Swamy, V.; Muscat, J.; Gale, J. D.; Harrison, N. M. *Surf. Sci.* **2002**, *504*, 115-124.
- (218) Charlton, G.; Howes, P. B.; Nicklin, C. L.; Steadman, P.; Taylor, J. S. G.; Muryn, C. A.; Harte, S. P.; Mercer, J.; McGrath, R.; Norman, D.; Turner, T. S.; Thornton, G. *Phys. Rev. Lett.* **1997**, *78*, 495-498.
- (219) Lindsay, R.; Wander, A.; Ernst, A.; Montanari, B.; Thornton, G.; Harrison, N. M. *Phys. Rev. Lett.* **2005**, *94*, 246102 1 - 4.
- (220) Fischer, S.; Munz, A. W.; Schierbaum, K. D.; Gopel, W. *Surf. Sci.* **1995**, *337*, 17-30.
- (221) Henderson, M. A. *Langmuir* **1996**, *12*, 5093-5098.
- (222) Epling, W. S.; Peden, C. H. F.; Henderson, M. A.; Diebold, U. *Surf. Sci.* **1998**, *413*, 333-343.
- (223) Bikondoa, O.; Pang, C. L.; Ithnin, R.; Muryn, C. A.; Onishi, H.; Thornton, G. *Accepted for publication by Nature Materials* **2006**.
- (224) Wendt, S.; Schaub, R.; Matthiesen, J.; Vestergaard, E. K.; Wahlstrom, E.; Rasmussen, M. D.; Thostrup, P.; Molina, L. M.; Laegsgaard, E.; Stensgaard, I.; Hammer, B.; Besenbacher, F. *Surf. Sci.* **2005**, *598*, 226-245.
- (225) Onishi, H.; Iwasawa, Y. *Surf. Sci.* **1994**, *313*, L783-L789.
- (226) Maksymovych, P.; Mezheny, S.; Yates, J. T. *Chem. Phys. Lett.* **2003**, *382*, 270-276.
- (227) Sakthivel, S.; Kisch, H. *Angew. Chem. Int. Ed.* **2003**, *42*, 4908-4911.
- (228) Tachikawa, T.; Tojo, S.; Kawai, K.; Endo, M.; Fujitsuka, M.; Ohno, T.; Nishijima, K.; Miyamoto, Z.; Majima, T. *J. Phys. Chem. B* **2004**, *108*, 19299-19306.
- (229) Nakano, Y.; Morikawa, T.; Ohwaki, T.; Taga, Y. *Appl. Phys. Lett.* **2005**, *87*, 052111 1- 3.
- (230) Di Valentin, C.; Pacchioni, G.; Selloni, A. *Chem. Mater.* **2005**, *17*, 6656-6665.
- (231) Dvoranova, D.; Brezova, V.; Mazur, M.; Malati, M. A. *Appl. Catal. B-Environ.* **2002**, *37*, 91-105.
- (232) Martin, S. T.; Morrison, C. L.; Hoffmann, M. R. *J. Phys. Chem.* **1994**, *98*, 13695-13704.
- (233) Li, X. Y.; Yue, P. L.; Kutal, C. *New J. Chem.* **2003**, *27*, 1264-1269.

- (234) Piera, E.; Tejedor-Tejedor, M. I.; Zorn, M. E.; Anderson, M. A. *Appl. Catal. B-Environ.* **2003**, *46*, 671-685.
- (235) Zhao, X. F.; Meng, X. F.; Zhang, Z. H.; Liu, L.; Jia, D. Z. *J. Inorg. Mater.* **2004**, *19*, 140-146.
- (236) Wu, S. X.; Ma, Z.; Qin, Y. N.; He, F.; Jia, L. S.; Zhang, Y. J. *Acta Phys.-Chim. Sin.* **2003**, *19*, 967-969.
- (237) Choi, W. Y.; Termin, A.; Hoffmann, M. R. *J. Phys. Chem.* **1994**, *98*, 13669-13679.
- (238) Karvinen, S.; Hirva, P.; Pakkanen, T. A. *J. Mol. Struct.-Theochem.* **2003**, *626*, 271-277.
- (239) Panayotov, D. A.; Yates, J. T. *Chem. Phys. Lett.* **2005**, *410*, 11-17.
- (240) Livingston, J. D. *Electronic Properties of Engineering Materials*; John Wiley and Sons, Inc.: New York, 1999.
- (241) Yamakata, A.; Ishibashi, T.; Onishi, H. *Chem. Phys. Lett.* **2001**, *333*, 271-277.
- (242) Rothenberger, G.; Moser, J.; Gratzel, M.; Serpone, N.; Sharma, D. K. *J. Am. Chem. Soc.* **1985**, *107*, 8054-8059.
- (243) Baraton, M. I.; Merhari, L. *Nanostruct. Mater.* **1998**, *10*, 699-713.
- (244) Iyengar, R. D.; Codell, M. *Adv. Coll. Int. Sci.* **1972**, *3*, 365-388.
- (245) Howe, R. F. *Adv. Coll. Int. Sci.* **1982**, *18*, 1-55.
- (246) Xiao-e, L.; Green, A. N. M.; Haque, S. A.; Mills, A.; Durrant, J. R. *J. Photoch. Photobio. A* **2004**, *162*, 253-259.
- (247) Tan, T.; Beydoun, D.; Amal, R. *J. Photoch. Photobio. A* **2003**, *159*, 273-280.
- (248) Du, Y. K.; Rabani, J. *J. Phys. Chem. B* **2003**, *107*, 11970-11978.
- (249) Nakamura, R.; Nakato, Y. *J. Am. Chem. Soc.* **2004**, *126*, 1290-1298.
- (250) Goto, H.; Hanada, Y.; Ohno, T.; Matsumura, M. *J. Catal.* **2004**, *225*, 223-229.
- (251) Shkrob, I. A.; Sauer, M. C. *J. Phys. Chem. B* **2004**, *108*, 12497-12511.
- (252) Lana-Villarreal, T.; Bisquert, J.; Mora-Sero, I.; Salvador, P. *J. Phys. Chem. B* **2005**, *109*, 10355-10361.
- (253) Henderson, M. A.; Epling, W. S.; Peden, C. H. F.; Perkins, C. L. *J. Phys. Chem. B* **2003**, *107*, 534-545.

- (254) Thompson, T. L.; Yates Jr., J. T. *Accepted, Journal of Physical Chemistry B* **2006**.
- (255) Zubkov, T.; Stahl, D.; Thompson, T. L.; Panayotov, D.; Diwald, O.; Yates Jr., J. T. *J. Phys. Chem. B* **2005**, *109*, 15454-15462.
- (256) Neumann, A. W.; Good, R. J. Techniques of Measuring Contact Angles. In *Surface and Colloid Science, Experimental Methods*; Good, R. J., Stromberg, R. R., Eds.; Plenum: New York, 1979; Vol. II.
- (257) Adamson, A.; Gast, A. *Physical Chemistry of Surfaces*; Wiley-Interscience: New York, 1997.
- (258) Sun, R. D.; Nakajima, A.; Fujishima, A.; Watanabe, T.; Hashimoto, K. *J. Phys. Chem. B* **2001**, *105*, 1984-1990.
- (259) Miyauchi, M.; Nakajima, A.; Fujishima, A.; Hashimoto, K.; Watanabe, T. *Chem. Mater.* **2000**, *12*, 3-5.
- (260) Nakajima, A.; Koizumi, S.; Watanabe, T.; Hashimoto, K. *J. Photoch. Photobio. A* **2001**, *146*, 129-132.
- (261) Sakai, N.; Fujishima, A.; Watanabe, T.; Hashimoto, K. *J. Phys. Chem. B* **2001**, *105*, 3023-3026.
- (262) Sakai, N.; Fujishima, A.; Watanabe, T.; Hashimoto, K. *J. Phys. Chem. B* **2003**, *107*, 1028-1035.
- (263) Nakajima, A.; Koizumi, S.; Watanabe, T.; Hashimoto, K. *Langmuir* **2000**, *16*, 7048-7050.
- (264) Miyauchi, M.; Kieda, N.; Hishita, S.; Mitsuhashi, T.; Nakajima, A.; Watanabe, T.; Hashimoto, K. *Surf. Sci.* **2002**, *511*, 401-407.
- (265) Sakai, N.; Wang, R.; Fujishima, A.; Watanabe, T.; Hashimoto, K. *Langmuir* **1998**, *14*, 5918-5920.
- (266) Wang, R.; Sakai, N.; Fujishima, A.; Watanabe, T.; Hashimoto, K. *J. Phys. Chem. B* **1999**, *103*, 2188-2194.
- (267) Bouzoubaa, A.; Markovits, A.; Calatayud, M.; Minot, C. *Surf. Sci.* **2005**, *583*, 107-117.
- (268) Gao, Y. F.; Masuda, Y.; Koumoto, K. *Langmuir* **2004**, *20*, 3188-3194.
- (269) Wang, C. Y.; Groenzin, H.; Shultz, M. J. *Langmuir* **2003**, *19*, 7330-7334.
- (270) Nakamura, M.; Makino, K.; Sirghi, L.; Aoki, T.; Hatanaka, Y. *Surf Coat Tech* **2003**, *169*, 699-702.

- (271) Onishi, H.; Iwasawa, Y. *Phys. Rev. Lett.* **1996**, *76*, 791-794.
- (272) Li, M.; Hebenstreit, W.; Diebold, U.; Henderson, M. A.; Jennison, D. R. *Faraday Discuss.* **1999**, *114*, 245-258.
- (273) Li, M.; Hebenstreit, W.; Diebold, U. *Phys. Rev. B* **2000**, *61*, 4926-4933.
- (274) Wu, X. Y.; Selloni, A.; Lazzeri, M.; Nayak, S. K. *Phys. Rev. B* **2003**, *68*, 241402 1-4.
- (275) Knotek, M. L.; Feibelman, P. J. *Phys. Rev. Lett.* **1978**, *40*, 964-967.
- (276) Ramsier, R. D.; Yates Jr., J. T. *Surf. Sci. Rep.* **1991**, *12*, 243-378.
- (277) Heinrich, V. E.; Cox, P. A. *The Surface Science of Metal Oxides*; Cambridge University Press: Cambridge, 1994.
- (278) Recently it was noted that the annealing temperature recorded in Science 299 (2003) 377 was incorrect. The actual annealing temperature was 900 K. (personal communication)
- (279) Thompson, T. L.; Diwald, O.; Yates, J. T. *Chem. Phys. Lett.* **2004**, *393*, 28-30.
- (280) Umebayashi, T.; Yamaki, T.; Tanaka, S.; Asai, K. *Chem. Lett.* **2003**, *32*, 330-331.
- (281) Umebayashi, T.; Yamaki, T.; Yamamoto, S.; Miyashita, A.; Tanaka, S.; Sumita, T.; Asai, K. *J. Appl. Phys.* **2003**, *93*, 5156-5160.
- (282) Miao, L.; Tanemura, S.; Watanabe, H.; Mori, Y.; Kaneko, K.; Toh, S. *J. Cryst. Growth.* **2004**, *260*, 118-124.